Event-Triggered Adaptive Position-Force Control of Robotic Manipulators in Medical and Cooperative Industrial Applications

A Thesis Submitted
in Partial Fulfilment of the Requirements
for the Degree of

DOCTOR OF PHILOSOPHY

By

MOHAMED ABBAS
(Roll No: 186103022)

Department of Mechanical Engineering
Indian Institute of Technology Guwahati
Guwahati - 781 039, INDIA.

October, 2022

Event-Triggered Adaptive Position-Force Control of Robotic Manipulators in Medical and Cooperative Industrial Applications

MOHAMED ABBAS

Declaration

I declare that this thesis entitled "**Event-Triggered Adaptive Position-Force Control of Robotic Manipulators in Medical and Cooperative Industrial Applications**", submitted by me is a presentation of my original research work done under the guidance of Dr. Santosha K. Dwivedy, Professor, Department of Mechanical Engineering, Indian Institute of Technology Guwahati. This work has not been submitted to any other University or Institute for the award of any degree or diploma.

Mohamed Abbas
Research Scholar,
Department of Mechanical Engineering,
Indian Institute of Technology Guwahati,
Guwahati, Assam, INDIA 781039,
Email: *abbas@iitg.ac.in, mohabbas9262@gmail.com*

Place: IIT Guwahati

Certificate

This is to certify that the thesis entitled "**Event-Triggered Adaptive Position-Force Control of Robotic Manipulators in Medical and Cooperative Industrial Applications**", submitted by **MOHAMED ABBAS** (186103002), a research scholar in the *Department of Mechanical Engineering, Indian Institute of Technology Guwahati*, for the award of the degree of **Doctor of Philosophy**, is a record of an original research work carried out by him under my supervision and guidance. The thesis has fulfilled all requirements as per the regulations of the Institute and in my opinion has reached the standard needed for submission. The results embodied in this thesis have not been submitted to any other University or Institute for the award of any degree or diploma.

Dated: 20.10.2022
Guwahati, Assam, India.

Prof. Santosha K. Dwivedy
Professor
Dept. of Mechanical Engg.
Indian Institute of Technology Guwahati
Guwahati - 781039, India.

Dedicated to

the memory of my mother

Acknowledgements

It gives me immense pleasure to thank each individual who supported me directly or indirectly in completing this journey. First, I would like to express my wholehearted gratitude to my supervisor Prof. Santosha K. Dwivedy, for his exceptional support and guidance throughout my doctoral work. Moreover, his dedication to his duties and research always inspires me. I will always be indebted to him for several thought-provoking ideas and the academic freedom he has given me. Besides, I would like to thank my doctoral committee members, namely, Prof. Shyamanta M. Hazarika, Prof. Nelson Mutu, and Prof. Dr. Harshal B. Nemade, for their constructive suggestions towards shaping my research goals as well as the entire thesis. My sincere gratitude go to the country in which I spent the best time of my life with many unforgettable memories, India. This country has allowed me to discover myself, meet new friends, and recognize amazing culture while feeling at home outside the home. Moreover, I would like to thank my parent organization, Al-baath university, Syria, for the financial support during my higher studies.

Fortunately, I have met with a few great fellow labmates during my doctoral journey with whom I have spent quality time. I am privileged to mention Mr. Jyotindra Narayan, the first guy I met in the early days of joining the Mechatronics and Robotics Laboratory. I am really grateful for all the research collaborations and constructive feedback on my progress. I will carry all the shared memories with you back home, and as we always say, "For sure, you have to visit us." I would also like to express my gratitude to Dr. Sami Al Issa for introducing me to the event-triggered mechanism which helped me throughout this thesis. I extend my acknowledgments to Mr. Bhavik Patel and Mr. Rahul Bharti, who supported my journey from several perspectives.

I was also lucky to be surrounded by many friends who shared the sad and happy moments during this journey away from home. Special thanks go to Ali Youness for being the real friend who I can share all my thoughts and problems with him. I also thank the Syrian friends on the IITG campus, Malek, Ali, Ghadir, Juana, and Nouma, who have been a family with whom I spent great times. I would further like to thank my university friends in Syria, Suliman, Siraj, Rasheed, and Ali, for their emotional support and for

being great friends all these years despite the distances.

Last but not least, I would like to thank my family members for their constant support, love, motivation, and faith in me. From the core of my heart, I would like to thank my father for showering immense love and moral support from the childhood until this moment. My thanks also go to my second family (my wife's family) for their unconditional love and support. Special thanks to my brother Husein who stood by me, bear with me, and took the headache of every day paper work and signatures during this journey. Finally, my most sincere thanks go to my dear wife, Nour, for all her patience, support, and unconditional love during my higher studies and for having faith in my academic carrier. The whole Ph.D. journey could not have come true without your day-to-day support and encouragement.

Mohamed Abbas

Abstract

Motivated by human dexterity and coordination, robotic manipulators have drawn the attention of researchers in recent years. These manipulators can mimic the human manipulation property and provide assistance at improved accuracies far exceeding those of human operators. Therefore, the adoption of robotic manipulators is demanded in diverse medical and industrial scenarios to fulfill several tasks such as ultrasound scans, rehabilitation exercises, and cooperative manipulation. On the other hand, networked control systems (NCSs) have become very popular in the last few years, introducing several benefits such as flexibility, reliability, and ease of maintenance for practical robotic applications. However, the implementation of such communication poses different constraints, including limited bandwidth channels. Moreover, parametric uncertainties and interaction forces are crucial to consider in the human-robot and robot-environment interaction tasks. Therefore, designing an appropriate controller to achieve the desired position and force tracking for robotic manipulators under the network-induced limited bandwidth, parametric uncertainties, and interaction forces is challenging and open to research. This thesis proposes a few simultaneous position-force control schemes to overcome the aforementioned challenges and maintain the performance and stability of the robotic manipulators in different medical and cooperative industrial applications.

The first part of the thesis is primarily dedicated to designing event-triggered simultaneous position-force controllers for single robotic manipulators in different medical applications, i.e., ultrasound examination and passive and active-assist rehabilitation exercises. The first study presents an event-triggered adaptive hybrid position-force control (ETAHPFC) scheme for the ultrasound manipulator to perform a transversal abdomen scan. An adaptive backstepping position controller with an online adaptation law is designed to ensure the stability of the ultrasound robot in the presence of parametric uncertainties. A proportional-integral-derivative (PID) force controller is utilized to maintain a constant interaction force during the scan process. Rather than periodic time-triggered (TT) implementation, the Lyapunov-based triggering condition is proposed to update the control inputs in an aperiodic manner, reduce the communication burden, and preserve the stability of the robotic system during the task. In the second study,

the event-triggered adaptive backstepping admittance control (ETABAC) scheme is devised to address the uncertainties, limited communication, and patient-robot interaction challenges during the upper limb rehabilitation exercises. The same adaptive backstepping approach and Lyapunov-based event-triggered (ET) mechanism are utilized to deal with dynamic uncertainties and overcome the limited communication challenge. The admittance controller is integrated to maintain a compliant patient-robot interaction and consider the participation of the patient in the therapeutic sessions.

In the second part of the thesis, the ETAHPFC and ETABAC are further extended for the framework of cooperative manipulators to tackle the parametric uncertainties in the models of the object and manipulators, environmental interaction, and limited communication constraints. Firstly, the adaptive backstepping position controller is augmented with a positional error-based state variable and the nonlinear damping term to improve the trajectory tracking performance during the cooperative manipulation of a common object. Moreover, the force control scheme is established to maintain constant internal forces. After that, the improved position controller is combined with the external and internal admittance models to project an impedance relation and achieve a compliant interaction between manipulators/object and object/environment during the cooperative manipulation task. Based on the Lyapunov analysis, the event-triggered mechanism is designed to alleviate the controller-to-robot communication burden and preserve the system stability of the cooperative system. The effectiveness of the proposed control strategies is investigated based on several comparison studies with different time-triggered and event-triggered adaptive control schemes. Moreover, the designed triggering mechanism is compared with various triggering conditions presented in the literature. Based on the several simulation runs, the proposed controllers have shown promising tracking behavior, appropriate compliant interaction, and efficient utilization of the network resources during different medical and cooperative manipulation applications.

In addition to simulation and comparison results, the experimental validation of the proposed event-triggered adaptive control schemes is conducted for two scenarios, i.e., upper-limb passive rehabilitation training for different subjects and cooperative manipulation of a common object. To overcome the hardware restrictions of the commercial voltage- and position-controlled robotic manipulators, the dynamic model of these robots is modified to admit the direct voltage and position commands as control inputs which are desirable in practical implementations. From the experimental results, the proposed control schemes are found to achieve a promising tracking performance and substantial saving of channel bandwidth in the presence of parametric uncertainties, which confirms the suitability of the theoretical propositions for practical network-based applications.

Contents

List of Figures

List of Tables

List of Acronyms

ACTC	Adaptive computed torque control
ADLs	Daily living activities
APFC	Adaptive position force control
ASMC	Adaptive sliding model control
BLF	Barrier Lyapunov Function
C-R	Controller-to-robot channel
COM	Center of mass
DMI	Desired Motion Intention
DOF	Degree of freedom
EERR	End-effector type rehabilitation robot
ET	Event-triggered
ETABAC	Event-triggered adaptive backstepping admittance control
ETAC	Event-triggered adaptive control
ETAHPFC	Event-triggered adaptive hybrid position force control
ETSMC	Event-triggered sliding mode control
ExoRR	Exoskeleton type rehabilitation robot
FTS	Flight Telerobotic Servicer
GBD	Global burden of disease
GCC	Gravity compensation controller
IAE	Integral absolute error

ISE	Integral of square error
NCS	Networked control system
NN	Neural network
PD	Proportional derivative
PI	Performance index
PID	Proportional-integral-derivative
PUMA	Programmable Universal Machine for Assembly
PWM	pulse width modulation
RBFNN	Radial basis function neural network
R-C	Robot-to-controller channel
RMSE	Root-mean-square-error
ROM	Range of motion
RR	Rehabilitation robots
SCI	Spinal cord injury
SMC	Sliding model control
TT	Time-triggered
TT-ACTC	Adaptive computed torque control
TT-APFC	Adaptive position-force control
USR	Ultrasound robots
ZOH	Zero-order-hold

List of Symbols

$\forall$	For all
inf	Infimum
$\in$	Belong to
$\dagger$	Pseudo inverse
$\lvert\cdot\rvert$	Absolute value of a scalar argument
$\lVert\cdot\rVert$	Euclidian norm for vectors and spectral norm for matrices
$(\cdot)^T$	Transpose of the argument (vector or matrix)
$\max(\cdot)$	The maximum of the arguments
$\min(\cdot)$	The minimum of the arguments
$S(\cdot)$	Skew-symmetric matrix operator
$\lambda_{min}(\cdot)$	Minimum eigenvalue of the argument
$\Im_{e,i}$	Coordinate frame at the i-th manipulator's end-effector
$\Im_o$	Coordinate frame attached to the object's center of mass
$\Im_w$	World reference frame
$\mathbb{R}$	The space of real numbers
$\mathbb{R}^n$	The space of real valued vectors of dimension n
$\mathbb{R}^{n\times m}$	The space of real valued $n \times m$ matrices
Π	Regression matrix
Π_{x_o}	Regression matrix of cooperative manipulators
α	Virtual control law
β	Arbitrary real vector
φ	Vector of unknown parameters
$\tilde{\varphi}$	Estimation error
$\hat{\varphi}$	Estimation of the unknown parameters
φ_{x_o}	Vector of unknown parameters of cooperative manipulators
μ	Arbitrary known vector
$\dot{\theta}_m$	Velocity of motor shaft
$\ddot{\theta}_m$	Acceleration of motor shaft
ρ_1, ρ_2	Positive constant
τ_f	Force controller

τ_{int}	Vector of interaction torque
τ_m	Motor torque
τ_p	Position controller
τ_R	Control input
$\bar{\tau}_R$	Event-triggered control input
ω_o	Angular velocity of the object frame
ζ	User-defined positive parameter
Γ	Positive definite diagonal matrix
$C_o(x_o, \dot{x}_o)$	Centrifugal and Coriolis effects matrix
$C_R(\dot{q}, q)$	Coriolis and centrifugal effects matrix
$C_T(x_o, \dot{x}_o)$	Total Centrifugal and Coriolis effects matrix for cooperative manipulators
e_f	Force error
e_k	k-th element of error vector
e_m	Measurement error
e_p	End-effector position error
e_q	Joint position error
e_x	Tracking error in X-direction
e_y	Tracking error in Y-direction
e_z	Tracking error in Z-direction
F_d	Desired force
F_{env}	Vector of forces applied to the environment by the object
F_{ex}	Resultant forces at the manipulated object
F_E	External force
F_{int}	Interaction force
F_I	Internal force
$G_o(x_o)$	Vector of gravitational forces
$G_R(q)$	Vector of gravitational torques
$G_T(x_o)$	Vector of gravitational forces for cooperative manipulators
I_n	Identity matrix of dimension n
J	Jacobian matrix
k_1, k_2	Positive diagonal gain matrix of backstepping
K_{env}	Stiffness matrix
M_{ad}, C_{ad}, K_{ad}	Symmetric positive definite admittance matrices
$M_R(q)$	Inertia matrix
$M_o(x_o)$	Inertia matrix of manipulated object
$M_T(x_o)$	Total inertia matrix for cooperative manipulators
n	Number of degree of freedom
N_e	Number of error points

p_o	Position vector of the object frame
q	Joint position
q_d	Desired joint position
$\dot{q}$	Joint velocity
$\dot{q}_d$	Desired joint velocity
$\ddot{q}$	Joint acceleration
R_o	Rotation matrix of the object frame
S	Compliance selection matrix
t	Time in second
$T_{con}(e_m, z_1, z_2)$	Designed triggering function
v_1, v_2, v_3, v_4	Positive constants
V_1, V_2	Lyapunov function
W	Grasp matrix
x_e	Vector of end-effector pose
x_{ed}	Vector of end-effector desired pose
x_{er}	Vector of end-effector reference pose
x_{env}	Position of the contact point
x_o	Vector of manipulated object pose
$x_{o,d}$	Vector of manipulated object desired pose
$x_{o,r}$	Vector of manipulated object reference pose
$\dot{x}_e$	Vector of end-effector velocity
$\dot{x}_o$	Vector of manipulated object velocity
$\ddot{x}_e$	Vector of end-effector acceleration
$\ddot{x}_o$	Vector of manipulated object acceleration
X	State vector
z_1, z_2	Error variables

1

Introduction

Contents

1.1 Background

The early realization of the robotic system returns to the 1950s by George Devol, who invented the first robotic manipulator with the company Unimation. This robot was only devoted to performing repetitive tasks and transferring objects from one position to another. A few years later, the same company produced a Programmable Universal Machine for Assembly (PUMA) robot for more complicated tasks like welding and assembly. Many companies started in the subsequent years setting up the market in the field of robotics and automation with limited applications to the industries. However, due to their potential in facilitating human life and performing multiple tasks, the last three decades have witnessed increased integration of the single robotic manipulators in a wide range of fields such as construction [1], medical [2], military [3], agriculture [4], space [5], and sea exploration [6]. For instance, the robotic manipulator can replace humans in hazardous environments such as mining and manipulating radioactive substances in nuclear power plants. It can also carry out rehabilitation exercises for patients with impaired limbs.

Although the employment of a single robotic manipulator is efficiently feasible in many applications; however, the need for multitasking, better work productivity, cost-effectiveness, and flexible automation triggered the development of cooperative manipulators with human-like distinctive features [7]. These cooperative manipulators can mimic the human manipulation property and provide a higher carrying capacity than single-arm manipulators. Therefore, the adoption of cooperative manipulators is demanded to fulfill several complex tasks such as the assembly of mechanical parts [8], transportation of immense objects [9], and grinding works [10]. The development of cooperative robots significantly impacts the medical field, where it can help the nurses in patient-transferring tasks and monitor the patients' statistics [11]. Moreover, it can be utilized to perform medical surgeries with less time and cost for the patients [12].

The early recognition of cooperative manipulation with the concept of a tele-operated dual-arm manipulator was found between the 1940s and 1950s. It was utilized to transmit the bimanual dexterity of the operator to a remote place and avoid human intercalation in a dangerous environment [13, 14]. In another work by Goertz at Argonne National Laboratory [15], a cooperative robotic manipulator was constructed and used further to manipulate radioactive substances in a hot tank without the presence of a human. In 1958, Mosher built a cooperative dual-arm master-slave robot named Handyman at General Electric Company. This robot had two electrohydraulic arms (10 DOFs each), and two fingers at the end effector [16]. In 1969, NASA decided to construct Flight Telerobotic Servicer (FTS) to help the astronauts to organize the space station and for manipula-

tion purposes [17]. Thereafter, the essential concepts behind cooperative manipulation were investigated, such as motion coordination, control strategies, motion planning, and grasping. Kurono [18], in 1972, proposed a master-slave force control strategy for controlling two artificial hands. In 1974, Nakano [19] utilized the same control scheme to coordinate the motion of two robotic arms holding a common object and emphasized the usage of force control in cooperative manipulation. From 1980 to 1990, several new definitions and theoretical concepts were proposed for the well-known connotations of the single-arm manipulator [20]. The concepts were devoted to understanding the kinematic [21], dynamic [22] and control [23–25] for the closed cooperative workspace between the manipulators and the handled objects.

1.2 Motivation

The growth of interest in the use of medical robots has been dramatic over the last two decades [26]. This include but not limited to surgical robots [27], ultrasound robots (USR) [28], rehabilitation robots (RR) [29, 30], and disinfection robots [31]. This thesis partly addresses the implementation of robotic systems in the ultrasound examination and rehabilitation tasks. According to the literature, most radiologists examine musculoskeletal strain due to the repetitive physical interaction with the ultrasound (US) probe [32]. The quality of the acquired image through the ultrasound probe highly depends on its position, orientation, and applied force during the scan process [33, 34]. Therefore, many research studies have been conducted on integrating ultrasound scanning with robotic systems [35–37]. The importance of ultrasound robots lies in their ability to provide accurate, dexterous, and repeatable control of the probe in an awkward posture [35]. Furthermore, the ultrasound robots allow the remote diagnosis and prevent the shoulder and neck strain accompanied with the traditional ultrasound process [38].

On the other hand, neurological diseases such as stroke, spinal cord injury (SCI), and multiple sclerosis adversely impact the social and personal living standards of human beings. In most cases, the regular supply of blood flow to the brain is blocked by the impaired blood vessels [39]. A study by Global Burden of Disease (GBD) [40] affirmed the 'stroke' as the second principal cause of disability in 2019 for elderly people (> 50 years). The majority of the stroke survivors suffer from hemiplegia in which they face different auguries such as muscle feebleness, postural instability, abnormal muscle structure, and restrained movements [41]. The hemiplegic subjects can recuperate their mobility functions and perform daily living activities (ADLs) using physical rehabilitation therapies. The traditional rehabilitation approaches, carried out by physical therapists, have been used extensively to improve the motor functionality of the upper limbs. However,

such approaches suffer from exhaustive training periods, skilled labor involvement, and less cost-effectiveness and sustainability [42]. Therefore, from the last decade, a robot-assisted rehabilitation system draws researchers' attention to overcome these problems and improve motor functions [43, 44].

The motivation for using the cooperative manipulators in various fields, such as industrial, medical, space, military, and daily life, are as follows. First, the feasibility to perform complex tasks that cannot be achieved by a single-arm manipulator without any special tools viz. cloths folding [45] and the assembly task of the bolts and nuts [46]. Second, mimicking the human appearance and movements to work cooperatively in the same environment without redesigning the workspace [47–49]. Therefore, in this way, it can be used in a teleoperation task where the operator's bimanual dexterity can be transmitted to remote place and execute the same task using the dual-arm [50]. Third, using cooperative manipulators, the performance of a serial manipulator can be combined with the stiffness of parallel manipulator to achieve robust design features. Fourth, the productivity of the work and cost-effectiveness of the automation process can be improved with overall reduction in process time. However, the cooperative manipulators incorporate an additional intricacy over the conventional manipulator and pose huge challenges due to the requirement of advanced embedded systems and different control approaches.

In recent years, networked control systems (NCSs) have attracted the attention of researchers in both academia and industry. A paradigm shift in the ways feedback controllers interact with the system dynamics have been witnessed in control engineering. The classical port-to-port based control is found to be incompetent in meeting the requirements of growing practical applications. Therefore, it is being discarded nowadays by placing a shared communication network between the control system components. This implementation leads to a flexible architecture and reduces the maintenance time and cost [51]. Besides, it allows the control systems to have less wiring which is beneficial to satisfy many operational constraints. These advantages open the door of many practical applications such as remote-controlled robotic systems [52], haptic robot-assisted system, unmanned aerial vehicles, production lines, and chemical plants. However, different constraints and imperfections may occur due to the integrated communication network in the feedback loop. These imperfections include limited channel bandwidth, time delay, and drop of packages which, if not considered, may degrade the performance and cause the instability of the networked control system [53]. Hence, the design and stability analysis of control strategy that communicate with the robotic system over a network channel is an emerging topic of interest and a challenging task for researchers [54].

The key objective of this thesis is to design and implement robust networked control schemes for the single and cooperative manipulator systems in different medical and

cooperative industrial applications while addressing their corresponding challenges. The following Section 1.3 presents the detailed literature of the control strategies utilized in the field of single and cooperative manipulator systems along with their research provocations. Based on the review, potential research gaps are identified in Section 1.4 which motivates to carry out the present research work. The objectives of the present work are highlighted in Section 1.5. Finally, the organization of the thesis is outlined in Section 1.6.

1.3 Literature Review

In this section, the applications of robotic manipulator system in different fields are presented at first. Thereafter, the state-of-the-art researches related to the available control strategies of robotic manipulator systems in medical and cooperative manipulation applications are discussed in details. Finally, the types and configurations of event-triggered mechanism are given in the last subsection.

1.3.1 Robotic Applications

The applications of the robotic manipulators in medical and cooperative industrial fields along with their categories and types are presented below.

Ultrasound Robots

The design of the ultrasound robot can be classified into three main categories. In the first category [55, 56], a haptic device is dedicated to move the manipulator by the sonographer remotely. Moreover, the sonographer can control the applied force on the patient's skin with the help of force feedback measurement. This category is commonly known as a tele-operated ultrasound robot. Conti et al. [55] presented a 6-DOFs tele-operated ultrasound robot with a 3-D visualization system. Moreover, Geng et al. [56] utilized velocity-based master-slave control to perform the ultrasound scanning using a UR5 robotic manipulator. In the second category, named human-ultrasound robot cooperation, the human participates along with the robot to control some degree of freedom [57]. The third category, called autonomous ultrasound robot [58, 59], provides automatic scanning of the desired location without the sonographer's help. Seitz et al. [59] utilized a KUKA LBR robotic manipulator to perform an autonomous ultrasound scan with motion and breathing compensation. The preservation of a 5N contact force is achieved for different breathing amplitudes. Janvier et al. [58] proposed a 6-DOFs ultrasound robot to scan the lower limb vessels based on the regeneration of taught trajectory.

Rehabilitation Robots

According to the literature [60], the robot-assisted upper limb rehabilitation system can be classified into two categories, i.e., exoskeleton type rehabilitation robot (ExoRR) [61–63] and end-effector type rehabilitation robot (EERR) [64–67]. In general, three therapy modes are used to assist the upper-extremity movements: passive, active-assist, and active-resist [41]. The exoskeleton type robots mimic the human's upper- and lower-limb and offer a synchronous joint movement during rehabilitation training. However, in EE-type robots, the partial or complete movement of the subject's limb is guided by the proximal end of the robotic device. This thesis is limited to the literature of only existing EERRs. For instance, EEULRebot [64] is an EERR that consists of a rear-arm and forearm mechanical link to assist hemiplegic subjects using straight-line and circular trajectory tracking. Moreover, handle support and elbow base to are provided to place the subject's arm in a comfortable posture. Sivan et al. [65] proposed another EERR, named hCAAR, for the upper-limb rehabilitation measures and tested with 17 stroke subjects. In other work on recovering nerve strength, PARM [66] robot with a parallel configuration is exploited for both subject-passive and active therapeutic measures on the upper-limb. Becker et al. [67] utilized an EERR, named Iiwa 14 by KUKA, to improve the muscle capabilities using 3-dimensional exercises and compared the robot-aided training outcomes with the results of freely performed ones.

Cooperative Manipulators

Cooperative manipulators are defined as several harmonious manipulators which accomplish the desired task by imitating the cooperative movement of human arms effectively. This wide definition of cooperative manipulators covers many different manipulation approaches: dual-arm manipulations, fingers' movements with respect to the hand, a group of separate manipulators collaborating together, and a human collaboration with robotic manipulators in their workspace [68,69]. According to the coordination of the performed task, the cooperative manipulators can be divided into two types: Simultaneous-Coordinated: the manipulators physically interact with the same object, e.g., two arms trying to pick and place a box from one location to another or three robotic fingers holding a common cup. Task-Coordinated: the manipulators perform the same task without physical interaction between them. e.g., two manipulators prepare a cup of tea where one manipulator holds the cup and the other one pours the hot water inside it.

1.3.2 Control of Robotic Manipulators

The control of robotic manipulators (single or cooperative) can be classified into two main categories i.e., kinematic control and dynamic control. In kinematic control, the joint positions are calculated based on the inverse kinematic equations to achieve

the desired motion defined at the end-effector level (task space). However, this control suffers some demerits which can affect the performance of the manipulator. It does not consider the load dynamics of the manipulator and\or manipulated object in the design process which may increase the steady state error. It also ignore the effects of uncertainties and disturbances such as unknown dynamical parameters and fractional forces. Moreover, this approach is not adequate to provide the manipulator with the required complaint behavior. This behavior is necessary in many applications, including the interaction of the robot with human or the interaction between the manipulated object and external environment. In dynamic control, the desired motion in joint space or task space is attained by calculating the required torques or forces to act at the joints of the manipulator. This control strategy overcome the limitations of kinematic controller and allow to regulate not only the motion of the manipulators but also the interaction forces to achieve a proper compliant behavior. Moreover, it can be designed to reject any undesirable dynamical behavior and tackle the various challenges mentioned below.

Interaction Forces

Several applications in medical field require the robotic manipulator to interact with human while performing a specific operation. For example, the ultrasound probe should follow certain motion while applying a forces on human body to obtain a clear image in the robot-assisted ultrasonic examination. A compliant patient-robot interaction should also be maintained to achieve a proper rehabilitation exercise using the therapeutic manipulator. These interaction forces need to be controlled along with the motion of the manipulator to fulfill the desired task without hurting the patients. On the other hand, during the cooperative manipulation tasks (e.g., transportation of a common object), a set of closed kinematic chain constraints develops on the motion of the whole system, which leads to the generation of internal forces. In addition, unavoidable external forces are produced due to the interaction between the object and the unknown external environment. Controlling these internal and external forces is indispensable to avoid the grasp failure and the damage of the manipulators or the manipulated object. Therefore, the traditional position-based control schemes are insufficient for these applications and there is an essential need to investigate the design of simultaneous position-force control strategies.

According to the literature, hybrid position-force control [70, 71] and impedance/ admittance control [72] have been extensively devoted to maintain a safe grasp without the development of high contact forces during the different robotic interaction tasks. In the hybrid position-force control, a continuous switch between the position and force modes is required during the changes of contact and non-contact cases. The delay in the switch-

ing mechanism may lead to a considerable deviation in the position tracking [73] without maintaining a perfect compliant behavior [74]. However, this control scheme is suitable for robotic manipulators designed to perform tasks that require precise position and force tracking performance. In the impedance/admittance control, a proper compliance behavior can be achieved by imposing a mechanical impedance/admittance relationship between the position errors and the interaction forces [75]. The controller generates the forces due to the motion deviation (position errors) in the impedance control. However, the opposite takes place for admittance control; and a new reference trajectory is generated as a response to the interaction forces. This control scheme is suitable for applications require to maintain a compliant behavior rather than precise regulation of interaction forces at predefined values. Therefore, the switching process accompanied with hybrid control is avoided in impedance/admittance control.

Parametric Uncertainties

There is a lack of knowledge about the exact dynamic model of the robotic manipulator by the user/designer in practical applications. The dynamic parameters of the robotic manipulator and the manipulated object (such as inertia, mass, link length) might be unknown or slowly varying with time (payload variation), resulting in parametric uncertainties. These uncertainties, if not considered, may degrade the performance of the control scheme and destabilize the whole robotic system. Therefore, the design of an efficient dynamic control strategy that ensure an acceptable performance of the manipulators and proper compliant behavior during the interaction in the presence of the parametric uncertainties become more challenging task.

Limited Communications

The architecture of a classical networked control system where the components of the robotic manipulator (sensors, actuators, and the controller) communicate via a shared wired or wireless channel is shown in Figure 1.1. Wired networks offer high bandwidth and provide low communication delay and jitter, making them suitable for applications where large amounts of data must be transferred quickly and reliably. However, they are expensive to install and maintain the physical cabling infrastructure. Moreover, fixed wiring can limit flexibility in the network configuration. They also have limited mobility compared to wireless networks and are vulnerable to physical damage, such as construction or accidents. On the other hand, wireless networks use radio waves to transmit data, allowing devices to communicate without being physically tethered to a network and providing greater flexibility and mobility. However, wireless networks can be affected by various environmental factors, such as distance, obstacles, and interference resulting in more limited bandwidth compared to wired ones. The actual bandwidth can also vary

depending on the specific wireless standard being used and the conditions of the wireless environment.

The communication between components of NCS is enabled through different protocols which define the format, syntax, semantics, and synchronization of communication while ensuring the accurate, reliable, and efficient data transmission. In the wired networked control systems, several communication protocols are found in the literature such as Controller Area Network (CAN), Modbus, and Ethernet for Control Automation Technology (EtherCAT). CAN, serial communication protocol, is used in automotive and industrial applications for real-time control and monitoring. It is known for its high reliability and robustness. On the other hand, Modbus defines the format of the messages sent between devices, the types of data that can be exchanged, and how errors are detected and handled. EtherCAT is a real-time communication protocol based on Ethernet technology. It is optimized for use in control applications and is designed to provide low communication latencies and high data throughput rates.

Talking about the wireless NCSs, Wi-Fi, Bluetooth, Zigbee, and Z-Wave are common examples of the communication protocols used for robotic applications. Wi-Fi provides high-speed data transfer over short to medium distances and commonly implemented for teleoperated robotics applications. Bluetooth offers low-power data transfer over short distances and is often used for applications such as human-robot interaction. Zigbee is another low-power wireless communication protocol that can be used for data transmission between sensors and robots. It provides a low data rate over long distances and is often used for sensor networks. In the time-triggered implementation of NCSs, the transmission instants are continuously generated (Figure 1.1). Every sampling time dt, the system states and control commands are sent over the network regardless of the requirement of the robotic system, resulting in ineffective usage of the network resources, viz. channel-bandwidth, energy, and computational efforts. Therefore, the event-triggered (ET) mechanism has been introduced recently to be an effective solution to alleviate the unwarranted waste of resources for efficient network-based applications [76], especially for wireless network where the limited bandwidth is one of the main drawback that affect the transmitted data in the controller-to-robot (C-R) and robot-to-controller (R-C) channels.

Hardware Restrictions

From the perspective of experimental validation, the dynamic control schemes which generate the required torque signals cannot be directly implemented on the real-time robotic systems. This is attributed to the fact that most of the available robotic manipulators in the market are either actuated by permanent magnet DC motors or servo motors (driven via position signals). The DC motors are driven by electronic drivers via the pulse width

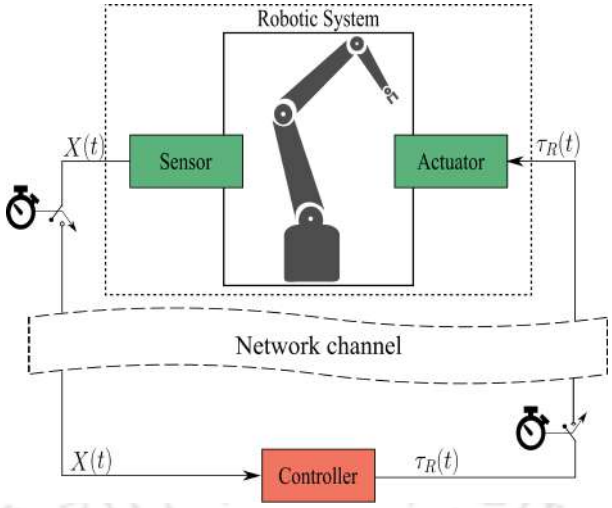

Figure 1.1: The architecture of classical time-triggered NCS.

modulation (PWM). However, the servo motors accept the direct position signals and contain internal kinematic controller to regulate these input signals. On the other hand, the characteristics of these motors and the internal parameters of the servo controllers are not always provided by the manufacturers. Therefore, a proper modification is required to allow the implementation of the dynamic control schemes on commercial robotic systems. However, such modifications make the design process of the controller more challenging.

In the following subsection 1.3.2.1, the available control strategies for the single manipulator in the ultrasound examination and rehabilitation applications are presented. Thereafter, the control schemes to achieve the cooperative manipulation using multiple robotic manipulators are discussed in subsection 1.3.2.2. The event-triggered control schemes and the hardware restrictions are brought in subsection 1.3.2.3.

1.3.2.1 Controllers for Robotic Manipulators in Medical Applications

The most commonly used strategies in controlling the robotic manipulators depend on position or stiffness control [77, 78]. These strategies can be utilized to attain an acceptable position tracking performance in the presence of dynamic uncertainties and external disturbances [79–81]. However, to achieve a visible live US scanning, the control strategies designed for the ultrasound robots should ensure not only the accurate location of the US probe; but also precise control of the contact force between the US probe and the patient's skin. Zhu et al. [82] designed a controller for a 6-DOFs manipulator to perform ultrasound carotid artery diagnosis. The desired position and force are achieved based on an inner loop velocity tracking controller. Mathiassen et al. [83] utilized a compliance control strategy proposed by Siciliano et al. [84]. This technique is employed

to control the UR5 robot while performing the ultrasound scanning. The same approach is dedicated to maintain contact between the US probe and the patient's skin during the autonomous liver scanning [85]. Fang et al. [35] utilized an admittance force control to follow the motion of the sonographer during the scanning process. Moreover, it is also used to magnify the forces applied by the operator to obtain a steady US image. Karar [86] proposed an adaptive fuzzy proportional-integral-derivative (PID) force control to maintain the force applied during the ultrasound abdomen scanning at the desired level. The fuzzy logic approach is utilized to tune the PID gains to compensate for the respiratory motion. It has been observed that the acceptable force range for liver scanning varies from 3N to 5.5N. Victorova et al. [87] utilized the hybrid control proposed by Craig [70] to maintain the contact forces at the desired level while performing the scoliosis scanning. However, the above methods do not include the nominal model of the robotic system in the controller's design. In the practical application, better tracking performance is achieved by incorporating the system information in the controller design.

Conventional hybrid position-force control intends to control both the end-effector motion and the interaction force in two independent directions. This decomposition is achieved either by the selection matrices acting on both the desired and actual quantities [70] or with the help of the projection matrix obtained from the gradient of surface equation [88]. This hybrid position-force control approach may attain a reasonable performance during the motion and force tracking control; however, cannot ensure the system stability in the presence of parametric uncertainties and disturbances. Therefore, some adaptation laws have been integrated with the hybrid position-force control to incorporate the dynamic of the robot and compensate for parametric uncertainties [89–94]. These strategies are found to be limited to the robotic manipulators in industrial applications. Moreover, they are restricted by the model complexity and the large number of adaptive parameters to ensure the stability and the behavior of robotic manipulator. It has also been observed that existing control schemes in the field of ultrasound robot are devoted to maintain the contact forces at the desired level without the consideration of trajectory tracking in the position-controlled subspaces [35, 83]. Moreover, the parametric uncertainties and the external disturbances are not considered in the design of the controllers. On the other hand, no stability analysis is performed to ensure the robustness of the proposed schemes while completing the scan process [85–87].

At the early stage of post-stroke, passive-assist therapy becomes helpful in the muscles' contraction and motor recovery at the expense of increased range of motion (ROM) [95]. This mode of therapy does not require the subject to move his/her upper limb and apply any force towards the robotic device. Therefore, researchers have proposed several position control schemes for the robot-aided upper extremity rehabilitation to mimic

a manual therapist's job satisfactorily and regain the impaired limbs' functionality in passive-assist mode. O'Malley et al. [96] designed a classical PD controller for an EERR, named Ricewrist, to follow a predefined trajectory. In other work by Rahman et al. [97], a passive training of the upper extremity is offered by using a PID control and gravity compensated compliance control on a 4-DOFs robot. A backstepping control scheme is proposed for a 7-DOFs rehabilitation device to provide the biomechanical movements of upper extremity joints [98]. Additionally, the passive wrist therapy is performed using the gravity-compensated control on a 3-DOFs ExoRR [99]. A modified sliding mode control scheme is devoted to carry out passive rehabilitation exercises to eliminate undesired chattering phenomena [100]. On the other hand, in the active-assist therapy, the subjects can also apply some or significant amount of force from their side towards the rehabilitation device. Therefore, in the last few years, researchers have started to work on impedance/admittance control schemes for rehabilitation robots. Luna et al. [101] presented admittance control schemes for active and active-assistive rehabilitation modes and tested with 7-DOFs upper-extremity rehabilitation robot (ETS-MARSE). Akdoğan et al. [102] proposed an impedance and hybrid impedance control to assist the wrist and forearm in five different therapy modes and tested with healthy subjects and patients.

The conventional position and impedance/admittance control require a good knowledge of the nonlinear dynamic model of the rehabilitation robot, which is uncertain in practical situations. Moreover, unexpected external forces can be generated during the training process depending upon different subjects' masses. Therefore, to address such perturbations, researchers have explored the adaptive control schemes for the upper- and lower-extremity rehabilitation devices [103–108]. The literature of this work is limited to adaptive control schemes of upper-extremity devices only. Khan et al. [103] exploited a passivity-based adaptive control on an ExoRR to track the estimated Desired Motion Intention (DMI) of upper-limbs. The proposed control scheme helped to deal with the modeling errors of the exoskeleton device for different subjects. Tee et al. [104] introduced the adaptive-backstepping admittance control based on an improved Barrier Lyapunov Function (BLF) under the dynamic perturbations. The reference trajectory of the EERR is generated within the constrained task space to allow compliant external forces. He et al. [105] extended the concept of constrained task space for physical human-robot collaboration and applied neural network-based integral BLF to follow the reference trajectory. Moreover, a radial basis function neural network (RBFNN) is employed to address the uncertain dynamics and external interference. In other work on adaptive control, Wu et al. [106] designed an admittance control scheme to include human participation during the active-assist therapy process. Moreover, they exploited the RBFNN-based disturbance observer, which ensures the training process under parametric perturbations and mod-

eling error. Recently, Omrani and Moghaddam [107] proposed a model reference-based adaptive impedance controller for an end-effector rehabilitation robot where time-delay estimation approach is exploited to estimate the unknown and uncertain dynamic parameters. The controller gains are adjusted using the adaptation law. Few other works on regulating the control parameters lack adequate datasets, become computationally expensive, and less practical during rehabilitation [109,110]. Few researchers have exploited the adaptive control to adjust the controller parameters for the upper limb rehabilitation robot [109, 110]. However, these strategies lack sufficient training datasets and impose high computation efforts that make practical implementation challenging.

1.3.2.2 Controllers for Robotic Manipulators in Cooperative Manipulation

In the hybrid position-force approach, the velocities and forces at the manipulators' end-effector should be mapped to their counterparts at the manipulated object, allowing the simultaneous control of the position and force variables. Several control strategies were developed considering the known dynamical model of the coordinated manipulators [111, 112]. Hsu [111] proposed a hybrid position-force control approach to execute part-matching tasks. Moreover, Lie et al. [112] coordinated the motion of a multi-fingered hand with the computed torque-based control scheme. However, the dynamic uncertainties may lead to a degradation in the control performance and affect the stability of the system [113]. Therefore, many researchers have considered the parametric uncertainties in the design of robust hybrid-position control strategies for cooperative manipulators [114–122]. Hu and Goldenberg [114] proposed an adaptive control scheme to estimate the unknown parameters during the manipulation of a common object by dual-arm manipulators. Zhu and Schutter [115] proposed a unified adaptive control scheme to coordinate the motion of dual-arm manipulators holding a raw egg. Sarikaya et al. [116] and Ren et al. [117] designed an adaptive control scheme to deal with the dynamic and kinematic uncertainties in the cooperative manipulation tasks. Monfaredi et al. [118] presented a combination of proportional derivative (PD) and adaptive sliding mode controllers to handle a common object with unknown inertia and geometry. In work presented by Jimenez J and Perez [119], the adaptation law is combined with the hybrid control approach to ensure the stable grasp of the manipulated object during the cooperative task. Gueaieb et al. [120] extended the work presented by Parra-Vega et al. [121] where the sliding mode-based hybrid control scheme is proposed to control the motion of the object and attain the internal forces at the desired level.

Moreover, the intelligent control presented using the fuzzy and neural network (NN) systems has been exploited to overcome the dynamic uncertainties in the cooperative tasks [123]. Rani and Kumar [124] presented a model-based control strategy with a

radial basis function neural network to handle the unmodeled dynamic and external disturbances during tracking desired trajectory and internal forces. The traditional backstepping control scheme [125] can be improved by introducing a new state variable and adopting a fuzzy approximator during the controller design process. Baigzadehnoe et al. [126] exploited the state augmented backstepping approach with an adaptive fuzzy logic approximator to estimate the dynamics of the cooperative manipulators under external disturbances. Pham et al. [127] introduced the dynamic surface-based sliding mode control and NN principles to deal with the uncertainties of cooperative manipulators. The above strategies could achieve adequate behavior through motion and internal force tracking control. Nevertheless, they are limited by the complexity of the model and many adaptation parameters to guarantee the stability of a cooperative dual-arm system.

In the framework of admittance control, Bonitz and Hsia [128] utilized the internal impedance control scheme to control the internal forces developed on the manipulated object. Computed torque-based impedance control is proposed to maintain a compliant interaction between the manipulated object and the environment without developing high external forces (external impedance) [129]. Caccavale et al. [130] combined the internal and external impedance in a unified framework to control the internal and external forces generated by the interaction between the manipulators/object and object/environment during the cooperative manipulation, respectively. A proportional-integral-derivative controller (PID) is proposed for each manipulator to form the inner motion loop at the joint level. Moosavian and Rastegari [131] developed a multiple impedance control strategy to impose both the object and internal impedance relationships during the manipulation of a common object by a space-free-flying robotic system. Pierri et al. [132] utilized the architecture of the internal/external impedance control scheme to grasp an unknown object with the help of three flying robots. A model-based controller is utilized to form the inner motion loop and guide the vehicle through the generated reference trajectory. AzizZadeh et al. [133] implemented the hybrid impedance control on three industrial manipulators allowing interaction with the external environment during the manipulation of a workpiece. It can be noticed from the previous discussion that most of the studies assume the exact knowledge of the dynamics of the cooperative manipulators. However, this assumption is not valid in practical application, and the dynamic uncertainties of the manipulators are always present. Therefore, several efforts have been put in to design robust and adaptive admittance based control strategies to maintain an acceptable tracking performance and incorporate the dynamic uncertainties [10,134–136].

Li et al. [134] combined the admittance control scheme with an adaptive neural network position controller to consider the dynamic uncertainties and provide an acceptable object position tracking performance. However, this study does not consider the ob-

ject/environment interaction, and no results for the developed internal forces during the cooperative manipulation task are provided. Zhai et al. [10] presented the adaptive radial basis function neural network sliding mode approach in the inner loop motion controller for cooperative manipulator system. This scheme is integrated with the impedance approach to estimate the unknown dynamical parameters and compensate for the workspace uncertainties. Ren et al. [137] extended the impedance model presented in [130] and developed a biomimetic object impedance with variable damping and stiffness matrices. These matrices are changed adaptively based on the various object/environment interactions. The proportional-derivative control scheme (PD) is combined with the gravity and friction compensation law to generate the required torques in the inner motion loop. Jinjun et al. [138] proposed the adaptive admittance control strategy to obtain the damping matrix online and maintain the internal forces at the desired level considering trajectory deviation caused by external disturbance forces during the cooperative dual-arm manipulation tasks. Hu and Cao [139] utilized the sliding mode approach with the adaptive variable impedance control to perform a slabstone installation task using dual-arm manipulators. However, the adaptation laws in these studies [137–139] are limited to adjust the stiffness and damping matrices without considering the dynamic uncertainties of the cooperative manipulators.

1.3.2.3 Event-Triggered Controllers and Hardware Restrictions

It is to be noted that the foregoing discussed studies for robotic manipulators in medical and cooperative industrial applications exploit the periodic time-triggered (TT) approach where the control input is sent to the robot at each sample time irrespective of the actual requirement. This is inappropriate for the networked control application and foists high transmission costs and ineffective resource allocation. Therefore, the event-triggered control strategy presents an alternative solution to overcome the limited resource constraints and alleviate the unnecessary transmission over the network [76, 140]. Several event-based control schemes are exploited in the literature to realize proper tracking performance with the alleviation of network burden in the existence of dynamic uncertainties [See: [141–143] for linear systems, [144–150] for nonlinear systems]. Xing et al. [145] proposed a switching event-triggered mechanism between predefined fixed and relative thresholds to reduce the number of transmitted packets in the controller-to-plant channel. Later, an improved ET threshold, derived from Lyapunov analysis, is developed by Al Issa et al. [144] for a general class of uncertain non-linear NCSs. Kumari et al. [146] exploited the ET sliding mode controller for uncertain Euler-Lagrange systems. Zhang et al. [147] proposed an event-triggered-based adaptive backstepping strategy with a relative threshold for a class of nonlinear systems. In the robotics domain, the ET mechanism have

been actively explored in several works to lessen the communication burden [See [151–159] for robotic manipulators, [160–162] for mobile robots, [163, 164] for quadrotor]. However, this thesis is limited to the discussion about the event-triggered mechanism for robotic manipulators in different applications.

Bu et al. [151] utilized the event-triggered mechanism with a fixed threshold to preserve the tracking performance of a single-arm manipulator under the uncertainties and external disturbances. Gao et al. [152] investigated the motion tracking control of the robotic manipulators under the implementation of dynamic triggering condition in the presence of nonlinear uncertainties. Kamboj et al. [153] integrated the event-triggered mechanism with the learning- based incremental PID to reduce the control updates while maintaining an acceptable trajectory tracking performance. Benitez-Garcia et al. [154] implemented the periodic event-triggered control scheme experimentally for the stabilization problem of robotic manipulator. Tripathy [155] employed the event-triggering mechanism with fixed threshold based on the optimal control for uncertain two-link SCARA manipulator. Qiu et al. [156] utilized the same fixed threshold along with the disturbance observer and adaptive NN tracking control to reduce the energy consumption and compensate for uncertainties during the motion of robotic manipulator. Baek et al. [157] proposed event-triggered time delay sliding mode control scheme to overcome the limited bandwidth and uncertainties for 2-DOFs robotic manipulator. Li et al. [158] the command filtered backstepping controller is combined with the relative threshold for robotic manipulator with output constraints. However, these studies are intended for single-arm manipulators without considering interaction forces in the controller design. Therefore, they cannot be extended to the medical and cooperative manipulators in which the control of contact forces is crucial to obtain a proper human-robot interaction and stable grasp.

Diverting our attention to the robotic systems in medical applications, it has been observed that very few works have recently started to consider the event-triggered implementation [165–167]. These studies are still limited to the lower limb exoskeleton rehabilitation robots. Wang et al. [165] presented an ET-based sliding mode control to track the pre-specified trajectory using a lower-extremity exoskeleton robot. Similarly, Llorente-Vidrio et al. [166] combined the Electromyography-based ET sliding mode control with the deep differential neural network for a lower limb exoskeleton device. Zuo et al. [167] proposed the hybrid torque-position control scheme for the ankle rehabilitation while implementing the event-triggered mechanism to reduce the control updates. On the other hand, the event-triggered scheme with the multiple networked Euler–Lagrange systems is recently exploited [168–171]. It is worth mentioning that a few works have considered the event-triggered mechanism in the context of cooperative manipulators [172, 173], and

they are still in their infancy. The distributed impedance control is investigated under the event-triggered mechanism to perform a cooperative manipulation task [172]. The dynamic uncertainties and the interaction between the object and environment are not considered in this work. An event-based synchronization control strategy is incorporated with an adaptive neural network to cope with dynamic uncertainties and limited communication during the manipulation task [173]. The theoretical analysis for the boundedness of internal forces is given. However, there are no results on the developed internal forces at the manipulated object. The external forces caused by the environmental interactions are not considered in this framework. Therefore, one may conclude from the above discussions that the problem of simultaneous position and force tracking control of robotic manipulators in medical and cooperative industrial applications in the presence of parametric uncertainties, interaction forces, and limited bandwidth has rarely been attempted sofar.

It can be observed from the previous studies that the majority of the designed dynamic control systems are based on the torque control approach in which the dynamics of the actuator are not incorporated in the controller design. These torque based control schemes are accompanied by some practical implementation challenges [174, 175]. *The most critical challenge is that the torque signals cannot always be applied directly to some commercial robots, available in the market, which are actuated by voltage or position signals.* To address these limitations and account for the dynamical coupling effects between joints, the torque controlled motors which admit direct torque signals can be utilized. The controller of these motors can be designed to incorporate the dynamical coupling and provide the robot with higher tracking performance and a proper compliant behavior [176]. However, there are few available robots with direct torque control capability [177]. This is attributed to the need of low friction and no backlash in the gearbox, resulting in high cost motors. This in turns make the replacement of the servos of commercial robot not very feasible. Therefore, several attempts have been made to benefit the advantages of dynamic controller in the voltage- and position-controlled manipulators and incorporate the dynamical effects in the controller design [See: [178–180] for voltage-controlled manipulator and [181–184] for position-controlled manipulators].

Fateh [178] proposed a voltage based control scheme to control an electrically-driven manipulator with the help of current feedback. Shafiei and Soltanpour [179] included the actuator dynamics in designing a neural network-based backstepping approach for the tracking control of a robotic manipulator. Ahanda et al. [180] exploited the command-filtered-based adaptive backstepping approach to deal with the uncertainties in the electrically -driven robotic manipulator. Khatib et al. [181] introduced a torque-to-position transformer based on the modeling of the motor transfer function. This transformer

converts the calculated torque signals into joint position inputs to guide the position controlled manipulator. Del Prete et al. [182] presented another framework to implement the torque controller on the position controlled robotic system. Three parts torque controller was constructed to estimate the joints torques based on the model of the robot and the data acquired through the end-effector torque sensor. This controller is experimentally validated on HRP-2 humanoid robot. Adhikary and Mahanta [183] devised a simplified version of the torque-to-position transformer proposed in [181]. This transformer was combined with the backstepping sliding mode-based high level controller to overcome the effect of uncertainties and maintain the robustness of the system. Shao et al. [184] addressed the lack of accuracy and limited performance problems of the low level kinematic controller of the position controlled manipulators. An adaptive control law and switching approach were utilized to cope with the parametric uncertainties and motor saturation. Thereafter, the torque control signal was converted to joint position inputs. However, the above studies are based on the traditional time-triggered (TT) implementation with the assumption of the ideal communication which is not preferable in networked control applications. Moreover, the controllers in [181–184] assume that the electrical dynamics of motor model is negligible and consider the parameters of the internal controllers to be known for the users.

1.3.3 Event-triggered Mechanism

In the event-triggered mechanism, it is considered that the robotic system states and control inputs are updated/transmitted over the network subjected to the violation of a pre-designed triggering condition i.e., the data is not transmitted at each sampling time. At other instances, the last-received data signals are held constant till the next triggering event arrives. This aperiodic update of data leads to less number of transmission packets, resulting into efficient utilization of resources. However, designing a triggering condition that effectively determines the triggering instants to always ensures the system stability in tandem with a satisfactory performance is of great importance and a challenging task. Another benchmark problem while designing an event-triggered control scheme is the exclusion of Zeno behavior i.e., the triggering mechanism shall not generate an infinite number of events within a finite time. Therefore, the inter-event time between two consecutive triggering instants should always be lower bounded for the practical feasibility of the event-triggered control scheme.

1.3.3.1 Types of Triggering Condition

Due to the event-triggered implementation, measurement error between the actual signal and received signal transmitted over the network is generated. This measurement

error is utilized to design several triggering conditions in the literature. These conditions are defined based on different thresholds and employed to determine the instants for new signal transmission over the network channel.

- **Fixed threshold** [156, 185]. The triggering instants in this type of threshold depends on a predefined constant as follows.

$$\begin{aligned} t_1 &= 0, \\ t_{j+1} &= \inf\{t > t_j \mid \quad |e_m(t)| \geq \varpi_1\}, \end{aligned} \tag{1.1}$$

where $e_m(t) = S(t) - \bar{S}(t)$ denotes the measurement error, $S(t)$ is the actual calculated signal (i.e., control input $\big(S(t) = \tau_R(t)\big)$ or robot state $\big(S(t) = X(t)\big)$, $\bar{S}(t)$ is the received signal, $\varpi_1 > 0$ is a positive constant. The measurement error in this triggering condition is bounded by a predefined constant. To design and implement such triggering condition is simple; however, the desired objectives (resource utilization and system performance) could not be easily achievable. Therefore, network-based applications prefer time-varying thresholds where performance is a critical design attribute.

- **Relative threshold** [147, 186, 187]. In this condition, the magnitude of event triggered transmitted signal is utilized to determine the triggering instants as follows.

$$\begin{aligned} t_1 &= 0, \\ t_{j+1} &= \inf\{t > t_j \mid \quad |e_m(t)| \geq \varrho|\bar{S}(t)| + \varpi_2\}, \end{aligned} \tag{1.2}$$

where $0 < \varrho < 1$ and $\varpi_2 > 0$ denote positive constants. The threshold is varying in view of the magnitude of $\bar{S}(t)$. This threshold is more flexible and expected to outperform the fixed ones for better performance. However, it may fail in the presence of large transmitted signals where sudden jump could occur and deteriorate the system performance.

- **Switching threshold** [145]. This triggering condition is the amalgamation of benefits of fixed and relative thresholds as follows.

$$\begin{aligned} t_1 &= 0, \\ t_{j+1} &= \begin{cases} \inf\{t > t_j \mid \quad |e_m(t)| \geq \varpi_1\} & \text{if } |\bar{S}(t)| \geq \Xi \\ \inf\{t > t_j \mid \quad |e_m(t)| \geq \varrho|\bar{S}(t)| + \varpi_2\} & \text{if } |\bar{S}(t)| < \Xi \end{cases} \end{aligned} \tag{1.3}$$

where Ξ is a user-defined parameter. As the fixed threshold does not rely on the magnitude of the transmitted signal $\bar{S}(t)$; therefore, it is exploited to alleviate the sudden jump in case of large signals.

- **Lyapunov-based threshold**. The negative definiteness property of the derivative of Lyapunov function is used to design this triggering condition in such a way that the overall robotic system will be stable as follows.

$$\begin{aligned} t_1 &= 0, \\ t_{j+1} &= \inf\{t > t_j \mid \quad \dot{V} \geq 0\}, \end{aligned} \tag{1.4}$$

where $\dot{V}$ denotes the time derivative of Lyapunov function. This implies that there is no requirement to transmit a new signal over the network; the last transmitted signal is retained as long as the derivative of the Lyapunov function is negative definite. However, this signal should be updated when this condition is violated to preserve the system's performance and stability.

1.3.3.2 Configurations of Event-triggered Mechanism

As per the design requirements of a network-based applications, the triggering mechanism could be placed in two ways, i.e., controller-to-robot channel and robot-to-controller channel as discussed below and shown in Figure 1.2.

- **Controller-to-robot channel.** In this configuration (Figure 1.2 (a)), the event-triggered (ET) condition is evaluated at the controller-side [145, 156, 157, 187–189]. This configuration is simple in design, analysis, and implementation as the measurement error appears in the control input only. Therefore, it can be directly incorporated with any traditional control approaches in a straightforward manner. In addition, there is no need for smart sensors or extra computational unit at the sensor-side in this configuration. However, as the actual control law is always required to calculate the measurement error and check the triggering condition, the computational efforts cannot be alleviated in such cases. Moreover, the system states are assumed to be always available on the controller side.

- **Robot-to-controller channel.** In this configuration (Figure 1.2 (b)), the triggering condition is evaluated at the sensor-side [149, 150, 185]. The measurement error is defined between the actual and last-transmitted system states. The system states are transmitted over the network only when the designed triggering condition gets violated, and the control law is then updated according to the new received states. Therefore, the computational efforts can also be decreased in this configuration since the control law is not always required to be computed and transmitted over the network. However, incorporating such triggering scheme with traditional control approaches is not a straightforward as the measurement errors will appear at each state, and the available controller is to be redesigned based on the

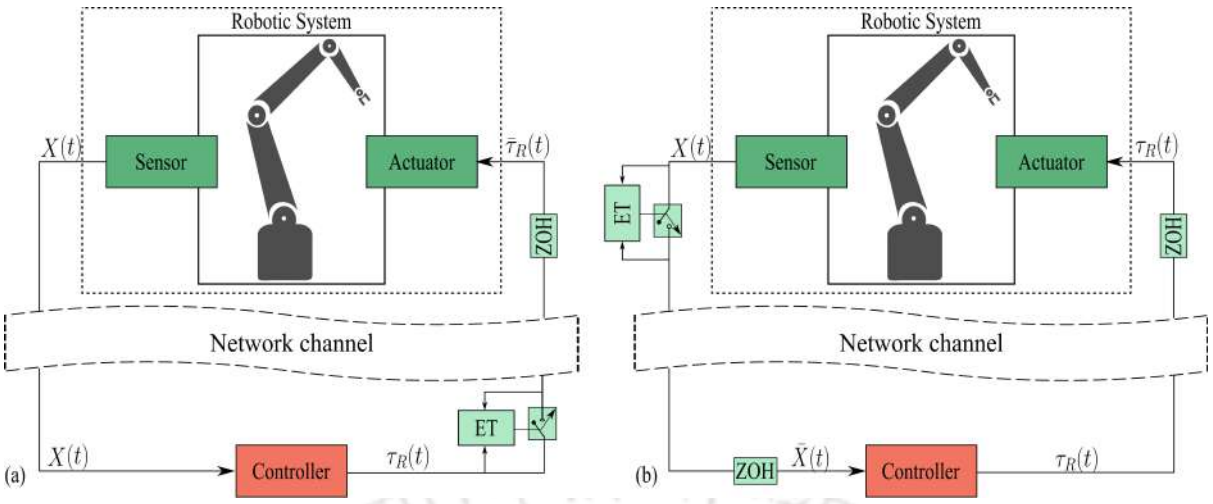

Figure 1.2: Configurations of event-triggered mechanism. (a) controller-to-robot configuration, (b) robot-to-controller configuration

event-triggered states. In addition, this configuration requires smart sensors with computational abilities or extra computation unit on the sensor-side in order to evaluate the triggering condition.

1.4 Potential Research Gap

Many researchers have attempted to design different control strategies with an aim to maintain superior performance of the uncertain robotic system during several interaction applications. However, adopting a communication network in the feedback loop to control such systems has dramatically increased and emerged as a fertile research problem. This implementation opened up many practical applications, such as remote-controlled robotic systems, haptic robot-assisted systems, and unmanned aerial vehicles, and introduced a new research direction for control theorists and roboticists. As such, the design and stability analysis of a dynamic controller communicating over a limited bandwidth wireless network channel with an uncertain robotic system during robot-human interaction is not straightforward. These issues become more challenging while considering the manipulation of common object tasks using a cooperative manipulator system. Therefore, all traditional control strategies seem incompetent to deal with network-induced challenges such as limited bandwidth, time delay, and packet loss, and some modifications are required in the controller design process.

In addition to the above network induced constraints, the presence of parametric uncertainties in the dynamics of the robotic manipulator impose further complications to the design of networked control system. The effect of these uncertainties become more

obvious and may result in undesirable performance during the cooperative manipulation tasks. Hence, the adaptive backstepping control approach is among the rewarding strategies to reduce the effect of parametric uncertainties. This approach through its online adaptation law can continuously estimate the dynamical parameters of the robotic manipulator and maintain a consistent performance of the control system. It is worth mentioning that other control approaches suffer from the difficulties of heuristic selection of an appropriate Lyapunov function. However, since backstepping is a Lyapunov based approach, it provides a systematic tool to derive the control law and simple method to construct the Lyapunov function and analysis the stability of the nonlinear robotic system.

On the other hand, the interaction between the robotic system and human is necessary in many practical scenarios. Moreover, a compliant behavior is to be maintained between manipulators/object and object/environment during the different cooperative manipulation tasks of a common object. Such interactions make the above discussed problem much more intractable. In these situations, the simultaneous position and force control need to be invoked. This control can be accomplished by one of the well know techniques i.e., hybrid position-force control and admittance control. The adoption of these schemes is basically based on the desired interaction task. Hence, it is not a difficult task to infer that adaptive position-force based control strategies are undoubtedly potential techniques to ensue an acceptable performance and attain a proper compliant behavior during the various interaction scenarios of robotic system. However, translating adaptive position-force control design for single robotic manipulators and cooperative manipulators to meet the rigorous performance requirements and robustness to network constraints in nonlinear networked control systems is not trivial and has seldom been addressed in the open literature.

Diverting our focus to practical applications, the implementation of existing theories and methodologies of networked control systems to real robotic systems is of paramount engineering relevance. These methodologies provide promising advantages for the remote online application of the rehabilitation robots, cooperative manipulations of a large object, industrial automation, and many others. However, real-time implementation of these control schemes is always accompanied by hardware restrictions in addition to the preceding discussed challenges. Most of the available industrial manipulators and commercial robotic arms in the market are equipped with servo motors. These servo actuators adopt low-level internal controllers (i.e., PID or its variations), which admit the joint position as the input and feedback signals [190]. Thus, the robotic manipulators can only be actuated by position-based control commands, named position-controlled manipulators. However, these low-level controllers are designed to operate each joint independently, ignoring the

coupled dynamical effects between the joints and resulting in a kinematic control approach only [191]. Moreover, manufacturers usually do not provide the parameters of this internal controller and the electrical characteristics of the motors. These unknown parameters, along with the changes in mechanical parameters and payload variations, make the internal controller inefficient and may degrade the performance of the robotic systems during the motion of the manipulator [181]. Therefore, how to benefit from the advantages of dynamic control and incorporate the dynamical effects in the controller design of the position-controlled manipulators to overcome these hardware restrictions is of great practical importance.

The aforementioned discussion reveals that the controller design of nonlinear robotic manipulator systems with dynamic uncertainties and compliant interaction under the network constraints and its applications to medical and cooperative manipulations is still an open problem and needs further investigation.

1.5 Objectives of the Present Work

The first part of the thesis intends to the design of event-triggered adaptive position-force controllers for single robotic manipulator in medical applications. The second part discusses the extension of these controllers to tackle the problem of cooperative manipulation of a common object using multiple robotic manipulators. In both parts, the robotic system is controlled over a network subjected to limited bandwidth in controller-to-robot channel. In addition, parametric uncertainties encountered in the system model and interaction between the robot-human, robots/object, and object/environment are also considered. To achieve these objectives, following works are carried out:

- The design of event-triggered adaptive hybrid position-force control scheme for uncertain robot-assisted ultrasonic examination system under limited communications and robot-human interaction.
- The design of event-triggered adaptive admittance control scheme for uncertain upper-limb end-effector type rehabilitation robot in passive and active-assist mode under limited communications.
- The implementation of the developed event-triggered adaptive position control scheme on a real voltage-controlled end-effector type rehabilitation robot to perform passive rehabilitation training.
- The design of improved event-triggered adaptive hybrid position-force control scheme for uncertain cooperative manipulators during manipulators/object interaction and under limited communications.

- The design of improved event-triggered adaptive admittance control scheme for uncertain cooperative manipulators during the manipulators/object and object/ environment interaction and under limited communications.

- The implementation of the improved event-triggered adaptive position control scheme on a real position-controlled dual-arm Dagu manipulators to perform a cooperative manipulation task.

1.6 Organization of the Thesis

This thesis is organized into two main parts, each addressing a particular research problem as elaborated in the previous section. The first part of the thesis discusses the theoretical and practical results obtained for the position-force control schemes under event-triggered communication of single robotic manipulator in medical field and consists of the following chapters:

- **Chapter 2:** In this chapter, the event-triggered hybrid position-force controller (ETAHPFC) for ultrasound manipulator is derived based on the backstepping approach. The effectiveness of this control scheme is investigated through a comparison study with the existing control methods and validation in V-REP software.

- **Chapter 3:** This chapter investigates the design of an event-triggered adaptive backstepping admittance controller (ETABAC) to tackle the uncertainties and limited communications problems for the end-effector type rehabilitation robot during the patient-robot interaction in a unified framework.

- **Chapter 4:** Experimental validation on a real end-effector type rehabilitation robot during passive rehabilitation training for different healthy subjects is presented in this chapter. A modified dynamic model is introduced to overcome the hardware restrictions of the electrically-driven rehabilitation robot.

  The second part of the thesis present the event-triggered position-force control problem of multiple robotic manipulator in cooperative manipulation task. This part consists of the following chapters:

- **Chapter 5:** The theoretical results obtained in Chapter 2 are extended for the cooperative manipulator system. The adaptive backstepping position controller is improved by introducing different terms in the design process to guarantee an acceptable trajectory tracking of the manipulated object while maintaining small internal forces in the presence of uncertainties and limited communication.

- **Chapter 6:** The admittance control framework presented in Chapter 3 is extended for the cooperative manipulator system to maintain a proper compliant behavior during the the manipulators/object and object/environment interactions during different cooperative manipulation tasks and various environmental interaction cases.
- **Chapter 7:** This chapter presents experimental validation of the event-triggered adaptive position controller designed in Chapter 5 on a real position-controlled cooperative manipulators. The dynamics of each manipulator is modified to overcome the hardware restriction and admit the position commands as input signals.
- **Chapter 8:** This chapter concludes the research work and outlines the scope for future research.

2

Event-Triggered Adaptive Hybrid Position-Force Control for Robot-Assisted Ultrasonic Examination System

Contents

2.1 Introduction

Motivated by the remote application of the ultrasound robot, this chapter aims to design an event-triggered adaptive hybrid position-force control (ETAHPFC) scheme for ultrasound robot. An adaptive backstepping position controller is proposed to achieve acceptable trajectory tracking during the transversal ultrasound scan of the patient's abdomen. This controller is designed based on the dynamic model of the ultrasound robot with an adaptation law to compensate for the parametric uncertainties. A PID force controller is proposed to maintain stable contact during the scan process. Based on Lyapunov stability analysis, a triggering condition is derived to reduce network resource utilization and guarantee the stability of the closed-loop system. A comparative study between the proposed event-triggered (ET) control scheme and different time-triggered (TT) adaptive control approaches is performed. Furthermore, the proposed event-triggered mechanism is compared with the most common triggering conditions in literature, i.e., fixed and relative thresholds. Additional validation of the proposed control scheme is conducted in the virtual robot experimentation platform (V-REP) during the abdominal scan process.

The chapter is organized as follows: In Section 2.2, the framework of the ultrasound robot is presented. The dynamic modeling of the constrained ultrasound robotic system is developed in Section 2.3. The proposed hybrid position-force control strategy is elaborated in Section 2.4, along with the derivation of the triggering condition. Section 2.5 presents the simulation results, the comparative analysis, and the validation based on the SCORBOT-ER VPlus robotic manipulator in the V-REP platform. Finally, the outcomes of this chapter are highlighted in Section 2.6.

2.2 Framework of Ultrasound Robot

The main components of the ultrasound robot are illustrated in Figure 2.1. They are briefed as follows: a robotic manipulator equipped with an ultrasound probe to perform the required scanning, an ultrasound imaging unit devoted to display the captured sonograms (scanning images) for the analysis proposes, robot controller to ensure the tracking of the desired trajectory and maintain a proper force on the patient's body. Besides, a tracking system to determine the location of the ultrasound probe in the space and estimate the initial scanning position.

To perform an abdominal ultrasound scanning, the patient should be in the supine position on an exam table. A hypoallergenic water-soluble gel is applied on the patient's abdomen to prevent the air from getting between the scanned area and the ultrasound probe. The robot gently moves the ultrasound probe over the patient's abdomen, generating a light pressure on the examined area. The ultrasound probe produces and receives

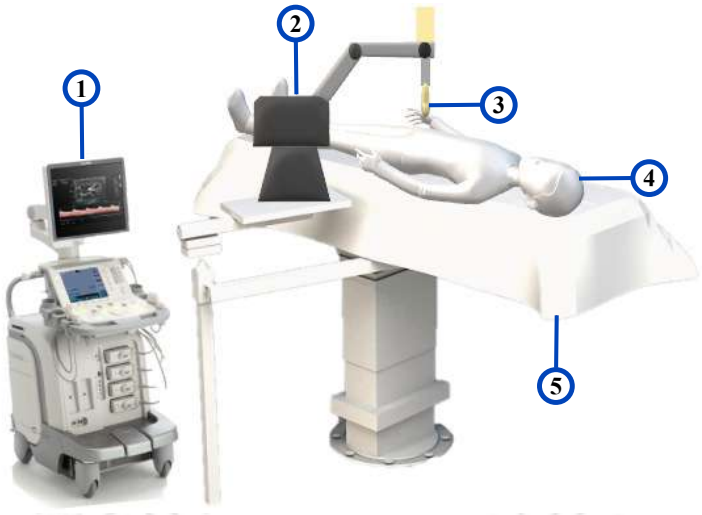

Figure 2.1: Ultrasound robotic system (1- Ultrasound imaging unit; 2- Robotic manipulator; 3- Ultrasound probe; 4- Patient; 5- Exam table)

high-frequency sound waves. These patterns are processed in the ultrasound imagining unit and transformed into detailed sonograms. These sonograms can show any diseased or damaged tissues and determine abnormal growth, enabling the sonographers to diagnose the desired area accurately.

The abdomen's ultrasound examination protocol is usually divided into scanning of the sagittal and transverse planes [85]. The probe is aligned with a plane that partitions the body into left and right parts in the sagittal scan. Moreover, the sagittal scan can be further divided into parasagittal scans (the probe moves around the area of interest) and intercostal scans (the probe is angled cephalad under the ribs to obtain a clear image). On the other hand, the transverse scan is performed in two steps: the transversal scan around the area of interest and the subcostal scan.

The ultrasound robot is a 5-axis robotic manipulator equipped with an ultrasound probe. The joints of the manipulator are revolute type. The first three joints are responsible for the position of the probe's tip in the space. The last two joints (wrist joints) are dedicated to provide the desired orientation of the probe. A force sensor is placed at the wrist of the ultrasound robot to detect the feedback force. This force is generated during the contact between the ultrasound probe and the patient's abdomen. The circular trajectory is generated to perform a transversal ultrasound scan on the abdomen area of the patient. Moreover, the ultrasound robot should maintain a constant force perpendicular to the scan area while performing the transversal scan. The flowchart of the procedure is depicted in Figure 2.2.

Here, the communication between the ultrasound robot and the controller is over a limited bandwidth network. Therefore, an event-triggered (ET) mechanism is imple-

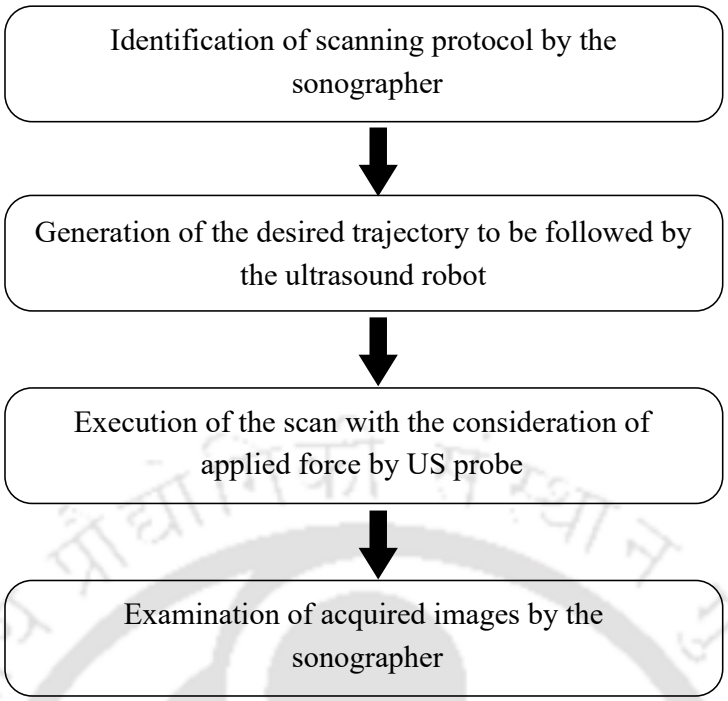

Figure 2.2: Flowchart for ultrasound imagining process

mented to overcome the communication channel's constraints and efficiently utilize the resources. Due to ET implementation, the ultrasound robot is now not actuated by the actual control inputs τ_R. Instead of that, it is actuated by the ET control inputs $\bar{\tau}_R$. Because of the ET mechanism, the control input is communicated over the network just at the time instants when a pre-designed triggering condition gets violated. At other times moments, the ultrasound robot is actuated by last-received control inputs. It is to be mentioned that this triggering condition is designed by ensuring the negative semi-definiteness of the derivative of the Lyapunov function. The violation of this condition indicates the need for a new control signal update over the network to maintain the system's stability. The triggering time-instants are described as

$$\begin{aligned} \bar{\tau}_R(t) &= \tau_R(t_j), \forall\ t \in [t_j, t_{j+1}) \\ t_{j+1} &= \inf\{t | t > t_j,\ T_{con}(e_m, z_1, z_2) > 0\} \end{aligned} \tag{2.1}$$

where, $e_m(t) = \tau_R(t) - \bar{\tau}_R(t)$ is the measurement error and $T_{con}(e_m, z_1, z_2)$ is the triggering threshold to be calculated in Section 2.4.

2.3 Dynamic Model of Constrained Ultrasound Robot

The dynamic equation of n-joint robotic manipulator in contact with an environment can be expressed in the joint space as follows [192]:

$$M(q)\ddot{q} + C(\dot{q}, q)\dot{q} + G(q) = \bar{\tau}_R - \tau_{int} \tag{2.2}$$

where $q, \dot{q}, \ddot{q} \in \mathbb{R}^n$ symbolize the joint position, velocity, and acceleration, respectively. $M(q) \in \mathbb{R}^{n\times n}$ denotes the inertia matrix, $C(\dot{q}, q) \in \mathbb{R}^{n\times n}$ is the matrix of Coriolis and centrifugal effects, $G(q) \in \mathbb{R}^n$ represents the gravitational torques, $\bar{\tau}_R \in \mathbb{R}^n$ stands for the vector of ET control torques, and $\tau_{int} \in \mathbb{R}^n$ is the vector of interaction torque between the environment and robot. When the joints of the robotic manipulator are actuated by a DC servo motors, the dynamic of these motors should be considered for more rigorous modeling of the robotic system. The dynamic of the motor can be given as:

$$J_m\ddot{q}_m + B_m\dot{q}_m + r^{-1}\tau_R = \tau_m \tag{2.3}$$

where $q_m, \dot{q}_m, \ddot{q}_m \in \mathbb{R}^n$ are the position, velocity, and acceleration of the motor shaft, $J_m \in \mathbb{R}^{n\times n}$ denotes the inertia of the motors, $B_m \in \mathbb{R}^{n\times n}$ is the coefficient of viscous friction at the motor bearing, $r \in \mathbb{R}^{n\times n}$ is the matrix of gear ratio, and $\tau_m \in \mathbb{R}^n$ is the motor torque. The angular position q_m and torque of the motor shaft τ_m are related to the joint angle q and torque τ_R as defined below

$$q_m = rq, \quad \tau_m = r^{-1}\tau_R \tag{2.4}$$

Therefore, the combined manipulator-motor dynamics is obtained using (2.2-2.4) as:

$$M_R(q)\ddot{q} + C_R(\dot{q}, q)\dot{q} + G_R(q) = \bar{\tau}_R - \tau_{int} \tag{2.5}$$

where $M_R(q) = M(q) + r^2J_m$, $C_R(\dot{q}, q) = C(\dot{q}, q) + r^2B_m$, and $G_R(q) = G(q)$. The following properties are introduced to be utilized in the derivation of the adaptive hybrid position-force controller [84]:

Property 1 The total inertia matrix M_R is symmetric, positive definite, and satisfies the following condition:

$$v_1\|\beta\|^2 \leq \beta^T M_R(q)\beta \leq v_2\|\beta\|^2 \quad \forall\beta \in \mathbb{R}^n \tag{2.6}$$

where v_1 and v_2 are positive constants and $\|\cdot\|$ is the Euclidian norm of $(\cdot)$.

Property 2 The matrix $\dot{M}_R - 2C_R$ is skew-symmetric, i.e., for any arbitrary vector

$\beta \in \mathbb{R}^n$ satisfies:

$$\beta^T \big(\dot{M}_R(q) - 2C_R(q,\dot{q})\big)\beta = 0 \tag{2.7}$$

Property 3 For arbitrary known vector μ, the joint space dynamics equation can be linearly parameterized as follows:

$$M_R(q)\dot{\mu} + C_R(\dot{q},q)\mu + G_R(q) = \Pi\varphi \tag{2.8}$$

where $\Pi \in \mathbb{R}^{n\times p}$ is the regression matrix of known functions and $\varphi \in \mathbb{R}^p$ is the vector of unknown parameters.

The following direct kinematic relation defines the relation between the end-effector position and the variable of the joints:

$$x_e = T(q) \tag{2.9}$$

where $x_e = \begin{bmatrix} p_e \\ \phi_e \end{bmatrix} \in \mathbb{R}^l$ represents the pose (position and orientation) of the end-effector, p_e is the position of the end-effector which has the following components $p_e = (p_{e,x}, p_{e,y}, p_{e,z})^T$, ϕ_e is the orientation of the end-effector, and $T(\cdot) \in \mathbb{R}^l$ is the vector function of $(\cdot)$.

The relation between the torques and forces exerted by the robot on the environment is given by:

$$\tau_{int} = J^T(q)F_{int} \tag{2.10}$$

where $F_{int} = [f_{int_1},\ f_{int_2},\ ...,\ f_{int_l}]^T \in \mathbb{R}^l$ denotes the interaction force at the end-effector and $J(q) \in \mathbb{R}^{l\times n}$ represents the Jacobian matrix of the robotic manipulator. The patient's body with which the ultrasound robot interacts is modeled as a spring with constant stiffness. Therefore, the interaction force developed at the contact point is given by:

$$f_{int_i} = \begin{cases} k_{env_i}(x_{e_i} - x_{env_i}) & \forall x_{e_i} > x_{env_i} \\ 0 & \forall x_{e_i} \leq x_{env_i} \end{cases} \tag{2.11}$$

where $1 \leq i \leq l$, $K_{env} = \text{diag}(k_{env_1},\ k_{env_2}, ..., k_{env_l})$ is the stiffness matrix, and $x_{env} = [x_{env_1},\ x_{env_2},\ ...,\ x_{env_l}]^T$ is the position of the contact point.

The dynamic model of the n-joint ultrasound robot 2.5 can be rewritten in the parametric strict feedback form as follows.

$$\begin{aligned} \dot{x}_1 &= x_2 \\ \dot{x}_2 &= M_R^{-1}(q)(\bar{\tau}_R - C_R(\dot{q},q)\dot{q} - G_R(q) - \tau_{int}) \end{aligned} \tag{2.12}$$

where $X = (x_1, x_2)^T = (q, \dot{q})^T$ represents the state vector.

2.4 ETAHPFC Design for Ultrasound Robot

Here, an adaptive hybrid position-force controller is designed to control the motion and interaction force of the ultrasound robot. This controller is employed to guarantee the tracking of the desired trajectory, in the presence of parametric uncertainty, during the transversal ultrasound scan. Simultaneously, the controller is utilized to maintain a constant force, applied by the ultrasound probe, on the patient's abdomen to obtain a clear scan sonogram. Raibert and Craig [70] propose the general framework of the hybrid position-force control. The architecture of this control strategy is based on the implementation of task constraints into the controller's design. Therefore, the degree of freedom is partitioned into two subspaces, position-controlled and force-controlled subspaces, by the natural constraints and the selection matrices. The control signal τ_R consists of two complementary sets- one exploited for the motion control task, and the other one addresses the force control task as expressed in the following equation:

$$\tau_R = \tau_p + \tau_f \tag{2.13}$$

The joint position error e_q and force error e_f can be defined as follows:

$$e_q(t) = q(t) - q_d(t) \tag{2.14}$$

$$e_f(t) = F_d(t) - F_{int}(t) \tag{2.15}$$

where τ_p and τ_f are the position and force control laws, respectively, q_d denotes the desired joint position to be followed, and F_d is the desired force.

2.4.1 Adaptive Backstepping Position Controller Design

Here, the adaptive backstepping approach [125] is utilized to design a position tracking control law. This controller is devoted to control the dynamic model of ultrasound robot, in the presence of unknown parameters, through a predefined trajectory. Moreover, the stability of the proposed control law is guaranteed based on the Lyapunov theorem. The error variables for the robotic manipulator are defined as follows.

$$z_1 = e_q = x_1 - q_d \tag{2.16}$$

$$z_2 = \dot{q} - \alpha = x_2 - \alpha \tag{2.17}$$

where α is the virtual control law (stabilization function) to be designed during the stabilization of the subsystems throughout the backstepping design process. The aim is to ensure that the joint position vector q can track the desired trajectories q_d in the

existence of unknown parameters. Therefore, the design of the adaptive backstepping position control law is achieved using the subsequent systematic steps.

Step 1: At this step, the virtual control input α is designed to stabilize the first subsystem (error variable z_1). In other words, letting the error variable z_1 converge to a small neighborhood of zero. The derivation of the first error variable is expressed as.

$$\dot{z}_1 = \dot{x}_1 - \dot{q}_d = x_2 - \dot{q}_d = z_2 + \alpha - \dot{q}_d \tag{2.18}$$

The first Lyapunov function candidate is selected as

$$V_1 = \frac{1}{2} z_1^T z_1 \tag{2.19}$$

By differentiating the equation (2.19) and substituting the equation (2.18), the derivative of the Lyapunov function becomes

$$\dot{V}_1 = z_1^T \dot{z}_1 = z_1^T (z_2 + \alpha - \dot{q}_d) \tag{2.20}$$

If the virtual controller is designed as

$$\alpha = -k_1 z_1 + \dot{q}_d \tag{2.21}$$

where k_1 is a positive diagonal gain matrix, then the derivative of the Lyapunov function becomes

$$\dot{V}_1 = -z_1^T k_1 z_1 + z_1^T z_2 \tag{2.22}$$

The negative definiteness of $\dot{V}_1$ and the convergence of z_1 to a small neighborhood of zero is guaranteed if the second error variable is equal to zero. Therefore, the stabilization of z_2 is carried out in the subsequent step.

Step 2: The derivation of the second error variable (2.17) is expressed as

$$\begin{aligned} \dot{z}_2 &= \dot{x}_2 - \dot{\alpha} \\ &= M_R^{-1}(q)\big(\bar{\tau}_R - \tau_{int} - C_R(\dot{q}, q)\dot{q} - G_R(q)\big) - \dot{\alpha} \end{aligned} \tag{2.23}$$

The Lyapunov function candidate can be selected using **Property 1** as follows.

$$V_2 = V_1 + \frac{1}{2} z_2^T M_R(q) z_2 \tag{2.24}$$

The derivative of the previous equation (2.24) is written as

$$\dot{V}_2 = \dot{V}_1 + z_2^T M_R(q)\dot{z}_2 + \frac{1}{2} z_2^T \frac{d\big(M_R(q)\big)}{dt} z_2 \tag{2.25}$$

By exploiting **Property 2** and equation (2.17), the Lyapunov function derivative can be rewritten as follows:

$$\begin{aligned}\dot{V}_2 &= \dot{V}_1 + z_2^T\big(M_R(q)\dot{z}_2 + C_R(\dot{q},q)z_2\big)\\ &= \dot{V}_1 + z_2^T\big(-M_R(q)\dot{\alpha} - C_R(\dot{q},q)\alpha - G_R(q) + \bar{\tau}_R - \tau_{int}\big)\end{aligned} \tag{2.26}$$

Using **Property 3** and exploiting the definition of measurement error i.e., $e_m = \tau_R - \bar{\tau}_R$, the previous equation is re-formulated as follows

$$\dot{V}_2 = \dot{V}_1 + z_2^T\big(-\Pi\varphi + \tau_R - e_m - \tau_{int}\big) \tag{2.27}$$

Due to the presence of uncertainties in the dynamical parameters of the ultrasound robot, the design of adaptation law is required to estimate the unknown parameters φ. Therefore, the Lyapunov candidate in equation (2.24) should be modified to include the estimation errors and complete the stability proof as follows.

$$V_2 = V_1 + \frac{1}{2}z_2^T M_R(q)z_2 + \frac{1}{2}\tilde{\varphi}^T\Gamma^{-1}\tilde{\varphi} \tag{2.28}$$

where $\tilde{\varphi} = \varphi - \hat{\varphi}$, $\hat{\varphi}$ is the estimation of the unknown parameters φ, and Γ is a positive definite matrix. The derivative of the modified Lyapunov function (2.28) can be written as

$$\dot{V}_2 = \dot{V}_1 + z_2^T\big(-\Pi\varphi + \tau_R - e_m - \tau_{int}\big) - \tilde{\varphi}^T\Gamma^{-1}\dot{\hat{\varphi}} \tag{2.29}$$

The term $z_2^T\Pi\hat{\varphi}$ is added and subtracted to the right side of (2.29)

$$\dot{V}_2 = \dot{V}_1 - z_2^T\Pi\tilde{\varphi} - z_2^T\Pi\hat{\varphi} + z_2^T\big(\tau_R - e_m - \tau_{int}\big) - \tilde{\varphi}^T\Gamma^{-1}\dot{\hat{\varphi}} \tag{2.30}$$

By taking the transpose of the second term at the right side of equation (2.30), one can obtain:

$$\dot{V}_2 = \dot{V}_1 - \tilde{\varphi}^T\big(\Pi^T z_2 + \Gamma^{-1}\dot{\hat{\varphi}}\big) - z_2^T\Pi\hat{\varphi} + z_2^T\big(\tau_R - e_m - J^T F_{int}\big) \tag{2.31}$$

The position control and adaptation laws can be designed as

$$\tau_p = \Pi\hat{\varphi} - z_1 - k_2 z_2 \tag{2.32}$$

$$\dot{\hat{\varphi}} = -\Gamma\Pi^T z_2 \tag{2.33}$$

where k_2 is the positive definite diagonal gain matrix.

The error variables are mapped from the joint space to the position-controlled subspace

using the following transformation:

$$\begin{aligned} z_1 &= q - q_d = J^{-1} e_p^m = J^{-1}(I - S)e_p \\ z_2 &= \dot{q} - \alpha = J^{-1}(I - S)\dot{e}_p + k_1 J^{-1}(I - S)e_p \end{aligned} \tag{2.34}$$

where $e_p^m = (I - S)e_p$ is the mapped error in the position-controlled subspace, $e_p = x_e - x_{ed}$ denotes the error in the end-effector position, I is the identity matrix, x_e and x_{ed} are the vectors of actual and desired end-effector position, respectively, and $S = \begin{bmatrix} s_1 & & & 0 \\ & s_2 & & \\ & & \ddots & \\ 0 & & & s_l \end{bmatrix} \in \mathbb{R}^{l \times l}$ is a compliance selection matrix that specifies the position-controlled degrees of freedom, i.e., s_j =0, and the force-controlled degrees of freedom, i.e., $s_j = 1$. Therefore, S specifies the directions with no motion due to the physical constraints ($S\dot{x}_e$=0) and $(I-S)$ corresponds to the free motion directions $\big((I-S)F = 0\big)$.

By substituting (2.34) in 2.32, the position control law is expressed as follows:

$$\tau_p = \Pi\hat{\varphi} - (k_2 k_1 + I)J^{-1}(I - S)e_p - k_2 J^{-1}(I - S)\dot{e}_p \tag{2.35}$$

2.4.2 Force Controller Design

Here, a proportional-integral-derivative (PID) controller is exploited to maintain the force applied by the ultrasound probe at the desired value. Therefore, clear and visible sonograms can be achieved without hurting the patient's body.

The force error in equation (2.15) is mapped into the force-controlled subspace using the selection matrix S and given by:

$$e_f^m = S e_f(t) \tag{2.36}$$

This error is transformed again into joint space with the help of the Jacobian matrix:

$$\tau_{e_f}(t) = J^T e_f^m \tag{2.37}$$

Based on (2.37), the force control signal is designed as follows:

$$\tau_f = J^T F_d + k_{fp}\tau_{e_f}(t) + k_{fi}\int \tau_{e_f}(t)dt + k_{fd}\tau_{e_f}(t) \tag{2.38}$$

where $J^T F_d$ denotes the force feedforward term, τ_{e_f} is the mapped force tracking error, k_{fp}, k_{fi}, and k_{fd} are the force proportional, integral, and derivative force controller gains, respectively.

The hybrid position-force control can be written as follows:

$$\begin{aligned}\tau_R =& \Pi\hat{\varphi} - (k_2k_1 + I)J^{-1}(I - S)e_p - k_2J^{-1}(I - S)\dot{e}_p \\ &+ J^T F_d + k_{fp}\tau_{e_f}(t) + k_{fi}\int \tau_{e_f}(t)dt + k_{fd}\tau_{e_f}(t)\end{aligned} \tag{2.39}$$

By replacing the equations (2.32), (2.33), and (2.39) into (2.31) and based on the fact that the interaction forces are in the null space of $(I - S)$, i.e., $\big((I - S)F\big) = 0$, the derivative of Lyapunov candidate becomes

$$\dot{V}_2 = -z_1^T k_1 z_1 - z_2^T k_2 z_2 - z_2^T e_m \tag{2.40}$$

2.4.3 Event-triggered Mechanism

The triggering condition is designed in the following based on the measurement error e_m that appears in the last term of the previous equation (2.40). This condition determines the transmission instants of a new control signal over the network to ensure the stability of the system and maintain the negative semi-definiteness of the Lyapunov function derivative. In other words, the event is defined as violating the pre-designed dynamic condition, which triggers the update and transmission of a new control signal over the network. By exploiting Young's inequality in equation (2.40).

$$\begin{aligned}\dot{V}_2 &\leq -z_1^T k_1 z_1 - z_2^T k_2 z_2 + \|z_2^T\|\|e_m\| \\ &\leq -\big(z_1^T k_1 z_1 + z_2^T k_2 z_2\big) + \frac{\|z_2^T\|^2}{2} + \frac{\|e_m\|^2}{2}\end{aligned} \tag{2.41}$$

By adding and subtracting the terms $\zeta\big(z_1^T k_1 z_1 + z_2^T k_2 z_2\big)$, one can obtain:

$$\dot{V}_2 \leq -(1 - \zeta)\big(z_1^T k_1 z_1 + z_2^T k_2 z_2\big) - \zeta\big(z_1^T k_1 z_1 + z_2^T k_2 z_2\big) + \frac{\|z_2^T\|^2}{2} + \frac{\|e_m\|^2}{2} \tag{2.42}$$

where ζ is a user-defined positive parameter. In the previous equation (2.42), if $0 < \zeta < 1$ and the following inequality remains true

$$\frac{\|z_2^T\|^2}{2} + \frac{\|e_m\|^2}{2} \leq \zeta\big(z_1^T k_1 z_1 + z_2^T k_2 z_2\big) \tag{2.43}$$

then, the negative semi-definiteness of Lyapunov function derivative is guaranteed, and the triggering function in equation (2.1) can be defined as follows:

$$T_{con}(e_m, z_1, z_2) = \|e_m\|^2 + \|z_2^T\|^2 - 2\zeta\big(z_1^T k_1 z_1 + z_2^T k_2 z_2\big) \tag{2.44}$$

It should be emphasized that the control input signal is updated and transmitted over the network in case this triggering function is greater than zero. Other than that, the robotic

manipulator is driven by the last received control signal. This maintains the negative semi-definiteness of the Lyapunov function derivative and causes a significant reduction in the number of transmissions over the network.

Proposition 1. *The ultrasound robotic system (2.5) actuated by the designed controller (2.39) and under the proposed event-triggered mechanism (2.44) is stable in the sense of Lyapunov and all the closed-loop signals are guaranteed to be bounded. The proper choice of the controller parameters provides a safe interaction during the ultrasound scan and ensures the convergence of tracking errors to a small neighborhood near zero. Moreover, the Zeno behavior is avoided under the designed event-triggered control strategy.*

Proof. The derivative of Lyapunov function can be written as follows

$$\dot{V}_2 \leq -\Theta V_2 + \Omega \tag{2.45}$$

where $\Theta = \min\left\{2\lambda_{min}(k_1), \frac{2\lambda_{min}(k_2)-\frac{\|1\|^2}{\zeta}}{\lambda_{max}\left(M_R(q)\right)}\right\}$, $\Omega = \frac{\zeta\|e_m\|^2}{2}$, and $\lambda_{min}(\cdot)$, $\lambda_{max}(\cdot)$ are the minimum and maximum eigenvalues of $(\cdot)$, respectively. To guarantee $\Theta > 0$, the parameters of motion controller k_1, k_2, ζ should be appropriately chosen to fulfill the following: $\lambda_{min}(k_1) > 0$, $\lambda_{min}(k_2) - \frac{\|1\|^2}{2\zeta} > 0$, and $0 < \zeta < 1$.

Multiplying both sides of (2.45) by $e^{\Theta t}$, one can get

$$\frac{d}{dt}(V_2 e^{\Theta t}) \leq \Omega e^{\Theta t} \tag{2.46}$$

By integrating (2.46) over the time $t = [0, t]$, the following equation is obtained

$$0 \leq V_2 \leq \left(V_2(0) - \frac{\Omega}{\Theta}\right)e^{-\Theta t} + \frac{\Omega}{\Theta} \tag{2.47}$$

and the tracking errors converge to the following sets

$$\|z_1\| \leq \sqrt{2\bar{V}}\ , \quad \|z_2\| \leq \sqrt{\frac{2\bar{V}}{\lambda_{max}\left(M_R\right)}} \tag{2.48}$$

where $\bar{V} = \max\left\{V_2(0), \frac{\Omega}{\Theta}\right\}$. This emphasize that all the closed-loop signals are ultimately bounded and the stability of the ultrasound robot can be ensured under the proposed event-triggered control scheme.

To complete the proof and avoid the Zeno behavior, a lower bound of the inter-event time is shown to be exist under the proposed event-triggered mechanism. Recalling, $e_m = \tau_R - \bar{\tau}_R$, then $\dot{e}_m = \dot{\tau}_R - \dot{\bar{\tau}}_R = \dot{\tau}_R \ \forall\ t \in [t_j, t_{j+1})$. Since τ_R is a function of bounded signals, therefore, there exists a positive upper bound ρ_1 that satisfies $|\dot{\tau}_R| \leq \rho_1$.

Moreover, $\forall\ t \in [t_j, t_{j+1})\ \dot{e}_m = \dot{\tau}_R$ then $|\dot{e}_m| \leq \rho_1$.

$$|\tau_R(t_{j+1}) - \tau_R(t_j)| = \left| \int_{t_j}^{t_{j+1}} \dot{\tau}_R(\psi) d\psi \right| \leq \int_{t_j}^{t_{j+1}} \left|\dot{\tau}_R(\psi)\right| d\psi \leq \int_{t_j}^{t_{j+1}} \rho_1 d\psi = \rho_1(t_{j+1} - t_j) \tag{2.49}$$

Let $e_m(t_j) = 0$ and $\lim_{t \to t_{j+1}^-} e_m(t) = \rho_2$ where ρ_2 is a positive constant depending on j, then we can write

$$\rho_2 \leq |\tau_R(t_{j+1}) - \tau_R(t_j)| \tag{2.50}$$

From the equations (2.49) and (2.50), one can obtain

$$\rho_2 \leq |\tau_R(t_{j+1}) - \tau_R(t_j)| \leq \rho_1(t_{j+1} - t_j) \tag{2.51}$$

Thus,

$$(t_{j+1} - t_j) \geq \frac{\rho_2}{\rho_1} \tag{2.52}$$

This ensures a lower bound of the inter-event time (i.e., $t^* = \frac{\rho_2}{\rho_1}$) [145]. The obtained bound satisfies $(t_{j+1} - t_j) \geq t^*\ \forall t \in [t_j, t_{j+1})$ and leads to the exclude of the Zeno behavior. Therefore, the corresponding proof is completed. □

2.5 Results and Discussions

To investigate the effectiveness of the proposed control strategy, the simulation test using a 5-DOFs ultrasound robot is conducted. The specifications of the robot and the required abdomen scan are explained in Section 2.2. The dynamic model of the general ultrasound robot is expressed by (2.5), where the detailed description of each matrix is given in Appendix A.1. The physical parameters of the robotic manipulator are given in Table A.2. These dynamical matrices and the physical parameters are consistent with the SCORBOT-ER VPlus manipulator. The ultrasound robot is dedicated to follow a circular trajectory on the x-y plane of the patient's abdomen. The applied force, by the ultrasound probe, is assumed to be 5 N in the Z-direction, which is sufficient to obtain clear sonograms [86]. During the assigned transversal ultrasound scan, two types of constraints are considered. The first one is the position constraint in the Z-direction, where the ultrasound probe cannot move freely in this direction to avoid hurting the patient. The second constraint is the force constraints in the X- and Y-directions. These constraints are utilized to define the compliance matrix S, which specifies the force- and position-controlled degree of freedom. The position of the end-effector can be selected as $x_e = (p_{e,x}, p_{e,y}, p_{e,z})^T$. The parametric form of the circular trajectory to be tracked by the ultrasound robot is expressed as follows:

$$p_{ed,x}(t) = R\cos(\omega_d t) + h, \quad p_{ed,y}(t) = R\sin(\omega_d t) + c \tag{2.53}$$

where h and c are constants, R and ω_d denote the radius and desired angular velocity of circular trajectory, respectively, t is the time.

It has been observed that there is no need to run all the motors of the ultrasound robot while performing the desired ultrasound scan. Therefore, the control strategy is applied upon three joints (base, shoulder, and elbow). The joints of the robot are revolute type (i.e., $q = \theta$). The simulation runs are conducted using MATLAB for $t = 6.28$ s and with a sampling time of 0.01 s. The parametric uncertainties are considered to be exist in the system. All the model parameters of the ultrasound robot are assumed to be altogether uncertain. Accordingly, the initial values of the estimated parameters vector are selected to be zero, i.e., $\hat{\varphi}(0) = 0$ (100% uncertainty (error) with respect to their actual value). This assumption is extended to all subsequent chapters of the thesis. The initial states are chosen as $x_1(0) = (31^\circ, -22.5^\circ, 69.3^\circ)^T, x_2(0) = (0, 0, 0)^T \ \frac{\text{deg}}{\text{s}}$, the selection matrix is defined as $S = \text{diag}(0, 0, 1)$, the position controller parameters are given as $k_1 = \text{diag}(80, 80, 80), k_2 = \text{diag}(100, 100, 100), \Gamma = \text{diag}(10, 10, 10), \zeta = 0.8$, and the parameters of the force controller are $F_d = (0, 0, 5)$ N, $k_{fp} = \text{diag}(1000, 1000, 1000)$, $k_{fi} = \text{diag}(1, 1, 1)$, and $k_{fd} = \text{diag}(1000, 1000, 1000)$. The position and force controller gains are tuned based on the trial and error method to maintain acceptable system performance in tandem with a minimum number of transmissions over the network. The actual force applied by the ultrasound probe is estimated in the simulation runs using the equation (2.11) where $K_{env} = 9 \times 10^5 \ \frac{\text{N}}{\text{m}}$. The parameters of the circular trajectory are $R = 0.1$ m, $\omega_d = 1 \ \frac{\text{rad}}{\text{s}}$, and $h = c = 0.15$ m.

2.5.1 Comparison Study

A comparative study between the proposed control strategy and the traditional time-triggered adaptive control schemes, i.e., adaptive position-force control (TT-APFC) [89] and the adaptive computed torque control (TT-ACTC) [193], is carried out in the presence of unknown parameters. These control schemes are devoted to follow a circular trajectory on the patient's abdomen and apply a constant force in the vertical plane by the proposed ultrasound robot. The effectiveness of the proposed control strategy is estimated in terms of position and force tracking errors and the number of transmitted control signals over the network. The root-mean-square error (RMSE) and the integral absolute error (IAE) are calculated to analyze the performance of the control strategy and defined as follows:

$$RMSE = \sqrt{\frac{1}{N_e}\sum_{k=1}^{N_e} e_k^2}, \quad IAE = \int |e| \ dt \tag{2.54}$$

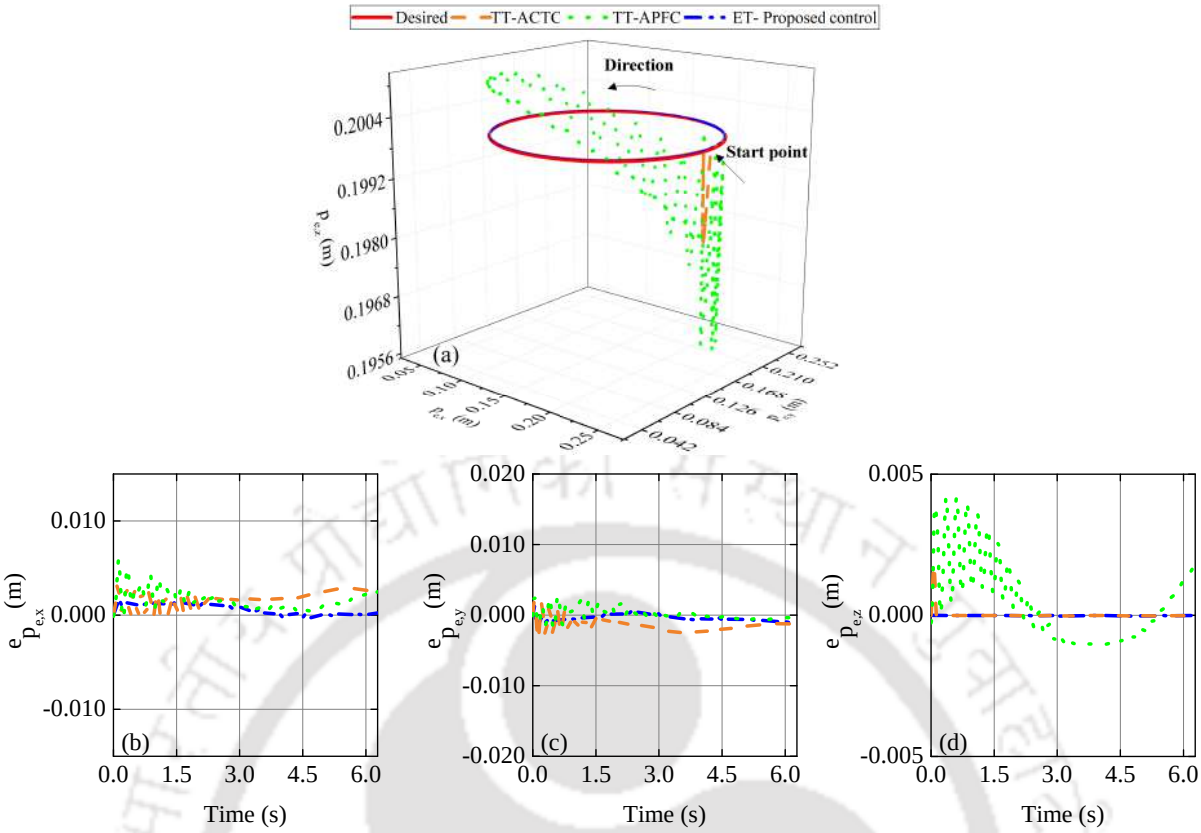

Figure 2.3: Trajectory tracking with ET and time-triggered control schemes. (a) Desired and actual trajectories. (b) Tracking error in X-direction. (c) Tracking error in Y-direction. (d) Tracking error in Z-direction

where e_k is the k-th element of error vector (e) and e: $e_{p_{e,x}} = p_{ed,x} - p_{e,x}$, is tracking error in X-direction; $e_{p_{e,y}} = p_{ed,y} - p_{e,y}$, is tracking error in Y-direction; $e_{p_{e,z}} = p_{ed,z} - p_{e,z}$, is tracking error in Z-direction; e_f, is the force tracking error; e_q, is the angular error, and N_e denotes the number of error points. It is to be noted that a smaller RMSE and IAE represent a better tracking performance.

Table 2.1: Comparison of ET and time-triggered schemes in joint space

Control strategy	θ_1		θ_2		θ_3	
	RMSE (deg)	IAE (deg)	RMSE (deg)	IAE (deg)	RMSE (deg)	IAE (deg)
TT-APFC [89]	0.3	1.7	0.28	1.5	0.28	1.7
TT-ACTC [193]	0.75	4	0.09	0.4	0.26	1.4
Proposed controller	0.2	1.3	0.03	0.18	0.1	0.57

The simulation results of the trajectory tracking for the proposed ET scheme and traditional time-triggered control schemes, i.e., TT-APFC [89] and TT-ACTC [193], are presented in Figure 2.3 (a). Moreover, the positional tracking errors in X-, Y-, and Z-

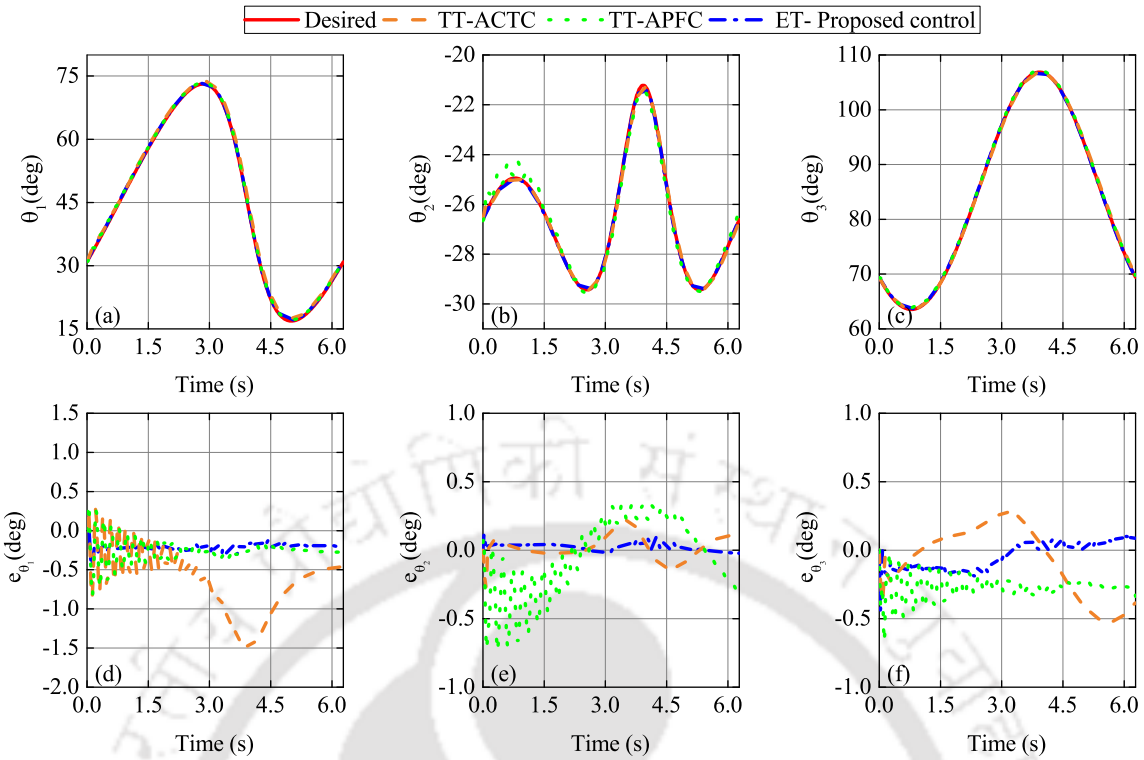

Figure 2.4: Joint variables with ET and time-triggered control schemes. Desired and actual joint trajectories for (a) first joint, (b) second joint, and (c) third joint. Angular error at (d) first joint, (e) second joint, (f) and third joint

directions are illustrated in Figure 2.3 (b, c, d). One can observe from the right side view in Figure 2.3 (a) that the proposed control scheme causes the faster convergence of the ultrasound robot to the desired trajectory with a better steady-state tracking performance than TT-APFC and TT-ACTC. Moreover, the positional tracking errors are still smaller and acceptable for the proposed ET control strategy compared to TT-APFC and TT-ACTC schemes. Therefore, with the implementation of the proposed approach, the parametric uncertainties cannot affect the performance of the ultrasound robot. The RMSE values in the X-direction are 0.8 mm, 1.81 mm, and 1.93 mm for the proposed control strategy, TT-APFC, and TT-ACTC, respectively. In the Y-direction, the RMSE of position tracking error is equal to 0.5 mm for the proposed scheme and 0.83 mm, 1.67 mm for TT-APFC and TT-ACTC, respectively. Furthermore, the Z-direction position error converges to zero because there is no motion of the ultrasound probe in this direction. Regarding the IAE, the event-triggered control scheme scores smaller values in the X- and Y-directions (4 mm, 3.2 mm) as compared with TT-APFC (9.6 mm, 3.9 mm) and TT-ACTC (11.2 mm, 9.7 mm).

Figure 2.4 (a, b, c) illustrates the tracking of the joint space's desired trajectories. These trajectories are calculated based on the inverse kinematic equations. Figure 2.4 (d, e, f)

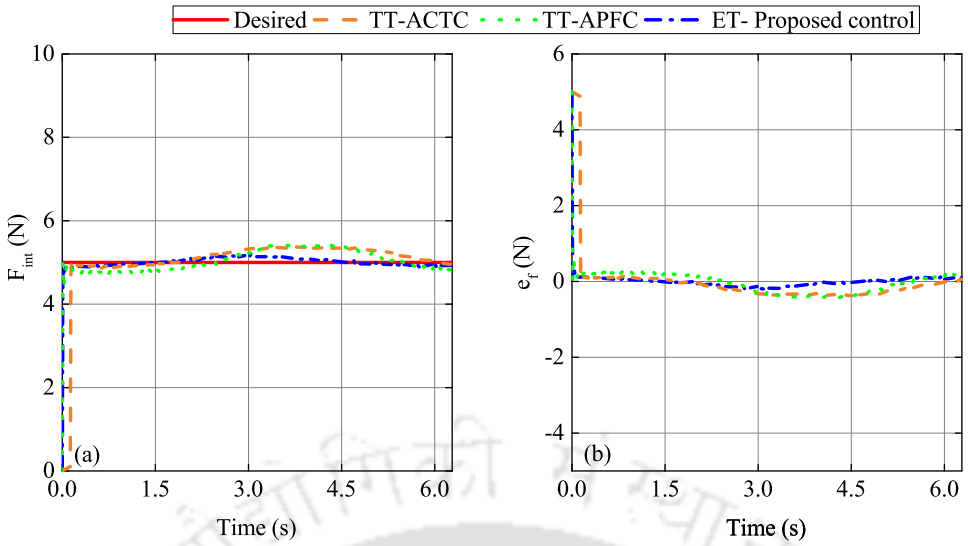

Figure 2.5: Tracking of the static force with ET and time-triggered control schemes. (a) Desired and actual force trajectories in Z-direction. (b) Force tracking error in Z-direction

represents the angular tracking error for the first, second, and third joints, respectively. Table 2.1 shows the RMSE and IAE at first, second, and third joints for the proposed control, TT-APFC, and TT-ACTC schemes. From Figure 2.4 and Table 2.1, it can be seen that the proposed ET control scheme still guarantees an accurate tracking performance during the scan process. Moreover, a smaller deviation from the desired trajectory is achieved compared with the traditional time-triggered control schemes.

Figure 2.5 (a) represents the tracking of a desired static force during the ultrasound scanning. The applied force by the ultrasound probe on the patient's abdomen should be within the range of 3 N-5.5 N. This range is defined to obtain clear sonograms without hurting the patient [86]. The force tracking error is depicted in Figure 2.5 (b). It can be observed that the proposed ET control strategy still provides a superior tracking accuracy with a smaller error deviation as compared with TT-APFC and TT-ACTC. The RMSE is equal to 0.21 N, 0.54 N, and 0.8 N for the proposed scheme, TT-APFC, and TT-ACTC, respectively. On the other hand, the designed controller scores a smaller IAE, i.e., 0.54 N compared to 1.43 N, 1.9 N for TT-APFC and ACTC, respectively.

The control inputs are dedicated to drive the joint actuators of the ultrasound robot through the predefined trajectory. Figure 2.6 (a, b, c) represents the control inputs at the first, second, and third joints, respectively. In the time-triggered implementation, the controller inputs are updated continuously and transmitted over the network. However, with the ET mechanism, the controller inputs are updated after a time gap, as shown in the zoomed area in Figure 2.6 (a). This aperiodic update reduces the number of required transmissions over the network. Moreover, it keeps the desired trajectory tracking

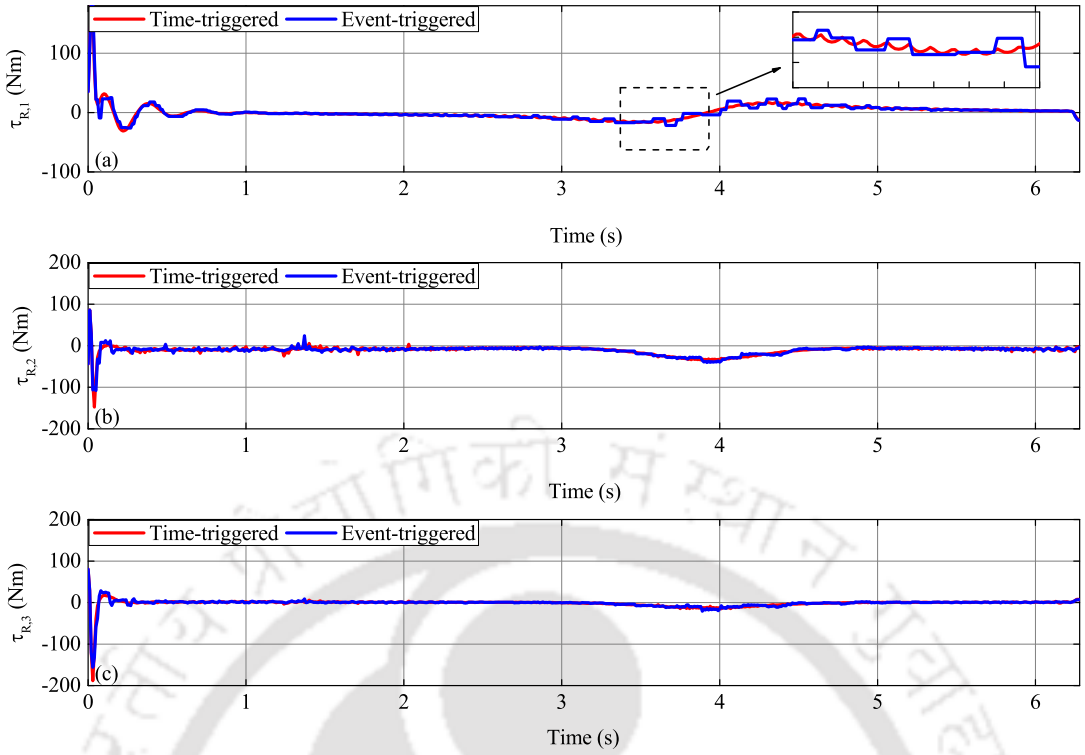

Figure 2.6: Controller inputs with ET and time-triggered control implementation at (a) first joint, (b) second joint, and (c) third joint

accuracy within desirable limits without losing contact with the patient's body.

To further investigate the efficiency of the proposed event-triggered scheme in terms of resource utilization, the designed Lyapunov-based triggering condition is compared with the most utilized triggering rules in the literature, i.e., fixed [145,194] and relative thresholds [145], which are defined in equations (1.1) and (1.2), respectively. This comparison is conducted based on the trajectory tracking errors, channel usage, and the number of transmissions over the network. For the sake of fair comparison, similar parameters for position and force controllers are utilized during the simulations of the fixed and relative thresholds. Moreover, the thresholds design parameters are selected to maintain an acceptable tracking performance with the lowest number of transmissions over the network. The channel usage can be calculated using the following equation:

$$CS = 100 \times N \times \frac{t}{dt} \tag{2.55}$$

where t is the total simulation time, dt is the sampling time, and N indicates the number of events.

In Figure 2.7, the trajectory tracking of the circular trajectory and the positional tracking errors are illustrated. Moreover, the time-instants where the triggering condition gets

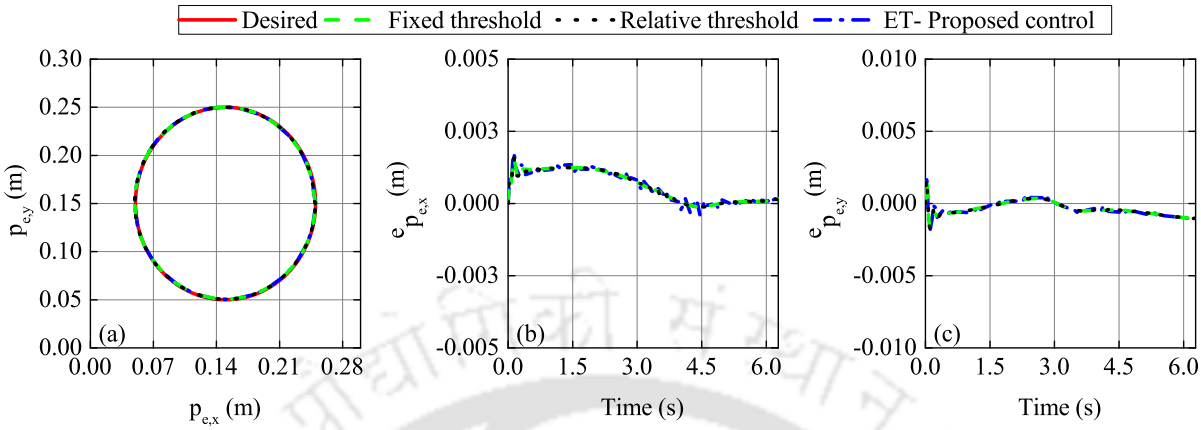

Figure 2.7: Trajectory tracking with proposed ET, fixed threshold, and relative threshold. (a) Desired and actual trajectories on the x-y plane. (b) Tracking error in X-direction. (c) Tracking error in Y-direction

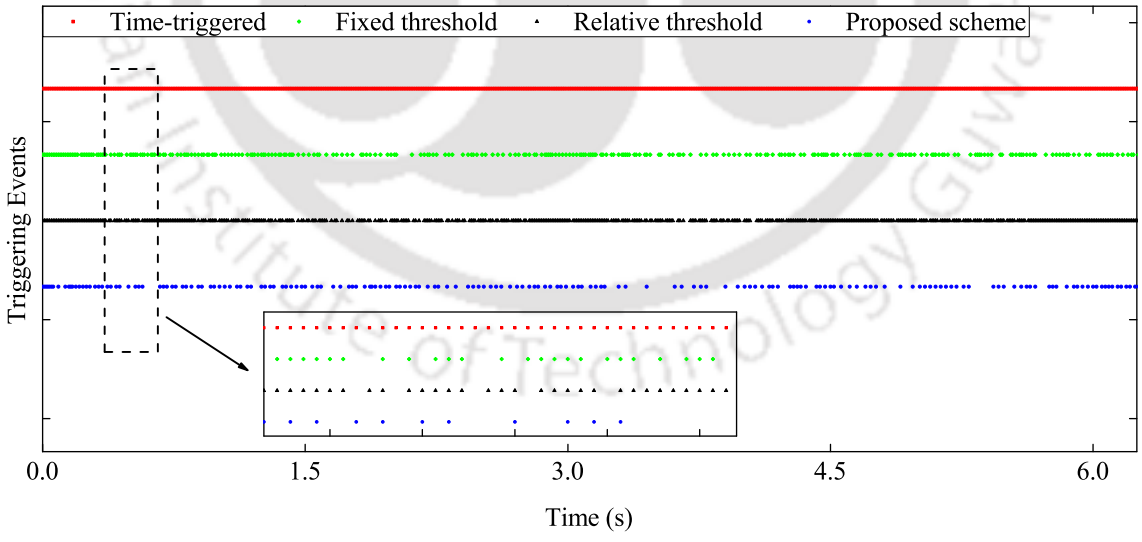

Figure 2.8: Triggering events for proposed ET, fixed threshold, and relative threshold

Table 2.2: Comparison of proposed ET condition, fixed threshold, relative threshold, and time-triggered schemes

	Time triggered		Fixed threshold [145, 194]	Relative threshold [145]	Proposed scheme
	APFC [89]	ACTC [193]			
Number of transmissions	628	628	306	522	170
Channel usage (CS)	100%	100%	48.7%	83%	27%
Maximum of inter-event time	0.01	0.01	0.09	0.04	0.15
IAE in X-direction (mm)	9.6	11.2	3.93	3.93	4
IAE in Y-direction (mm)	3.9	9.7	3.13	3.14	3.2

violated are depicted in Figure 2.8. It is worth mentioning that the control inputs are updated and transmitted over the network just at these instants. It can also be noted from Figure 2.7 that almost similar tracking performance is achieved for the proposed scheme, fixed threshold, and relative threshold. However, it is evident from Figure 2.8 that, under the developed ET scheme, a more significant saving of channel resources is achieved in terms of the number of transmissions. This resource-saving is accompanied with an acceptable tracking performance as compared with fixed and relative thresholds.

It can be observed from Table 2.2 that 73% of network-resources are saved under the proposed ET mechanism. However, the fixed and relative threshold strategies result in 51.3% and 17% savings in the resources. Moreover, there is no considerable increase in the positional tracking error as compared with the fixed and relative thresholds. The performance of the proposed scheme is still superior to the time-triggered control schemes presented in [89] and [193].

2.5.2 Validation on SCORBOT-ER VPlus in V-REP

To further validate the performance of the proposed control scheme, a SCORBOT-ER VPlus robotic arm is utilized to conduct the transversal scan of the patient's abdomen in a more realistic platform, i.e., V-REP robot simulator [195]. This virtual platform presents a more realistic simulation environment with a user-friendly interface and various functions that can be integrated through different embedded scripts and a detailed application interface (API). Moreover, it provides an effective solution to economize the cost and time and examine the performance of different control schemes in various applications before the implementation on real robotic systems. The model of the manipulator is designed in SolidWorks software and imported to V-REP through URDF Plugin. The SCORBOT-ER VPlus is equipped with an ultrasound probe and force sensor to simulate the desired ultrasound scanning task more realistically, as illustrated in Figure 2.10. The proposed ET control scheme is developed in MATLAB software and linked with the

V-REP environment using the Remote API feature. This control scheme is devoted to control SCORBOT-ER VPlus through the circular trajectory on the abdomen of patient while maintaining a constant force in the Z-direction.

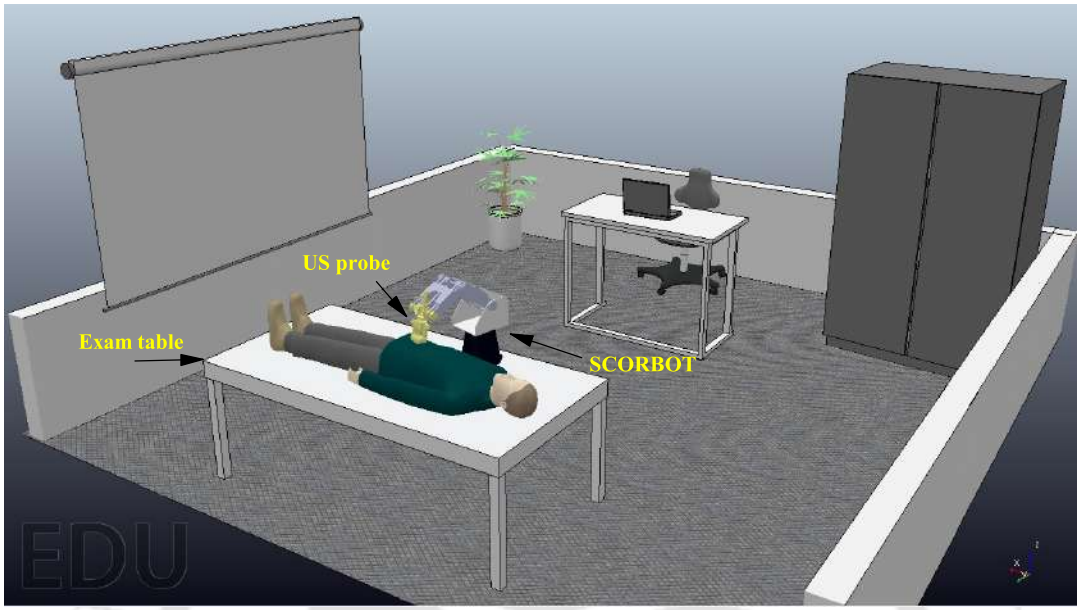

Figure 2.9: V-REP setup for ultrasound robot

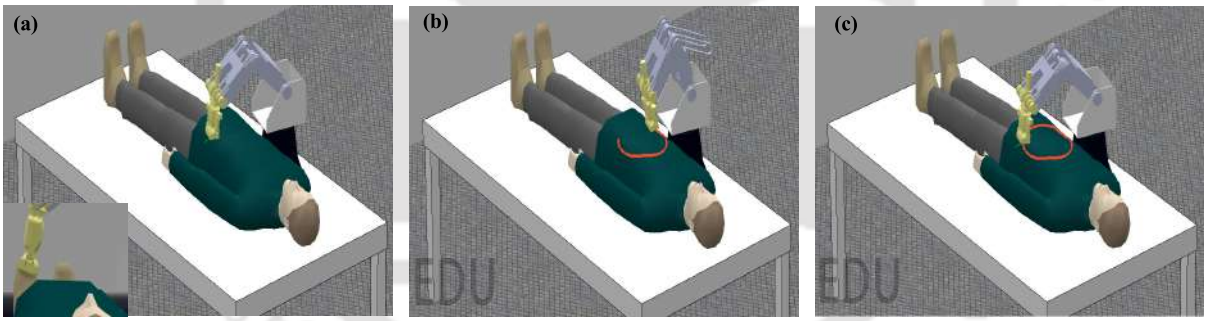

Figure 2.10: Validation results of SCORBOT-ER VPlus during the scan process of circular trajectory. (a) Initial position of ultrasound probe. (b) Ultrasound robot in the middle of scan task. (c) Final position of ultrasound probe

The initial state of the robot is chosen to have no contact between the ultrasound probe and the patient's abdomen, as shown in Figure 2.10 (a). The tracking of the desired circular trajectory and the positional errors are depicted in Figure 2.10 and Figure 2.11 (a, b, c). Further, force tracking and force errors are shown in Figure 2.11 (d, e). It can be noted from Figure 2.10 that the SCORBOT-ER VPlus successfully finishes the scan process under the proposed control scheme. Moreover, the circular trajectory is precisely tracked with a small positional tracking error, as illustrated in Figure 2.11 (a,

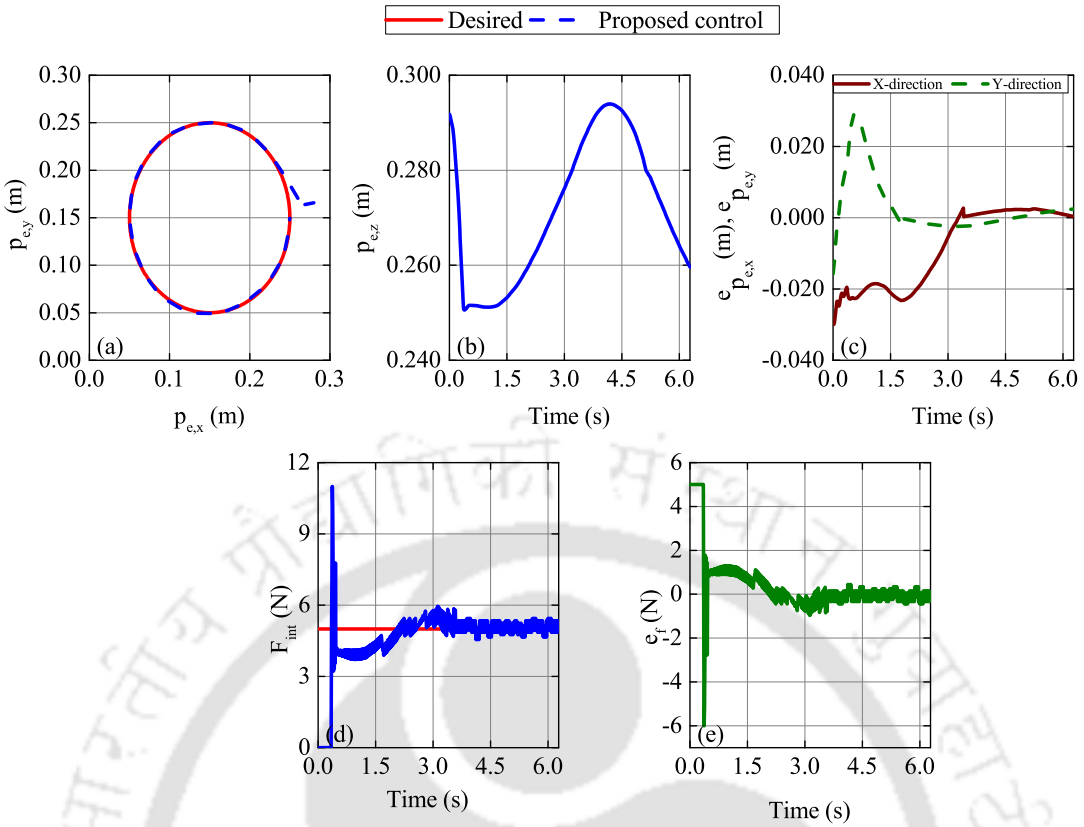

Figure 2.11: Position and force trajectory tracking with proposed ET control scheme during V-REP validation. (a) Desired and actual position trajectories on the x-y plane. (b) Actual position trajectory in the Z-direction. (c) Tracking errors in X-, Y-directions. (d) Desired and actual force trajectories in Z-direction. (e) Force tracking error in Z-direction

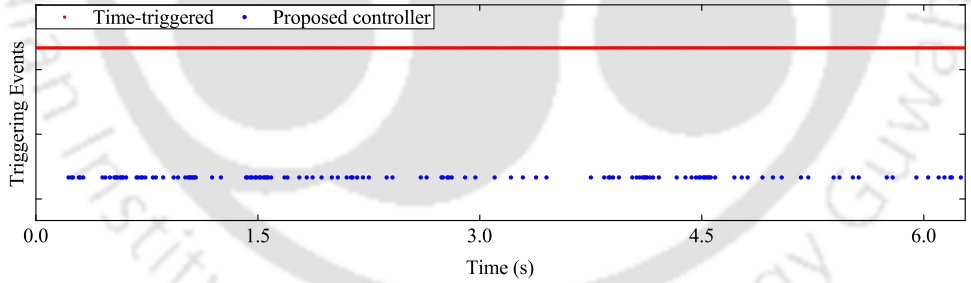

Figure 2.12: Triggering events during V-REP validation

c). Since the human abdomen surface is not flat and even, the trajectory tracking in the Z-direction is also presented in Figure 11 (b). On the other hand, a constant contact force during the scan process is successfully maintained, as presented in Figure 2.11 (d). The triggering events are shown in Figure 2.12. It can be observed that a significant saving of the network resources (about 80%) is obtained under the proposed ET scheme during the scan process compared to the TT implementation.

2.6 Summary

In this chapter, an event-triggered adaptive hybrid position-force control strategy is developed. This strategy is utilized to control an uncertain ultrasound robotic manipulator over a network during the scanning process of the patient's abdomen. The unknown parameters are estimated based on an adaptive backstepping approach. Moreover, the tracking of a static contact force is also ensured to obtain clear sonograms. On the other hand, the Lyapunov stability approach is employed to develop the triggering rule and ensure the stability of the closed-loop system. A comparison study with several controllers and event-triggered schemes from literature is conducted. The simulation results show that the proposed control scheme is superior and more applicable in position and force tracking accuracy. Moreover, the transmission of the control inputs over the network is reduced by 80% under the proposed triggering mechanism. Additional validation of the proposed scheme on the SCORBOT-ER 5Plus in the V-REP environment has been presented. Although precise position and force tracking is achieved using the hybrid position-force controller, some applications, such as robot-assisted rehabilitation exercises, require the robot to provide compliance without strictly regulating the contact forces to desired values. Therefore, in the next chapter, the event-triggered adaptive admittance control is presented to incorporate the robot-subject interaction and consider the active participation of the subject during the therapeutic exercises.

3

Event-Triggered Adaptive Admittance Control for Upper-Limb Robot-Assisted Passive and Active Rehabilitation Exercises

Contents

3.1 Introduction

In upper-limb robot-assisted rehabilitation exercises, the active participation of the subject should be considered without the requirement of direct regulation of subject-robot interaction forces. Moreover, compensating for parametric uncertainties and alleviating the bandwidth utilization in the network-based applications of end-effector type rehabilitation robot (EERR) is of great importance. Therefore, this chapter aims to design an event-triggered adaptive backstepping admittance controller (ETABAC) to tackle the parametric uncertainties and limited communication problems for the EERR during the patient-robot interaction in a unified framework. An adaptive backstepping position controller is designed to provide accurate rehabilitation exercises and maintain robustness against the parametric uncertainties associated with the EERR. Moreover, the admittance control strategy is integrated to deal with the reflex-based interaction forces and provide a compliant behavior to the patient during the therapeutic exercises. A dynamic event-triggered mechanism is designed based on the Lyapunov analysis to deal with the limited communication challenge, provide aperiodic control updates, and maintain the system stability. The passive and active-assist therapeutic exercises are carried out to investigate the effectiveness of the designed control strategy in providing a proper rehabilitation performance. Moreover, a comparison analysis is conducted with various time-triggered approaches to emphasize the proposed controller's ability to handle the uncertainties, limited communication, and interaction forces challenges.

This chapter is organized as follows. Section 3.2 presents the framework of the robot-assisted rehabilitation exercises. The dynamic of the rehabilitation robot is brought into Section 3.3. Section 3.4 elaborates on the design of the outer and inner control modules. Section 3.5 illustrates the simulation results and the comparative study. Finally, the conclusions of this chapter is highlighted in Section 3.6.

3.2 Framework of Robot-Assisted Rehabilitation Exercises

The robot-assisted rehabilitation system consists of three main components: the physiotherapist, the end-effector type rehabilitation robot (EERR), and the host control unit, as illustrated in Figure 3.1. The physiotherapist conducts an extensive assessment of the patient condition to decide the efficient therapeutic plan, type of rehabilitation exercise, and the desired training trajectory to be followed by the patient limb during the therapeutic session. The patient should be sitting on the exam chair in front of the rehabilitation

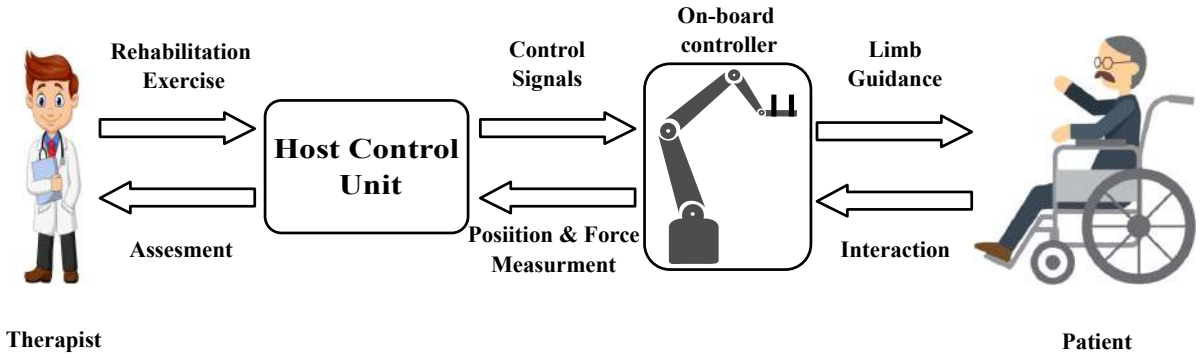

Figure 3.1: Framework of robot-assisted rehabilitation exercises

robot. The upper limb of the patient should be appended to the forearm support using the two arm splints. The host control unit processes the data provided by the therapist using the integrated control strategy to generate the required control signals for actuating the rehabilitation robot. Based on these commands, the EERR guides the impaired limb of the patient throughout the training trajectory to achieve a proper rehabilitation exercise and maintain a compliant patient-robot interaction. The measured position and interaction forces at the end-effector level are fed back to the host control unit through the on-board controller. This information is processed again, enabling the therapist to evaluate the progress of the rehabilitation process. The upper-limb rehabilitation protocol consists of two main therapeutic modes based on the patient's degree of participation, i.e., passive and active modes. The passive mode is performed at the early stage after stroke to reduce the muscle tone and increase the range of movement for the upper arm. Moreover, it includes no voluntary motion of the patient's limb throughout the exercise. However, a sudden muscle reflex in the impaired limb may occur at this rehabilitation stage. In the active mode, the patient restores the muscle strength partially and can be engaged in the therapeutic exercise. This therapy can be divided into active-assist therapy and active-resist therapy. Moreover, it is performed at the recovery stage after stroke. In active-assist therapy, the force applied by the patient (muscle strength) is not sufficient to follow the desired training trajectory. Therefore, the rehabilitation robot assists the patient to complete the therapeutic exercise successfully. However, the rehabilitation robot applies a resistive force in the opposite direction of limb motion during the resistive therapy.

The EERR utilized in this work is a serial manipulator equipped with a customized end-effector (forearm support) to handle the upper limb of the patient as shown in Figure 3.2. This manipulator consists of five revolute joints with a stationary base. The ranges of the manipulator's joints can cover the range of motion (ROM) of the human arm in the daily living activities (ADLs). Therefore, the flexion/extension and internal/external rotation

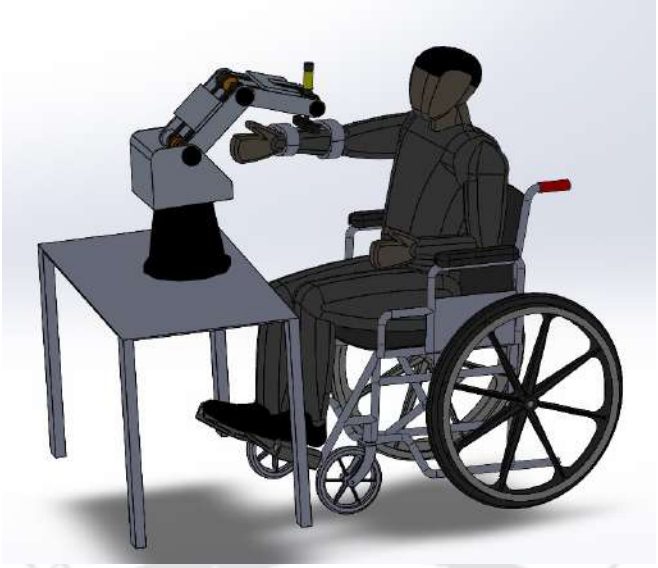

Figure 3.2: End-effector type rehabilitation robot with dummy subject

movements for the shoulder and elbow joints can be achieved. It should be noted that the right and the left arm of the patient can be trained using the EERR by changing the arm appended to the forearm support. A force sensor is placed at the wrist of the rehabilitation robot. This sensor is utilized to measure the interaction force between the patient's upper limb and the EERR. An eight-shape trajectory is generated to perform the passive and active-assist rehabilitation exercises for the patient's upper limb.

In the studied framework, the control inputs are calculated at the remote host control unit and transmitted to the EERR over a limited-bandwidth network channel. This necessitates an efficient utilization of the resources in tandem with accurate execution of the desired training exercises. Therefore, an event-triggered mechanism is placed at the controller-to-robot channel to avoid the periodic update of the control signals, reduce the communication burden, and maintain the stability of the rehabilitation robot. In place of continuous update of the control signals at each sampling time, the motors receive the actuation signals in an aperiodic manner with the said mechanism. In other words, the last control signals are held constant until a predefined condition gets violated. At this moment, the new actuation signal is generated and transmitted to the rehabilitation robot. The triggering instants can be defined as follows:

$$\begin{aligned} \bar{\tau}_R(t) &= \tau_R(t_j), \forall\ t \in [t_j, t_{j+1}) \\ t_{j+1} &= \inf\{t | t > t_j,\ T_{con}(e_m, z_1, z_2) > 0\} \end{aligned} \tag{3.1}$$

where τ_R is the control signal to be designed using backstepping approach, $\bar{\tau}_R$ is the event-triggered generated control signal, $e_m = \tau_R - \bar{\tau}_R$ is the measurement error, and

$T_{con}(e_m, z_1, z_2)$ the dynamic triggering condition to be designed based on Lyapunov analysis in the subsequent sections.

3.3 Dynamic Model of Rehabilitation Robot

The EERR consists of n degrees of freedom with a stationary base. The combined dynamics of the EERR with the patient-robot interaction can be expressed in the joint-space using the Lagrangian approach as follows:

$$M_R(q)\ddot{q} + C_R(\dot{q}, q)\dot{q} + G_R(q) = \bar{\tau}_R - \tau_{int}; \quad \tau_{int} = J^T(q)F_{int} \tag{3.2}$$

where $q, \dot{q}, \ddot{q} \in \mathbb{R}^n$ symbolize the joint position, velocity, and acceleration, respectively. $M(q) \in \mathbb{R}^{n\times n}$ denotes the inertia matrix, $C(\dot{q}, q) \in \mathbb{R}^{n\times n}$ is the matrix of Coriolis and centrifugal effects, $G(q) \in \mathbb{R}^n$ represents the gravitational torques, $\bar{\tau}_R \in \mathbb{R}^n$ stands for the vector of ET control torques, and $\tau_{int} \in \mathbb{R}^n$ is the vector of interaction torque between the environment and robot. The joint space dynamical representation of EERR (3.2) can be transformed into the Cartesian task space as follows [84]:

The first and second derivatives of the kinematics equation (2.9) can be written as:

$$\dot{x}_e = J(q)\dot{q} \tag{3.3}$$

$$\ddot{x}_e = J(q)\ddot{q} + \dot{J}(q)\dot{q} \tag{3.4}$$

where $\dot{x}_e$ and $\ddot{x}_e$ are the velocity and acceleration at the end-effector of the robotic manipulator. Therefore, the joint space velocity and acceleration are formulated as follows:

$$\dot{q} = J^{-1}\dot{x}_e \tag{3.5}$$

$$\ddot{q} = J^{-1}\ddot{x}_e - J^{-1}\dot{J}J^{-1}\dot{x}_e \tag{3.6}$$

These equations relate the joint space velocity and accelerations to the their counterparts at the task space. Substituting for $\dot{q}$ and $\ddot{q}$ in (3.2) and multiply both side of the equation by J^{-T}, the dynamics of EERR in the task space can be expressed as follows:

$$M_{R_x}(x_e)\ddot{x}_e + C_{R_x}(\dot{x}_e, x_e)\dot{x}_e + G_{R_x}(x_e) = \bar{F}_R - F_{int} \tag{3.7}$$

where x_e is the position of the end-effector of the rehabilitation robot in the Cartesian coordinate, $M_{R_x} = J^{-T}M_RJ^{-1}$, $C_{R_x} = J^{-T}(C_R - M_RJ^{-1}\dot{J})J^{-1}$, $G_{R_x} = J^{-T}G_R$, and $\bar{F}_R = J^{-T}\bar{\tau}_R$.

The properties of the robotic manipulator dynamics in the joint space can be extended to the task space as below [84]:

Property 4 The matrix M_{R_x} is symmetric and positive definite and satisfies the following condition:

$$v_3\|\beta\|^2 \leq \beta^T M_{R_x}(x_e)\beta \leq v_4\|\beta\|^2 \quad \forall\beta \in \mathbb{R}^n \tag{3.8}$$

Property 5 The matrix $M_{R_x} - 2C_{R_x}$ is skew-symmetric, i.e., for any arbitrary vector $\beta \in \mathbb{R}^n$ satisfies:

$$\beta^T\big(\dot{M}_{R_x}(x_e) - 2C_{R_x}(\dot{x}_e, x_e)\big)\beta = 0 \tag{3.9}$$

Property 6 For arbitrary known vector μ, the task space dynamics equations can be linearly parameterized as follows:

$$M_{R_x}(x_e)\dot{\mu} + C_{R_x}(\dot{x}_e, x_e)\mu + G_{R_x}(x_e) = \Pi_x\varphi_x \tag{3.10}$$

where $\Pi_x \in \mathbb{R}^{n\times p}$ is the regression matrix of known functions and $\varphi_x \in \mathbb{R}^p$ is the vector of unknown parameters.

3.4 Control Architecture

The architecture of the designed controller comprises two modules (i.e., outer and inner control modules), as depicted in Figure 3.3. The outer module is utilized to maintain a compliant interaction between EERR and the patient's upper limb during the therapeutic exercises. This compliant behavior is achieved by adopting the admittance control strategy in the outer loop. On the other hand, the inner module is dedicated to obtain accurate and repetitive guidance of the impaired upper limb throughout the reference trajectory in the presence of dynamic uncertainties and limited resources. This is realized via the event-triggered adaptive backstepping control scheme. The detailed design of the outer and inner control modules is carried out in the following subsections.

3.4.1 Outer Control Module

At the early stage of stroke, the sudden involuntary movement of the upper limb may occur during the passive therapeutic exercises due to neurological disorders and muscle reflex. This involuntary movement exerts sudden interaction forces at the end-effector of the rehabilitation robot. These forces, if not considered, may harm the patient and cause a serious injury to the upper limb. On the other hand, the impaired limb of the patient restores the motor function partially without the ability to reach the full range of motion (ROM) after extensive passive rehabilitation exercises. This voluntary movement (active participation) should be considered in the controller design process. Therefore, an

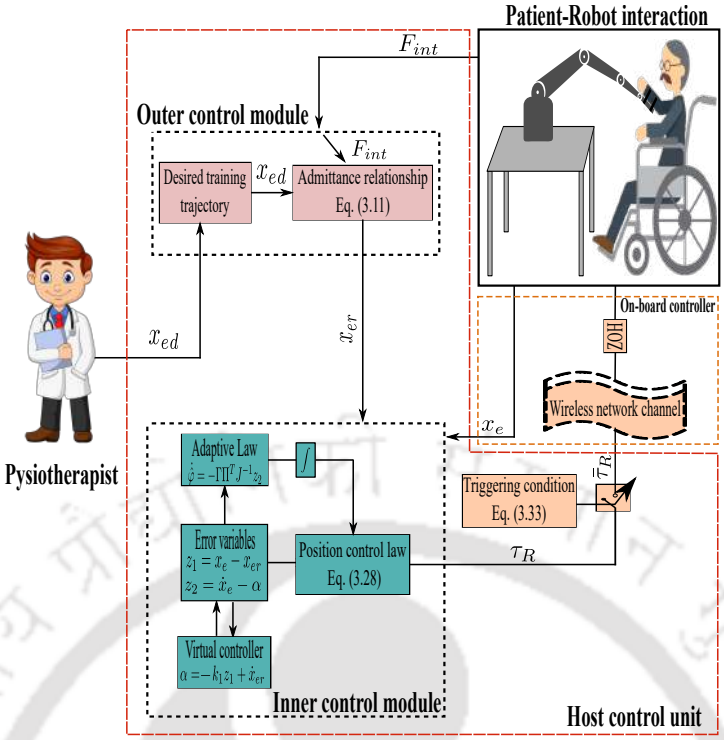

Figure 3.3: Block diagram of the proposed control scheme

admittance relationship is imposed between the EERR and the upper limb of the patient to attain a compliant interaction behavior, safety, and comfort throughout rehabilitation sessions. This admittance controller regenerates the desired trajectory based on the measured interaction forces, eliminating excessive forces between the EERR and the patient upper limb and maintaining the flexibility of the EERR during the therapeutic exercises. The description of the admittance control strategy can be defined as follows.

$$\begin{aligned} M_{ad}\Delta\ddot{x} + C_{ad}\Delta\dot{x} + K_{ad}\Delta x &= F_{int} \\ \Delta x &= x_{ed} - x_{er} \end{aligned} \tag{3.11}$$

where x_{ed} is the desired training trajectory defined by the therapist to mimic a certain therapeutic exercise, x_{er} is the output of the admittance relationship and denotes the reference training trajectory generated in response to the interaction forces, M_{ad}, C_{ad}, and K_{ad} are the symmetric positive definite admittance matrices. This matrices should be adjusted to achieve the desired compliance behavior. The desired training trajectory should be followed by the end-effector of the rehabilitation robot in the absence of interaction forces (if $F_{int} = 0$ then $x_{er} = x_{ed}$). Otherwise, the reference trajectory x_{er} is generated by the integration of the admittance equation (3.11). This reference trajectory is the input

to the inner control module in which an accurate position controller is designed in the following subsection.

3.4.2 Inner Control Module

To achieve efficient therapeutic rehabilitation, maintain accurate tracking of the reference training trajectory, and overcome the challenges of parametric uncertainties and limited resources, the design of an adaptive backstepping position controller is carried out in this subsection. In addition, the Lyapunov-based triggering condition is proposed here to reduce the number of transmissions over the network channel and attain the stability of the EERR. In other words, the adaptive backstepping approach is applied to guarantee that the actual training trajectories x_e follow the admittance generated reference trajectories x_{er} and to ensure the boundedness of the closed-loop system in the presence of uncertainties and limited communication. The dynamic model of the EERR (3.7) can be reformulated in the state space as follows.

$$\begin{aligned} \dot{x}_1 &= x_2 \\ \dot{x}_2 &= M_{R_x}^{-1}(x_e)(\bar{F}_R - C_{R_x}(\dot{x}_e, x_e)\dot{x}_e - G_{R_x}(x_e) - F_{int}) \end{aligned} \tag{3.12}$$

where $X = (x_1, x_2)^T = (x_e, \dot{x}_e)^T$ represents the state vector. The error variables for the EERR conducting the rehabilitation exercise are defined as follows.

$$z_1 = x_e - x_{er} = x_1 - x_{er} \tag{3.13}$$

$$z_2 = \dot{x}_e - \alpha = x_2 - \alpha \tag{3.14}$$

where α symbolizes the virtual controller.

Step 1: At this step, the virtual controller α is designed to stabilize the first error variable. The first Lyapunov function candidate is selected as.

$$V_1 = \frac{1}{2} z_1^T z_1 \tag{3.15}$$

Then, the time derivative of equation (3.15) becomes.

$$\dot{V}_1 = z_1^T \dot{z}_1 = z_1^T (z_2 + \alpha - \dot{x}_{er}) \tag{3.16}$$

If the virtual controller is designed as

$$\alpha = -k_1 z_1 + \dot{x}_{er} \tag{3.17}$$

where k_1 is a positive diagonal gain matrix, then the derivative of the Lyapunov function

becomes

$$\dot{V}_1 = -z_1^T k_1 z_1 + z_1^T z_2 \tag{3.18}$$

The negative definiteness of $\dot{V}_1$ and the convergence of z_1 to a small neighborhood of zero is guaranteed if the second error variable is equal to zero. Therefore, the stabilization of z_2 is carried out in the subsequent step.

Step 2: At this step, the Lyapunov function candidate can be selected using **Property 4** as follows.

$$V_2 = V_1 + \frac{1}{2} z_2^T M_{R_x}(x_e) z_2 \tag{3.19}$$

The derivative of the previous equation (3.19) is written as

$$\dot{V}_2 = \dot{V}_1 + z_2^T M_{R_x}(x_e)\dot{z}_2 + \frac{1}{2} z_2^T \frac{d\big(M_{R_x}(x_e)\big)}{dt} z_2 \tag{3.20}$$

By exploiting **Property 5** and equation (3.14), the Lyapunov function derivative can be rewritten as follows:

$$\begin{aligned} \dot{V}_2 &= \dot{V}_1 + z_2^T \big(M_{R_x}(x_e)\dot{z}_2 + C_{R_x}(\dot{x}_e, x_e) z_2\big) \\ &= \dot{V}_1 + z_2^T \big(- M_{R_x}(x_e)\dot{\alpha} - C_{R_x}(\dot{x}_e, x_e)\alpha - G_{R_x}(x_e) + \bar{F}_R - F_{int}\big) \end{aligned} \tag{3.21}$$

Mapping the dynamic matrices to the joint space using (3.7), one can obtain the following.

$$\dot{V}_2 = \dot{V}_1 + z_2^T \big(- J^{-T}\big(M_R\big(J^{-1}\dot{\alpha} - J^{-1}\dot{J}J^{-1}\alpha\big) + C_R J^{-1}\alpha + G_R - \bar{\tau}_R + J^T F_{int}\big)\big) \tag{3.22}$$

Using **Property 6** and exploiting the definition of measurement error i.e., $e_m = \tau_R - \bar{\tau}_R$, the previous equation is re-formulated as follows:

$$\dot{V}_2 = \dot{V}_1 + z_2^T J^{-T} \big(- \Pi\varphi + \tau_R - e_m - J^T F_{int}\big) \tag{3.23}$$

Due to the presence of uncertainties in the dynamical parameters of the rehabilitation robot, the design of adaptation law is required to estimate the unknown parameters φ. Therefore, the Lyapunov candidate in equation (3.19) should be modified to include the estimation errors and complete the stability proof as follows.

$$V_2 = V_1 + \frac{1}{2} z_2^T M_{R_x}(x_e) z_2 + \frac{1}{2} \tilde{\varphi}^T \Gamma^{-1} \tilde{\varphi} \tag{3.24}$$

where $\tilde{\varphi} = \varphi - \hat{\varphi}$, $\hat{\varphi}$ is the estimation of the unknown parameters φ, and Γ is a positive definite matrix. The derivative of the modified Lyapunov function (3.24) can be written as

$$\dot{V}_2 = \dot{V}_1 + z_2^T J^{-T} \big(- \Pi\varphi + \tau_R - e_m - J^T F_{int}\big) - \tilde{\varphi}^T \Gamma^{-1} \dot{\hat{\varphi}} \tag{3.25}$$

The term $z_2^T J^{-T}\Pi\hat{\varphi}$ is added and subtracted to the right side of (3.25)

$$\dot{V}_2 = \dot{V}_1 - z_2^T J^{-T}\Pi\tilde{\varphi} - z_2^T J^{-T}\Pi\hat{\varphi} + z_2^T J^{-T}\big(\tau_R - e_m - J^T(q)F_{int}\big) - \tilde{\varphi}^T\Gamma^{-1}\dot{\hat{\varphi}} \tag{3.26}$$

By taking the transpose of the second term at the right side of equation (3.26), one can obtain:

$$\dot{V}_2 = \dot{V}_1 - \tilde{\varphi}^T\big(\Pi^T J^{-1} z_2 + \Gamma^{-1}\dot{\hat{\varphi}}\big) - z_2^T J^{-T}\Pi\hat{\varphi} + z_2^T J^{-T}\big(\tau_R - e_m - J^T(q)F_{int}\big) \tag{3.27}$$

The control and adaptation laws can be designed as

$$\tau_R = \Pi\hat{\varphi} + J^T(q)\big(-z_1 - k_2 z_2 + F_{int}\big) \tag{3.28}$$

$$\dot{\hat{\varphi}} = -\Gamma\Pi^T J^{-1} z_2 \tag{3.29}$$

where k_2 is the positive definite diagonal gain matrix. Therefore, the derivative of Lyapunov function becomes

$$\dot{V}_2 = -z_1^T k_1 z_1 - z_2^T k_2 z_2 - z_2^T J^{-T} e_m \tag{3.30}$$

The triggering condition is designed in the following based on the measurement error e_m that appears in the last term of the previous equation (3.30). This condition determines the transmission instants of a new control signal over the network to ensure the stability of the system and maintain the negative semi-definiteness of the Lyapunov function derivative. By exploiting Young's inequality in equation (3.30).

$$\begin{aligned}\dot{V}_2 &\leq -z_1^T k_1 z_1 - z_2^T k_2 z_2 + \|z_2^T J^{-T}\|\|e_m\| \\ &\leq -(1-\zeta)\big(z_1^T k_1 z_1 + z_2^T k_2 z_2\big) - \zeta\big(z_1^T k_1 z_1 + z_2^T k_2 z_2\big) + \frac{\|z_2^T J^{-T}\|^2}{2} + \frac{\|e_m\|^2}{2}\end{aligned} \tag{3.31}$$

In the previous equation (3.31), if $0 < \zeta < 1$ and the following inequality remains true

$$\frac{\|z_2^T J^{-T}\|^2}{2} + \frac{\|e_m\|^2}{2} \leq \zeta\big(z_1^T k_1 z_1 + z_2^T k_2 z_2\big) \tag{3.32}$$

Then, the negative semi-definiteness of Lyapunov function derivative is guaranteed, and the triggering function in equation (3.1) can be defined as follows:

$$T_{con}(e_m, z_1, z_2) = \|e_m\|^2 + \|z_2^T J^{-T}\|^2 - 2\zeta\big(z_1^T k_1 z_1 + z_2^T k_2 z_2\big) \tag{3.33}$$

It should be emphasized that the control input signal is updated and transmitted over the network in case this triggering function is greater than zero. Other than that, the EERR is driven by the last received control signal. This maintains the negative semi-definiteness of the Lyapunov function derivative and causes a significant reduction in the number of

transmissions over the network.

Proposition 2. *The end-effector type rehabilitation robot actuated by the designed controller (3.28) with the adaptation law (3.29), the admittance scheme (3.11), and under the proposed event-triggered mechanism (3.33) is stable in the sense of Lyapunov and all the closed-loop signals are guaranteed to be bounded. The proper choice of the controller parameters provides a compliant behavior during the therapeutic exercises and ensures the convergence of tracking errors to a small neighborhood near zero. Moreover, the Zeno behavior is avoided under the designed event-triggered control strategy.*

Proof. The triggering condition (3.33) is designed to render the derivative of Lyapunov function negative semi-definite. This derivative can be written as follows:

$$\dot{V}_2 \leq -\Theta V_2 + \Omega \tag{3.34}$$

where $\Theta = \min\left\{2\lambda_{min}(k_1), \frac{2\lambda_{min}(k_2) - \frac{\|J^{-T}\|^2}{\zeta}}{\lambda_{max}\left(M_{R_x}(x_e)\right)}\right\}$, $\Omega = \frac{\zeta\|e_m\|^2}{2}$, and $\lambda_{min}(\cdot)$, $\lambda_{max}(\cdot)$ are the minimum and maximum eigenvalues of $(\cdot)$, respectively. Therefore, similar to the analysis in Proposition 1, the convergence of tracking errors to the following sets can be ensured:

$$\|z_1\| \leq \sqrt{2\bar{V}}\ , \quad \|z_2\| \leq \sqrt{\frac{2\bar{V}}{\lambda_{max}\left(M_{R_x}\right)}} \tag{3.35}$$

where $\bar{V} = \max\left\{V_2(0),\ \frac{\Omega}{\Theta}\right\}$. This emphasizes that all the closed-loop signals are ultimately bounded and the stability of the EERR can be ensured under the proposed event-triggered control scheme. Moreover, the proof of avoiding the Zeno behavior presented in Proposition 1 is still valid and can be directly applied in the case of adaptive admittance control of EERR. □

3.5 Results and Discussions

In this section, the effectiveness of the proposed control scheme is analyzed for three different cases of rehabilitation modes, i.e., passive with sudden reflex, active-assist with high admittance parameters, and active-assist with low admittance parameters. These variations in the admittance parameters are utilized to examine their effects on the degree of flexibility provided to the patient. A human dummy with age, weight, and height of 23 years, 60 kg, and 173 cm is assumed in the human-robot collaboration to mimic the experimental effect in the simulation environment. The description of the dynamical matrices for the rehabilitation robot presented in the framework section and utilized during the simulation runs is given in Appendix A.1. These dynamical matrices and the physical parameters are similar to the SCORBOT-ER VPlus robotic manipulator. An eight shape

Table 3.1: Comparative performance analysis of the proposed control over the contrast controllers during the passive rehabilitation with sudden reflex

Controller	Tracking error in X-direction		Tracking error in Y-direction		Number of transmissions
	RMSE (mm)	PI (%)	RMSE (mm)	PI (%)	
PID	1.687	87.72	2.944	93.44	3143
ASMC	1.023	79.76	1.908	89.88	3143
Proposed Controller	0.207	-	0.193	-	607

trajectory is considered as the desired trajectory to be followed by the subject in the horizontal plane i.e., $x_{ed}(t) = [p_{ed,x}, p_{ed,y}]^T = [0.1 + \frac{0.05\sin(\omega_d t)\cos(\omega_d t)}{1+\sin^2(\omega_d t)}, 0.1 + \frac{0.05\sin(\omega_d t)}{1+\sin^2(\omega_d t)}]^T$. The upper limb movement involved in the proposed exercise includes the shoulder horizontal flexion/extension, shoulder internal/external rotation, and elbow flexion/extension. The range of motion covered during the exercise can be tentatively expected to be 20°, 25°, 34° for each movement, respectively. The duration of each rehabilitation exercise is set to be 12.57 s with 0.004 s as sampling time and $\omega_d = 1\ \frac{\text{rad}}{\text{s}}$. This trajectory is visualized as sinusoidal and cosine trajectory in X- and Y-directions with the following initial position $[p_{e,x}(0) = 0.1\ \text{m}, p_{e,y}(0) = 0.15\ \text{m}]^T$ and velocity equals to zero. It has been noticed that there is no need to run all the motors simultaneously to perform the designed rehabilitation exercises throughout the defined trajectory. Therefore, the actuation signals are restricted upon the first three joints of the robot. For each case, the performance of the proposed controller is further compared with two contrast control techniques, i.e., proportional-integral-derivative (PID) [97] and adaptive sliding mode control (ASMC) [196]. The parameters for the proposed control scheme are selected as: $k_1 = \text{diag}(50, 50, 50)$, $k_2 = \text{diag}(100, 100, 100)$, $\zeta = 0.95$, and $\Gamma = \text{diag}(0.01, 0.01, 0.01)$. The control law and the selected gain parameters for the contrast controllers are given in Appendix A.2. The simulation results for above-mentioned cases are discussed using two different performance metrics as root-mean-squared error (RMSE) and performance index (PI), defined as follows:

$$RMSE = \sqrt{\frac{1}{N_e}\sum_{k=1}^{N_e} e_k^2}, \quad PI = \frac{RMSE_{TT-cont} - RMSE_{ET-proposed}}{RMSE_{TT-cont}} \times 100\% \tag{3.36}$$

where e: $e_{p_{e,x}} = p_{er,x} - p_{e,x}$, is the error in X-direction; $e_{p_{e,y}} = p_{er,y} - p_{e,y}$ is the error in Y-direction, and *cont* denotes the contrast controller i.e., PID or ASMC.

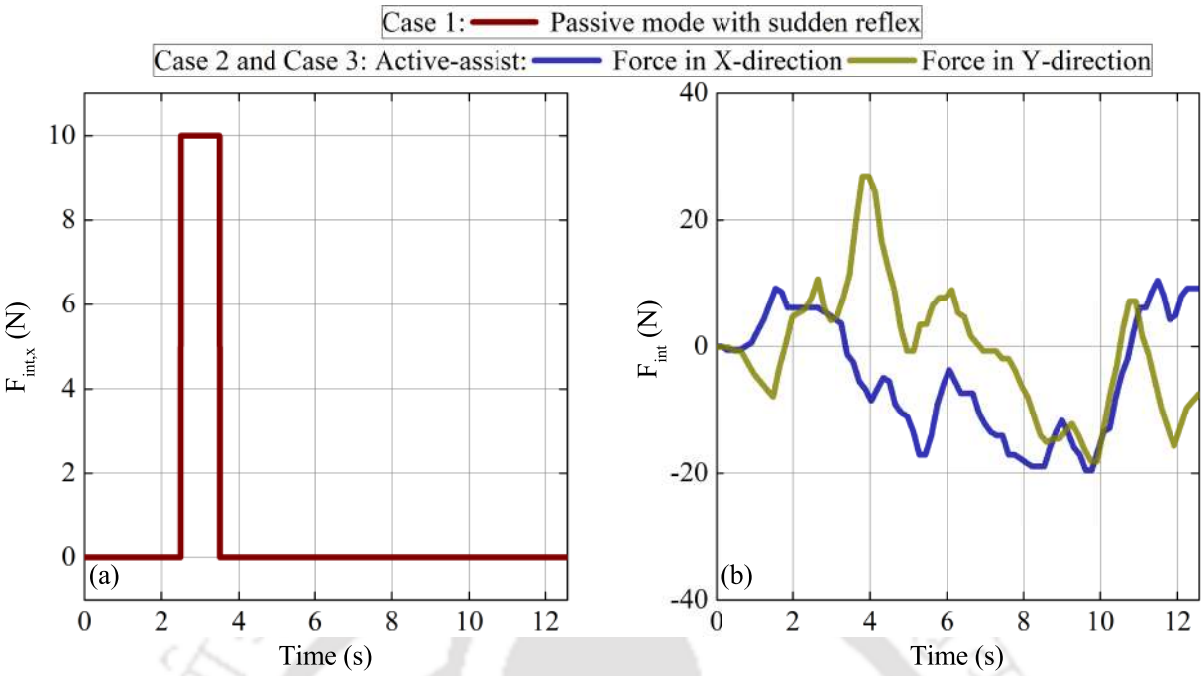

Figure 3.4: Interaction forces during different therapeutic exercises. (a) Applied sudden reflex during passive rehabilitation. (b) Applied forces during active-assist rehabilitation

3.5.1 Case 1: Passive Training Mode with Sudden Reflex

In this case, the subject's arm is passively guided by the EERR, assuming that the subject does not exert any force from his\her side. This kind of therapy is beneficial in the early stages of the stroke, where muscle strength is minimal. However, sometimes, EERR experiences sudden reflexes due to convulsive movement from residual motor strength. Invoking the admittance-position model, the robot can be marginally flexible to compensate for the sudden force and then take a quick comeback to track the reference trajectory. Therefore, a reasonably high admittance parameters for the EERR are selected: $M_{ad} = \text{diag}(0.5, 0.5, 0.5)$, $C_{ad} = \text{diag}(100, 100, 100)$, and $K_{ad} = \text{diag}(1750, 1750, 1750)$. The same values are selected for the contrast controllers to maintain a fair comparison analysis. The sudden reflex is modeled as a pulse function that appears at certain time intervals in the X-direction as shown in Figure 3.4(a) and defined in the following equation:

$$F_{int,x}(t) = \begin{cases} A_{int}, & \text{if } t^s_{int} \leq t \leq t^e_{int} \\ 0, & \text{otherwise} \end{cases} \tag{3.37}$$

where $A_{int} = 10$ N is the amplitude of the modeled reflex and $t^s_{int} = 2.5$ s, $t^e_{int} = 3.5$ s represent the starting and ending time intervals for the sudden forces, respectively.

After applying the proposed control scheme, the reference $(p_{er,x}, p_{er,y})$ and actual tra-

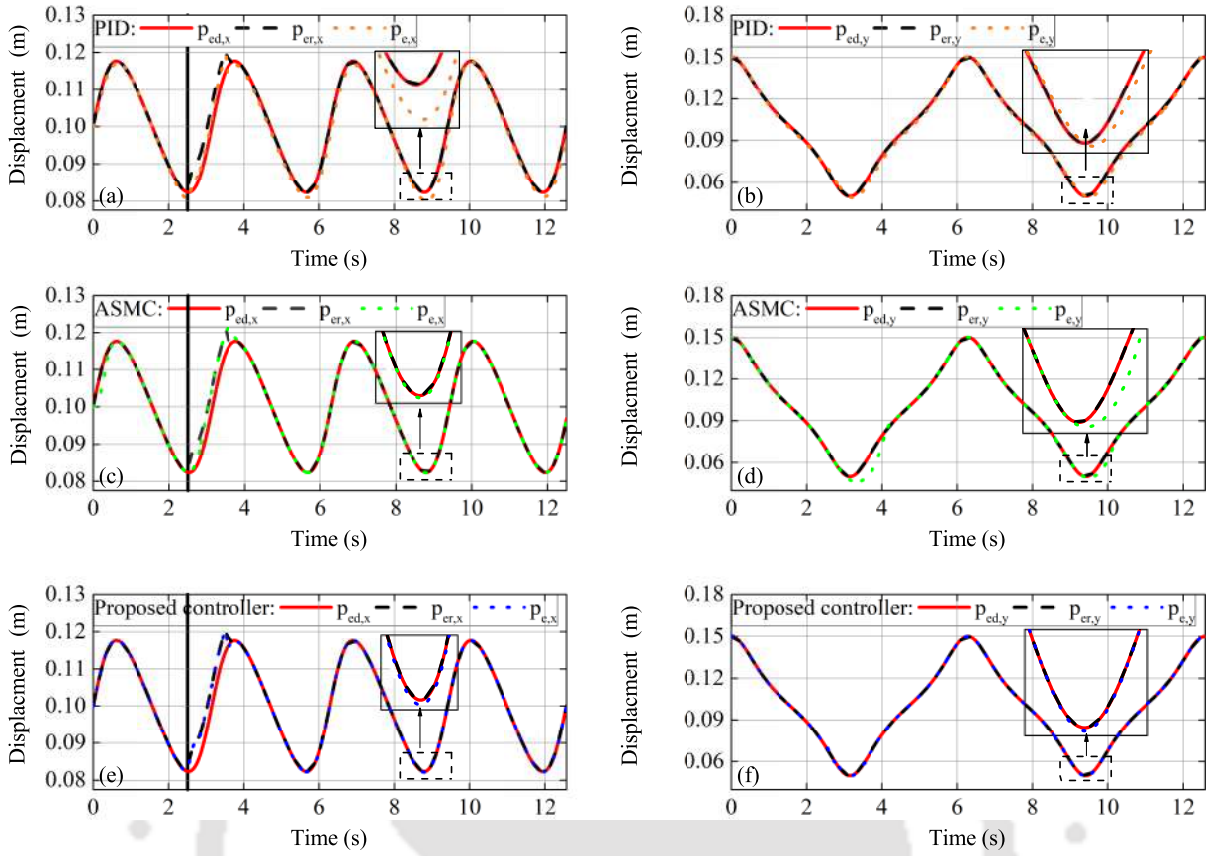

Figure 3.5: Reference and actual trajectories in X- and Y-directions during passive rehabilitation with sudden reflex for different control schemes. Top: PID controller. Middle: ASMC controller. Bottom: proposed controller.

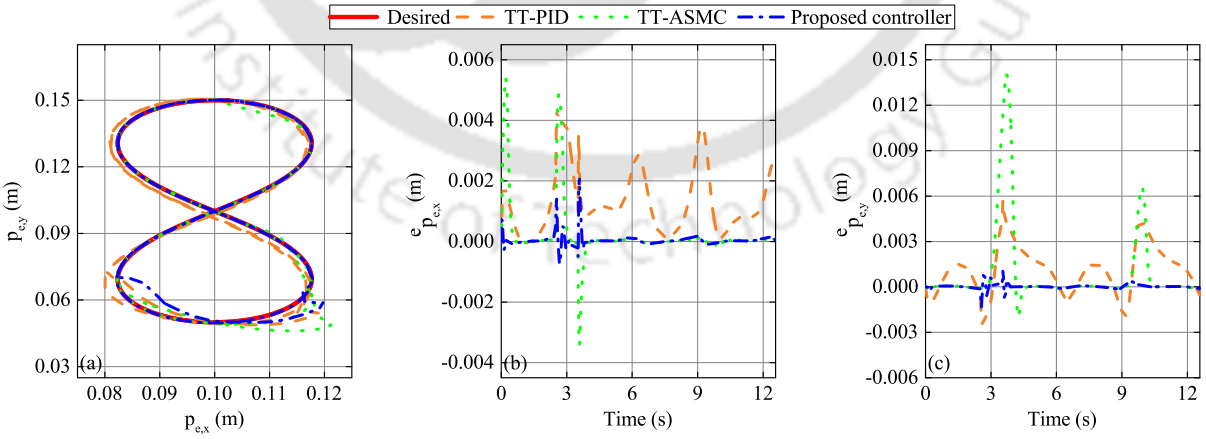

Figure 3.6: Eight shape trajectory tracking during passive rehabilitation with sudden reflex for different control schemes. (a) Trajectory tracking in x-y plane. (b) Position error in X-direction. (c) Position error in Y-direction

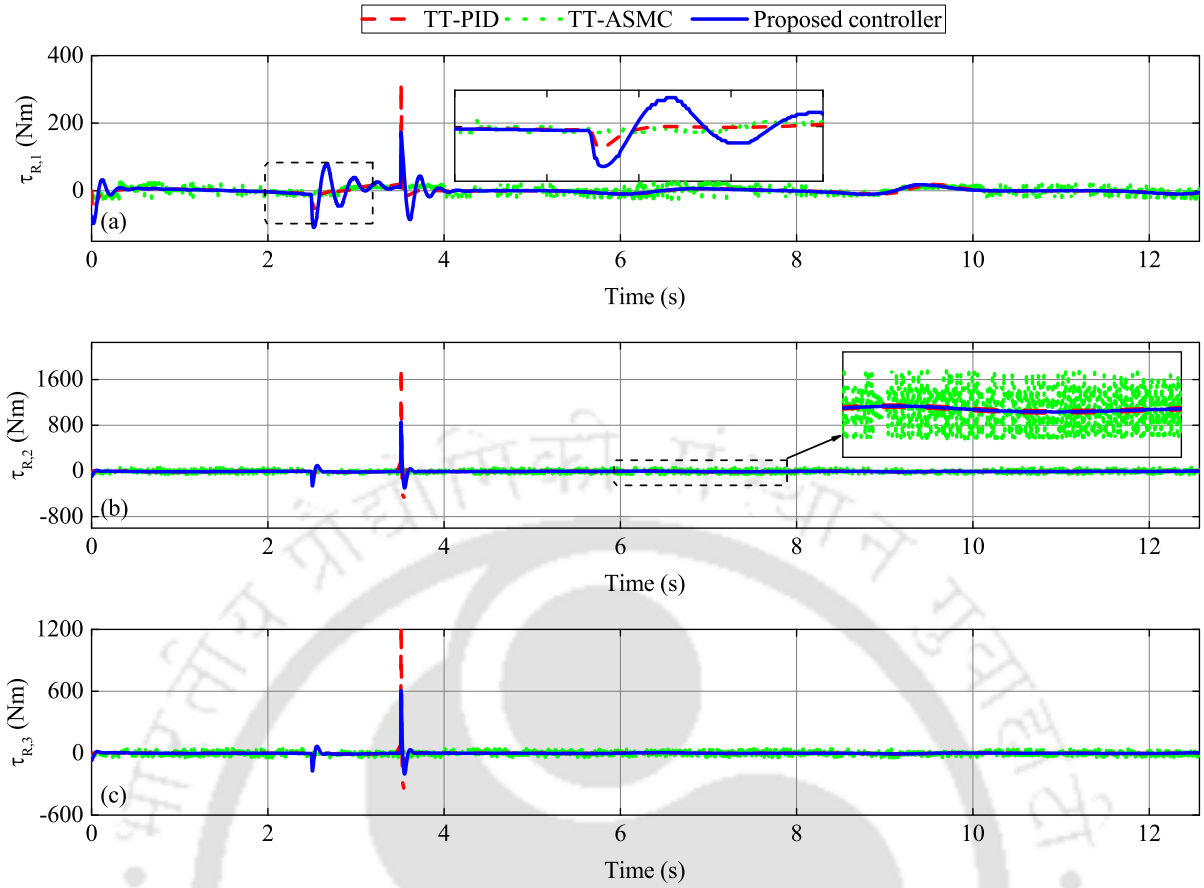

Figure 3.7: Controller inputs during passive rehabilitation with sudden reflex for different control schemes at: (a) First joint. (b) Second joint. (c) Third joint

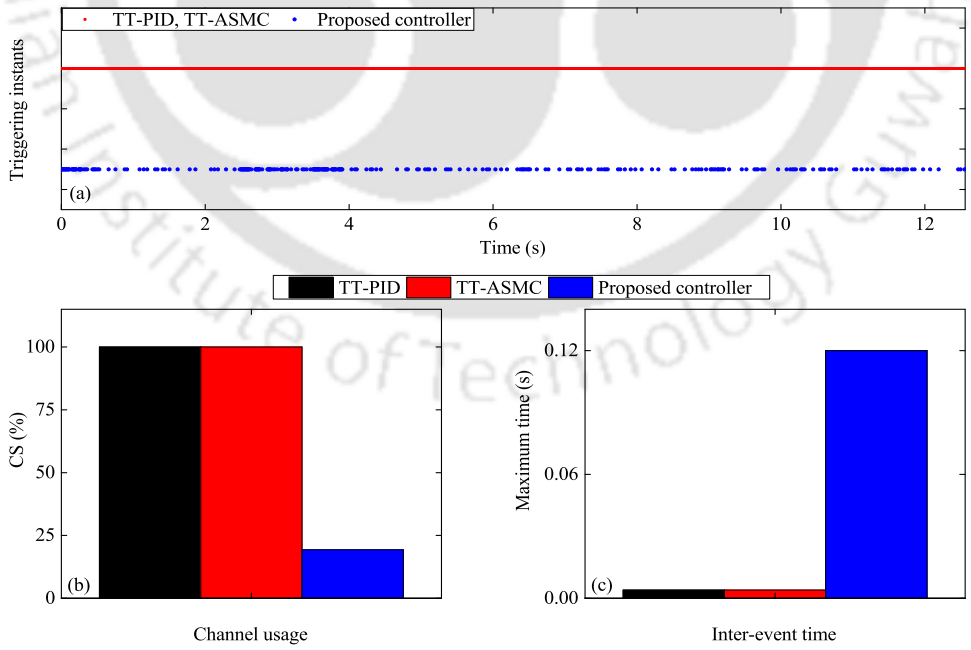

Figure 3.8: Simulation results of (a) triggering instants, (b) channel usage, and (c) inter-event time during passive rehabilitation with sudden reflex for different control schemes

jectories $(p_{e,x}, p_{e,y})$ for the contrast and proposed control schemes are shown in Figure 3.5. The tracking results for PID, ASMC, proposed control in X- and Y-directions are shown in Figures 3.5(a)-(f). In these figures, the vertical black lines correspond to the moment of the sudden reflex appearance. Figures 3.6(a), 3.6(b), and 3.6(c) present the trajectory tracking in x-y plane, tracking error in X-direction, and tracking error in Y-direction, respectively. Referring to the results in X-direction, it can be observed that the implementation of the outer admittance control module allows the robot to deviate a little from the desired trajectory at the expense of sudden force for the three different controllers. However, as the exertion of sudden force gets over, the proposed control allows rapid convergence of the actual trajectory to the desired one compared to contrast control schemes. Before and after the application region of sudden force, the inner position control module plays an important role in tracking the desired and reference trajectories, respectively. From Table 3.1, the RMSE values for proposed controller $(x, y : 0.207 \text{ mm}, 0.193 \text{ mm})$ is found to be less than the PID $(x, y : 1.687 \text{ mm}, 2.944 \text{ mm})$ and ASMC $(x, y : 1.023 \text{ mm}, 1.908 \text{ mm})$. Consequently, the PI of proposed control over PID and ASMC in X-direction is 87.72% and 79.76%, respectively. On the other hand, the respective values of PI in the Y-direction is 93.44% and 89.88%. Figure 3.7 presents the actuator torques for three joints of the EERR. As observed from Figure 3.7(a)-(c), the maximum absolute values of joint torques are observed at the last moment of sudden force exertion, i.e., when the actual trajectory abruptly return to track the desired trajectory. The maximum values of joint torques are higher in the case of PID and ASMC over the proposed control scheme. A significant amount of chattering phenomena can also be observed for ASMC compared to PID and the proposed controller. Moreover, the control signals of the proposed controller are held constant during the trajectory tracking task due to the implementation of the event-triggered mechanism, as illustrated from the zoomed view. The triggering instant, channel usage (CS), and inter-event time are illustrated in Figures 3.8(a) and 3.8(b), 3.8(c) respectively. It can be observed that the designed triggering condition results in aperiodic control updates and a huge reduction in the communication burden with 19.5% of channel usage compared with 100% usage in the case of PID and ASMC. Moreover, a higher number of triggering instants is required during the presence of sudden reflex, as shown in Figure 3.8(a). This increased number of transmitted control signals is attributed to the suddenly applied interaction forces that lead to a sudden change in the reference trajectory. This abrupt change needs more control updates to compensate for the deviation and re-follow the generated reference trajectory.

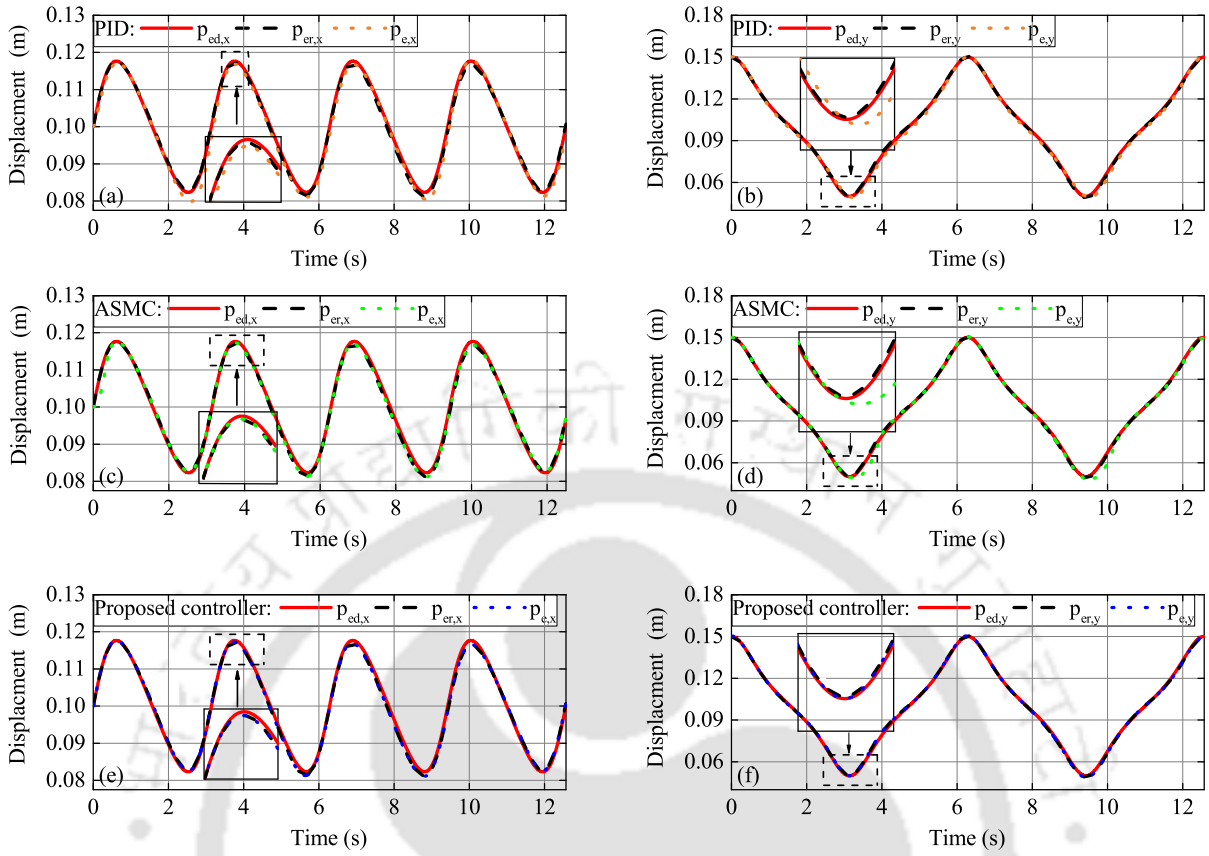

Figure 3.9: Reference and actual trajectories in X- and Y-directions during active-assist rehabilitation with high admittance parameters for different control schemes. Top: PID controller. Middle: ASMC controller. Bottom: proposed controller.

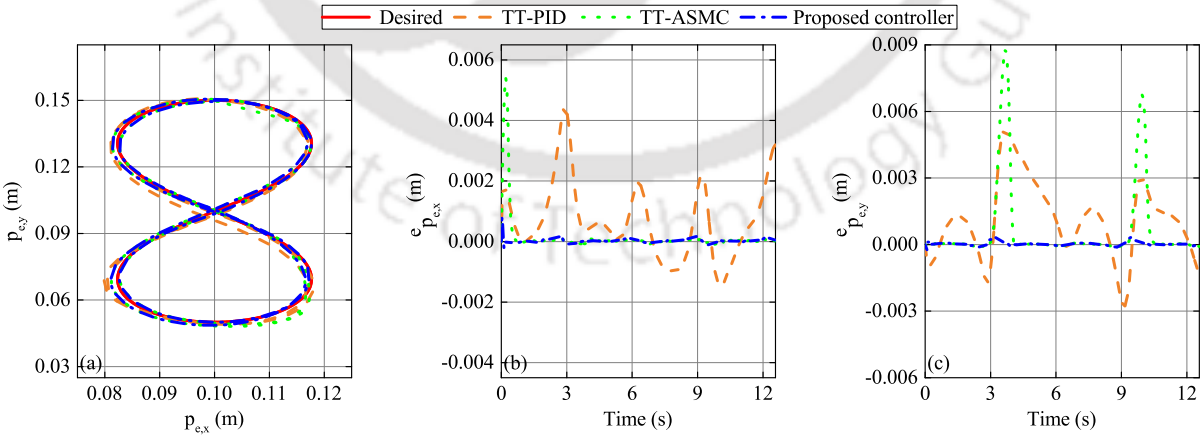

Figure 3.10: Eight shape trajectory tracking during active-assist rehabilitation with high admittance parameters for different control schemes. (a) Trajectory tracking in x-y plane. (b) Position error in X-direction. (c) Position error in Y-direction

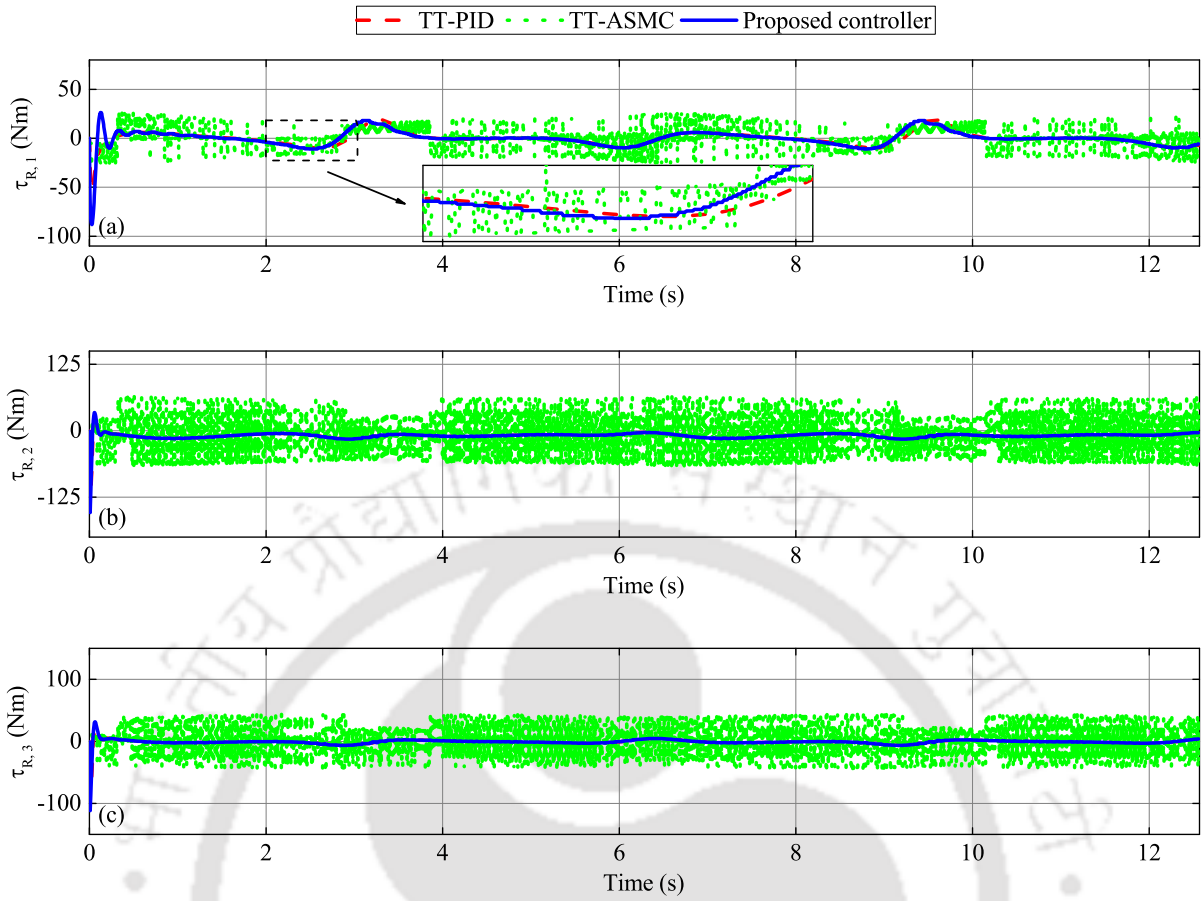

Figure 3.11: Controller inputs during active-assist rehabilitation with high admittance parameters for different control schemes at: (a) First joint. (b) Second joint. (c) Third joint

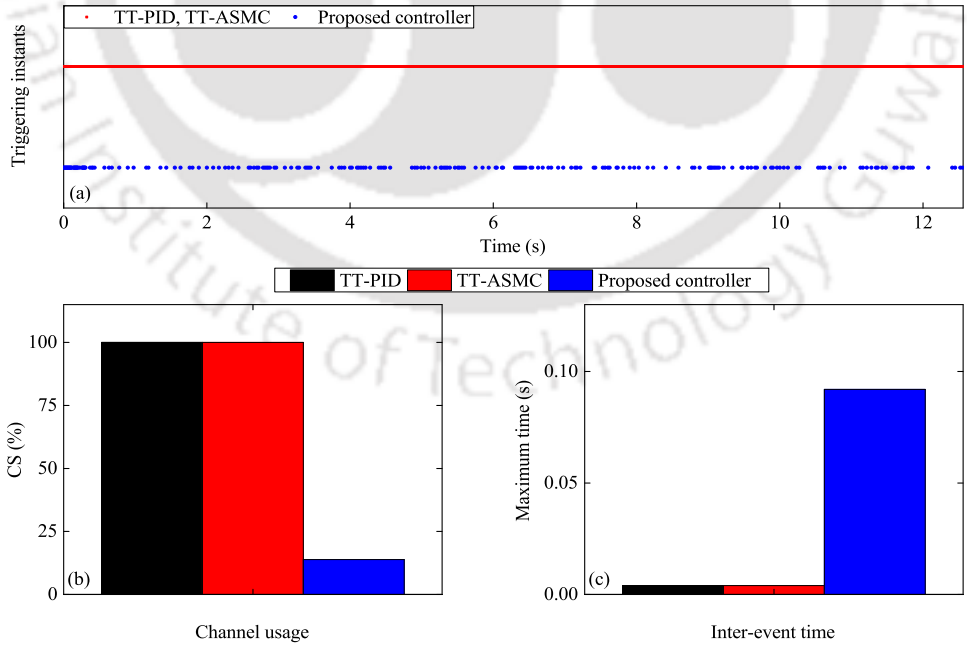

Figure 3.12: Simulation results of (a) triggering instants, (b) channel usage, and (c) inter-event time during active-assist rehabilitation with high admittance parameters for different control schemes

3.5.2 Case 2: Active-Assist Training Mode with High Admittance Parameters

As per the active-assist mode, the subject is intended to apply a certain amount of force from his\her side throughout the complete trajectory. In this work, real human-robot interactive forces are obtained from the experimental study by Wu and Chen [197] and applied as the subject's effort while tracking the eight-shape trajectory, as shown in Figure 3.4(b). These forces are a realistic presentation of the interaction between the rehabilitation robot and the upper limb of the patient. They indicate that the patient is experiencing difficulty maintaining consistent effort during the rehabilitation exercises. In this case, high admittance parameters are selected similar to the *Case 1*. At the expense of proposed control scheme, the reference $(p_{er,x}, p_{er,y})$ and actual trajectories $(p_{e,x}, p_{e,y})$ for the contrast and proposed control schemes are presented in Figure 3.9. For different control schemes, the tracking of desired trajectory in X-direction are displayed in Figures 3.9(a), 3.9(c), and 3.9(e), respectively. The respective results in Y-direction are shown in Figures 3.9(b), 3.9(d), and 3.9(f). Moreover, Figures 3.10(a), 3.10(b), and 3.10(c) demonstrates the tracking in x-y plane, tracking error in X-direction and tracking error in Y-direction, respectively. Due to the selected high admittance parameters, less compliance is permitted at the end-effector of the rehabilitation robot. Therefore, the admittance-generated reference trajectory slightly deviates from the desired trajectory in response to the interaction forces, as shown in Figure 3.10(a). On the other hand, it is evident from Figures 3.10(b), 3.10(c), and Table 3.2 that the least deviation from the reference trajectory is noted for the proposed controller (RMSE- x, y : 0.081 mm, 0.094 mm) as compared to PID (RMSE- x, y : 1.429 mm, 2.032 mm) and ASMC (RMSE- x, y : 0.704 mm, 1.957 mm). Following the RMSE values, the tracking performance of the proposed control in X-direction is increased by 94.30% and 88.43% over PID and ASMC. On the other hand, the respective improvement in Y-direction is noted as 95.37% and 95.19% during the active-assist mode. The joint actuator torques are shown in Figures 3.11(a)-(c). A negligible amount of noise can be seen in the case of the proposed controller and PID scheme over the ASMC. The triggering instants, channel usage, and related inter-event time are shown in Figures 3.12(a), 3.12(b), and 3.12(c). The number of transmissions and channel usage under the proposed controller are found to be 436 and 13.8%, respectively, as presented in Figure 3.12 (a) and Table 3.2. This resource-saving is found to be higher in the case of active-assist compared to the passive mode with sudden reflex. It can be interpreted as due to the absence of the sudden interaction forces that lead to a sudden change in the trajectory. Finally, from the above results, it can be concluded that the proposed controller allows the tracking of the desired trajectory with limited subject-robot collab-

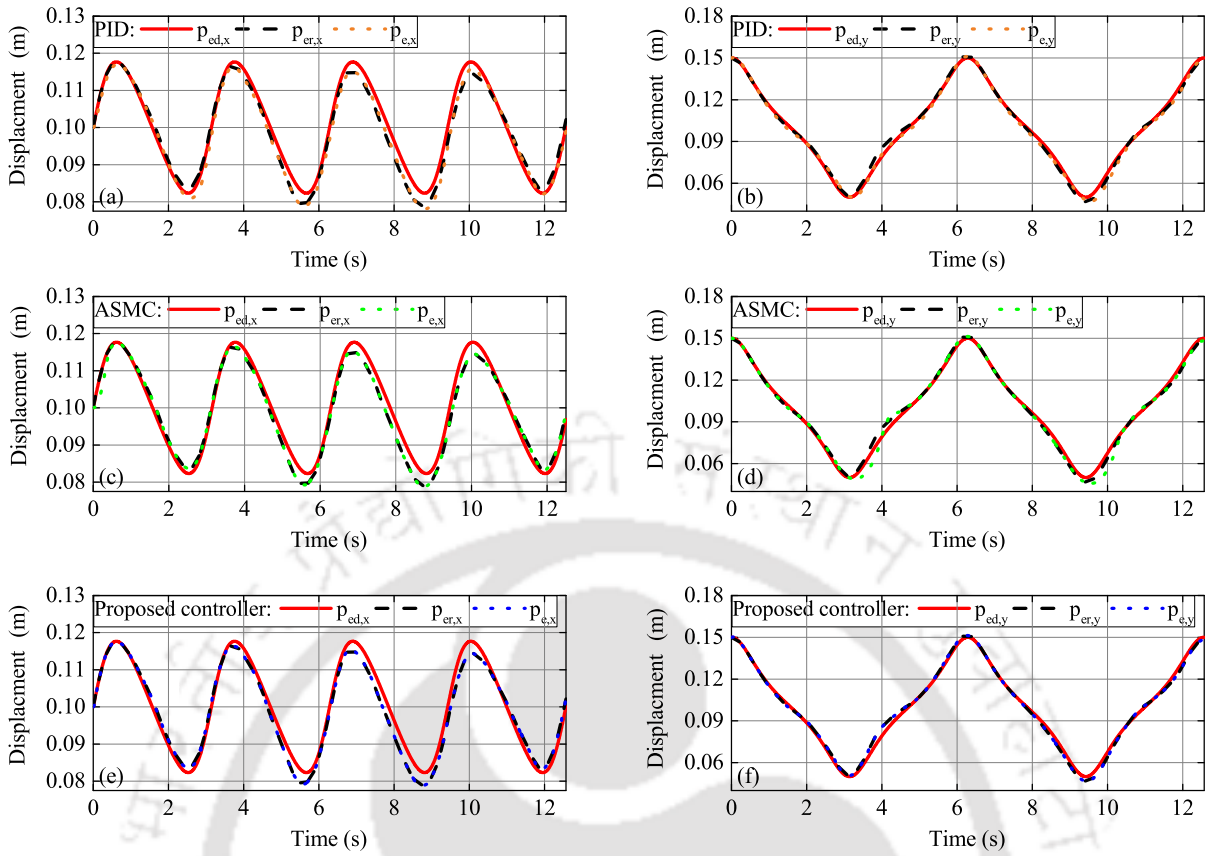

Figure 3.13: Reference and actual trajectories in X- and Y-directions during active-assist rehabilitation with low admittance parameters for different control schemes. Top: PID controller. Middle: ASMC controller. Bottom: proposed controller.

oration. This training mode is beneficial for the stroke subjects who have crossed the early stages of recovery and achieved minimal muscle strength in their limbs.

3.5.3 Case 3: Active-Assist Training Mode with Low Admittance Parameters

In this case, the low admittance parameters for the EERR are considered while performing the rehabilitation in the active-assist mode. The values for admittance parameters are selected as $M_{ad} = \text{diag}(0.1, 0.1, 0.1)$, $C_{ad} = \text{diag}(20, 20, 20)$, and $K_{ad} = \text{diag}(350, 350, 350)$. Similar to the *Case 2*, a periodic sinusoidal force is applied to mimic the continuous effort of the subject while trying to follow the eight-shape trajectory. The results of tracking the reference and actual trajectories $(p_{er,x}, p_{er,y})$ and actual trajectories $(p_{e,x}, p_{e,y})$ are given in Figure 3.13. The respective trajectory for PID, ASMC, and proposed controller in X-direction is shown in Figures 3.13(a), 3.13(c), and 3.13(e). In Y-direction, the respective trajectory for PID, ASMC, and proposed control scheme is shown in Figures

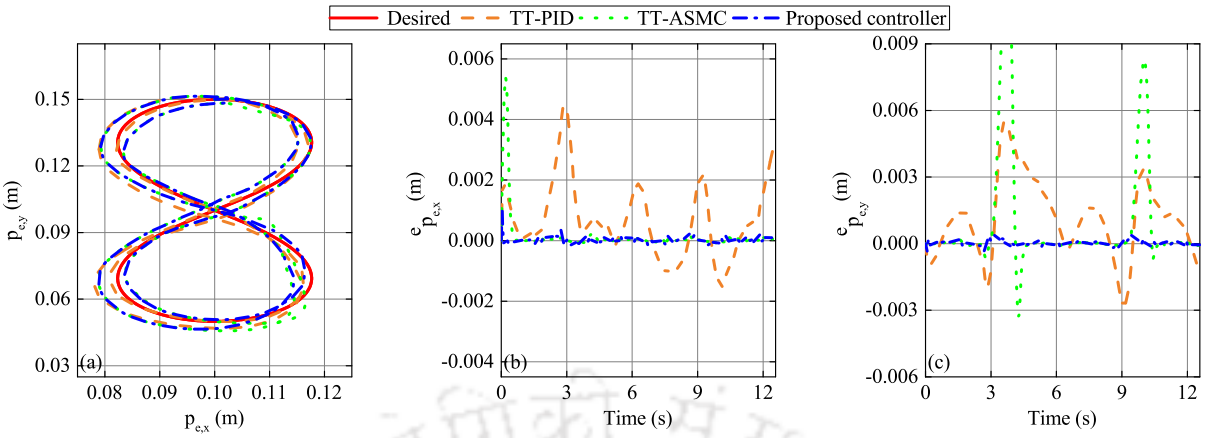

Figure 3.14: Eight shape trajectory tracking during active-assist rehabilitation with low admittance parameters for different control schemes. (a) Trajectory tracking in x-y plane. (b) Position error in X-direction. (c) Position error in Y-direction

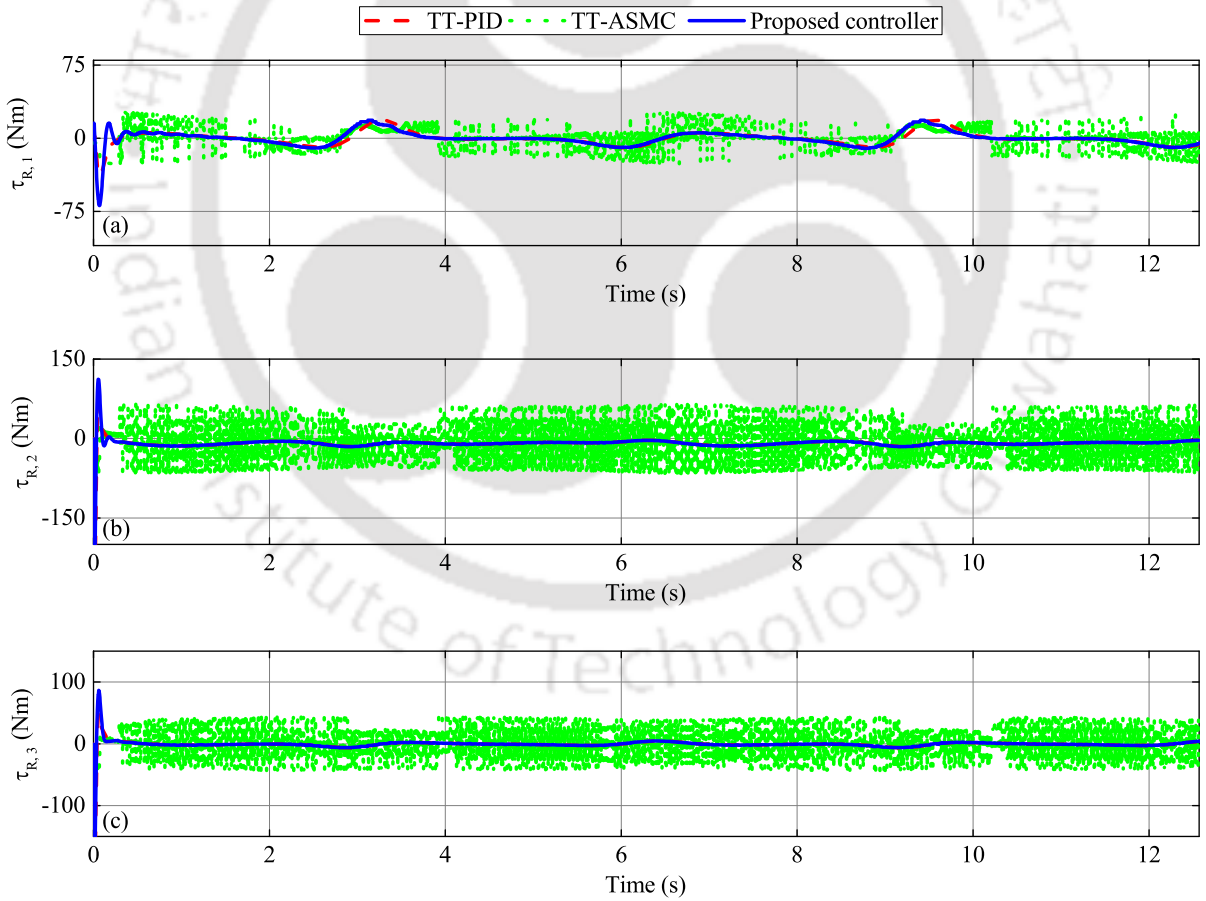

Figure 3.15: Controller inputs during active-assist rehabilitation with low admittance parameters for different control schemes at: (a) First joint. (b) Second joint. (c) Third joint

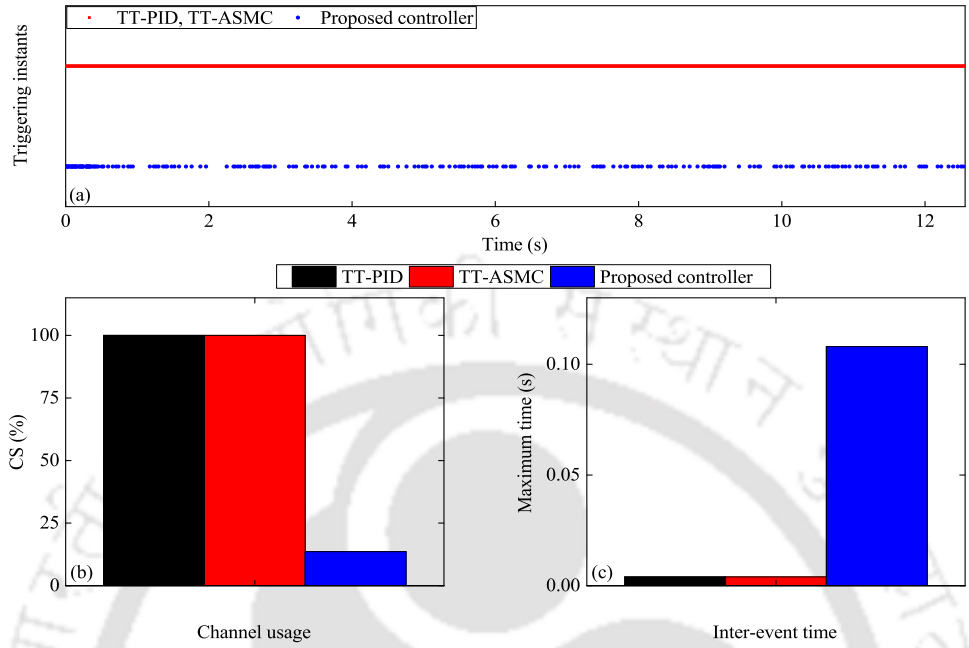

Figure 3.16: Simulation results of (a) Triggering instants, (b) channel usage, and (c) inter-event time during active-assist rehabilitation with low admittance parameters for different control schemes

Table 3.2: Comparative performance analysis of the proposed control over the contrast controllers during the active rehabilitation

Admittance conditions	Controller	Tracking error in X-direction		Tracking error in Y-direction		# Transmissions
		RMSE (mm)	PI (%)	RMSE (mm)	PI (%)	
High admittance	PID	1.429	94.30	2.032	95.37	3143
	ASMC	0.704	88.43	1.957	95.19	3143
	Proposed Controller	0.0814	-	0.094	-	436
Low admittance	PID	1.421	93.24	3.058	96.37	3143
	ASMC	0.699	86.26	2.076	94.65	3143
	Proposed Controller	0.096	-	0.111	-	427

3.13(b), 3.13(d), and 3.13(f). The trajectory tracking in the x-y plane along with the tracking errors are depicted in Figure 3.14. It is shown in Figures 3.14(a) that the selection of the low admittance parameters results in higher flexibility at the end-effector level and leads to more deviation from the desired trajectory in response to the applied patient forces. However, it is clear from Figures 3.14(b) and 3.14(c) that the proposed controller can accurately follow the generated reference trajectory with faster response and least tracking errors compared with PID and ASMC. The RMSE values for proposed control (x, y: 0.0961 mm, 0.111 mm) are still less than the RMSE of PID control (x, y: 1.421 mm, 3.058 mm) and ASMC (x, y: 0.699 mm, 2.076 mm). The performance index of the proposed controller in X-direction is 93.23% and 86.26% over PID and ASMC. On the other hand, in the Y-direction, the respective improvement in the performance is observed as 96.37% and 94.65%. The joint actuator torques for three joints of EERR are shown in Figures 3.15(a)-(c). The demonstration of triggering instants, channel usage, and inter-event time is shown in Figures 3.16(a), 3.16(b) and 3.16(c). It can be realized from Figure 3.16 and Table 3.2 that the saving in the resources and the number of triggering instants under the low admittance parameters is almost equal to the case of the high admittance parameter. It is worth-noted from the above plots and tracking results that with low admittance parameters, the proposed control scheme is the most effective one for active human participation with reasonable deviation from the reference trajectory. This complete exercise is helpful for the stroke subjects who have already attained a significant amount of recovery in their limbs and require minimal assistance from the EERR.

3.6 Summary

In this chapter, the event-triggered adaptive backstepping admittance control has been designed to follow the desired training trajectory using an end-effector type rehabilitation robot during the passive and active-assist rehabilitation exercises. Primarily, the dynamic model of an n-DOFs rehabilitation robot interacting with the upper limb of the patient has been derived based on the Euler-Lagrange principle. The adaptive backstepping approach has been employed to deal with the parametric uncertainties and achieve an acceptable tracking performance. After that, the event-triggered mechanism has been designed based on the negative semi-definiteness of the Lyapunov function to reduce the number of transmissions over the network and maintain the stability of the system. The admittance control scheme has been incorporated to realize a proper interaction between the patient and the rehabilitation robot and allow the participation of the patient in the therapeutic exercises. Finally, the effectiveness of the proposed control scheme has been

evaluated based on comparative analysis with the time-triggered PID and ASM control schemes. The proposed controller has shown a prominent tracking performance with a significant reduction in resource utilization (about 80%) over the contrast controllers.

4

Experimental Implementation of Event-Triggered Adaptive Control for Upper-Limb Robot-Assisted Passive Rehabilitation Exercises

Contents

4.1 Introduction

This chapter aims to implement the designed event-triggered adaptive backstepping position tracking controller to tackle the limited communications and hardware restriction for uncertain electrically-driven upper limb end-effector type rehabilitation robot (EERR) in a unified framework. This robot is employed to perform real-time passive rehabilitation therapy to assist the subjects in amplifying the range of motion of upper limb. At first, the dynamic model of the EERR is modified to comply with the hardware restriction of electrically-driven rehabilitation robot and admit the direct voltage commands. An adaptive backstepping tracking controller is developed to cope with the unavailability of the internal parameters of the EERR and load variations caused by different subjects while performing the upper limb passive rehabilitation training. The adaption law is derived to estimate the unknown parameters of the robot and motors online and compensate for the parametric uncertainties. To deal with the limited communication, a dynamic triggering condition is developed based on Lyapunov stability analysis. This triggering condition provides the trade-off between resource utilization and the system performance and excludes Zeno behavior. The effectiveness of the designed control scheme is investigated by comparing with the various traditional time-triggered control schemes while experimentally performing passive rehabilitation training for different healthy subjects.

The chapter is organized as follows. In Section 4.2, the hardware specification of the EERR is presented along with the dynamic modeling and problem formulation. The development of the proposed event-triggered control strategy is presented in Section 4.3. Section 4.4 elaborates on the comparative analysis of the proposed control strategy with different time-triggered control schemes. This analysis is validated through an experimental setup for different passive training scenarios. Finally, Section 4.5 highlights the summary of the study.

4.2 Framework of End-Effector Type Rehabilitation Robot (EERR)

4.2.1 Specification of EERR

The passive rehabilitation exercises for multi-joint upper extremity are performed with the 5-DOFs manipulator, Scorbot-ER 5 Plus, manufactured by Intelitek. Scorbot-ER 5 Plus, as a tabletop robot, consists of a fixed base and five revolute joints. The first three degrees of freedom are utilized to provide the Cartesian position of the end-effector, while the rest two degrees of freedom are responsible for orienting the end-effector of

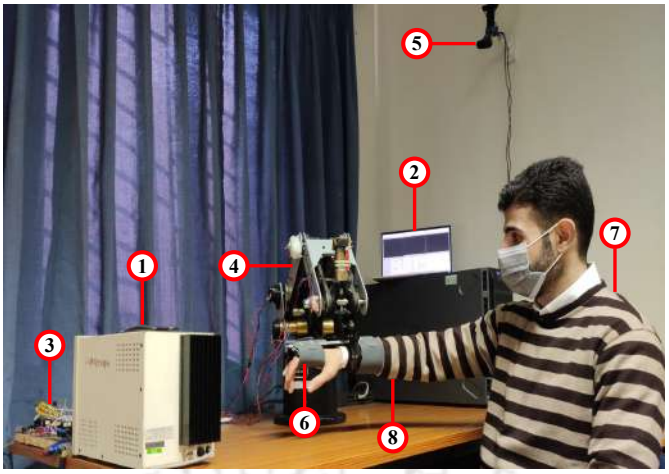

Figure 4.1: End-effector type rehabilitation robot with a healthy subject (1-Power supply; 2-Host computer; 3-Motor drivers; 4-Robotic system; 5-Camera; 6-Tynor splint; 7-Subject; 8-Subject forearm)

the robot. Moreover, the ranges of the robot joints can cover the range of human arm movements in daily life applications. During the training session, the subject has to sit on a chair in front of the rehabilitation robot. The forearm of the subject is appended to the customized robot's end-effector via three Tynor splints, as shown in Figure 4.1. These splints are used to ensure a proper connection between the robot and the subject's arm. The left and right arm of the subjects can be used as dominant throughout the passive rehabilitation exercises by changing the arm appended to the forearm support. Therefore, the impaired limb can execute the desired training exercises with the assistance of the robotic end-effector. The dynamic parameters and the range of workspace of the Scorbot-ER 5 Plus rehabilitation robot are presented in Appendix A.1.

On the other hand, the real-time control system is built-in Matlab/Simulink (2019b) with the Arduino Hardware Support Package. The host computer, ASUS VivoBook, is utilized to transform the Simulink model into executable C-type codes and calculate the control inputs. These control inputs are transferred to the arduino board via a wireless network established by an ESP13 WiFi shield. The Arduino Mega 2560 with ATmega2560 microcontroller and 16 MHz crystal oscillator is used in the control system. This board has 16 analog inputs and 54 digital input/output pins, 14 of which can be configured as pulse width modulation (PWM) outputs. The operational voltage of the pins is 5 V, with an external voltage supply range of 6 V-20 V. The Cartesian position of the robot end-effector is obtained using a wired vision system (camera) connected to the host computer. Therefore, there is no network constraints in the robot-to-controller communication channel. The Cartesian position is mapped into the joint space using the inverse kinematic equations. As a safety measure, an emergency shutdown button is

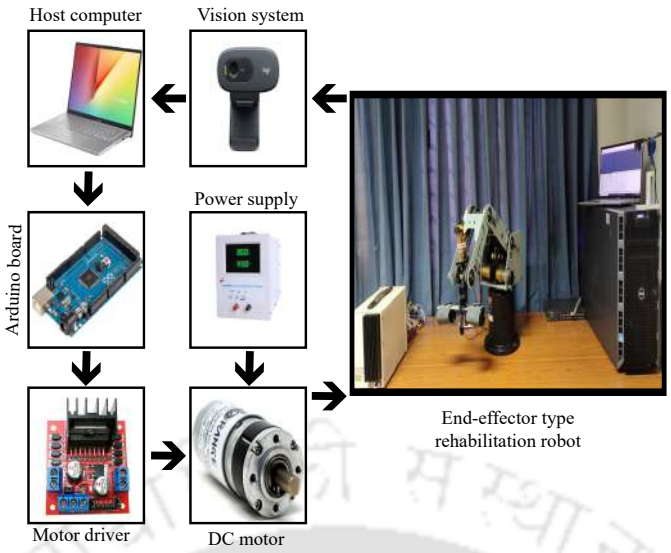

Figure 4.2: Components of the real-time control system driven by MATLAB/Simulink

provided on the training table to stop any unwanted movement of the robot. The joints of the robot are actuated using 12 V DC motors driven by L298 motor drivers. The L298 motor driver is a dual full-bridge driver that can control the direction and the speed of two DC motors simultaneously. This module supports a DC motor with 5 V to 35 V and a peak current of 2 A. Each motor can be driven in clockwise and anti-clockwise directions by enabling and disabling the corresponding (IN) pins. Moreover, the speed of motors is controlled by connecting the (ENA) and (ENB) pins to the PWM output of the Arduino board. The block diagram of the hardware components, constructing the control system with the experimental setup, is illustrated in Figure 4.2.

4.2.2 Dynamic Analysis of EERR

The motors of the end-effector type rehabilitation robot are driven by voltage signals as described in Subsection 4.2.1. However, the derived dynamic model of the manipulator in Section 2.3 of Chapter 2 admit torque commands only. Therefore, it cannot be utilized directly to devise the control scheme and guide the motors of the rehabilitation robot. To overcome this challenge, it is required to modify the dynamical model of the manipulator presented in equation (2.2) to consider both the mechanical and electrical parts of motor dynamics, allowing the voltage of the motor as an input signal.

The dynamic models of the end-effector type rehabilitation robot and the permanent magnet DC motor can be described similar to equations (2.2) and (2.3) after replacing

the joint position q by the joint angle θ since the joints of EERR are revolute-type ($q = \theta$):

$$M(\theta)\ddot{\theta} + C(\theta, \dot{\theta})\dot{\theta} + G(\theta) = \tau_R \tag{4.1}$$

$$J_m\ddot{\theta}_m + B_m\dot{\theta}_m + r^{-1}\tau_R = \tau_m \tag{4.2}$$

where $\theta, \dot{\theta}, \ddot{\theta} \in \mathbb{R}^5$ denote the vector of joint angles, angular velocity and angular acceleration, respectively. $\ddot{\theta}_m$ and $\dot{\theta}_m$ are the angular acceleration and velocity of the motor shaft, respectively. The angular position of the motor shaft θ_m is related to the joint angle θ as defined below.

$$\theta_m = r\theta \tag{4.3}$$

From a practical point of view, it is more convenient to consider the electrical parts of motor dynamics and utilize the voltage of the motor as an input signal. The electric circuit of the DC motor is represented by the following equation.

$$V_a = L_a\dot{I}_a + R_aI_a + K_b\dot{\theta}_m \tag{4.4}$$

where $V_a \in \mathbb{R}^5$ is the input voltage signal, L_a and $R_a \in \mathbb{R}^{5\times5}$ are the armature inductance and resistance matrices, respectively, and $K_b \in \mathbb{R}^{5\times5}$ is the back-emf constant. The relation between the motor torque τ_m and the armature current I_a can be described as.

$$\tau_m = K_aI_a \tag{4.5}$$

where $K_a \in \mathbb{R}^{5\times5}$ is the motor torque constant matrix.

By using the equations (4.1)-(4.5) and neglecting the inductance L_a due to its tiny value, the DC motor dynamic equation (4.2) can be rewritten as follows.

$$J_mr\ddot{\theta} + B_mr\dot{\theta} + r^{-1}\big(M(\theta)\ddot{\theta} + C(\theta, \dot{\theta})\dot{\theta} + G(\theta)\big) = K_aR_a^{-1}V_a - K_aR_a^{-1}K_br\dot{\theta} \tag{4.6}$$

By introducing the state vector $X = (x_1, x_2)^T = (\theta, \dot{\theta})^T$, the dynamic model of the end-effector type rehabilitation robot with the incorporation of motor dynamic can be written in the state space as follows.

$$\begin{aligned}
\dot{x}_1 &= x_2 \\
\dot{x}_2 &= \ddot{\theta} = -J_m^{-1}B_m\dot{\theta} - (r^{-1})^2J_m^{-1}\big(M_R(\theta)\ddot{\theta} + C_R(\theta, \dot{\theta})\dot{\theta} + G_R(\theta)\big) \\
&\quad + r^{-1}J_m^{-1}K_aR_a^{-1}V_a - J_a^{-1}K_aR_a^{-1}K_b\dot{\theta}
\end{aligned} \tag{4.7}$$

The above equation can be further rearranged as follows.

$$\begin{aligned}\dot{x}_1 &= x_2 \\ \dot{x}_2 &= \ddot{\theta} = b\big(M_R(\theta)\ddot{\theta} + C_R(\theta,\dot{\theta})\dot{\theta} + b^{-1}a\ \dot{\theta} + G_R(\theta)\big) + cV_a \\ &= \Pi(\theta,\dot{\theta},\ddot{\theta})\varphi + cV_a\end{aligned} \tag{4.8}$$

where $a = -J_m^{-1}B_m - J_m^{-1}K_aR_a^{-1}K_b$, $b = -(r^{-1})^2J_m^{-1}$, $c = r^{-1}J_m^{-1}K_aR_a^{-1}$, $\Pi(\theta,\dot{\theta},\ddot{\theta})$ is a known function of angular position, velocity, and acceleration, and φ is the vector of the unknown dynamic parameters.

4.2.3 Problem Formulation

In this chapter, an uncertain end-effector type rehabilitation robot is considered to perform the real-time passive training tasks. This rehabilitation robot is controlled via a limited bandwidth wireless network channel. The dynamic model of the rehabilitation robot presented in equation (4.8) can be rewritten as follows.

$$\begin{aligned}\dot{x}_1 &= x_2 \\ \dot{x}_2 &= \Pi(\theta,\dot{\theta},\ddot{\theta})\varphi + c\bar{V}_a\end{aligned} \tag{4.9}$$

where $\bar{V}_a$ is the event-triggered control input.

The inaccuracies of the system parameters due to the modeling errors and inaccessibility of the motor parameters in addition to the payload variation during rehabilitation exercises result in structured uncertainties. As such, it is difficult to obtain the exact values of the dynamic parameters φ and c in equation (4.9). Therefore, two adaptation laws are designed along with the backstepping control scheme to estimate the unknown dynamical parameters of the rehabilitation robot and maintain the stability of the system during the passive rehabilitation exercises.

To overcome the limited bandwidth restrictions, an event-triggered (ET) mechanism is placed at the controller-to-robot channel. As a result, the rehabilitation robot is not further driven by the actual control input V_a. Instead, it is actuated by the event-triggered control input $\bar{V}_a$. The triggering instants are defined as follows.

$$\begin{aligned}\bar{V}_a(t) &= V_a(t_j), \forall\ t \in [t_j, t_{j+1}) \\ t_{j+1} &= \inf\{t | t > t_j,\ T_{con}(e_m, z_1, z_2) > 0\}\end{aligned} \tag{4.10}$$

Here, $T_{con}(e_m, z_1, z_2)$ denotes the triggering condition to be designed in the subsequent section and e_m is the measurement error where $e_m = V_a - \bar{V}_a$.

The proposition of this chapter is to design an event-triggered adaptive tracking control

law based on the backstepping approach for the uncertain electrically-driven end-effector type rehabilitation robot. This controller is devoted to ensure the boundedness of the closed-loop signals and achieve acceptable passive training with minimum transmission over the network in the presence of parametric uncertainties and limited bandwidth.

4.3 Event-Triggered Adaptive Controller Design

In this section, an adaptive tracking position control scheme is developed based on the backstepping approach to control the upper-limb rehabilitation robot. This scheme is employed to achieve adequate passive rehabilitation training in the presence of uncertainties. Moreover, an event-triggered mechanism is designed to reduce the communication burden, maintain desired tracking performance, and preserve the stability of the system. To realize the control objectives, the error variables z_1 and z_2 are defined as follows.

$$z_1 = \theta - \theta_d = x_1 - \theta_d \tag{4.11}$$

$$z_2 = \dot{\theta} - \alpha = x_2 - \alpha \tag{4.12}$$

where θ_d is the vector of desired joint positions and α is the virtual controller to be designed during the subsequent steps. The adaptive backstepping control law is developed in the following steps to ensure that the vector of actual joint positions θ follows the desired trajectories θ_d in the presence of uncertainties and network restrictions.

Step 1: The time derivative of the first error variable is given as.

$$\begin{aligned} \dot{z}_1 &= \dot{x}_1 - \dot{\theta}_d \\ &= x_2 - \dot{\theta}_d = z_2 + \alpha - \dot{\theta}_d \end{aligned} \tag{4.13}$$

An appropriate choice of α leads to the stabilization of the previous error subsystem. One can define the Lyapunov function candidate for the first error subsystem as $V_1 = \frac{1}{2} z_1^T z_1$. Therefore, the derivative of the Lyapunov function is given as.

$$\dot{V}_1 = z_1^T \dot{z}_1 = z_1^T (z_2 + \alpha - \dot{\theta}_d) \tag{4.14}$$

One can select the virtual control law as

$$\alpha = -k_1 z_1 + \dot{\theta}_d \tag{4.15}$$

where k_1 is a positive gain matrix, then the derivative of the Lyapunov function can be written as.

$$\dot{V}_1 = -z_1^T k_1 z_1 + z_1^T z_2 \tag{4.16}$$

The first term on the right-side of equation (4.16) is stabilized, and the second term will be addressed in the following step.

Step 2: The derivative of the second error variable z_2 is described as.

$$\begin{aligned}\dot{z}_2 &= \dot{x}_2 - \dot{\alpha} \\ &= \Pi\varphi + c\bar{V}_a - \dot{\alpha}\end{aligned} \tag{4.17}$$

The second Lyapunov function candidate can be chosen as.

$$V_2 = V_1 + \frac{1}{2}z_2^T z_2 + \frac{1}{2}\tilde{\varphi}^T\Gamma_1^{-1}\tilde{\varphi} + \text{trace}(\frac{1}{2}\tilde{c}^T\Gamma_2^{-1}\tilde{c}) \tag{4.18}$$

where $\tilde{\varphi}, \tilde{c}$ are the estimation errors of the uncertainties and defined as $\tilde{\varphi} = \varphi - \hat{\varphi}$ and $\tilde{c} = c - \hat{c}$. $\hat{\varphi}$ denotes the estimation of unknown parameters φ, and Γ_1, Γ_2 are arbitrary positive constants. The derivative of the second Lyapunov candidate is obtained as.

$$\dot{V}_2 = \dot{V}_1 + z_2^T\dot{z}_2 - \tilde{\varphi}^T\Gamma_1^{-1}\dot{\hat{\varphi}} + \text{trace}(-\tilde{c}^T\Gamma_2^{-1}\dot{\hat{c}}) \tag{4.19}$$

By substituting (4.16) and (4.17) in the above equation, one can find the following description.

$$\dot{V}_2 = -z_1^T k_1 z_1 + z_1^T z_2 + z_2^T(\Pi\varphi + c\bar{V}_a - \dot{\alpha}) - \tilde{\varphi}^T\Gamma_1^{-1}\dot{\hat{\varphi}} - \text{trace}(\tilde{c}^T\Gamma_2^{-1}\dot{\hat{c}}) \tag{4.20}$$

The following equation is obtained by adding and subtracting the terms $z_2^T\Pi\hat{\varphi}$ and $z_2^T\hat{c}\bar{V}_a$ to the right-hand side of the equation (4.20)

$$\begin{aligned}\dot{V}_2 = &-z_1^T k_1 z_1 + z_1^T z_2 + z_2^T(\Pi\hat{\varphi} + \hat{c}V_a - \hat{c}e_m - \dot{\alpha}) \\ &+ z_2^T\Pi\tilde{\varphi} + z_2^T\tilde{c}\bar{V}_a - \tilde{\varphi}^T\Gamma_1^{-1}\dot{\hat{\varphi}} + \text{trace}(-\tilde{c}^T\Gamma_2^{-1}\dot{\hat{c}})\end{aligned} \tag{4.21}$$

By utilizing the trace properties and taking the transpose of $z_2^T\Pi\tilde{\varphi}$ and $z_2^T\tilde{c}\bar{V}_a$, the above equation can be written as.

$$\begin{aligned}\dot{V}_2 = &-z_1^T k_1 z_1 + z_1^T z_2 + z_2^T(\Pi\hat{\varphi} + \hat{c}V_a - \hat{c}e_m - \dot{\alpha}) \\ &+ \tilde{\varphi}^T(\Pi^T z_2 - \Gamma_1^{-1}\dot{\hat{\varphi}}) + \text{trace}\big(\tilde{c}^T(z_2\bar{V}_a^T - \Gamma_2^{-1}\dot{\hat{c}})\big)\end{aligned} \tag{4.22}$$

The adaptive laws can be chosen as.

$$\dot{\hat{\varphi}} = \Gamma_1\Pi^T z_2 \text{ and } \dot{\hat{c}} = \Gamma_2 z_2\bar{V}_a^T \tag{4.23}$$

Therefore, the derivative of the Lyapunov function becomes.

$$\dot{V}_2 = -z_1^T k_1 z_1 + z_1^T z_2 + z_2^T(\Pi\hat{\varphi} + \hat{c}V_a - \hat{c}e_m - \dot{\alpha}) \tag{4.24}$$

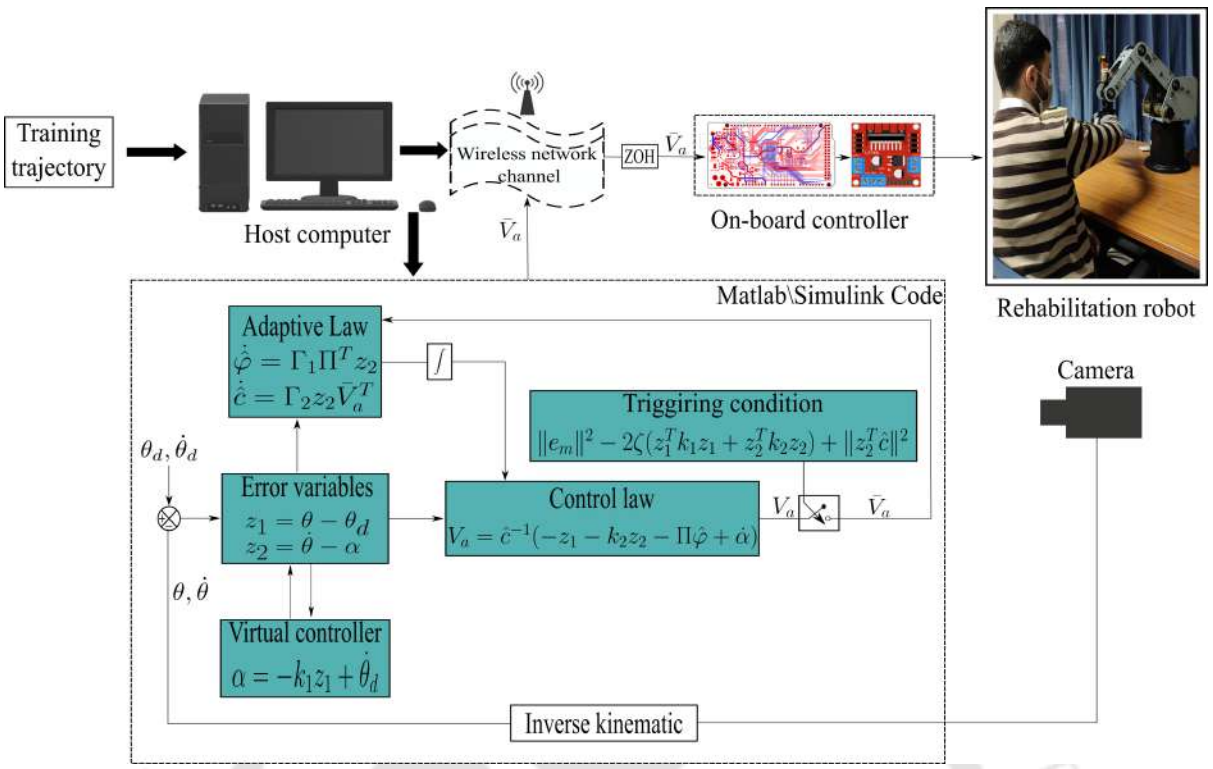

Figure 4.3: Block diagram of the proposed event-triggered control strategy

The control law can be designed as follows

$$V_a = \hat{c}^{-1}(-z_1 - k_2 z_2 - \Pi\hat{\varphi} + \dot{\alpha}) \tag{4.25}$$

where k_2 is a positive gain matrix. By substituting the designed control law in equation (4.24), one can get the following formula.

$$\dot{V}_2 = -z_1^T k_1 z_1 - z_2^T k_2 z_2 - z_2^T \hat{c} e_m \tag{4.26}$$

It can be observed from equation (4.26) that the last term includes the measurement error e_m. This error is devoted in the following stage to obtain the triggering condition. This triggering condition determines the updating\transmitting time of the new control signal over the network and ensures the negative semi-definiteness of the derivative of the Lyapunov function. Hence, the convergence of z_2 to the origin and the stability of the system can be maintained. By utilizing Young's inequality in the equation (4.26), one obtains the following:

$$\begin{aligned} \dot{V}_2 &\leq -z_1^T k_1 z_1 - z_2^T k_2 z_2 + \|z_2^T \hat{c}\| \|e_m\| \\ &\leq -(1-\zeta)(z_1^T k_1 z_1 + z_2^T k_2 z_2) - \zeta(z_1^T k_1 z_1 + z_2^T k_2 z_2) + \frac{\|z_2^T \hat{c}\|^2}{2} + \frac{\|e_m\|^2}{2} \end{aligned} \tag{4.27}$$

The negative semi-definiteness of the Lyapunov function derivative can be ensured if $0 < \zeta < 1$ and the following condition holds true.

$$\frac{\|z_2^T \hat{c}\|^2}{2} + \frac{\|e_m\|^2}{2} \leq \zeta(z_1^T k_1 z_1 + z_2^T k_2 z_2) \tag{4.28}$$

Therefore, the triggering function defined in equation (4.10) can be formulated as follows.

$$T_{con}(e_m, z_1, z_2) = \|e_m\|^2 - 2\zeta(z_1^T k_1 z_1 + z_2^T k_2 z_2) + \|z_2^T \hat{c}\|^2 \tag{4.29}$$

The transmission of new control input over the network channel occurs only if the triggering condition $T_{con}(e_m, z_1, z_2)$ is greater than zero. Otherwise, the rehabilitation robot is actuated by the last transmitted control signal. This mechanism leads to a significant reduction in the number of transmissions over the network. Furthermore, the proposed triggering condition presented in equation (4.29) guarantees the negative semi-definiteness of the derivative of the Lyapunov function. Therefore, by invoking the same analysis presented in Proposition 1, it can be concluded that the end-effector type rehabilitation robot actuated by the designed controller (4.25) and the adaptive law (4.23) with the implementation of triggering condition (4.29) is stable in the sense of Lyapunov analysis, and all the closed-loop signals are globally bounded. Moreover, the proof of the avoidance of Zeno behavior presented by the equations (2.49-2.52) is still valid and can be directly applied here to complete the proof.

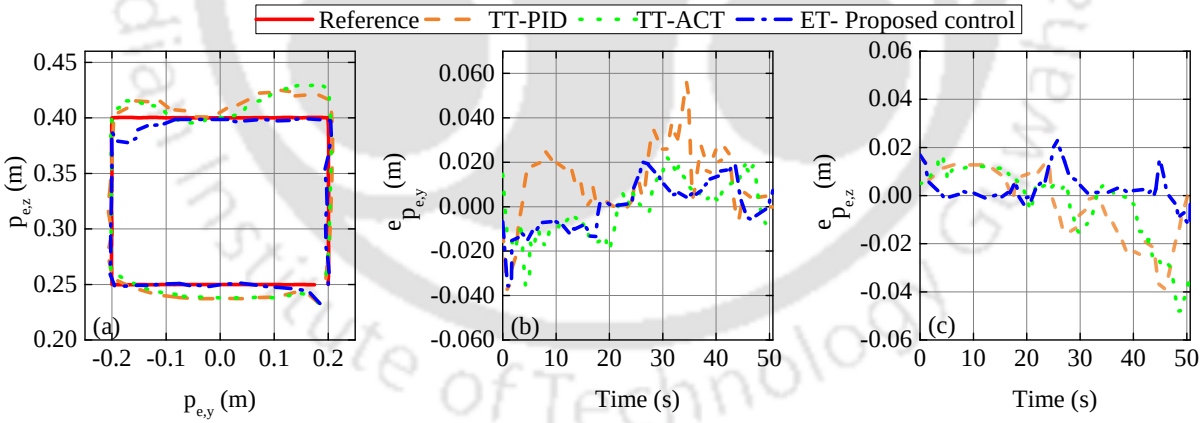

Figure 4.4: Experimental results of rectangular trajectory tracking for first subject S-1 using TT-PID, TT-ACT, and proposed ET control strategies. (a) Desired and actual trajectories on the y-z plane. Tracking errors in (b) Y-direction and (c) Z-direction

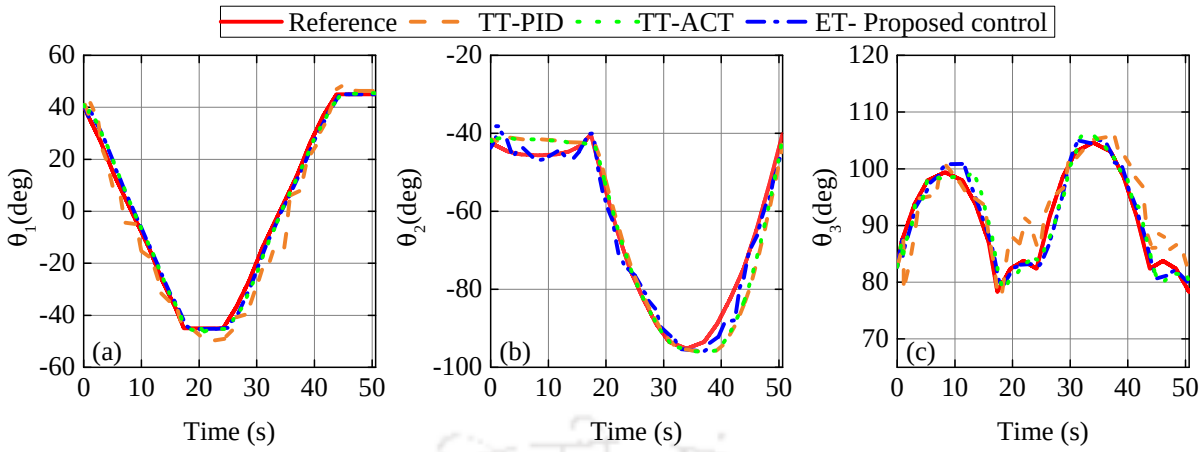

Figure 4.5: Experimental results of joint variables for first subject S-1 using TT-PID, TT-ACT, and proposed ET control strategies. Desired and actual joint trajectories for (a) first joint, (b) second joint, and (c) third joint

4.4 Experimental and Comparative Study

To validate the effectiveness of the proposed control strategy, three different scenarios of passive rehabilitation exercises are conducted in real-time by two healthy subjects (subject S1: female, age/29 years, height/1.67 m, weight/57 kg; subject S2: male, age/34 years, height/1.8 m, weight/64 kg). In the first scenario, the exercise is made to follow a rectangular trajectory. The shoulder flexion/extension, shoulder internal/external rotation, and elbow flexion/extension movements of the first healthy subject-S1 are achieved using the proposed control strategy. In the second scenario, two different time-triggered control strategies, i.e., adaptive computed torque [198] (TT-ACT) and proportional-integral-derivative [97] (TT-PID) control schemes, are devoted to repeat the same exercise for the first subject-S1. In the last scenario, the previous experimental session is carried out by the second healthy subject-S2 to investigate the performance of the proposed event-triggered control scheme with different physiological characteristics of the subjects and variable upper extremity masses. Moreover, the effect of the adjustable parameter ζ, presented in the designed triggering condition of equation (4.29), on the tracking accuracy and the number of transmissions over the network is evaluated. The desired rectangular trajectory for the rehabilitation training is generated in the y-z plane. This trajectory starts at the 0.2 m, 0.175 m, and 0.25 m in X-, Y-, and Z-direction, respectively. The duration of each experimental session is set to 50.6 s with 0.01 s as a sampling time for the real-time control system. The initial position of the rehabilitation robot is chosen as $(p_{e,x}(0) = 0.2 \text{ m}, p_{e,y}(0) = 0.185 \text{ m}, p_{e,z}(0) = 0.232 \text{ m})$. The initial values of the estimated parameters are chosen to be zero $\hat{\varphi}(0) = 0$ and $\hat{c}(0) = 0$. The detailed description of the matrix Π and the vector of dynamic parameters φ utilized during the

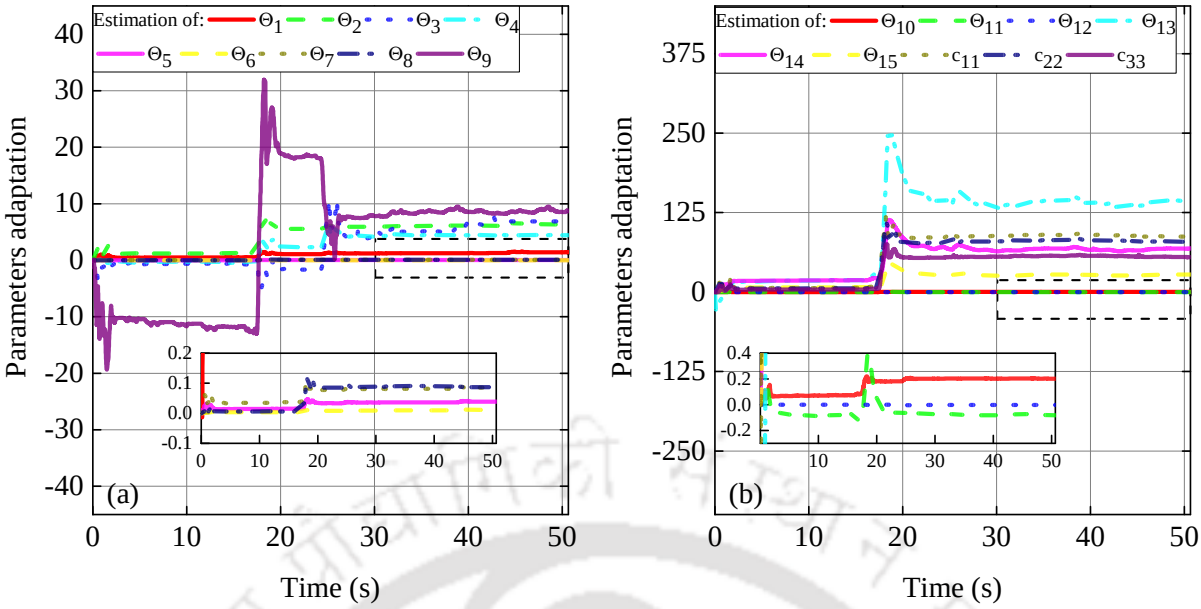

Figure 4.6: Parameters adaptation of φ and c for the rehabilitation robot with first subject-S1

different experiments are given in Appendix A.3. It has been observed that there is no requirement to activate the total joints of the robot. Therefore, the first three joints of the rehabilitation robot are devoted to carry out the passive rehabilitation training. The block diagram of the proposed scheme is presented in Figure 4.3. The ethical approval of the proposed experimental training sessions is obtained from Institute Human Ethics Committee of Indian Institute of Technology Guwahati, India.

4.4.1 Experimental Results

Scenario 1: The designed event-triggered adaptive controller given in equation (4.25) is implemented in real-time with the consideration of limited communications. The rehabilitation robot is devoted to perform the passive training process for the first subject through a rectangular trajectory. The parameters of the controller are chosen as follows: k_1 =diag(0.1, 6.5, 6.5), k_2 =diag(0.1, 0.5, 0.4), $\Gamma_1 = 0.01$, $\Gamma_2 = 0.1$, and $\zeta = 0.9$.

Discussion 1: The experimental results of the proposed control scheme during the rectangular trajectory tracking for the first subject are presented in Figures (4.4, 4.5). It can be observed that the desired trajectory is precisely tracked using the proposed controller with small tracking errors, as depicted in Figure 4.4 (b,c). The estimation of the parameters for the rehabilitation robot using the adaptation laws in equation (4.23) are shown in Figure 4.6. It can be noticed that the estimated parameters are bounded and converged to maintain the stability of the closed-loop system with acceptable tracking performance. However, the convergence of these parameters to their exact values is not

necessary. Due to the implementation of the proposed event-triggered mechanism, the control signals are updated after a time gap, as illustrated in Figure 4.7. This aperiodic update leads to a significant reduction in the number of transmitted signals over the network. The deviation at the corner point of the rectangle is higher than the other points of the trajectory. This deviation is due to the sudden change in the coordinates.

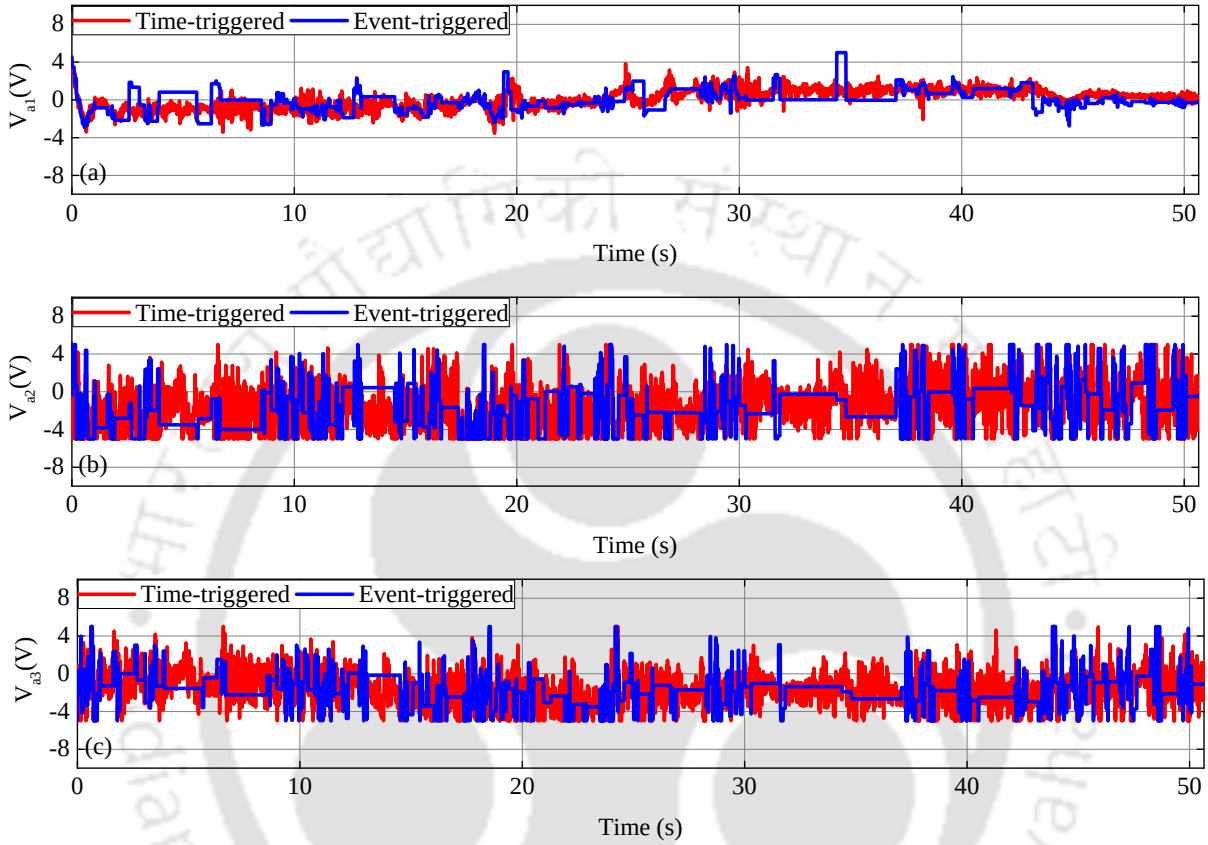

Figure 4.7: Event-triggered and time-triggered control inputs for first subject-S1 at (a) first joint, (b) second joint, and (c) third joint

Scenario 2: A comparison with two different traditional time-triggered control schemes, i.e., adaptive computed torque [198] (TT-ACT) and TT-PID [97], is conducted further to prove the effectiveness of the proposed event-triggered control strategy. These time-triggered approaches are dedicated to carry out the same training exercise presented in scenario 1 for the first subject (S1: female, age/29 years, height/1.67 m, weight/57 kg). The controllers' gains are selected after several experimental iteration to maintain accurate tracking performance during the training exercise as follows (For PID: $k_{pq} = \text{diag}(0.01, 0.01, 0.05)$,$k_{Iq} = \text{diag}(0.15,\ 0.09,\ 0.4)$, $k_{dq} = \text{diag}(1, 2, 0.8)$ and for ACT: $K_p = \text{diag}(1, 1, 1)$, $K_v = \text{diag}(5, 5, 5)$).

Discussion 2: Figures 4.4 and 4.5 (dotted and dashed lines) show the performance of the rehabilitation robot using the ACT and PID control strategies, respectively. It is noted

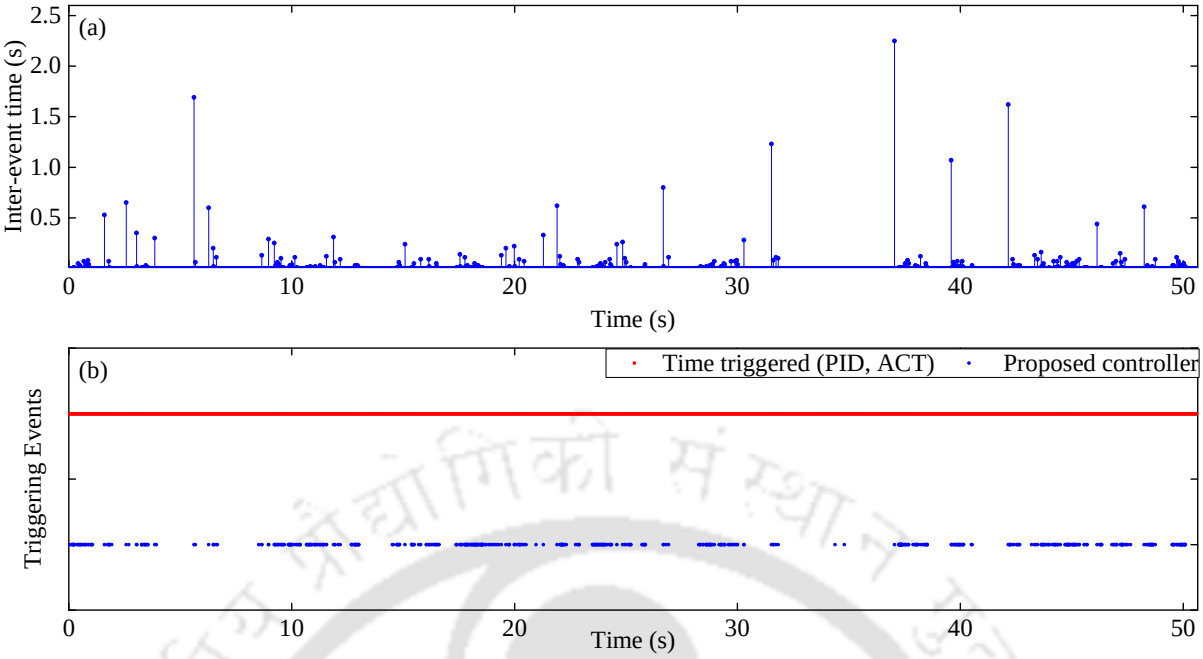

Figure 4.8: Inter-events time and triggering events for first subject-S1 and $\zeta = 0.9$

that the TT-ACT scheme seems to perform better than the TT-PID controller and achieve smaller tracking errors, as presented in Figure 4.4 (b,c). However, it is evident from the same figure that the proposed controller provides more sustainable tracking accuracy compared with TT-ACT and TT-PID. Moreover, this acceptable tracking accuracy is accompanied with a significant reduction in the number of transmissions over the network and long inter-event time (maximum: 2.5 s) compared to the periodically triggered ACT and PID controllers, as depicted in Figure 4.8.

Scenario 3: The passive training session is further conducted, for the second subject (S2: male, age/34 years, height/1.8 m, weight/64 kg), to examine the designed controller under different masses of the upper extremity. Moreover, the adjustable parameter ζ in (4.29) is altered during the training exercise. This change in the parameter ζ is incorporated to illustrate the effect of this parameter on the tracking performance and resource utilization. The controller parameters are the same as those adopted in the first scenario, and ζ takes the values (0.5, 0.7, 0.9).

Discussion 3: The results of the passive training exercise for the second subject-S2 are presented in Figure 4.9. The desired rectangular trajectory is followed by the second subject using the proposed ET control scheme, as shown in Figure 4.9 (a). Moreover, the proposed control scheme can preserve the stability of the system and maintain small tracking errors, as presented in Figure 4.9 (b,c). The estimation of the parameters are given in Figure 4.10. The triggering time instant, at which the control signals are updated

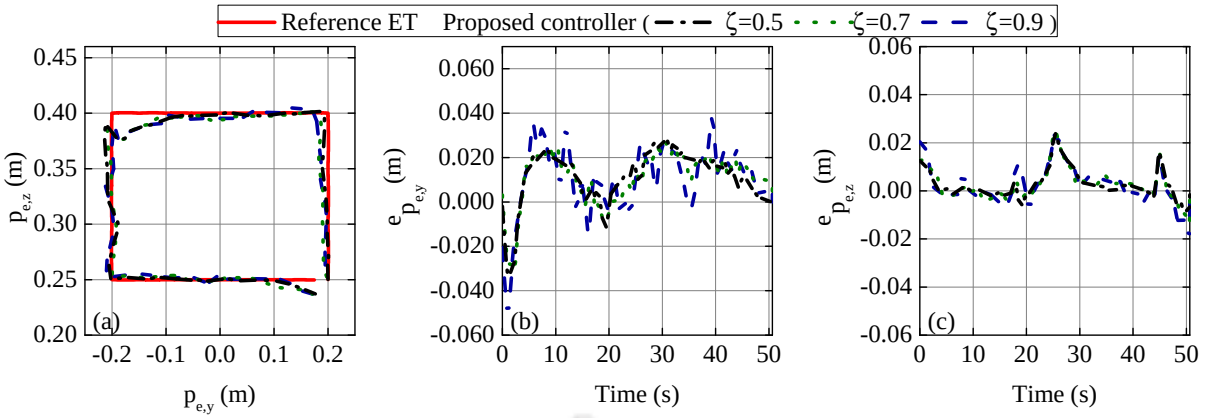

Figure 4.9: Experimental results of rectangular trajectory tracking for second subject S2 and several ζ values. (a) Desired and actual trajectories on the y-z plane. Tracking errors in (b) Y-direction and (c) Z-direction

Table 4.1: Performance analysis of passive training exercise with different control schemes ($\zeta = 0.9$).

Subject	Controller	Tracking Errors (mm)				Control performance (V)			Number of transmissions	Bandwidth usage
		Y-direction		Z-direction		V_{a1}	V_{a2}	V_{a3}		
		RMSE	IAE	RMSE	IAE		RMS_{input}			
S1	TT-PID	19.6	0.77	15.3	0.65	1.56	2.71	2.56	5065	100%
	TT-ACT	12.05	0.5	16.48	0.62	1.53	2.68	2.23	5065	100%
	Proposed control	11.4	0.47	6.61	0.21	1.15	2.5	2.4	553	11%
S2	TT-PID	17.4	0.73	15.9	0.65	1.6	3.15	3.13	5065	100%
	TT-ACT	7.5	0.28	18.2	0.68	1.9	3.1	2.48	5065	100%
	Proposed control	5	0.2	7.54	0.27	1.1	3.03	3.12	553	11%

and transmitted over the network, for different values of ζ are shown in Figure 4.11. It can be observed that the increase in ζ values leads to a reduction in the number of transmissions over the network. However, this transmissions reduction is at the expense of the tracking accuracy as shown in Figure 4.9.

4.4.2 Comparison Study

To further quantitatively analyze the tracking performance of the different control schemes, the integral absolute error (IAE) and root-mean-square error (RMSE) are calculated for two subjects with different physiological properties and changed arm weight and summarized in Table 4.1. It is evident from Table 4.1 that the proposed ET control scheme provides a superior tracking performance as compared with TT-ACT and TT-PID strategies for the two healthy subjects with different arm weights. Moreover, the control input effort of the proposed control scheme is relatively smaller than the results of PID and

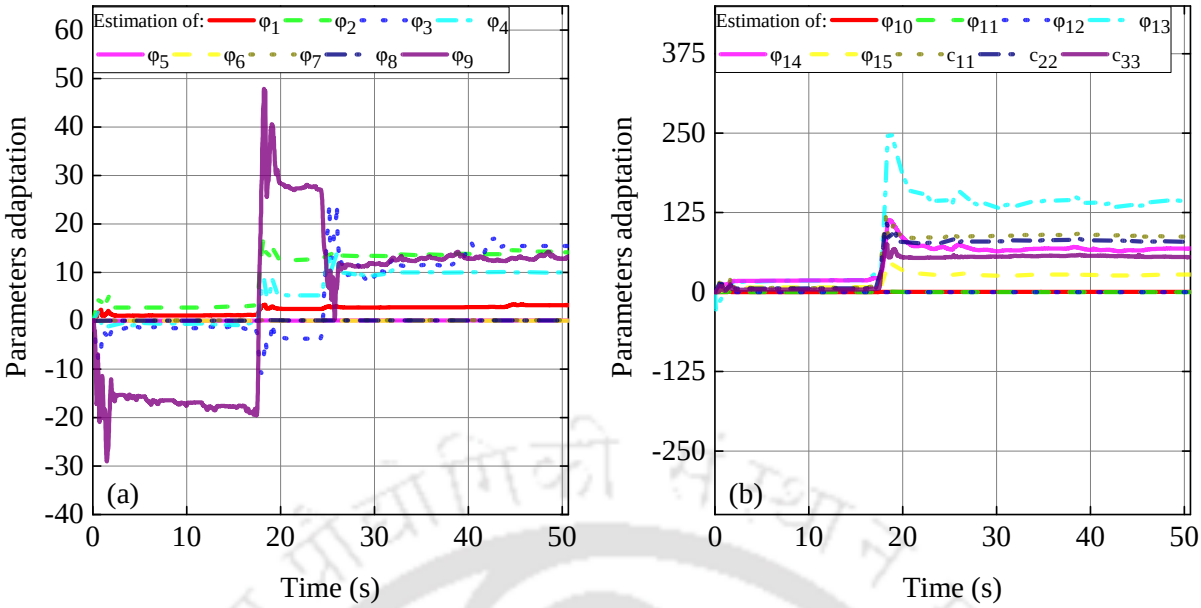

Figure 4.10: Parameters adaptation of φ and c for the rehabilitation robot with second subject-S2

Table 4.2: Performance analysis of passive training exercise for second subject-S2 and different values of ζ.

Controller	Tracking Errors (mm)				Control performance (V)			Number of transmissions	Bandwidth usage	Average inter-event times
	Y-direction		Z-direction		V_{a1}	V_{a2}	V_{a3}			
	RMSE	IAE	RMSE	IAE		RMS_{input}				
TT	4.6	0.185	6.45	0.2	0.91	2.57	2.21	5065	100%	0.01
ζ=0.5	4.74	0.189	6.5	0.21	0.93	2.63	2.36	3680	72.5%	0.013
ζ=0.7	4.8	0.194	6.9	0.24	1	3.02	3.04	1384	27%	0.036
ζ=0.9	5	0.2	7.54	0.27	1.1	3.03	3.12	553	11%	0.091

ACT. On the other hand, about 89% of the network resources are saved by implementing the proposed event-triggered mechanism compared with the time-triggered approaches. These results demonstrate the effectiveness of the proposed scheme in the execution of passive training exercises under the consideration of uncertainties and limited bandwidth restrictions. The experimental results for the second subject-S2 during the passive rehabilitation task with different ζ values are summarized in Table 4.2. It can be observed from this table that the increase of ζ values leads to more savings in the network resources. However, higher control inputs at the first, second, and third joints are required to maintain an acceptable tracking performance. Moreover, the tracking errors in the Y- and Z-directions are slightly increasing as the parameter ζ reaches one. Therefore, the balance between acceptable tracking performance and network utilization can be obtained by adjusting the parameter ζ.

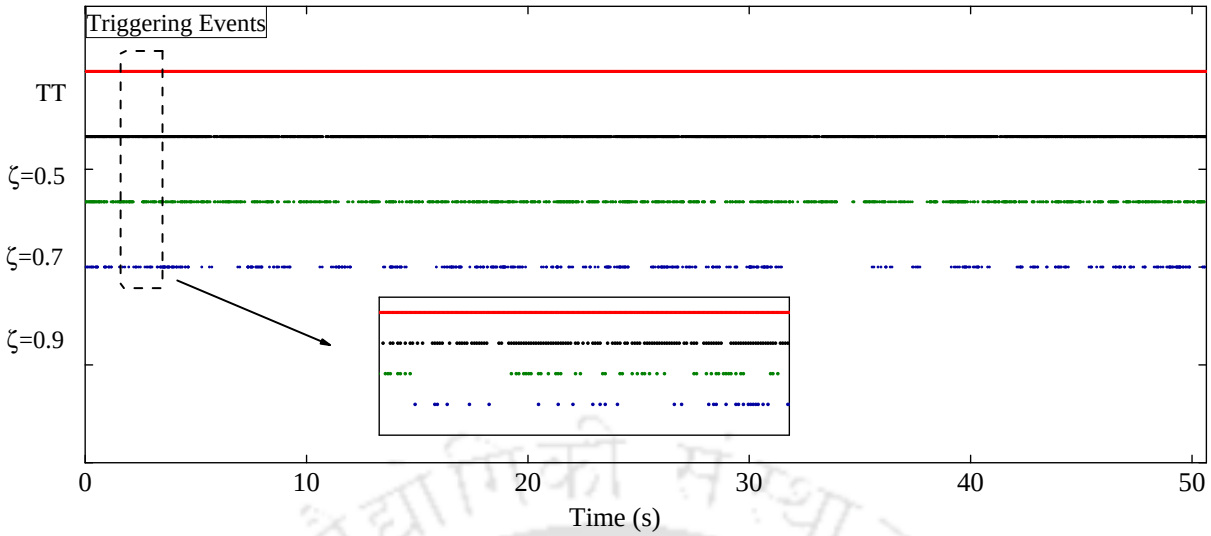

Figure 4.11: Triggering events for second subject-S2 and several ζ values

4.5 Summary

In this chapter, an adaptive backstepping control approach has been designed for an end-effector rehabilitation robot to perform upper extremity passive training exercises. The bandwidth restrictions in the controller-to-robot channel have been addressed using the event-triggered mechanism with the implementation of an adjustable Lyapunov based triggering condition. Several experimental tests have been conducted using two healthy subjects with different upper limb weights to demonstrate the effectiveness of the proposed control scheme. A comparison study between the proposed strategy and different time-triggered control approaches has been carried out. The results have shown a significant saving in the network resources (about 89%) using the proposed ET control schemes and still a superior tracking performance can be ensured with respect to other control strategies.

5

Event-Triggered Adaptive Hybrid Position-Force Control for Cooperative Manipulators

Contents

5.1 Introduction

This chapter addresses the control problem of uncertain cooperative robotic manipulators communicating with the control unit over a limited bandwidth network channel. The concept of hybrid position-force control scheme presented in Chapter 2 is extended to the cooperative manipulator system. This scheme cannot be directly applied and some modifications are required for success implementation. At first, the dynamic modeling of the cooperative manipulator system coupled with the manipulated object are presented. This coupled dynamic model inherits parametric uncertainties (robotic and object masses, moment of inertia, and link length). Moreover, internal forces could be developed due to the interaction between the manipulators and the objects. Therefore, an improved adaptive hybrid position-force controller based on the backstepping approach is developed to control the motion and the internal forces during the cooperative manipulation of a common object in the presence of parametric uncertainties and limited communication. A comparative analysis with the different robust and adaptive control strategies is carried out to investigate the effectiveness of the designed control algorithm. Furthermore, the designed triggering rule is compared with two triggering conditions presented in the literature. The validation of the proposed control approach is executed in the virtual robot experimentation platform (V-REP) during the transportation of a common object.

The chapter is organized as follows. The problem formulation is given in Section 5.2. The dynamic model of the cooperative robotic manipulators is formulated in Section 5.3. The adaptive controller design is elaborated in Section 5.4, along with the formulation of an event-triggered mechanism. Section 5.5 shows the simulation results, comparative study, and the validation of the designed control strategy in the V-REP platform. The conclusion and the future scope of work are highlighted in Section 5.6.

5.2 Problem Formulation

In this chapter, a cooperative manipulator system is considered, consisting of k single-arm manipulators securely handling a common rigid object, as illustrated in Figure 5.1. The manipulators consist of n joints with a stationary base. The object is immense and beyond the carrying capacity of single-arm manipulators. Moreover, there is no relative motion between the end-effector of the manipulators and the grasped object. Let $\Im_w - (X_w, Y_w, Z_w)$ denotes the world reference frame, $\Im_{e,i} - (X_{e,i}, Y_{e,i}, Z_{e,i})$; $1 \leq i \leq k$ represents the coordinate frame fixed at the center point of the i-th manipulator's end-effector, and $\Im_o - (X_o, Y_o, Z_o)$ is the coordinate frame attached to the center of mass of the object. The combined robot-motor dynamical model of the i-th manipulator is

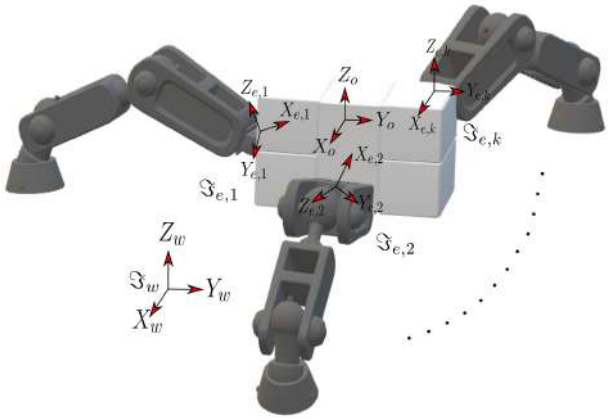

Figure 5.1: Cooperative manipulator system

expressed by the following equation [69]:

$$M_{R,i}(q_i)\ddot{q}_i + C_R(\dot{q}_i, q_i)\dot{q}_i + G_R(q_i) = \tau_{R,i} - \tau_{int,i}; \quad \tau_{int,i} = J_i^T(q_i)F_{int,i} \tag{5.1}$$

where for $1 \leq i \leq k$, $q_i = [q_{i,1}, q_{i,2}, ..., q_{i,n}]^T \in \mathbb{R}^n$ represents the vectors of joint variables, $M_{R,i}(q_i) \in \mathbb{R}^{n\times n}$ expresses the total inertia matrix of i-th manipulator, $C_R(q_i, \dot{q}_i) \in \mathbb{R}^{n\times n}$ denotes the matrix having the effect of Coriolis and centrifugal forces, $G_R(q_i) \in \mathbb{R}^n$ expresses the gravitational effect, $\tau_{R,i} \in \mathbb{R}^n$ symbolizes the vector of the actuator torques, $\tau_{int,i} \in \mathbb{R}^n$ are the torques at the joints work against the constraint, $J_i(q_i) \in \mathbb{R}^{m\times n}$ denotes the Jacobian matrix of i-th manipulator, and $F_{int,i}$ is the vector which represents the interaction forces applied from the end-effector of i-th manipulator to the manipulated object.

The dynamic model of k robotic manipulators can be combined in the following compact form:

$$M_R(q)\ddot{q} + C_R(\dot{q}, q)\dot{q} + G_R(q) = \bar{\tau}_R - \tau_{int}; \quad \tau_{int} = J^T(q)F_{int} \tag{5.2}$$

where $q = [q_1^T, q_2^T, ..., q_k^T]^T \in \mathbb{R}^{kn}$, $M_R(q) = \text{blockdiag}[M_{R,1}(q_1), M_{R,2}(q_2), ..., M_{R,k}(q_k)] \in \mathbb{R}^{kn\times kn}$, $C_R(\dot{q}, q) = \text{blockdiag}[C_{R,1}(\dot{q}_1, q_1), C_{R,2}(\dot{q}_2, q_2), ..., C_{R,k}(\dot{q}_k, q_k)] \in \mathbb{R}^{kn\times kn}$, $G_R(q) = [G_{R,1}(q_1)^T, G_{R,2}(q_2)^T, ..., G_{R,k}(q_k)^T]^T \in \mathbb{R}^{kn}$, $F_{int} = [F_{int,1}^T, F_{int,2}^T, ..., F_{int,k}^T]^T \in \mathbb{R}^{km}$, $J(q) = \text{blockdiag}[J_1(q_1), J_2(q_2), ..., J_k(q_k)] \in \mathbb{R}^{km\times kn}$, and $\bar{\tau}_R = [\bar{\tau}_{R,1}^T, \bar{\tau}_{R,2}^T, ..., \bar{\tau}_{R,k}^T]^T \in \mathbb{R}^{kn}$. The following assumptions are introduced for the simplification of the subsequent derivation:

Assumption 1. *The operation of each manipulator is away from the singularity condition. Therefore, the Jacobian matrix has a full-row rank [199].*

Assumption 2. *There is no interaction between the object and the external environment during the cooperative manipulation task.*

Remark 1. *The communication between the cooperative manipulators and the control*

unit is over a network channel. Therefore, the cooperative robotic manipulators are not actuated by the actual control signal (τ_R) due to communication constraints. Instead, they are driven by ($\bar{\tau}_R$) , which is defined as $\bar{\tau}_R = \tau_R - e_m$. This control signal is generated by the event-triggered mechanism based on the violation of a predetermined triggering condition. The triggering condition is designed in Subsection. 5.4.2 based on the measurement error.

The objective of the control is to design an improved event-triggered adaptive control scheme for the uncertain cooperative manipulators. This scheme is devoted to control the motion and the internal forces of the manipulated object in the presence of parametric uncertainties and limited communication. Moreover, it is utilized to maintain an acceptable tracking performance with a minimum number of transmissions over the network.

5.3 Dynamic Model of Cooperative Manipulators

Here, the task space dynamical model of the cooperative manipulator system is obtained by combining the dynamics equation of the manipulators (5.2) with the equations of motion of the object (5.3). For this purpose, the the closed kinematic chain is analyzed in the subsequent section to decompose the interaction forces F_{int} at the end-effector level. After that, the joint space variables are mapped into the position and orientation vector of object using the forward kinematics equations.

5.3.1 Closed Kinematic Chain Model

In this section, the analysis of the closed-chain and the decomposition of the interaction forces at the end-effector to their counterparts on the object level are carried out following the work in [130]. The dynamical model of the manipulated object is described as follows.

$$M_o(x_o)\ddot{x}_o + C_o(\dot{x}_o, x_o)\dot{x}_o + G_o(x_o) = F_{ex} - F_{env} \tag{5.3}$$

where $x_o = \begin{bmatrix} p_o \\ \phi_o \end{bmatrix} \in \mathbb{R}^m$ represents the pose (position p_o and orientation ϕ_o) of the manipulated object, $M_o(x_o)$, $C_o(\dot{x}_o, x_o)$, and $G_o(x_o)$ represent the inertia matrix, the matrix of centrifugal and Coriolis effects, and the vector of gravitational forces, respectively, $F_{ex} \in \mathbb{R}^m$ expresses the resultant forces developed at the object by the manipulators, and F_{env} expresses the forces applied to the environment by the object. This force can be given as follows.

$$F_{env} = \begin{cases} F_{env}(t), & \text{with interaction} \\ 0, & \text{no interaction} \end{cases} \tag{5.4}$$

The resultant forces can be mapped to their counterparts at the end-effector of the manipulator and described by the following equation:

$$F_{ex} = \sum_{i=1}^{k} W_i F_{int,i} \tag{5.5}$$

where $W = [W_1, W_2, ..., W_k] \in \mathbb{R}^{m \times km}$ is the grasp matrix with $W_i^T \in \mathbb{R}^{m \times m}$ denotes the Jacobian matrix from the i-th end-effector frame $\Im_{e,i}$ to the frame attached at the center of the mass of the object $\Im_o$. The matrix W is non-square, full row-rank, and it has nontrivial null space. Therefore, the inverse solution of equation (5.5) is given as follows [69].

$$F_{int} = W^{\dagger} F_{ex} + V F_{in} = F_E + F_I \tag{5.6}$$

where $W^{\dagger} \in \mathbb{R}^{km \times m}$ is the pseudoinverse matrix of W, $F_E = [F_{E,1}^T, ..., F_{E,k}^T]^T = W^{\dagger} W F_{int}$ is the forces that cause the motion of the object and balance its dynamic as well as the contact forces caused by the interaction with environment, V is a full-column rank matrix that spans the null space of the grasp matrix, $F_I = [F_{I,1}^T, F_{I,2}^T, ..., F_{I,k}^T]^T = V V^{\dagger} F_{int} \in \mathbb{R}^{km}$ is the internal forces that are in the null space of W, i.e., $(W F_I = 0)$, and $F_{I,i}$ represents the internal forces of the i-th manipulator. These internal forces do not affect the motion; however, they develop mechanical stresses at the object level and satisfy $\sum_{i=1}^{k} F_{I,i} = 0$. Therefore, the formulation of the interaction forces at the end-effector level can be obtained based on Assumption 2 (i.e, $F_{env} = 0$) and by substituting equation (5.3) in equation (5.6) as follows:

$$F_{int} = W^{\dagger}\big(M_o(x_o) + C_o(x_o, \dot{x}_o)\dot{x}_o + G_o(x_o)\big) + F_I \tag{5.7}$$

The closed-chain constraints imposed during the cooperative task on the motion variables of the object and the end-effector of the manipulators can be described in the following equations [130].

$$\begin{cases} p_{e,i} &= p_o + R_o r_i^o \\ R_{e,i} &= R_o \\ \dot{p}_{e,i} &= \dot{p}_o - S(R_o r_i^o)\omega_o \\ \omega_{e,i} &= \omega_o \\ \ddot{p}_{e,i} &= \ddot{p}_o - S(\omega_o)S(R_o r_i^o)\omega_o - S(R_o r_i^o)\dot{\omega}_o \\ \dot{\omega}_{e,i} &= \dot{\omega}_o \end{cases} \tag{5.8}$$

where $p_{e,i}$ and $R_{e,i}$ are the position vector and rotation matrix which represent the position and orientation of the i-th end-effector frame with respect to the inertial frame, respectively. p_o and R_o denote the position vector and rotation matrix which describe

the position and orientation of the object frame, respectively, $S(\cdot)$ is the skew-symmetric matrix operator, $\omega_{e,i}$ and ω_o are the angular velocities of $\Im_{e,i}$ and $\Im_o$, respectively, and r_i^o is the position vector from the i-th end-effector to the COM of the object with respect to $\Im_o$. The above kinematic relationships are obliged due to the geometry of the grasp and it is always satisfied during the cooperative task.

5.3.2 Mapping of Joint Space Variables to Object Variables

The Jacobian matrix of the i-th manipulator can be derived from the forward kinematics equation (2.9) as follows.

$$\dot{x}_{e,i} = J_i \dot{q}_i \tag{5.9}$$

The above equation can be written for the multi-arm manipulators as follows.

$$\dot{x}_e = J\dot{q} \tag{5.10}$$

where $\dot{x}_e = [\dot{x}_{e,1}^T, \dot{x}_{e,2}^T, ..., \dot{x}_{e,k}^T]^T \in \mathbb{R}^{km}$. The relationship between the vector of the object's velocity and the i-th end-effector velocity is given by:

$$\dot{x}_{e,i} = W_i^T \dot{x}_o \tag{5.11}$$

Substituting (5.9) into (5.11):

$$J_i \dot{q}_i = W_i^T \dot{x}_o \tag{5.12}$$

Based on Assumption 1, the joint velocity is mapped into the task space object's velocity as follows.

$$\dot{q} = J^{-1}(q) W^T \dot{x}_o = \eta(q)\dot{x}_o, \quad \eta(q) \in \mathbb{R}^{km \times n} \tag{5.13}$$

By differentiating (5.13) with respect to time, one can obtain:

$$\ddot{q} = J^{-1}(q) W^T \ddot{x}_o + \frac{d}{dt}\big(J^{-1}(q) W^T\big)\dot{x}_o = \eta(q)\ddot{x}_o + \iota(q)\dot{x}_o \tag{5.14}$$

The overall dynamical model of the cooperative manipulators is achieved by substituting equations (5.7), (5.13), and (5.14) in equation (5.2):

$$M_T(x_o)\ddot{x}_o + C_T(\dot{x}_o, x_o)\dot{x}_o + G_T(x_o) = \bar{\tau}_R - J^T(x_o) F_I \tag{5.15}$$

where $M_T(x_o) = M_R(q)\eta(q) + J^T(q)W^{\dagger} M_o(x_o) \in \mathbb{R}^{kn \times n}$, $C_T(\dot{x}_o, x_o) = M_R(q)\iota(q) + C_R(\dot{q}, q)\eta(q) + J^T(q)W^{\dagger} C_o(\dot{x}_o, x_o) \in \mathbb{R}^{kn \times n}$, $G_T(x_o) = G_R(q) + J^T(q)W^{\dagger} G_o(x_o) \in \mathbb{R}^{kn}$, and $J^T(x_o) = J^T(q) \in \mathbb{R}^{kn \times km}$.

To design the adaptive backstepping position-force controller, the dynamical model of the cooperative manipulator systems should satisfy the following properties [126]:

Property 7 For all $q \in \mathbb{R}^{kn}$ and $x_o \in \mathbb{R}^m$, the matrix $\eta^T M_T(x_o)$ is symmetric and positive definite.

Property 8 The matrix $\frac{d}{dt}\big(\eta^T(q)M_T(x_o)\big) - 2\eta^T(q)C_T(\dot{x}_o, x_o)$ is skew-symmetric and satisfies the following:

$$\beta^T\left(\frac{d}{dt}\big(\eta^T(q)M_T(x_o)\big) - 2\eta^T(q)C_T(\dot{x}_o, x_o)\right)\beta = 0, \forall \beta \in \mathbb{R}^m \tag{5.16}$$

Property 9 For arbitrary known vector μ, the left side of overall dynamics equations of the cooperative manipulators (5.15) can be linearly parameterized as follows:

$$\eta^T\big(M_T(x_o)\dot{\mu} + C_T(\dot{x}_o, x_o)\mu + G_T(x_o)\big) = \Pi_{x_o}\varphi_{x_o} \tag{5.17}$$

where Π_{x_o} is the regression matrix of known functions and φ_{x_o} is the vector of unknown parameters.

5.4 Controller Design

In this section, an adaptive backstepping hybrid position-force control strategy is obtained to control the motion and the internal force of the object during cooperative manipulation in the presence of uncertainties and limited communication. The state augmentation approach is utilized to improve the response of the cooperative manipulator system and enhance the robustness of the closed-loop system against uncertainties. This improvement is achieved by introducing a new state variable in the backstepping controller design process. The new state variable depends on the weighted integral of the object position error and is augmented at the first step of the controller design. This new variable leads to include the integral action in the backstepping control scheme. Therefore, the advantages of the integral action in alleviating steady-state errors and enhancing the system response in the presence of uncertainties are exploited [200]. Thereafter, the non-linear damping term, implemented in the design process of the control strategy for a general class uncertain non-linear systems [125], is extended to the cooperative manipulators system. The employment of this term improves the transient performance and reduces the number of transmitted signals over the communication channel. The block diagram of the designed control strategy is presented in Figure 5.2.

5.4.1 Adaptive Backstepping Controller

To design the adaptive backstepping controller, the new state-space variables are generated based on the object positional error, i.e., (position and orientation). These

state variables are combined with the weighted integral of the object positional error and introduced as error variables:

$$z_1 = \delta \int_0^t e_{x_o} dt = \delta \int_0^t (x_o - x_{o,d}) dt, \quad z_2 = x_o - \alpha_1, \quad z_3 = \dot{x}_o - \alpha_2 \tag{5.18}$$

where δ is a positive constant, $e_{x_o} = x_o - x_{o,d}$ is the error of object position and orientation, and $x_{o,d}$ is the desired position and orientation of the manipulated object, $\alpha_j (1 \leq j \leq 2)$ are the virtual controllers. These virtual controllers are intended to stabilize the subsystems based on the Lyapunov function. Therefore, the adaptive backstepping controller is designed by the following systematic recursive steps.

Step 1: The dynamics of the first error variable z_1 can be expressed as.

$$\dot{z}_1 = \delta \ (x_o - x_{o,d}) = \delta \ (z_2 + \alpha_1 - x_{o,d}) \tag{5.19}$$

The first virtual control law α_1 should be designed to stabilize the first error subsystem presented in the above equation. Therefore, one may choose the Lyapunov function candidate as:

$$V_1 = \frac{1}{2\delta} z_1^T z_1 \tag{5.20}$$

The derivative of the Lyapunov function becomes.

$$\dot{V}_1 = \frac{1}{\delta} z_1^T \dot{z}_1 = z_1^T z_2 + z_1^T (\alpha_1 - x_{o,d}) \tag{5.21}$$

The virtual control law is designed as

$$\alpha_1 = -k_1 z_1 + x_{o,d} = -k_1 \delta \int_0^t e_{x_o} dt + x_{o,d} \tag{5.22}$$

where k_1 is a positive gain matrix. Therefore,

$$\dot{V}_1 = - \ z_1^T k_1 z_1 + z_1^T z_2 \tag{5.23}$$

Here, if $z_2 = 0$ then, the convergence of the first error variable z_1 and the negative definiteness of the first Lyapunov function $\dot{V}_1$ can be guaranteed.

Step 2: By differentiating the second error variable in equation (5.18) with respect to time, one can obtain the following:

$$\dot{z}_2 = \dot{x}_o - \dot{\alpha}_1 = z_3 + \alpha_2 - \dot{\alpha}_1 \tag{5.24}$$

At this step, one can choose the Lyapunov function candidate as follows.

$$\bar{V}_2 = V_1 + V_2 = V_1 + \frac{1}{2} z_2^T z_2 \tag{5.25}$$

The derivative of the second Lyapunov function becomes.

$$\dot{\bar{V}}_2 = - \, z_1^T k_1 z_1 + z_1^T z_2 + z_2^T \dot{z}_2 \tag{5.26}$$

By substituting equation (5.24) in the previous equation. (5.26)

$$\dot{\bar{V}}_2 = - \, z_1^T k_1 z_1 + z_1^T z_2 + z_2^T z_3 + z_2^T \alpha_2 + z_2^T (k_1 \delta e_{x_o} - \dot{x}_{o,d}) \tag{5.27}$$

Therefore, the second virtual controller is designed as follows

$$\alpha_2 = -z_1 - k_2 z_2 - k_1 \delta e_{x_o} + \dot{x}_{o,d} \tag{5.28}$$

where k_2 is a positive gain matrix. The derivative of the second Lyapunov function becomes.

$$\dot{\bar{V}}_2 = - \, z_1^T k_1 z_1 - z_2^T k_2 z_2 + z_2^T z_3 \tag{5.29}$$

Step 3: The derivation of the third error variable z_3 is expressed as.

$$\begin{aligned} \dot{z}_3 &= \ddot{x}_o - \dot{\alpha}_2 \\ &= -M_T^{-1}(x_o) \left(C_T(\dot{x}_o, \, x_o) \dot{x}_o + G_R(x_o) - \bar{\tau}_R + J^T(x_o) \, F_I \right) - \dot{\alpha}_2 \end{aligned} \tag{5.30}$$

The Lyapunov function candidate is proposed based on **Property 7** as follows.

$$\bar{V}_3 = \bar{V}_2 + V_3 = \bar{V}_2 + \frac{1}{2} z_3^T \eta^T(q) M_T(x_o) z_3 \tag{5.31}$$

The derivative of the Lyapunov function is formulated based on equation (5.29) and **Property 8** as.

$$\begin{aligned} \dot{\bar{V}}_3 &= \dot{\bar{V}}_2 + z_3^T \eta^T(q) M_T(x_o) \dot{z}_3 + \frac{1}{2} z_3^T \frac{d \left(\eta^T(q) M_T(x_o) \right)}{dt} z_3 \\ &= \dot{\bar{V}}_2 + z_3^T \eta^T(q) \left(M_T(x_o) \dot{z}_3 + C_T(\dot{x}_o, x_o) z_3 \right) \end{aligned} \tag{5.32}$$

The term $\eta^T \left(M_T(x_o) \dot{z}_3 + C_T(\dot{x}_o, x_o) z_3 \right)$ in the previous equation can be calculated based on **Property 9**, (5.18), and (5.30) as follows.

$$\begin{aligned} \eta^T \left(M_T(x_o) \dot{z}_3 + C_T(x_o, \dot{x}_o) z_3 \right) &= \eta^T \big(- M_T(x_o) \dot{\alpha}_2 - C_T(\dot{x}_o, x_o) \alpha_2 \\ &\quad - G_T(x_o) + \bar{\tau}_R - J^T(x_o) F_I \big) \\ &= -\Pi_{x_o} \varphi_{x_o} + \eta^T \bar{\tau}_R - \eta^T J^T(x_o) F_I \end{aligned} \tag{5.33}$$

Since the dynamical parameters of the cooperative manipulators are unknown, there-

fore, an adaptation law will be proposed to estimate the nonlinear dynamic terms and complete the design of the controller. A new Lyapunov function is defined to include the estimation errors as follows:

$$V = \bar{V}_3 + \frac{1}{2}\tilde{\varphi}_{x_o}^T \Gamma \tilde{\varphi}_{x_o} \tag{5.34}$$

where $\tilde{\varphi}_{x_o} = \varphi_{x_o} - \hat{\varphi}_{x_o}$ is the estimation error, $\hat{\varphi}_{x_o}$ is the estimated vector of the unknown parameters φ_{x_o}, and Γ is an arbitrary positive definite matrix.

By using equations (5.32) and (5.33) and exploiting $e_m = \tau_R - \bar{\tau}_R$, the derivative of the last Lyapunov function V is derived as:

$$\dot{V} = \dot{\bar{V}}_2 + z_3^T \eta^T(q)\big(\tau_R - e_m - J^T(x_o)F_I\big) - z_3^T \Pi_{x_o}\varphi_{x_o} - \tilde{\varphi}_{x_o}^T \Gamma^{-1}\dot{\hat{\varphi}}_{x_o} \tag{5.35}$$

Adding and subtracting the term $z_3^T \Pi_{x_o}\hat{\varphi}_{x_o}$ and taking the transpose of $z_3^T \Pi_{x_o}\tilde{\varphi}_{x_o}$, one gets

$$\begin{aligned}
\dot{V} &= \dot{\bar{V}}_2 + z_3^T \eta^T(q)\big(\tau_R - e_m - J^T(x_o)F_I\big) - z_3^T \Pi_{x_o}\hat{\varphi}_{x_o} - \tilde{\varphi}_{x_o}^T\big(\Pi_{x_o}^T z_3 + \Gamma^{-1}\dot{\hat{\varphi}}_{x_o}\big) \\
&= - z_1^T k_1 z_1 - z_2^T k_2 z_2 + z_3^T \eta^T(q)\Big(\eta(q)\big(\eta^T(q)\eta(q)\big)^{-1} z_2 + \tau_R - e_m - J^T(x_o)F_I\Big) \\
&\quad - z_3^T \Pi_{x_o}\hat{\varphi}_{x_o} - \tilde{\varphi}_{x_o}^T\big(\Pi_{x_o}^T z_3 + \Gamma^{-1}\dot{\hat{\varphi}}_{x_o}\big)
\end{aligned} \tag{5.36}$$

where $z_2^T z_3 = z_3^T z_2 = z_3^T \eta^T(q)\eta(q)\big(\eta^T(q)\eta(q)\big)^{-1} z_2$. The overall control law τ_R comprises two parts, i.e., position control law τ_p and force control law τ_f . Therefore, the overall controller and the adaptation law can be designed in the following equations to complete the controller design process.

$$\tau_R = \overbrace{-\eta\big(\eta^T\eta\big)^{-1}(z_2 - \Pi_{x_o}\hat{\varphi}_{x_o}) - (\vartheta\|\Pi_{x_o}\|^2 + k_3)\eta z_3}^{\text{Position controller } (\tau_p)} + \overbrace{J^T\Big(F_{I,d} + k_{f_{I,p}} e_{f_I}(t) + k_{f_{I,i}}\int e_{f_I}(t)dt\Big)}^{\text{Force controller } (\tau_f)} \tag{5.37}$$

$$\dot{\hat{\varphi}}_{x_o} = -\Gamma\Pi_{x_o}^T z_3 \tag{5.38}$$

where $\vartheta, k_3, k_{f_{I,p}}$, and $k_{f_{I,i}}$ are positive constants, $e_{f_I} = F_{I,d} - F_I$ is the internal forces errors, and $F_{I,d}$ is the desired internal forces to be achieved. The non-linear damping term $\vartheta\|\Pi_{x_o}\|^2\eta z_3$ is added to the controller equation (5.37) to improve the transient response during the cooperative manipulation task.

Remark 2. *The following equation is derived based on the fact that the internal forces*

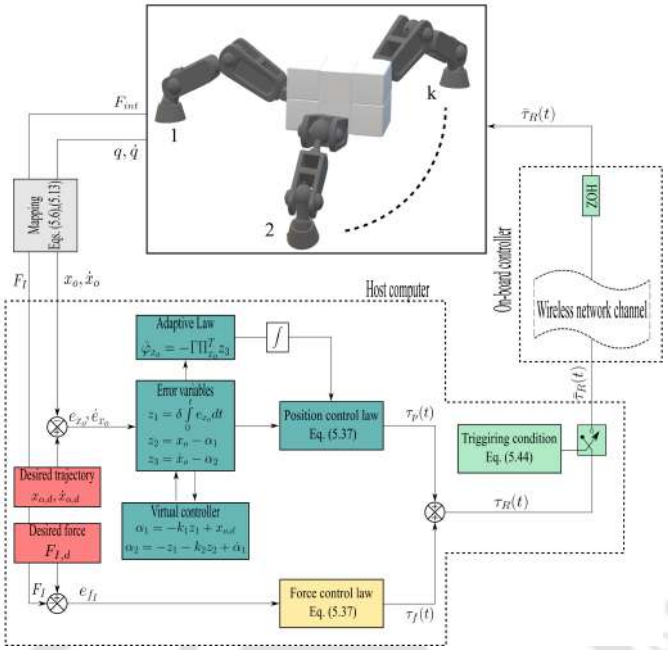

Figure 5.2: Block diagram of the proposed event-triggered control strategy

are in the null space of the grasp matrix W*, and by using equation (5.13):*

$$\eta^T(q)\left(J^T F_I - J^T F_{I,d} - k_{f_{I,p}} J^T e_{f_I}(t) - k_{f_{I,i}} J^T \int e_{f_I}(t)dt\right) = 0 \tag{5.39}$$

By substituting equations (5.37)-(5.39) in (5.36), the derivative of Lyapunov function becomes.

$$\dot{V} = - z_1^T k_1 z_1 - z_2^T k_2 z_2 - z_3^T \eta^T(q) k_3 \eta(q) z_3 - z_3^T \eta^T(q) \vartheta \|\Pi_{x_o}\|^2 \eta(q) z_3 - z_3^T \eta^T(q) e_m \tag{5.40}$$

5.4.2 Event-Triggered Mechanism

To eliminate the unnecessary transmission of the control signal over the network channel, which results in more efficient utilization of the network resources and decreases the network burden, an event-triggered mechanism is addressed in this section. This mechanism is based on the design of a triggering condition placed at the control end to maintain the stability of the cooperative system. The violation of the triggering condition causes the transmission of a new control input over the communication network. Otherwise, the last transmitted signal is preserved and utilized to guide the cooperative robotic system. The triggering time-instants are expressed in equation (2.1).

By applying Young inequality to equation (5.40), it yields:

$$\begin{aligned}\dot{V} &\leq -z_1^T k_1 z_1 - z_2^T k_2 z_2 - z_3^T \eta^T(q) k_3 \eta(q) z_3 - z_3^T \eta^T(q) \vartheta \|\Pi_{x_o}\|^2 \eta(q) z_3 + \|z_3^T \eta^T(q)\| \|e_m\| \\ &\leq -z_1^T k_1 z_1 - z_2^T k_2 z_2 - z_3^T \eta^T(q) \big(k_3 + \vartheta \|\Pi_{x_o}\|^2\big) \eta(q) z_3 + \frac{\|z_3^T \eta^T(q)\|^2}{2} + \frac{\|e_m\|^2}{2}\end{aligned} \tag{5.41}$$

Adding and subtracting the terms $\zeta\Big(z_1^T k_1 z_1 + z_2^T k_2 z_2 + z_3^T \eta^T(q)\big(k_3 + \vartheta\|\Pi_{x_o}\|^2\big)\eta(q) z_3\Big)$, one can obtain:

$$\begin{aligned}\dot{V} \leq &-(1-\zeta)\Big(z_1^T k_1 z_1 + z_2^T k_2 z_2 + z_3^T \eta^T(q)\big(k_3 \eta(q) z_3 + \vartheta \|\Pi_{x_o}\|^2 \eta(q) z_3\big)\Big) \\ &- \zeta\Big(z_1^T k_1 z_1 + z_2^T k_2 z_2 + z_3^T \eta^T(q)\big(k_3 + \vartheta\|\Pi_{x_o}\|^2\big)\eta(q) z_3\Big) + \frac{\|z_3^T \eta^T(q)\|^2}{2} + \frac{\|e_m\|^2}{2}\end{aligned} \tag{5.42}$$

Remark 3. *The last transmitted control input is preserved and utilized to actuate the cooperative manipulator system provided the negative definiteness of the Lyapunov function derivative. However, the violation of this condition updates/generates a further control signal to maintain the stability and the performance of the cooperative manipulators during the manipulation task.*

Then, the triggering condition can be derived based on Remark 3 as follows:

$$\frac{\|z_3^T \eta^T(q)\|^2}{2} + \frac{\|e_m\|^2}{2} \leq \zeta\Big(z_1^T k_1 z_1 + z_2^T k_2 z_2 + z_3^T \eta^T(q)\big(k_3 \eta(q) z_3 + \vartheta \|\Pi_{x_o}\|^2 \eta(q) z_3\big)\Big) \tag{5.43}$$

If the triggering condition (5.43) holds true and the user-defined parameter ζ is chosen as $0 < \zeta < 1$, then the derivative of the Lyapunov function (5.42) is ensured to be negative semi-definite, and the triggering threshold in equation (2.1) can be defined as follows.

$$T_{con} = \|e_m\|^2 - 2\zeta\Big(z_1^T k_1 z_1 + z_2^T k_2 z_2 + z_3^T \eta^T(q)\big(k_3 + \vartheta\|\Pi_{x_o}\|^2\big)\eta(q) z_3\Big) + \|z_3^T \eta^T(q)\|^2 \tag{5.44}$$

In view of the previous analysis, the following proposition can be concluded.

Proposition 3. *All the signals of the uncertain cooperative manipulators (5.15) actuated by the control input (5.37) along with the adaptation law (5.38) and event-triggered condition (5.44) are ultimately bounded. The convenient selection of the controller parameters can ensure the convergence of motion and internal forces tracking errors to small bounded values. Moreover, a lower bound of inter-event time between two successive triggering moments is guaranteed during the cooperative manipulation task.*

Proof. The triggering condition given in equation (5.44) is designed to maintain the negative semi-definiteness of Lyapunov function derivative. Based on the previous analysis,

the derivative of the Lyapunov function can be represented as

$$\dot{V} \leq -\Theta V + \Omega \tag{5.45}$$

where $\Theta = \min\left\{2\delta\lambda_{min}(k_1), 2\lambda_{min}(k_2), \frac{2\left(\lambda_{min}(k_3)+\vartheta\|\Pi_{x_o}\|^2-\frac{1}{2\zeta}\right)\lambda_{min}(\eta^T\eta)}{\lambda_{max}\left(\eta^T M_T(x_o)\right)}\right\}$, and $\Omega = \frac{\zeta\|e_m\|^2}{2}$. Similar to the analysis in Proposition 1, the convergence of tracking errors to the following sets can be ensured:

$$\|z_1\| \leq \sqrt{2\delta\bar{V}}\ , \quad \|z_2\| \leq \sqrt{2\bar{V}}\ , \quad \|z_3\| \leq \sqrt{2\bar{V}} \tag{5.46}$$

where $\bar{V} = \max\left\{V(0),\ \frac{\Omega}{\Theta}\right\}$. This implies the ultimate boundedness of the closed-loop signals. Furthermore, the dynamics error equation of the internal force tracking can be obtained by substituting the control law (5.37) in the overall dynamical model of the cooperative manipulators (5.15) as follows.

$$\begin{aligned} &J^T\left(e_{f_I} + k_{f_{I,p}}e_{f_I}(t) + k_{f_{I,i}}\int e_{f_I}(t)dt\right) = M_T(x_o)\ddot{x}_o + C_T(x_o,\dot{x}_o)\dot{x}_o + G_T(x_o) \\ &+ \eta\left(\eta^T\eta\right)^{-1}(z_2 - \Pi_{x_o}\hat{\varphi}_{x_o}) + (\vartheta\|\Pi_{x_o}\|^2 + k_3)\eta z_3 + e_m \end{aligned} \tag{5.47}$$

Since the signals of the closed-loop system are uniformly bounded, the equation (5.47) indicates that the convergence of internal force errors to small values can be achieved by the proper choice of the internal force controller parameters. Therefore, the boundedness of the closed-loop system and stability of the cooperative manipulators can be ensured under the proposed event-triggered control scheme. Moreover, the proof of avoiding the Zeno behavior presented in Proposition 1 is still valid and can be directly applied in the case of hybrid position-force control of cooperative manipulation system. □

Remark 4. *It can be observed from the equation (5.46) that the error signals can be ensured to converge to small values by increasing Θ and reducing Ω. Therefore, the increase in the position controller gains δ, k_1, k_2, and k_3 leads to improve the tracking performance of the proposed control strategy during the cooperative manipulation task. The steady-state error is reduced by introducing the integral action to the proposed control scheme using the new augmented state variable, and the k_1 gain is usually selected to be a small constant. The faster convergence to the estimated parameters is guaranteed by choosing a higher adaptation gain Γ. On the other hand, the increase in the adjustable parameter ζ of the proposed event-triggered mechanism causes a higher reduction in the transmissions over the network. However, this may degrade the performance of the closed-loop system and increase the tracking errors. Therefore, a trade-off between tracking performance and network utilization should be maintained while choosing the controller parameters. Furthermore, based on the previous equation (5.47) and since the signals of the closed-loop system are uniformly bounded, the selection of high gains of the internal forces controller (i.e., $k_{f_{I,p}}$ and $k_{f_{I,i}}$) guarantees a better tracking of the desired internal forces with minimum tracking error. However, the selection of high gains produce high control action, resulting in chattering phenomena. Therefore, these parameters should be selected carefully to maintain the required system performance without developing a high torque input. The new augmented state variable and the nonlinear damping term added*

to the proposed control scheme will improve the transient performance and reduce the steady-state error. Due to this improvement, there is no requirement to frequently send the control signals over the network from the very start. Therefore, fewer control signals are transmitted over the network during the transient response. In other words, the new augmented state variable and the nonlinear damping term will increase the negativity of the Lyapunov function derivative that leads to an increase in the stability of the closed-loop system. Moreover, the proposed triggering condition is designed based on the Lyapunov function and includes the new state variable and the nonlinear damping term (5.44). Therefore, a reduction in the number of the transmitted signals over the network can be achieved using the proposed control scheme.

5.5 Simulation Results and Comparative Study

To demonstrate the effectiveness of the proposed control strategy, the simulation runs have been carried out using uncertain cooperative dual-arm manipulators, as shown in Figure 5.3. The TrueTime network simulator is utilized to implement the proposed control scheme and mimic the real-time control scenario over a network channel [201]. Three computer kernel blocks are constructed to represent the sensor, actuator, and controller nodes in the TrueTime based simulation model. The control signal is generated based on the Simulink model of the proposed control scheme called by the controller node during the simulation runs. Moreover, a wireless communication network is placed at the controller-to-robot channel using the network block of the TrueTime toolbox. The network protocol is chosen to be IEEE 802.11b (WLAN). An additional random interfering traffic is generated over the network using an interference node. The dual-arm system consists of two 3-DOFs manipulators transporting a common object through a predefined trajectory. The manipulators have a revolute joint type with a stationary base. The world reference frame is assumed to be between the dual-arm manipulators with a distance of $l_{x,1} = 1$ m and $l_{x,2} = 1.2$ m from the first and second manipulator, respectively, as illustrated in Figure 5.3. The dynamic model of the implemented dual-arm manipulators can be expressed by equation (5.2) in which the vectors of joint angles $q_i = [\theta_{i,1}, \theta_{i,2}, \theta_{i,3}]^T \in \mathbb{R}^3$ for $i = 1, 2$, the inertia matrix $M_{R,i}(\theta_i) \in \mathbb{R}^{3\times3}$, the matrix of Coriolis and centrifugal forces $C_{R,i}(\theta_i, \dot{\theta}_i) \in \mathbb{R}^{3\times3}$, and the vector of the gravitational effect $G_{R,i}(\theta_i) \in \mathbb{R}^3$ are described in details in Appendix A.1. The dynamic model of the handled object is represented by equation (5.3) where $M_o(x_o) = \text{diag}(m_o, m_o, I_o)$, $C_o(x_o, \dot{x}_o) = 0$, and $G_o = [0, 0, m_o g]^T$. The physical parameters of the robotic manipulators are consistent with the SCORBOT-ER VPlus manipulator, with no motion at the fourth and fifth joints, as given in Appendix A.1.

The performance of the proposed control scheme is investigated during the cooperative manipulation task with the consideration of three different cases as follows.

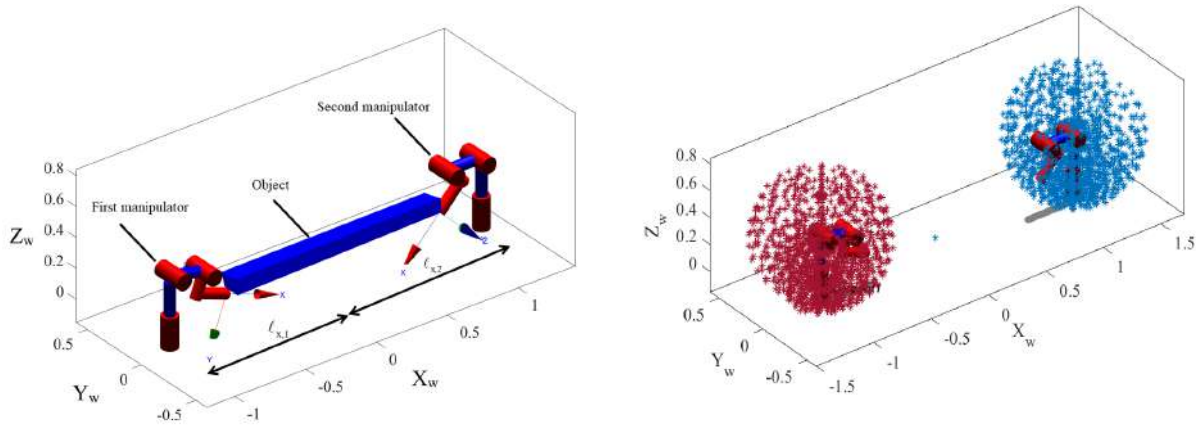

Figure 5.3: Cooperative dual-arm manipulators with the workspace of each manipulator

Case 1. The proposed event-triggered (ET) control strategy is compared with two different time-triggered (TT) control approaches, i.e., traditional adaptive backstepping strategy (TT-AB) [125] and the state augmented adaptive backstepping control (TT-AUAB) [126].

Case 2. The designed Lyapunov-based triggering rule is extended for the aforementioned time-triggered algorithms to investigate the effect of the new state variable and non-linear damping term on the tracking accuracy and the number of transmissions. Moreover, the proposed control scheme is examined under the assumption of packet dropout during the transmission over the network.

Case 3. An additional comparative study is carried out between the designed triggering mechanism and the various triggering rules presented in the literature [145,146]. These triggering rules are integrated with the sliding mode control scheme (ET-SMC) [146] and with adaptive control (ET-AC) [145].

All the above cases are implemented in the TrueTime network simulator during the transportation of a common object through a lemniscate trajectory in the x-z plane. Further, the internal forces developed at the manipulated object are controlled to eliminate the internal stresses and avoid the damage of the manipulators and\or the object. The generation of the desired lemniscate trajectory is expressed as $x_{o,d}(t) = \left[0.1 + \frac{0.05\sin(t)}{1+\sin^2(\omega_d t)}; 0;\ 0.1 + \frac{0.05\sin(\omega_d t)\cos(\omega_d t)}{1+\sin {\omega_d}^2(t)}\right]$. The desired internal forces are defined to be zero, i.e., $F_{I,d} = [0;\ 0;\ 0;\ 0;\ 0;\ 0]$. The simulation tests are conducted in a MATLAB environment for a total time of $t = 6.28$ s with a sampling rate of $dt = 0.01$ s and $\omega_d = 1\ \frac{\text{rad}}{\text{s}}$. The initial position the manipulated object is chosen as $x_o(0) = [0.15\ \text{m}, 0\ \text{m}, 0.1\ \text{m}]^T$ with velocity equals to zero. The initial conditions of the vector of parameter estimation are chosen to be zero. The object's physical parameters are chosen as follows: the object mass $m_o = 5$ kg, the object moment of inertia $I_o = 0.1$ kgm^2, and the object dimensions

are 1.5 m × 0.05 m × 0.1 m for the length, width, and height, respectively.

5.5.1 Simulation Results

Case 1. The designed ET control scheme is implemented in the TrueTime based simulation environment considering uncertainties and limited communication. The dual-arm robotic system is exploited to transport the common object through a lemniscate trajectory and maintain the internal forces at the desired level. A comparison study with two variations of the time-triggered backstepping strategy, i.e., traditional adaptive backstepping (TT-AB) [125] and the state augmented adaptive backstepping control (TT-AUAB) [126], is conducted. These approaches are exploited to carry out the same transportation task. The TT-AB and TT-AUAB control laws and the choice of the parameters are presented in Appendix A.4. The parameters of the proposed controller are chosen based on the heuristic method as follows: $k_1 = \text{diag}(0.1, 0.1, 0.1)$, $k_2 = \text{diag}(30, 30, 30)$, $k_3 = 6.5I_6$, $\delta = 50$, $\vartheta = 81I_6$, $\Gamma = 6500I_6$, $\zeta = 0.9$, $k_{f_{I,p}} = 0.1I_6$, and $k_{f_{I,i}} = 20I_6$.

Discussion 1. The tracking performance along with position tracking errors of TT-AB, TT-AUAB, and proposed ET control strategies, are illustrated in Figure 5.4. It is noted from the enlarged view of Figure 5.4 (a) that the designed control approach and TT-AUAB provide a better tracking performance as compared with TT-AB. However, a smaller position tracking errors with faster convergence to zero are achieved by implementing the proposed control strategy as depicted in Figure 5.4 (b, c, d). The tracking of desired internal forces for the first and second robots is presented in Figure 5.5 and Figure 5.6, respectively. The desired internal forces are assumed to be zero to avoid internal mechanical stresses at the manipulated object. It can be observed that a sufficient force tracking performance can be realized by implementing the different control schemes. However, the proposed ET control approach shows a faster response and smaller force tracking errors than TT-AB and TT-AUAB control strategies. Figure 5.7 (a, b, c) and Figure 5.7 (d, e, f) depict the control signals of the first and second manipulators, respectively. The control signals for the proposed ET control scheme are not transmitted continuously over the network, as observed from the enlarged view of these figures. Instead, it is updated after a time gap based on the violation of the predesigned triggering condition. Therefore, a smaller number of transmissions over the network is transmitted while maintaining a better position and force tracking performance during the cooperative manipulation task.

Case 2. The proposed Lyapunov-based triggering threshold is designed for the same control schemes presented in Case 1 (i.e., AB and AUAB). This implementation is conducted to examine the effect of integrating the new state variable and non-linear damping term on the number of transmissions over the network compared with ET-AB and ET-

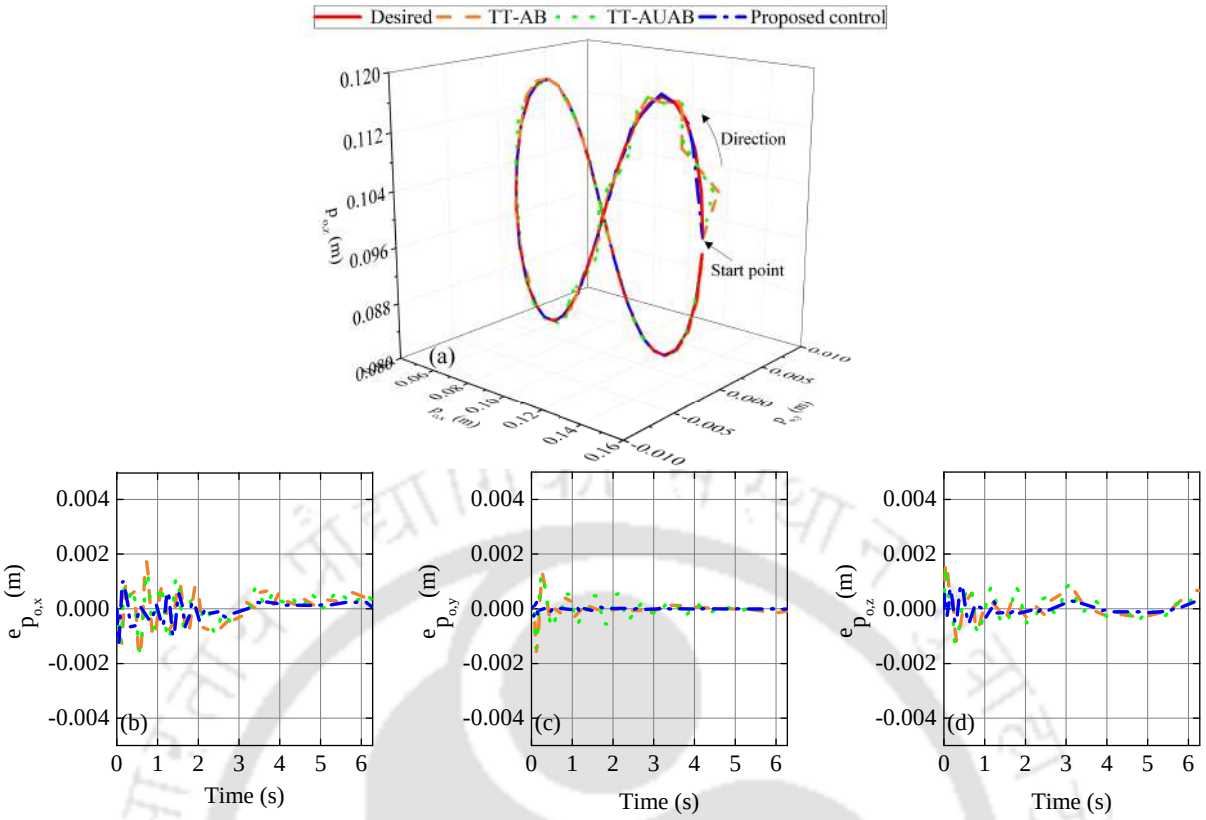

Figure 5.4: Trajectory tracking of the manipulated object for Case 1. (a) Desired and actual trajectories. Tracking error in (b) X-direction, (c) Y-direction, and (d) Z-direction

AUAB control strategies. For a fair comparison, the parameters of ET-AB and ET-AUAB are chosen similar to the parameters of Case 1 as given in Appendix A.4.

Discussion 2. The inter-event time and triggering events of the ET-AB, ET-AUAB, and the proposed ET control scheme are illustrated in Figure 5.8 and Figure 5.9, respectively. It can be noted from Figure 5.8 that a longer inter-event time is achieved in the case of the proposed control scheme. Moreover, a smaller number of transmissions over the network is guaranteed using the proposed approach, as depicted in Figure 5.9. Therefore, it is evident that the integration of the state variable and the non-linear term in the controller design process improves the performance of the controller and leads to a significant saving in the network resources compared with ET-AB and ET-AUAB control algorithms.

Case 3. An additional comparative study is carried out with two existing results in the literature [145, 146]. The event-triggered mechanism is integrated with the sliding mode control (ET-SMC) in [146] and with adaptive control (ET-AC) in [145] for non-linear systems. This comparison is conducted to prove the effectiveness of the proposed ET control strategy for cooperative manipulation in the presence of uncertainties and

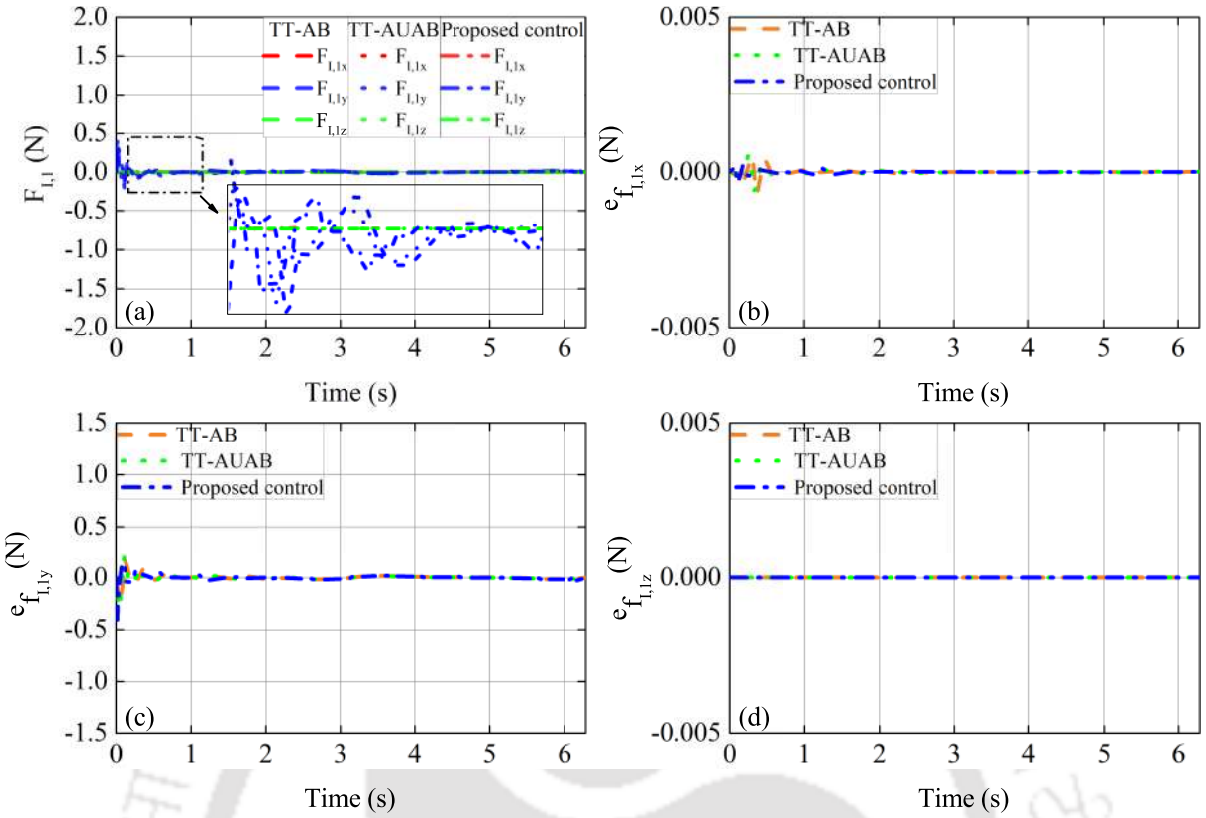

Figure 5.5: Tracking of internal forces for the first manipulator in Case 1. (a) Force trajectory tracking. Force error in (b) X-direction, (c) Y-direction, and (d) Z-direction

limited communication. The control approaches are devoted to perform the same transportation task through the lemniscate trajectory. For ease of reference, the ET-SMC control law and the selected gains of the controller are presented in Appendix A.4.

Discussion 3. The tracking performance along with tracking errors for ET-SMC, ET-AC, and proposed ET control schemes, are depicted in Figure 5.10. Moreover, the tracking of internal forces during the cooperative manipulation task is presented in Figure 5.11 and Figure 5.12. It is evident from Figures 5.10-5.12 that ET-SMC does not lead to the convergence of tracking errors to zero and causes a chattering in the internal force tracking profile. This chattering does not exist in the case of ET-AC and proposed ET control schemes. On the other hand, the proposed ET scheme delivers a superior tracking performance with smaller position and force tracking errors than ET-SMC and ET-AC. The control signals for the first and second manipulators are depicted in Figure 5.13. It can be noted that the chattering phenomena associated with SMC cannot vanish with the implementation of the ET mechanism. Moreover, the ET-SMC exhibits a shorter inter-event time and relatively higher triggering instants than ET-AC and the proposed ET control scheme, as depicted in Figure 5.14. However, the proposed control scheme

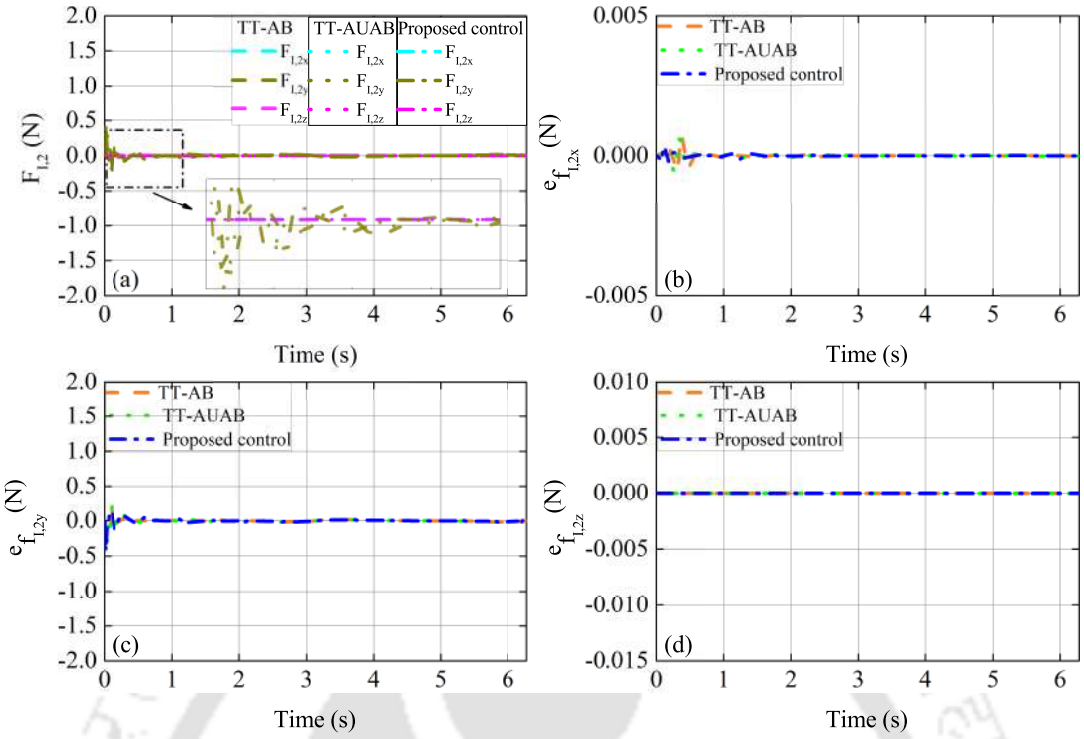

Figure 5.6: Tracking of internal forces for the second manipulator in Case 1. (a) Force trajectory tracking. Force error in (b) X-direction, (c) Y-direction, and (d) Z-direction

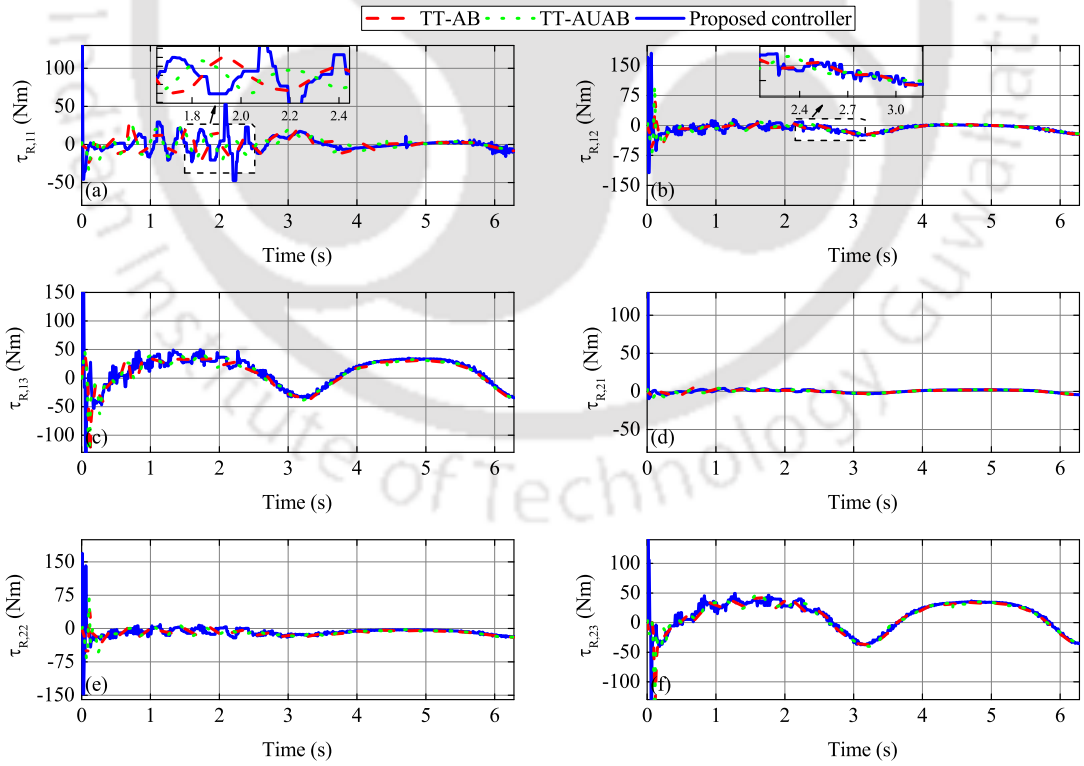

Figure 5.7: Control inputs for the first and second robots in Case 1. First robot: (a) first joint, (b) second joint, (c) and third joint. Second robot: (d) first joint, (e) second joint, and (f) third joint

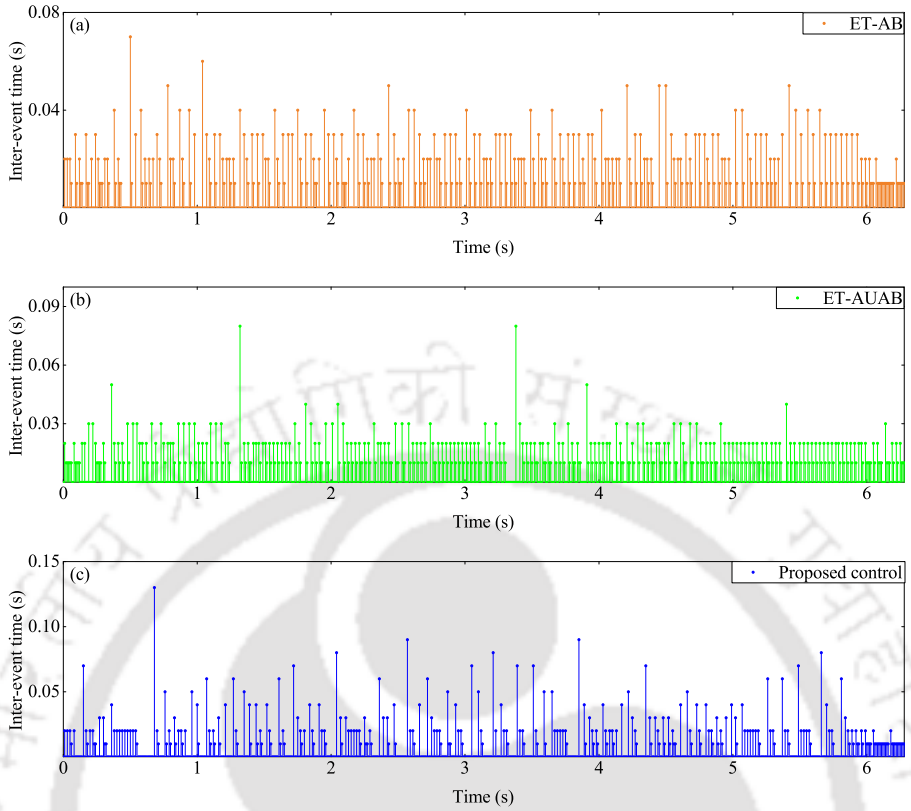

Figure 5.8: Inter-events time for (a) ET-AB. (b) ET-AUAB. (c) proposed control scheme in Case 2

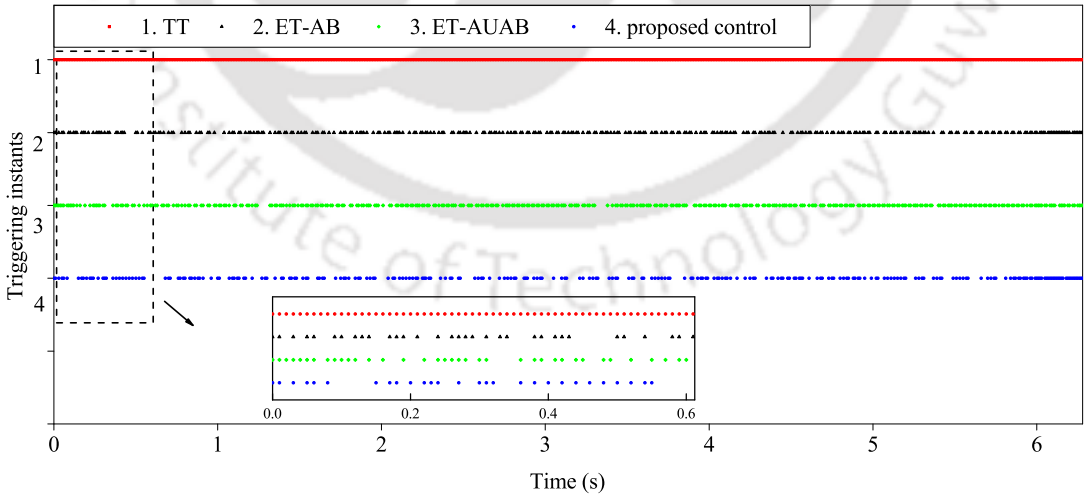

Figure 5.9: Triggering events for time-triggered, ET-AB, ET-AUAB, and proposed ET control scheme in Case 2

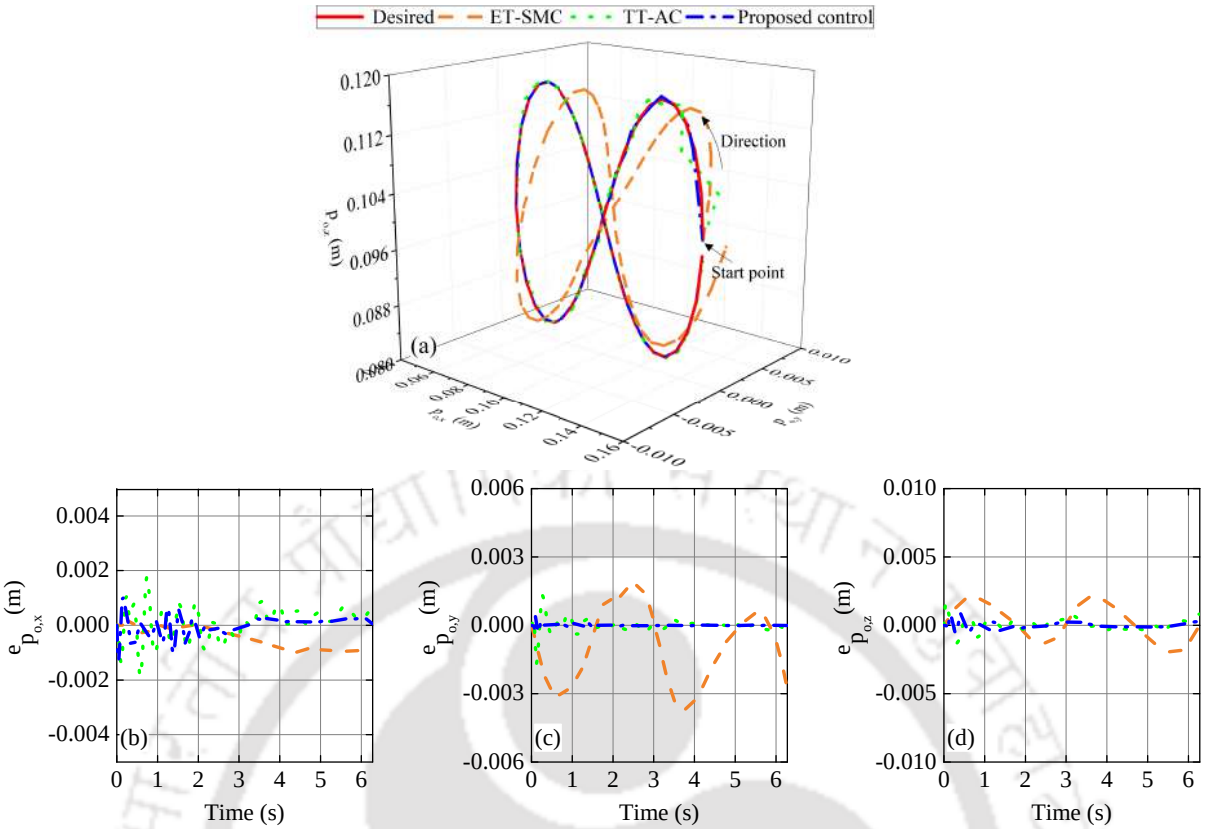

Figure 5.10: Trajectory tracking of the manipulated object for Case 3. (a) Desired and actual trajectories. Tracking error in (b) X-direction, (c) Y-direction, and (d) Z-direction

presents a noticeable reduction in the transmission over the network in tandem with a good position and force tracking accuracy during the cooperative transportation task compared with ET-SMC and ET-AC.

5.5.2 Comparative Study

To further investigate the tracking performance of the different control strategies in the various cases, the integral absolute error (IAE) and integral absolute value (IAV) of the control inputs are calculated during the cooperative manipulation task as given in equation (2.54) and summarized in Figure 5.15. On the other hand, the channel usage (CS) and the number of transmissions (N) for the controllers are quantified and brought in Figure 5.16 based on equation (2.55). It is to be mentioned that the transmissions over the network for the time-triggered control scheme occur at every sampling time. Therefore, the number of transmissions is equal to $\frac{t}{dt} = \frac{6.28}{0.01} = 628$. In equation (2.54), the error vector e: $e_{p_{o,x}} = p_{od,x} - p_{o,x}$, is object position tracking error in X-direction; $e_{p_{o,y}} = p_{od,y} - p_{o,y}$, is object position tracking error in Y-direction; $e_{p_{o,z}} = p_{od,z} - p_{o,z}$, is

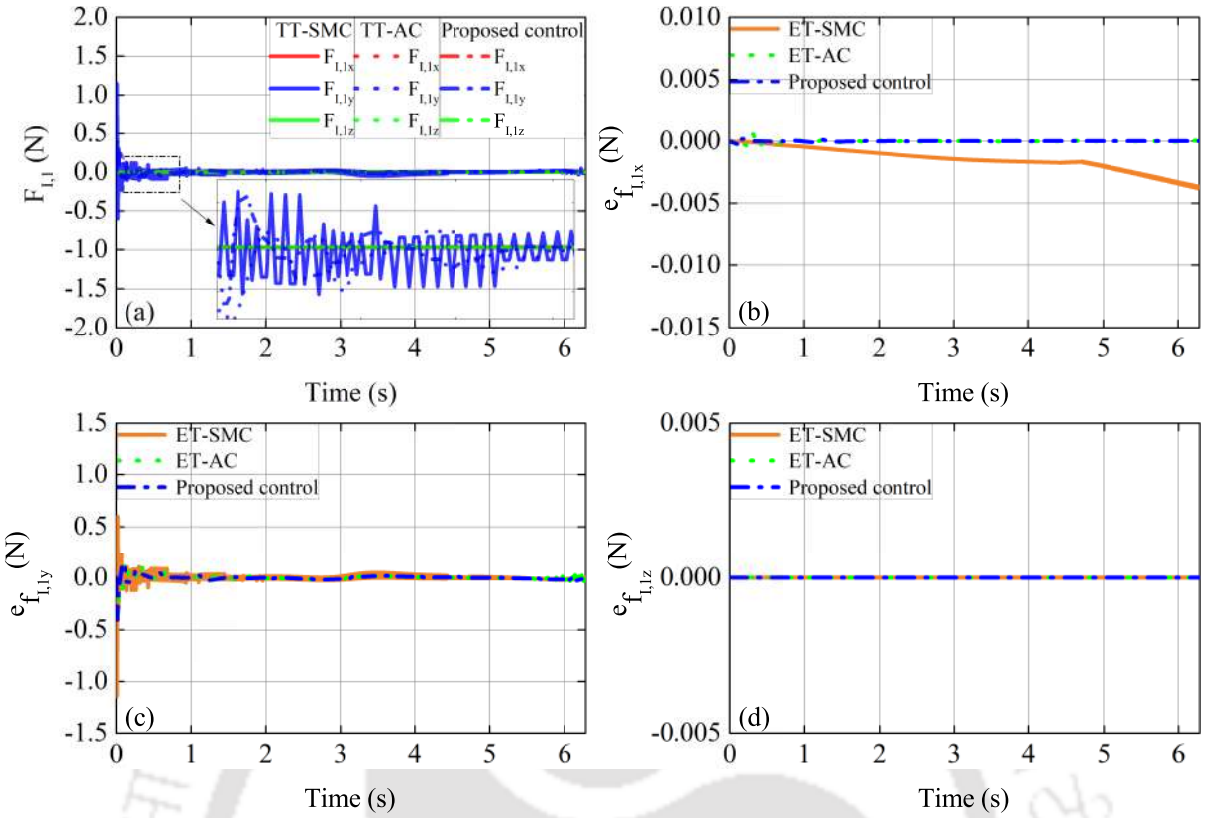

Figure 5.11: Tracking of internal forces for the first manipulator in Case 3. (a) Force trajectory tracking. Force error in (b) X-direction, (c) Y-direction, and (d) Z-direction

object position tracking error in Z-direction; $\tau_{R,ij}$, is the control input at the desired joint j of the i-th manipulator.

It can be observed from Figure 5.15 (a, b, c) that the proposed control approach provides a superior tracking performance with a minimal integral absolute value of the tracking errors in the three different cases. Moreover, the control efforts are not significantly increased by implementing the proposed control approach, and relatively small control efforts are still guaranteed at some joints compared with the other control schemes, as illustrated in Figure 5.15 (d, e, f). On the other hand, the proposed event-triggered mechanism leads to a notable saving in the network resources for AB and AUAB control schemes with similar tracking performance as presented in Case 2. However, it is evident from Figure 5.16 that the designed ET control strategy has the least number of triggering instants and the longest inter-event time compared with the other control strategies. Thus, it can be understood that the proposed control approach exhibits an outstanding tracking performance in tandem with a significant saving in the network resources during the cooperative manipulation task.

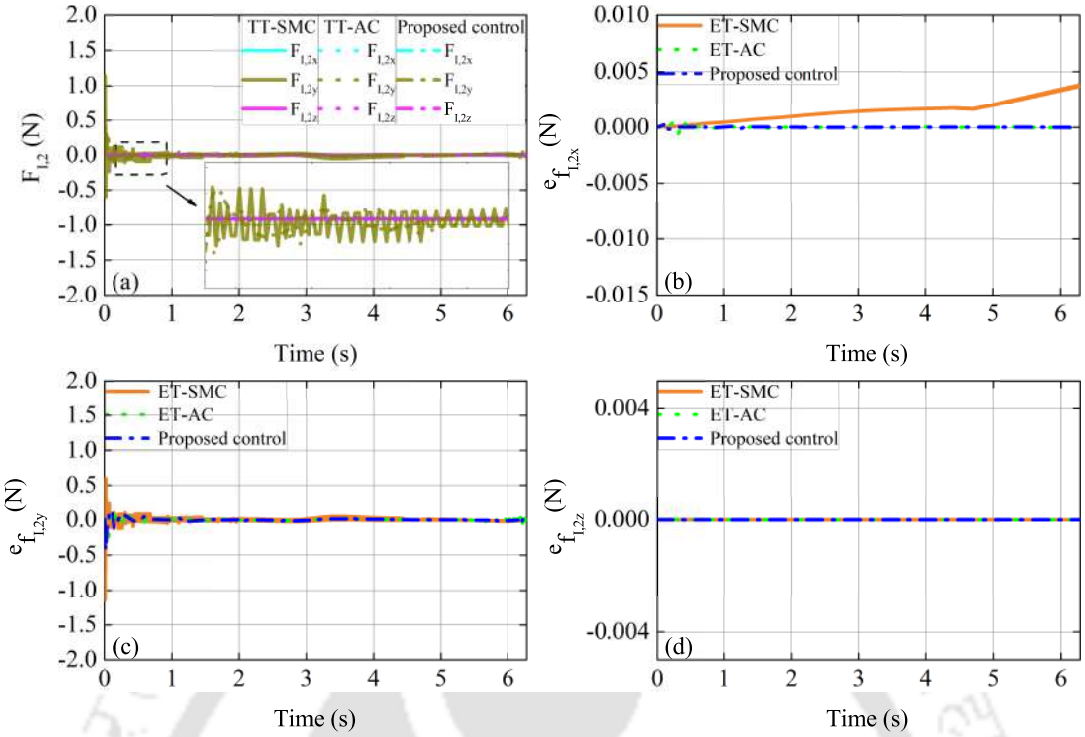

Figure 5.12: Tracking of internal forces for the second manipulator in Case 3. (a) Force trajectory tracking. Force error in (b) X-direction, (c) Y-direction, and (d) Z-direction

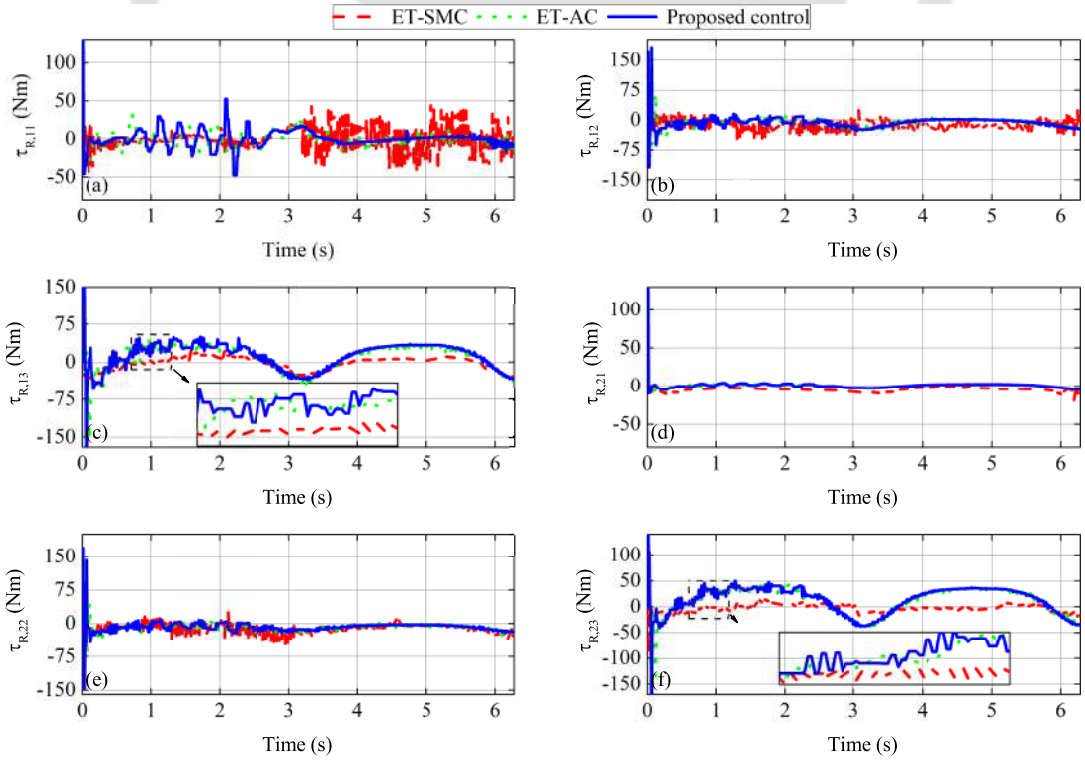

Figure 5.13: Control inputs for the first and second robots in Case 3. First robot: (a) first joint, (b) second joint, (c) and third joint. Second robot: (d) first joint, (e) second joint, and (f) third joint

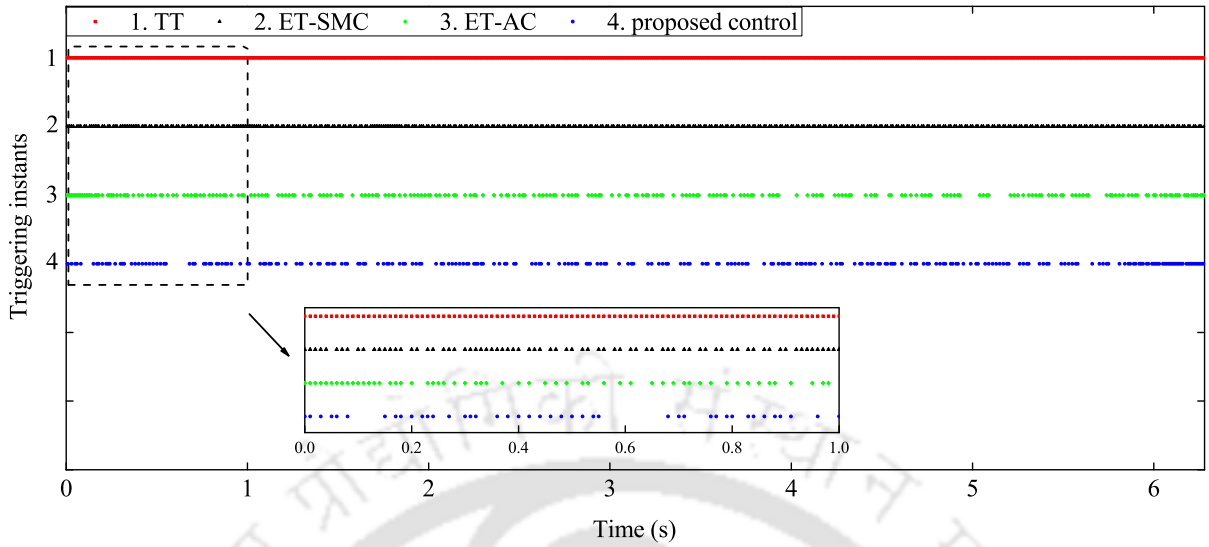

Figure 5.14: Triggering events for time-triggered, ET-SMC, ET-AC, and proposed ET control scheme in Case 3

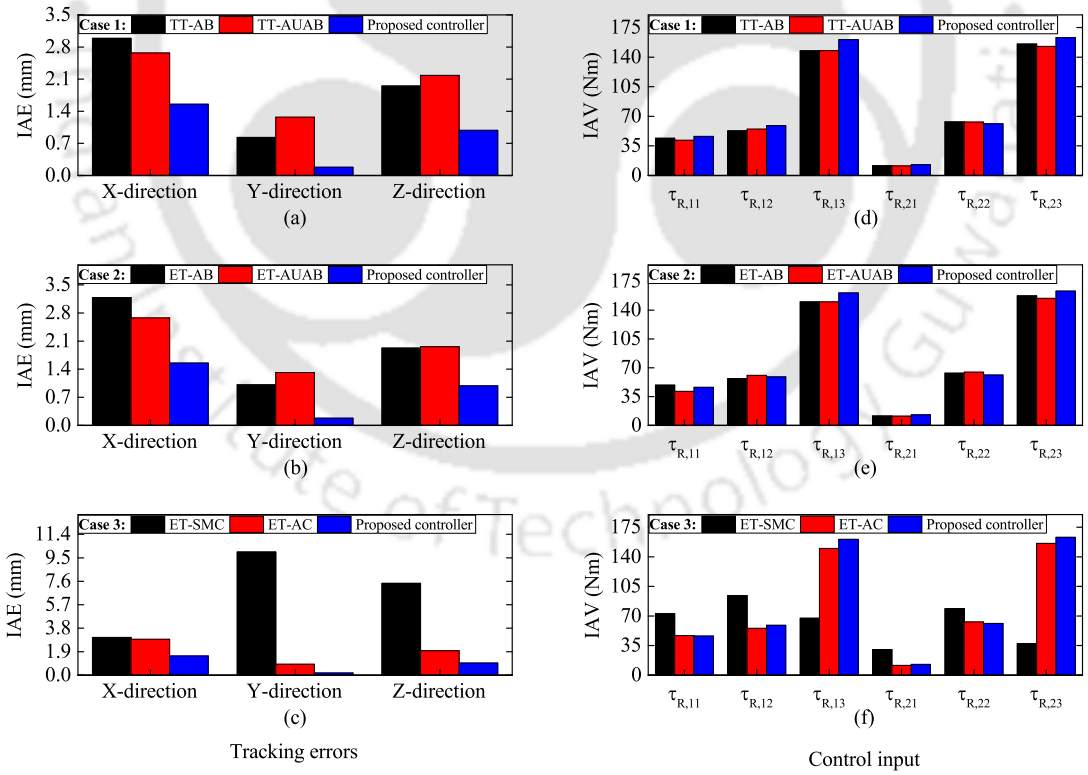

Figure 5.15: Comparison of tracking errors and control efforts for the three cases

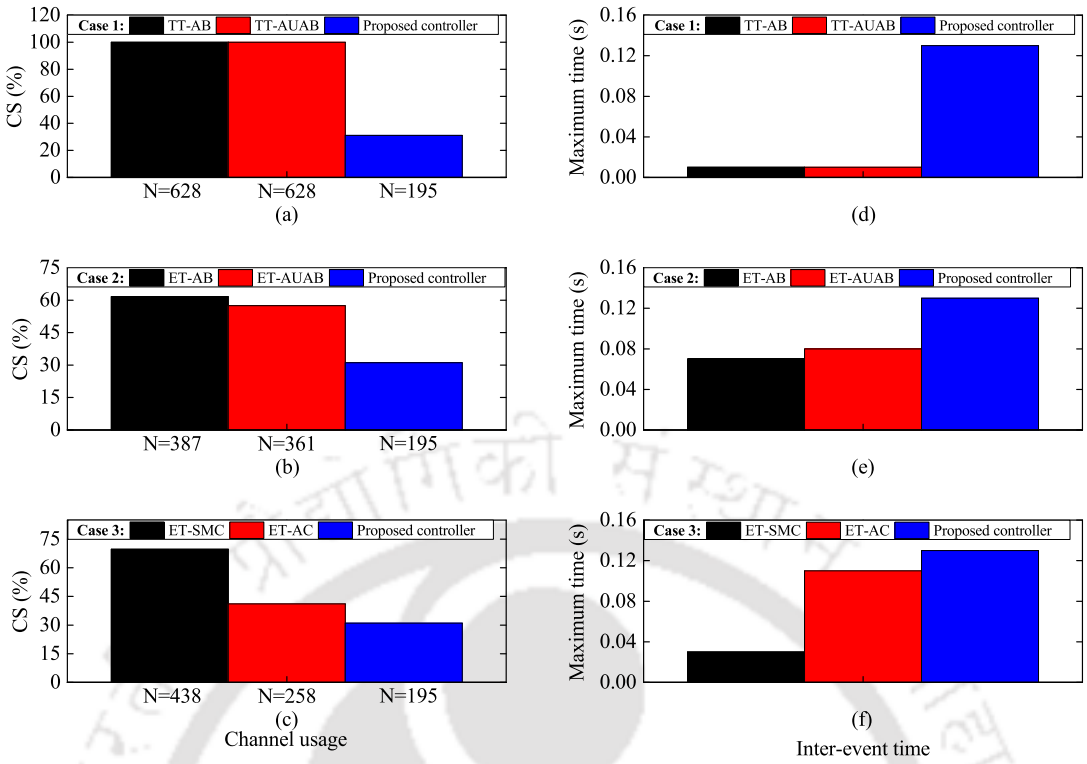

Figure 5.16: Comparison of proposed ET mechanism with different TT and ET control schemes in the three cases

5.5.3 Validation on Dual-Arm Manipulators in V-REP

To examine the validity of the proposed ET control strategy, a dual-arm robotics system is constructed to perform the cooperative transportation of a common object in the virtual robot experimentation platform (V-REP). A factory-like environment is built in the V-REP platform in which the cooperative dual-arm robotic system consists of two 5-DOFs SCORBOT-ER VPlus manipulators, as illustrated in Figure 5.17. The cooperative task is designed to transport a common object through a lemniscate trajectory. The object is immense and beyond the carrying capacity of each robotic arm (i.e., 5 kg). The proposed event-triggered control strategy is implemented in MATLAB software and transferred into the V-REP platform through an external API. The trajectory tracking results of the lemniscate trajectory using the cooperative dual-arm SCORBOT-ER VPlus manipulators are presented in Figure 5.18. As illustrated in Figure 5.18(a), the dual-arm manipulator system with the implementation of the proposed event-triggered control strategy transports the object successfully through the desired trajectory. In addition, the errors in the X-direction, Y-direction, and Z-direction are quite small, with a maximum absolute value of 1 mm, as depicted in Figure 5.18(b). It can be noticed from Figure 5.19 that the proposed event-triggered mechanism results in high inter-event time (0.21 s)

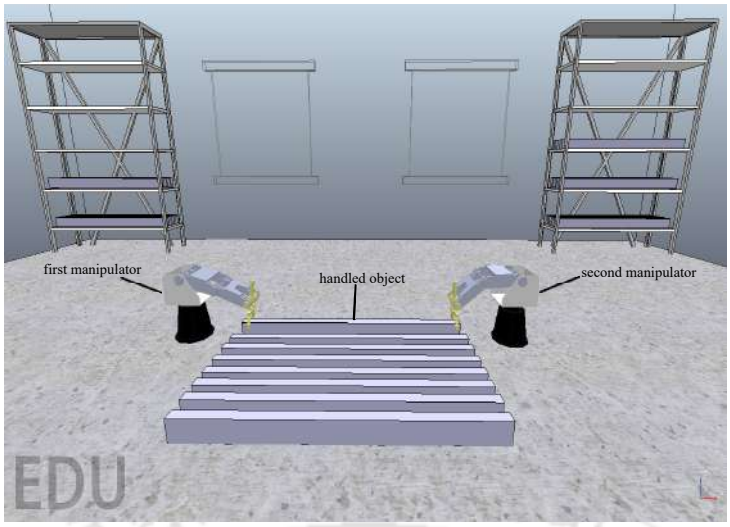

Figure 5.17: V-REP setup for cooperative manipulator system

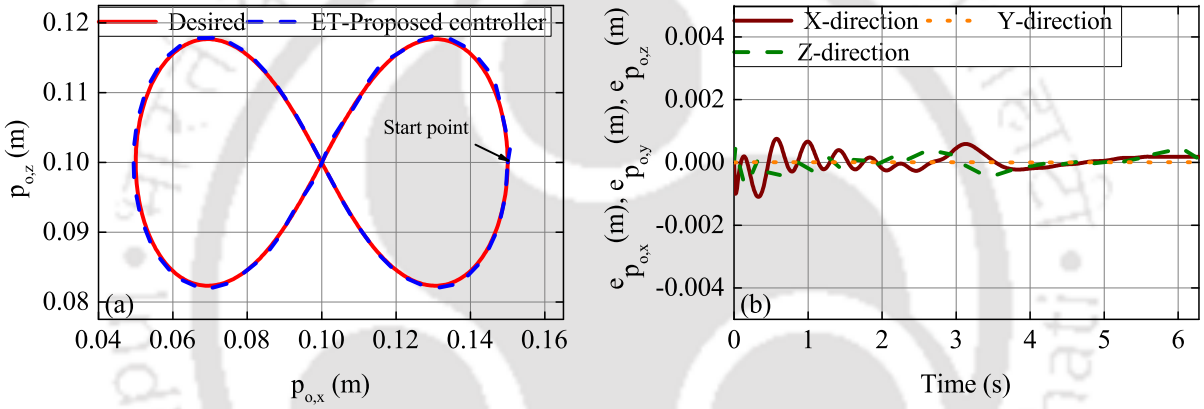

Figure 5.18: Trajectory tracking with proposed ET control scheme during V-REP validation. (a) Desired and actual trajectories on the x-z plane. (b) Tracking errors in X-direction, Y-direction, and Z-direction

with a considerable saving in the channel utilization (around 75%) as compared with the traditional time-triggered implementation. Based on the abovementioned discussion, the effectiveness of the proposed ET control scheme can be further verified for the dual-arm manipulator system during the cooperative manipulation task.

5.6 Summary

In this chapter, the coordination control problem of uncertain cooperative robotic manipulators under limited resources has been investigated. For this purpose, an improved adaptive backstepping position-force controller has been developed. This controller has been devoted to control the motion of the handled object through a predefined trajec-

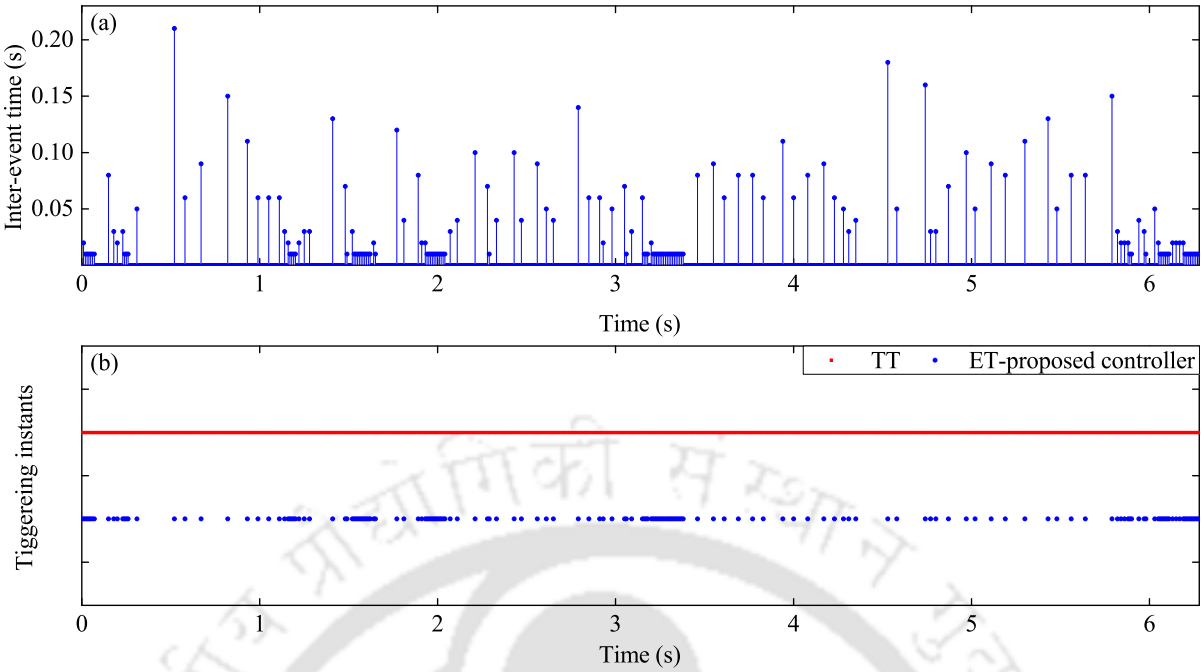

Figure 5.19: Inter-event time and triggering events for proposed ET control scheme during V-REP validation

tory while attaining constant internal forces in the presence of parametric uncertainties. Moreover, a Lyapunov-based event-triggered mechanism has been designed to reduce the network load and maintain the stability of the system. A comparative study between the designed control scheme and various control strategies and triggering conditions has been carried out in the TrueTime network simulator. Additional validation of the designed controller has been conducted using dual-arm SCORBOT-ERVPlus manipulators in the V-REP platform. Based on the simulation runs, the proposed algorithm presents promising results for position and force tracking with a significant reduction in the number of transmissions over the network during the cooperative task. However, the presented hybrid position-force controller is incompetent to appreciate the interaction of the object with the external environment during the cooperative manipulation task. Therefore, in the next chapter, the adaptive event-triggered adaptive admittance control is proposed to provide a compliant behavior for both manipulators/object and object/environment interactions.

6

Event-triggered Adaptive Admittance Control for Cooperative Manipulators

Contents

6.1 Introduction

The physical interaction between the object and environment due to unforeseen contact with the human or obstacles is of great importance when designing a networked control scheme for cooperative manipulator systems. Limiting these forces along with the internal forces in the presence of parametric uncertainties and limited communication is a challenging task and worth exploring. Therefore, this chapter aims to extend the design of the event-triggered adaptive backstepping admittance control (ETABAC) scheme presented in Chapter 3 to the framework of the cooperative manipulator. For the same, the improved adaptive backstepping position controller derived in the previous chapter is utilized to maintain an accurate motion of the manipulated object under parametric uncertainties and limited resources circumstances. The external and internal admittance control schemes are integrated to project an impedance relation and achieve compliant interaction between the object/environment and manipulators/object during the cooperative manipulation task. An event-triggered mechanism is designed based on Lyapunov analysis to alleviate the communication over the network and maintain the stability of the closed-loop system. The proposed control scheme is compared with various studies intended for the same cooperative manipulation task. Moreover, the effectiveness of the designed event-triggered mechanism is examined based on a comparative analysis with the well-known triggering conditions in the literature.

The structure of the chapter is organized as follows. The problem formulation is introduced in Section 6.2. The design of the proposed controller is elaborated in Section 6.3, followed by the simulation results in Section 6.4. Finally, the conclusion of this chapter is highlighted Section 6.5.

6.2 Problem Formulation

The manipulation task of a common rigid object through a predefined trajectory is performed using k uncertain single-arm manipulators controlled through a limited bandwidth network channel. Each manipulator comprises of a stationary base with n joints. It is assumed that the object is held rigidly, and there is no relative motion between the object and the end-effector of the manipulators. Moreover, the object/environment interaction is also considered along with manipulators/object interaction as illustrated in Figure 6.1, relaxing Assumption 2 of previous chapter. Each manipulator participating in the cooperative manipulation can be modeled in joint space similar to the equation (5.1) as follows:

$$M_{R,i}(q_i)\ddot{q}_i + C_R(q_i,\dot{q}_i)\dot{q}_i + G_R(q_i) = \tau_{R,i} - \tau_{int,i}; \quad \tau_{int,i} = J_i^T(q_i)F_{int,i} \tag{6.1}$$

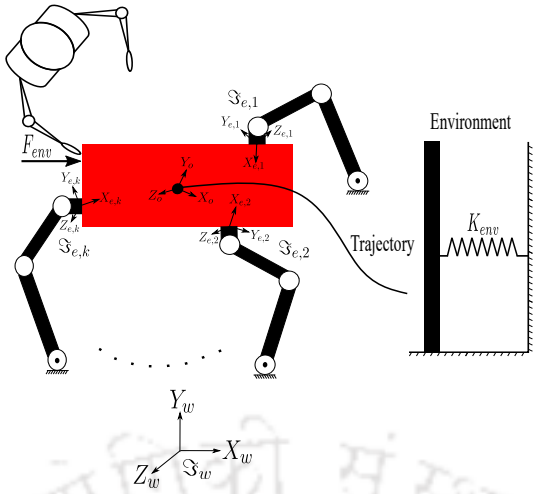

Figure 6.1: Cooperative manipulator system

The joint space dynamical model (6.1) can be reformulated in the Cartesian task space similar to equation (3.7) as follows.

$$M_{R_{x,i}}(x_{e,i})\ddot{x}_{e,i} + C_{R_{x,i}}(\dot{x}_{e,i}, x_{e,i})\dot{x}_{e,i} + G_{R_{x,i}}(x_{e,i}) = F_{R,i} - F_{int,i} \tag{6.2}$$

where $M_{R_{x,i}} = J_i^{-T} M_{R,i} J_i^{-1}$, $C_{R_{x,i}} = J_i^{-T}(C_{R,i} - M_{R,i} J_i^{-1} \dot{J}_i) J_i^{-1}$, $G_{R_{x,i}} = J_i^{-T} G_{R,i}$, and $F_{R,i} = J_i^{-T} \tau_{R,i}$.

Two admittance paradigms are adopted to maintain a compliant interaction between the environment\object and object\manipulators [132]. The external admittance is imposed to prevent large interaction forces between the object and the environment which obviate the damage of parts in contact. Moreover, the internal admittance is utilized to limit the large internal forces and avoid grasp failure.

Inspired by the operational space formulation [202], an adaptive backstepping motion controller is designed in the Cartesian space to maintain an accurate motion of the manipulated object during the tracking of the desired trajectory in the presence of dynamic uncertainties. Moreover, to eliminate the need for a hierarchical inner motion control loop and reduce the number of tunable controller design parameters.

To cope with the limited bandwidth burden and overcome the continuous update of control signals during the cooperative task, an event-triggered (ET) mechanism is placed at the controller-to-robot channel. As a consequence of ET implementation, the cooperative manipulators are actuated by the event-triggered control inputs $\bar{\tau}_{R,i}$ in lieu of the actual control signals $\tau_{R,i}$. The control laws are updated and transmitted over the network when the predefined condition $T_{con,i}$ gets violated. The triggering instants are

described as follows.

$$\begin{aligned} \bar{\tau}_{R,i}(t) &= \tau_{R,i}(t_j), \forall\ t \in [t_j, t_{j+1}) \\ t_{j+1} &= \inf\{t | t > t_j,\ T_{con,i}(e_{m,i}, z_{1,i}, z_{2,i}, z_{3,i}) > 0\} \end{aligned} \tag{6.3}$$

where $\tau_{R,i}$ and $\bar{\tau}_{R,i}$ are the actual and event-triggered control signals for the i-th manipulator, respectively. $e_{m,i} = \tau_{R,i} - \bar{\tau}_{R,i}$ represents the measurement error and $T_{con,i}$ is the triggering condition.

The objective of the control is to design an admittance-based Cartesian adaptive control scheme for the uncertain cooperative manipulators. This controller is dedicated to obtain a proper compliant interaction between the object/environment and manipulators/object and achieve a favorable tracking performance with minimum transmissions over the network during the manipulation task in the presence of uncertainties and limited resources.

6.3 Control Architecture

In this section, the design of an event-triggered admittance-based adaptive controller for a cooperative manipulator system is carried out. This controller is devoted to attain a compliant interaction between the manipulated object and the environment and limiting the mechanical stresses to small values. Simultaneously, this control scheme should guarantee the stability of the system with a superior trajectory tracking performance and minimum transmissions over the network in the presence of uncertainties and limited resources. The Block diagram of the proposed controller is depicted in Figure 6.2. The portions of the codes which are running on the host computer unit and the on-board controller are also illustrated in the same figure. The design of the admittance and motion controllers is presented in the following subsections.

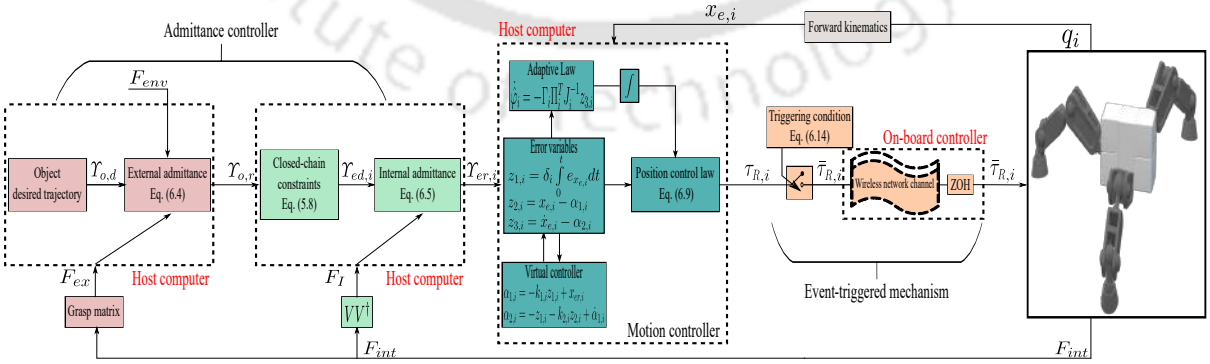

Figure 6.2: Block diagram of the proposed control scheme

6.3.1 Admittance Controller

The combined architecture of the external and internal admittance control strategy is proposed in [130]. This architecture is adopted here to realize the compliant interaction between the object/environment and manipulators/object. The external admittance is utilized to impose an impedance behavior between the pose of the manipulated object and the forces generated due to the object and environment interaction. As a result, bounded interaction forces can be guaranteed. The desired and reference motion variables of the object are defined as $\Upsilon_{o,d} = (\ddot{x}_{o,d}, \dot{x}_{o,d}, x_{o,d})$ and $\Upsilon_{o,r} = (\ddot{x}_{o,r}, \dot{x}_{o,r}, x_{o,r})$. Therefore, the description of the external admittance can be given as follows:

$$M_{ex}(\ddot{x}_{o,d} - \ddot{x}_{o,r}) + C_{ex}(\dot{x}_{o,d} - \dot{x}_{o,r}) + K_{ex}(x_{o,d} - x_{o,r}) = F_{env} \tag{6.4}$$

where $x_{o,d}$, $x_{o,r}$ are the desired and reference position and orientation of the object, respectively. M_{ex}, C_{ex}, and K_{ex} are the symmetric and positive definite matrices for external admittance. The output of the external admittance is the reference trajectory of the object, which can be calculated by substituting F_{env} from equation (5.3) and integrating equation (6.4). Thereafter, this reference trajectory is mapped to their counterpart at the grasp locations to form the end-effector desired trajectory for each manipulator using the closed-chain constraints presented in equation (5.8).

The internal admittance is intended to achieve limited internal forces and avoid developing high mechanical stresses at the object level. Therefore, an impedance behavior is established between the end-effector of each manipulator and the corresponding internal forces. The internal admittance can be represented by the following equation:

$$M_{in,i}(\ddot{x}_{ed,i} - \ddot{x}_{er,i}) + C_{in,i}(\dot{x}_{ed,i} - \dot{x}_{er,i}) + K_{in,i}(x_{ed,i} - x_{er,i}) = F_{I,i} \tag{6.5}$$

where $x_{ed,i}$, $x_{er,i}$ are the desired and reference position and orientation for the end-effector of i-th manipulator, respectively. $M_{in,i}, C_{in,i}$, and $K_{in,i}$ are the symmetric and positive definite matrices for internal impedance, and $F_{I,i}$ is the internal forces of the i-th manipulator. The inputs of the internal admittance equation are the actual internal forces and the end-effector desired trajectories obtained using the closed-chain constraints (5.8). The integration of the internal admittance equation results in the generation of the i-th end-effector reference trajectory i.e., $\Upsilon_{er,i} = (\ddot{x}_{er,i}, \dot{x}_{er,i}, x_{er,i})$ to be followed using an accurate motion controller. This motion controller is to be designed in the following subsection.

6.3.2 Motion Controller

The design of a Cartesian adaptive backstepping motion controller is carried out in this section. This control strategy is necessary to accurately track the end-effector reference trajectories and maintain an acceptable impedance behavior in the presence of dynamic uncertainties. Moreover, a Lyapunov-based triggering condition is derived in the last step of the controller design process to reduce the communication burden and maintain the stability of the cooperative manipulator system.

The three-steps of adaptive backstepping controller are derived to guarantee that the actual operational space positions $x_{e,i}$ follow the reference trajectories $x_{er,i}$ in the presence of uncertainties and limited communication. The dynamic model of the i-th manipulator (6.2) can be rewritten by introducing the state vector $X_i = (x_{1,i}, x_{2,i})^T = (x_{e,i}, \dot{x}_{e,i})^T$ as follows.

$$\begin{aligned} \dot{x}_{1,i} &= x_{2,i} \\ \dot{x}_{2,i} &= M_{R_{x,i}}^{-1}(x_{e,i})(\bar{F}_{R,i} - C_{R_{x,i}}(\dot{x}_{e,i}, x_{e,i})\dot{x}_{e,i} - G_{R_{x,i}}(x_{e,i}) - F_{int,i}) \end{aligned} \tag{6.6}$$

The error variables for the i-th robotic manipulator participating in the cooperative task are determined similar to equation (5.18) but at the end-effector level as follows.

$$z_{1,i} = \delta_i \int_0^t e_{x_{e,i}} dt = \delta_i \int_0^t (x_{e,i} - x_{er,i}) dt \ , \quad z_{2,i} = x_{e,i} - \alpha_{1,i} \ , \quad z_{3,i} = \dot{x}_{e,i} - \alpha_{2,i} \tag{6.7}$$

where $\alpha_{j,i}$ denotes the j virtual controller of the i-th manipulator determined in the succeeding steps to guarantee the convergence of the first and second error variables $z_{1,i}, z_{2,i}$ to a small values around zero.

Following the step by step design process of the motion controller presented in Subsection 5.4.1, the virtual controllers, control and adaptation laws can be designed as

$$\begin{aligned} \alpha_{1,i} &= -k_{1,i} z_{1,i} + x_{er,i} \\ \alpha_{2,i} &= -z_{1,i} - k_{2,i} z_{2,i} + \dot{\alpha}_{1,i} \end{aligned} \tag{6.8}$$

$$\tau_{R,i} = \Pi_i \hat{\varphi}_i + J_i^T(q_i)\big(- z_{2,i} - (\vartheta_i \|\Pi_i\|^2 + k_{3,i}) z_{3,i} + F_{int,i}\big) \tag{6.9}$$

$$\dot{\hat{\varphi}}_i = -\Gamma_i \Pi_i^T J_i^{-1} z_{3,i} \tag{6.10}$$

Therefore, the derivative of Lyapunov candidate becomes

$$\dot{V}_i = -z_{1,i}^T k_{1,i} z_{1,i} - z_{2,i}^T k_{2,i} z_{2,i} - z_{3,i}^T k_{3,i} z_{3,i} - z_{3,i}^T \vartheta_i \|\Pi_i\|^2 z_{3,i} - z_{3,i}^T J_i^{-T} e_{m,i} \tag{6.11}$$

6.3.3 Event-triggered Mechanism

The triggering condition is designed in the following based on the measurement error $e_{m,i}$ that appears in the last term of the previous equation (6.11). This condition determines the transmission instants of a new control signal over the network to ensure the stability of the system and maintain the negative semi-definiteness of the Lyapunov function derivative. By exploiting Young's inequality in equation (6.11).

$$\begin{aligned}\dot{V}_i &\leq -z_{1,i}^T k_{1,i} z_{1,i} - z_{2,i}^T k_{2,i} z_{2,i} - z_{3,i}^T k_{3,i} z_{3,i} - z_{3,i}^T \vartheta_i \|\Pi_i\|^2 z_{3,i} + \|z_{3,i}^T J_i^{-T}\| \|e_{m,i}\| \\ &\leq -(1-\zeta_i)\big(z_{1,i}^T k_{1,i} z_{1,i} + z_{2,i}^T k_{2,i} z_{2,i} + z_{3,i}^T (k_{3,i} + \vartheta_i \|\Pi_i\|^2) z_{3,i}\big) \\ &- \zeta_i \big(z_{1,i}^T k_{1,i} z_{1,i} + z_{2,i}^T k_{2,i} z_{2,i} + z_{3,i}^T (k_{3,i} + \vartheta_i \|\Pi_i\|^2) z_{3,i}\big) + \frac{\|z_{3,i}^T J_i^{-T}\|^2}{2} + \frac{\|e_{m,i}\|^2}{2}\end{aligned} \tag{6.12}$$

In the previous equation (6.12), if $0 < \zeta_i < 1$ and the following inequality remains true

$$\frac{\|z_{3,i}^T J_i^{-T}\|^2}{2} + \frac{\|e_{m,i}\|^2}{2} \leq \zeta_i \big(z_{1,i}^T k_{1,i} z_{1,i} + z_{2,i}^T k_{2,i} z_{2,i} + z_{3,i}^T (k_{3,i} + \vartheta_i \|\Pi_i\|^2) z_{3,i}\big) \tag{6.13}$$

then, the negative semi-definiteness of Lyapunov function derivative is guaranteed, and the triggering function in equation (6.3) can be defined as follows:

$$T_{con,i} = \|e_{m,i}\|^2 + \|z_{3,i}^T J_i^{-T}\|^2 - 2\zeta_i \big(z_{1,i}^T k_{1,i} z_{1,i} + z_{2,i}^T k_{2,i} z_{2,i} + z_{3,i}^T (k_{3,i} + \vartheta_i \|\Pi_i\|^2) z_{3,i}\big) \tag{6.14}$$

It should be emphasized that the control input signal is updated and transmitted over the network in case this triggering function is greater than zero. Other than that, the i-th robotic manipulator is driven by the last received control signal. This maintains the negative semi-definiteness of the Lyapunov function derivative and causes a significant reduction in the number of transmissions over the network.

Proposition 4. *The multiple manipulator system actuated by the designed controller (6.9) with the adaptation law (6.10), the external (6.4) and internal (6.5) admittance schemes, and under the proposed event-triggered mechanism (6.14) is stable in the sense of Lyapunov and all the closed-loop signals are guaranteed to be bounded. The proper choice of the controller parameters provides a compliant behavior during the cooperative manipulation task and ensures the convergence of tracking errors to a small neighborhood near zero. Moreover, the Zeno behavior is avoided under the designed event-triggered control strategy.*

Proof. The derivative of Lyapunov function of i-th manipulator can be written as follows

$$\dot{V}_i \leq -\Theta_i V_i + \Omega_i \tag{6.15}$$

where $\Theta_i = \min\left\{2\delta_i \lambda_{min}(k_{1,i}), 2\lambda_{min}(k_{2,i}), \frac{2\lambda_{min}(k_{3,i}+\vartheta_i\|\Pi_i\|^2) - \frac{\|J_i^{-T}\|^2}{\zeta_i}}{\lambda_{max}(M_{R_{x,i}})}\right\}$, and $\Omega_i = \frac{\zeta_i \|e_{m,i}\|^2}{2}$. Therefore, similar to the analysis in Proposition 1, the convergence of i-th manipulator

tracking errors to the following sets can be ensured:

$$\|z_{1,i}\| \leq \sqrt{2\delta_i \bar{V}_i}\ , \quad \|z_{2,i}\| \leq \sqrt{2\bar{V}_i}, \quad \|z_{3,i}\| \leq \sqrt{\frac{2\bar{V}_i}{\lambda_{max}(M_{R_{x,i}})}} \tag{6.16}$$

where $\bar{V}_i = \max\left\{V_i(0),\ \frac{\Omega_i}{\Theta_i}\right\}$. This emphasizes that all the closed-loop signals are ultimately bounded and the stability of the cooperative manipulator system can be ensured under the proposed event-triggered control scheme. Furthermore, the proof of Zeno exclusion presented in Proposition 1 is still valid and can be directly applied in this scenario. □

Remark 5. *The selection of the design parameters for the motion and admittance controllers is crucial to achieve an acceptable tracking performance and maintain the cooperative manipulator system stability. Therefore, the following criteria are given to be followed in the tuning process of the controller parameters:*

(i) Selection of motion controller parameters: The equation (6.16) shows that by increasing Θ_i and decreasing Ω_i, the error signals $\|z_{1,i}\|$, $\|z_{2,i}\|$, and $\|z_{3,i}\|$ can be ensured to converge to small values. As a result, increasing the motion controller gains $k_{1,i}$, $k_{2,i}$, and $k_{3,i}$ improves the tracking performance and reduces the positional errors during the desired task. On the other hand, the increase in the adaptation gains Γ_i guarantees a faster convergence of the estimated parameters to their actual values. However, these parameters cannot be selected too large in practical scenarios to avoid high-frequency noises. Thus, maintaining the acceptable performance of the system.

(ii) A lower number in the transmissions over the network can be obtained by increasing the user-defined parameter ζ_i of the event-triggered mechanism. However, the trade-off between tracking performance and network utilization should be attained since the excess increase in ζ_i may degrade the performance of the cooperative manipulator system.

(iii) Selection of admittance controller parameters: These parameters can be intuitively selected based on their physical indications. Therefore, the selection of large values of the desired stiffness $K_{ex,i}$, $K_{in,i}$ gains for internal and external admittance leads to the development of higher interaction and internal forces. On the other hand, the proper choice of the desired damping C_{ex} and $C_{in,i}$ can ensure a smooth transient behavior without high overshooting and oscillatory response. The inertia matrix M_{ex} of external admittance should be chosen proportional to the inertia matrix of the object M_o (i.e., $M_{ex} = PM_o$: P is a diagonal matrix with eigenvalues ≥ 1). This assumption is imposed due to the unavailability of accurate measurement of object acceleration [130].

6.4 Simulation Results

In this section, a series of simulation runs are conducted to illustrate the feasibility of the proposed admittance-based adaptive controller in the cooperative manipulation task. The simulation setup consists of a dual-arm manipulator system ($1 \leq i \leq k = 2$) handling a common object. Each manipulator has three revolute joint ($n_i = 3$) with stationary base as shown in Figure 5.3. The description of the dynamical matrices $M_{R,i}(q_i), C_{R,i}(\dot{q}_i, q_i)$, and $G_{R,i}(q_i)$ can be found in in Appendix A.1. The physical parameters of the manipulators are similar to SCORBOT-ER VPlus manipulator, with no motion at the fourth and fifth joints, as given in Appendix A.1. The object is rectangular shape with a mass of $m_o = 5$ kg, moment of inertia $I_o = 0.1$ kgm^2, and the following dimensions: 1.5 m $\times$ 0.05 m $\times$ 0.1 m for the length, width, and height, respectively. The inertial frame is located be between the dual-arm manipulators with a distance of $l_{x,1} = 1$ m and $l_{x,2} = 1.2$ m from the first and second manipulator, respectively, as illustrated in Figure 5.3. The following two cases are considered to evaluate the proposed controller performance:

Case 1. In this case, the designed controller is compared with two time-triggered admittance-based control strategies i.e., proportional-integral-derivative (TT-PID) [130] and the gravity compensation controller (TT-GCC) [137].

Case 2. In this case, the designed triggering condition is compared with the well-known triggering rules presented in the literature, i.e., (relative [147] and fixed [151, 186] thresholds).

In both cases, the task is to move the object cooperatively through two different trajectories (i.e., circular and lemniscate) in the x-z plane while maintaining small internal forces during the cooperative task. Moreover, compliant behavior has to be achieved in the presence of object-applied external environmental forces with a minimum number of transmissions over the network. Therefore, two different external environmental forces are considered during the cooperative manipulation tasks to validate the effectiveness of the proposed controller. Firstly, a static environmental force F_{env} is applied at the object's center of the mass in the X-direction. This force mimics the static pushing/pulling forces in real-time scenarios. Secondly, other environmental forces are produced due to the interaction between the object and the external environment (i.e., wall). This wall is assumed to be on the trajectory of the manipulated object. Thus, the object should slide along this wall without developing high interaction forces. The simulation runs for both trajectories are carried out in MATLAB environment for a total period of 12.56 s (2 cycles) with 4 ms as the sampling time. The initial configuration for the object position is chosen as $x_o(0) = [0.15 \text{ m}, 0 \text{ m}, 0.1 \text{ m}]^T$ with velocity equals to zero. The stiffness

of the external environment (i.e., wall) is assumed to be $K_{env} = 10000\ \frac{\text{N}}{\text{m}}$. The initial values of unknown parameters for each manipulator are chosen to be zero. The results and discussions for the two trajectories are given in the following subsections.

6.4.1 Tracking of Circular Trajectory

The dual-arm manipulators are assumed to handle the object in a circular trajectory with the presence of object-applied external environmental forces. The desired motion of the object should be achieved with compliant behavior and minimum internal forces to avoid the damage of the manipulators and the object. The desired circular trajectory of the object is defined as: $x_{o,d}(t) = [0.1\cos(\omega_d t) + 0.15, 0, 0.1\sin(\omega_d t) + 0.15]^T$, $\omega_d = 1\ \frac{\text{rad}}{\text{s}}$. The static external force applied at the object is equal to $F_{env} = 20$ N. This force occurs at the time $t = 5$ s and holds for 1 s. Moreover, the wall is presented at the location $x = 0.1$ m.

In Case 1, a comparative analysis with two different time-triggered admittance-based control strategies is conducted to demonstrate the performance of the proposed control scheme. The time-triggered controllers are the proportional-integral-derivative (TT-PID) [130] and the gravity compensation control scheme (GCC) [137]. These controllers are devoted to follow the admittance-generated trajectory during the cooperative manipulation task and described in Appendix A.5. The design parameters for the proposed controller are selected to achieve the lowest tracking errors in tandem with acceptable compliant behavior and the least number of transmissions over the network as follows: (for external admittance: $P = \text{diag}(1.5, 1.5, 1.5)$, $C_{ex} = \text{diag}(150, 150, 150)$, $K_{ex} = \text{diag}(500, 500, 500)$, for internal admittance ($i = 1, 2$): $M_{in,i} = \text{diag}(0.001, 0.001, 0.001)$, $C_{in,i} = \text{diag}(2, 2, 2)$, $K_{in,i} = \text{diag}(1500, 1500, 1500)$, for motion controller: $\delta_i = 20$, $\vartheta_i = 41 I_3$, $k_{1,i} = \text{diag}(1, 1, 1)$, $k_{2,i} = \text{diag}(100, 100, 100)$, $k_{3,i} = \text{diag}(45, 45, 45)$, $\Gamma_i = \text{diag}(0.01, 0.01, 0.01)$, $\zeta_i = 0.9$). For fair comparison and to maintain a consistent compliant behavior, the parameters of the external and internal admittance for TT-PID and TT-GCC are chosen similar to the proposed controller. However, the parameters of the motion controller are adopted to achieve an acceptable trajectory tracking with small tracking errors as presented in Appendix A.5.

The manipulation of the object along the desired circular trajectory for TT-PID, TT-GCC, and the proposed ET controller is depicted in Figure 6.3. The time-dependent trajectory tracking in X-, Y-, and Z-directions with the tracking errors are presented in Figure 6.4. The interaction and internal forces are brought in Figure 6.5. It is noticed from Figure 6.3 and Figure 6.4 that better trajectory tracking with smaller errors than TT-PID are achieved in the case of TT-GCC and the proposed ET control scheme. However, the proposed controller can accurately follow the desired trajectory with faster

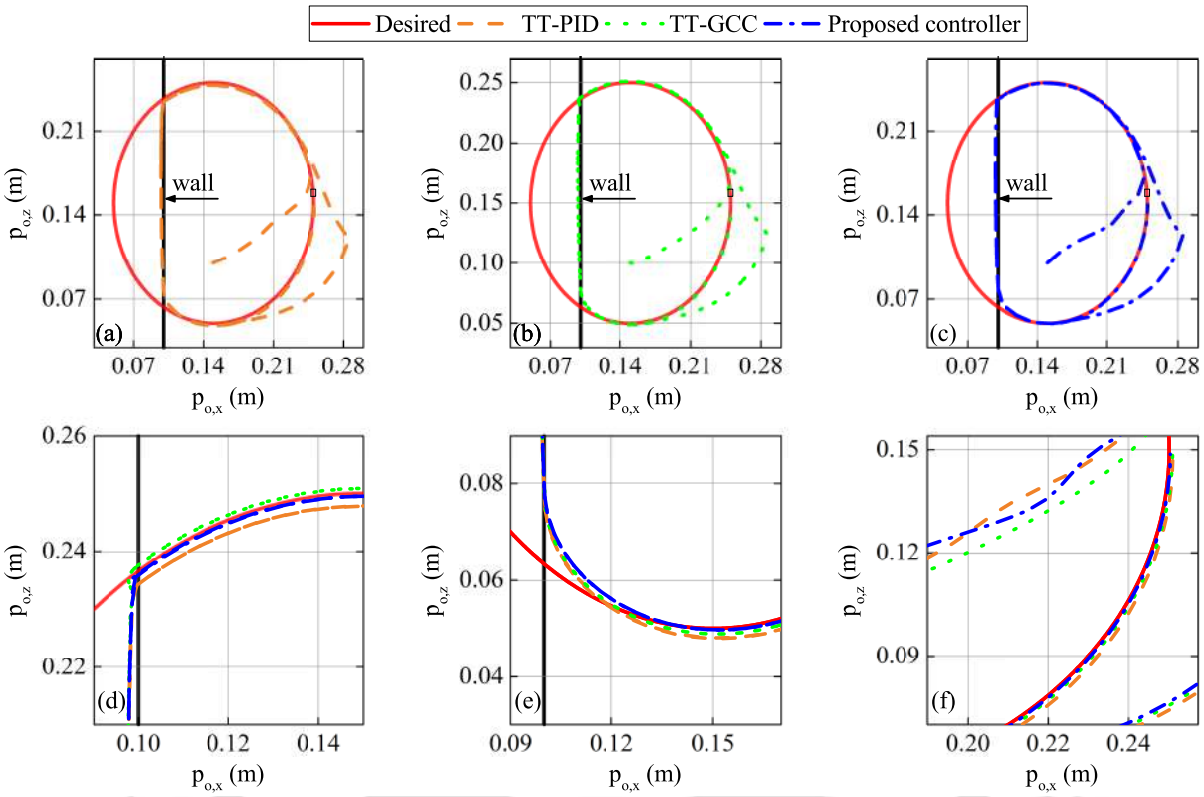

Figure 6.3: Object circular trajectory tracking in x-z plane for Case 1. (a) TT-PID, (b) TT-GCC, (c) proposed controller. Enlarged view at (d) beginning of contact (e) end of contact (f) end of trajectory.

convergence and smaller positional errors in the non-contact stage. On the other hand, the object exhibits a compliant behavior when the static external force is applied at the object, as shown in Figure 6.4 (a). The vertical yellow line in Figure 6.4 (a) corresponds to the time instant of applying the external force. Moreover, during the interaction with the external environment, the object slides along the wall without further movement towards the wall. This compliant behavior avoids the development of large external forces during the interaction with the environment, as shown in Figure 6.5 (a). Similar behavior for TT-PID, TT-GCC, and the proposed controller is maintained in the presence of static external forces and during interaction with the environment. However, the proposed controller exhibits a smoother interaction without sudden hikes in the external forces compared with TT-PID and TT-GCC, as illustrated in Figure 6.5 (a). It can be observed from Figure 6.5 (b) that the internal forces are limited to a small value for the three different controllers. However, the internal forces developed at the object are the least for the proposed controller even with the same internal admittance design parameters. The control signals for the first and second manipulators using TT-PID, TT-GCC, and proposed controller are depicted in Figure 6.6. At the initial stage of the simulation runs, these signals score high values due to the large initial errors. However, the three

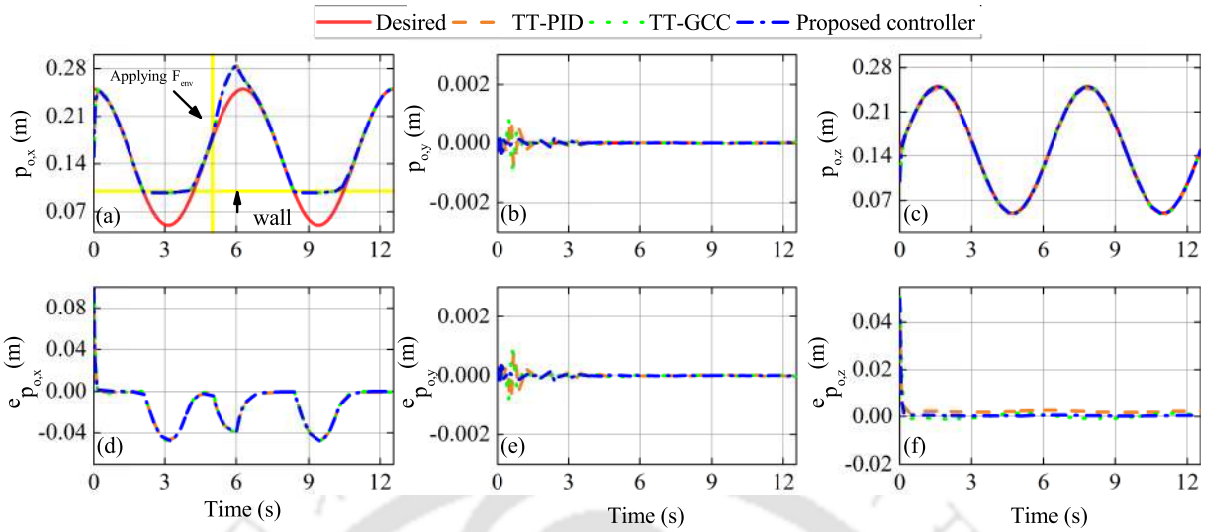

Figure 6.4: Position tracking for Case 1 in circular trajectory. Desired and actual trajectories in (a) X-direction, (b) Y-direction, (c) Z-direction. Position tracking errors in (d) X-direction, (e) Y-direction, (f) Z-direction.

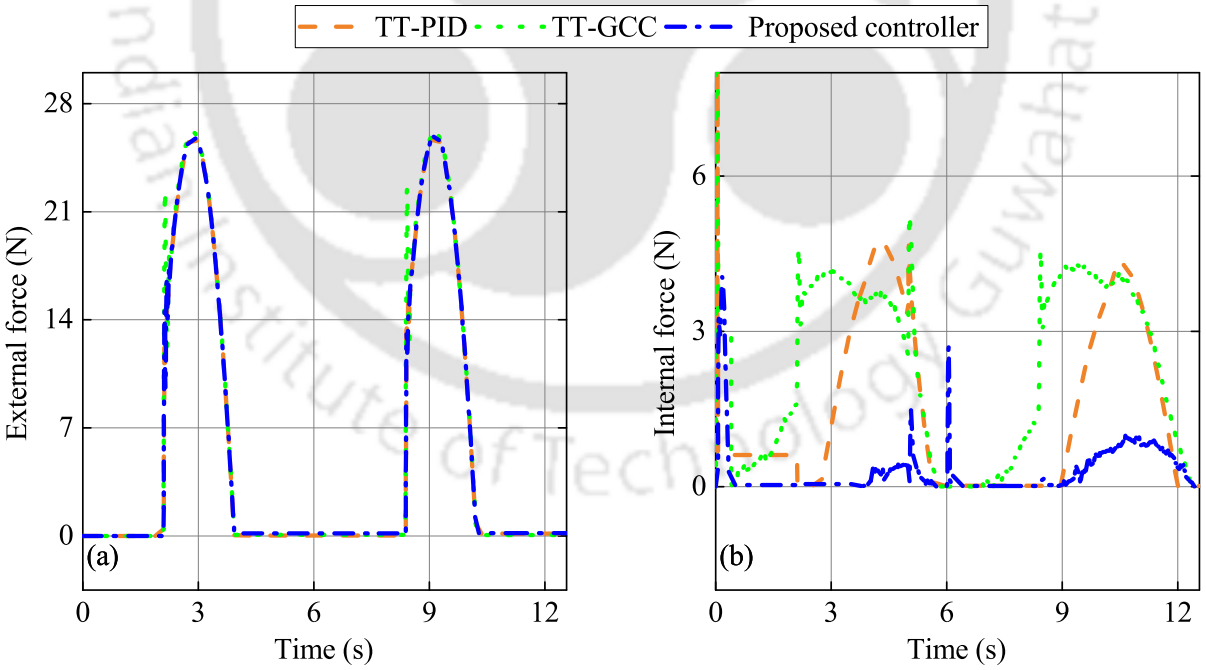

Figure 6.5: Forces exerted on object for Case 1 in circular trajectory tracking. (a) interaction force, (b) internal force.

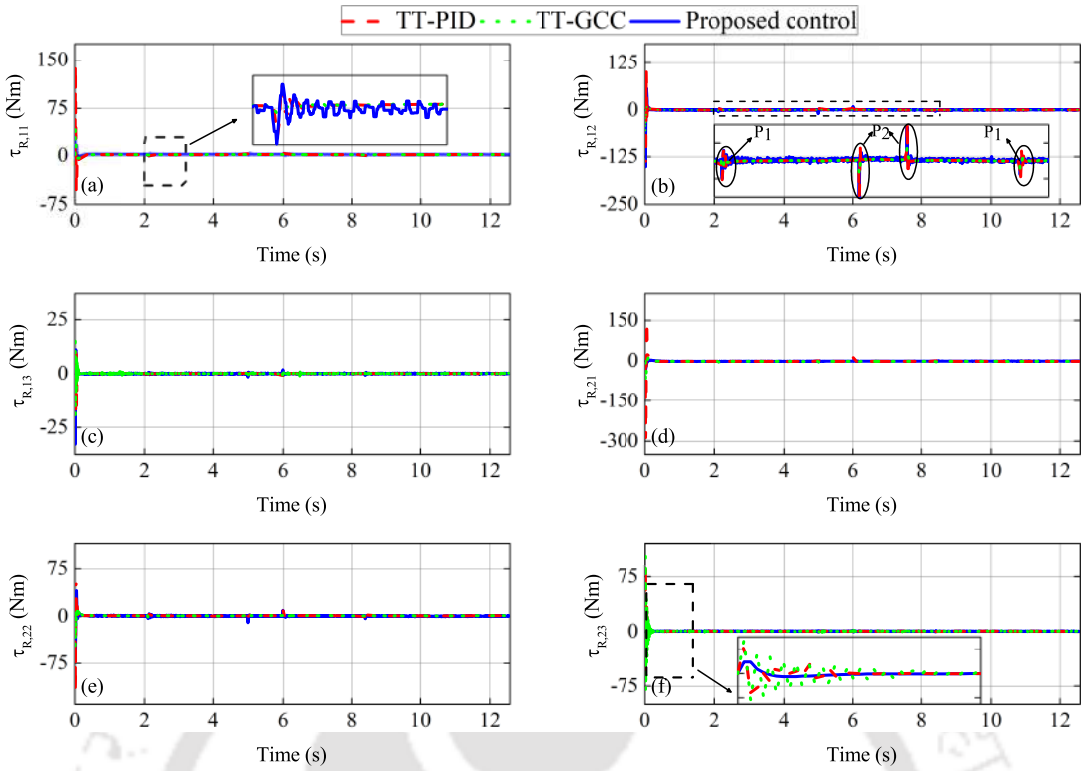

Figure 6.6: Control inputs for Case 1 in circular trajectory tracking. For first manipulator at: (a) first joint, (b) second joint, and (c) third joint. For second manipulator at: (d) first joint, (e) second joint, and (f) third joint

controllers converge to the steady-state with a smooth behavior during the cooperative manipulation task. The sudden peaks of the control signals, labeled by P_1 and P_2, in the zoomed view of Figure 6.6 (b) come from the interaction between the object and the wall and the applied static force at the object level, respectively. Specifically, it is generated in response of the admittance relation in equation (6.4) to move the object towards the deviated trajectory $x_{o,r}$. On the other hand, the control signals are transmitted over the network at every sampling time regardless of the cooperative manipulator system requirements for the traditional time-triggered PID and GCC. Consequently, there is no saving in the network resources, and the total number of transmissions over the network is equal to $N = \frac{t}{dt} = \frac{12.56}{0.004} = 3140$. However, with the designed triggering condition, the control signals are updated and transmitted over the network in an aperiodic manner, as shown in the enlarged views of Figure 6.6. This leads to efficient resources utilization and a significant reduction in the transmissions over the network, as shown in Figure 6.7. The channel usage (CS) and inter-event time for the first and second manipulators are presented in Figure 6.8. From this figure, about 87% savings in the first and second manipulator resources are obtained using the proposed ET control scheme.

The integral absolute error (IAE) and root-mean-square error (RMSE) are calculated

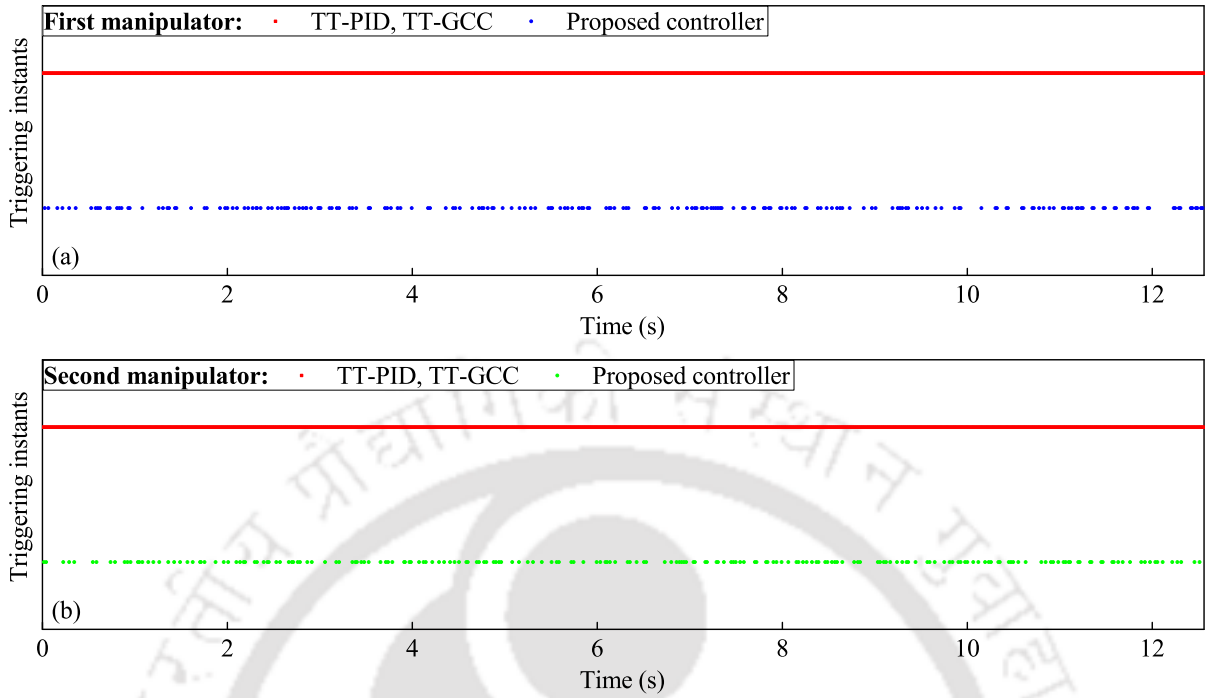

Figure 6.7: Triggering instants for TT-PID, TT-GCC, and proposed ET mechanism in Case 1 of circular trajectory tracking at: (a) first manipulator, (b) second manipulator

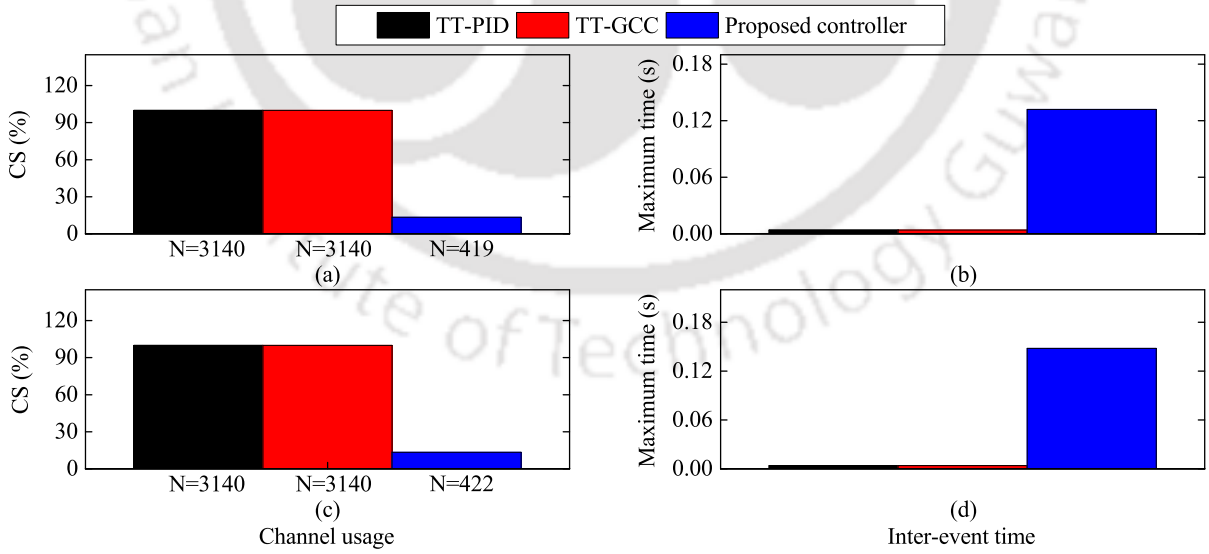

Figure 6.8: Comparison of proposed ET mechanism with different TT control schemes for Case 1 in circular trajectory tracking. Top: First manipulator. Bottom: Second manipulator.

Table 6.1: Comparison of tracking errors for the two cases in circular trajectory.

Cases	Controller	Tracking Errors					
		X-direction (mm)		Z-direction (mm)		Y-direction (mm)	
		RMSE	IAE	RMSE	IAE	RMSE	IAE
Case 1	TT-PID	22.71	186.21	3.39	28.52	0.1257	0.3316
	TT-GCC	22.94	185.89	3.69	13.97	0.1047	0.2967
	Proposed controller	22.63	183.96	2.57	7.16	0.0524	0.1745
Case 2	Relative threshold	22.63	183.6	2.52	6.95	0.0506	0.1745
	Fixed threshold	22.8	196.3	2.63	9.44	0.0541	0.2094
	Proposed controller	22.63	183.97	2.57	7.16	0.0524	0.1745

and summarized in Table 6.1. These metrics are utilized to quantitatively emphasize the performance of the proposed controller during the cooperative task. It is evident from Table 6.1 that the proposed controller scores the minimum IAE and RMSE compared with TT-PID and TT-GCC. Therefore, the proposed controller presents a superior tracking performance with minimal positional errors and substantial resource savings than TT-PID and TT-GCC.

In Case 2, an additional comparison study is carried out with two different triggering rules to verify the effectiveness of the proposed ET controller. The designed triggering condition is compared with the relative [147] and fixed [151, 186] thresholds during the execution of the same manipulation task. The number of control updates, the root-mean-square error, and the integral absolute error are the chosen criteria to evaluate the presented triggering conditions. In Figure 6.9 and Figure 6.10, the control signals and the triggering instants for relative threshold, fixed threshold, and designed ET controller are illustrated, respectively. Moreover, the channel usage and the inter-event time are depicted in Figure 6.11. The integral absolute and the root-mean-square values of the tracking errors are summarized in Table 6.1. Figure 6.9 shows that the control inputs are accompanied by continuous chattering in the case of the fixed threshold. This chattering is inappropriate and may lead to degraded system performance during the manipulation task. It can be observed from Figure 6.10 that the fixed threshold and designed triggering condition result in a less number of transmitted control signals over the network compared with relative thresholds. From Figure 6.11, the channel usage is equal to 62% and 32% for the relative and fixed thresholds, respectively. This usage is dramatically dropped down to 13.3% for the proposed triggering condition. According to Table 6.1, the significant saving in the resources is accompanied with acceptable tracking performance and non-considerable change in the tracking errors compared to the relative and fixed thresholds.

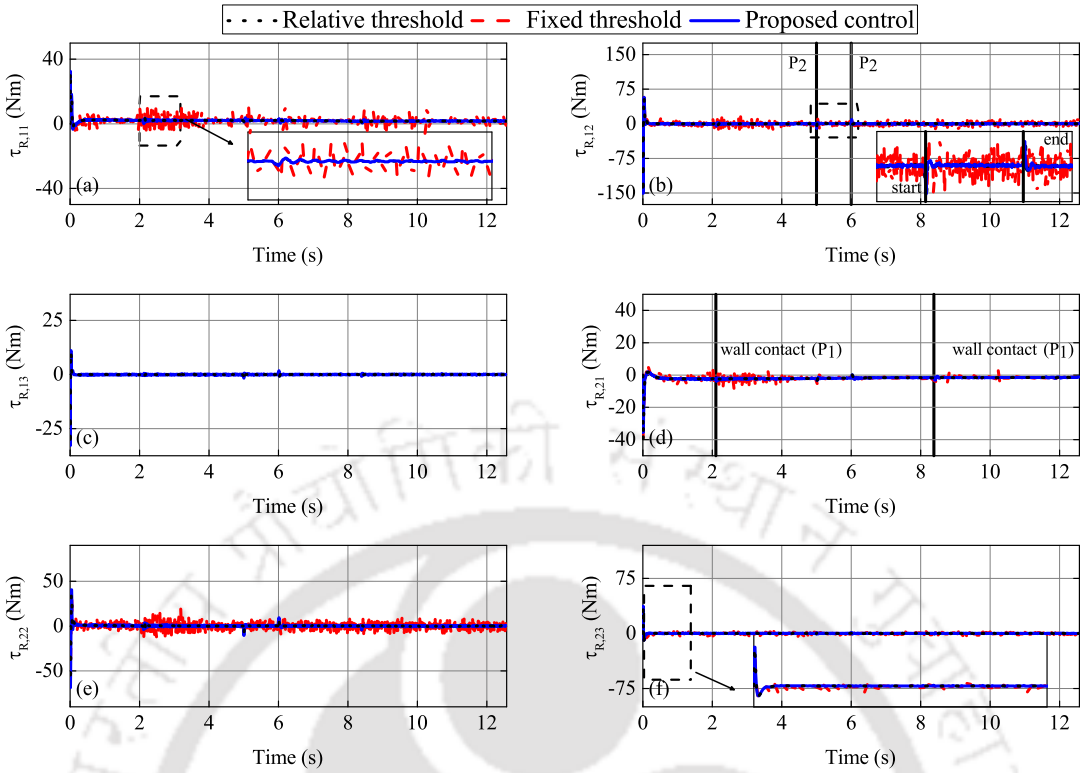

Figure 6.9: Control inputs for Case 2 in circular trajectory tracking. For first manipulator at: (a) first joint, (b) second joint, and (c) third joint. For second manipulator at: (d) first joint, (e) second joint, and (f) third joint

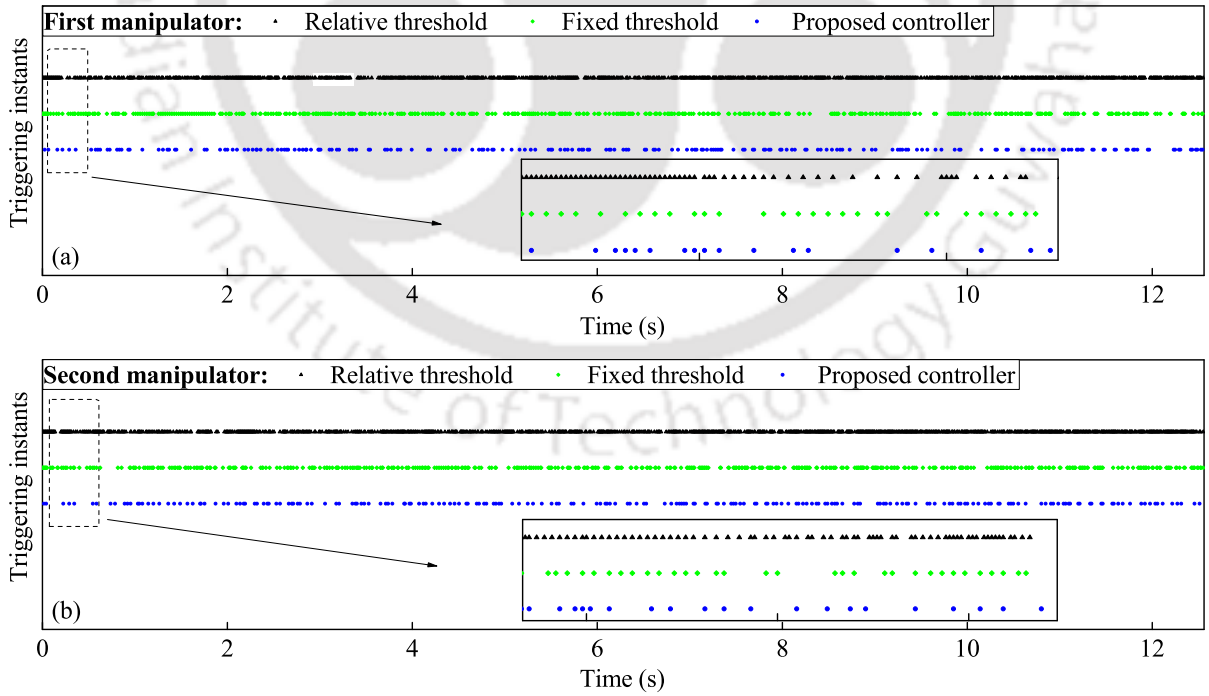

Figure 6.10: Triggering instants for proposed ET mechanism and different triggering conditions in Case 2 of circular trajectory tracking at: (a) first manipulator, (b) second manipulator.

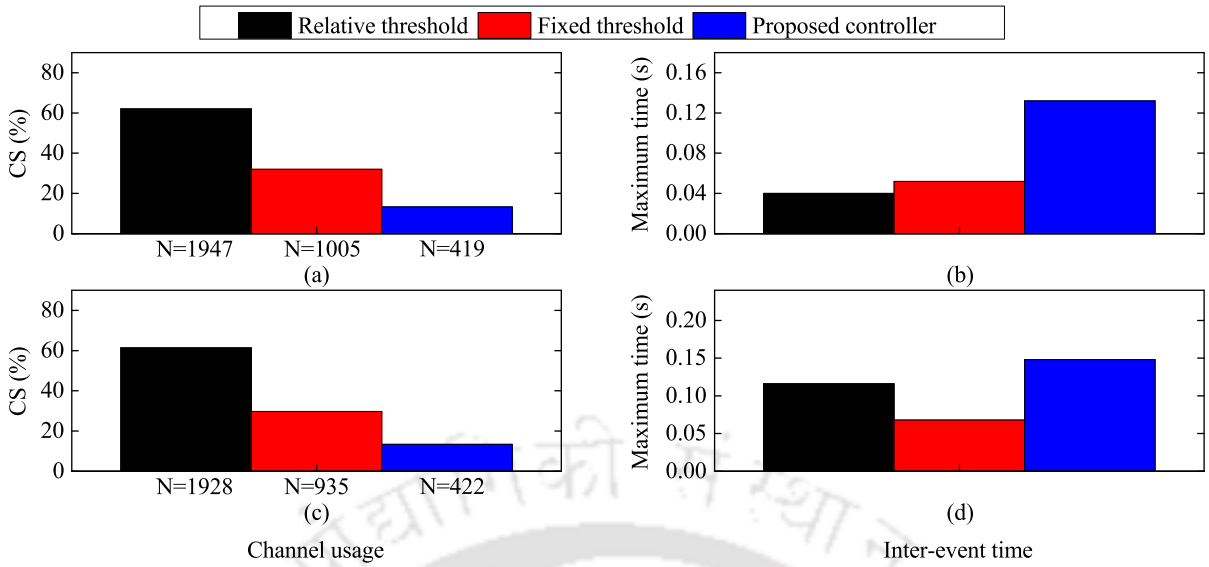

Figure 6.11: Comparison of proposed ET mechanism with different triggering conditions for Case 2 in circular trajectory tracking. Top: First manipulator. Bottom: Second manipulator.

6.4.2 Tracking of Lemniscate Trajectory

Here, an additional lemniscate trajectory is utilized to evaluate the performance of the proposed controller. The desired lemniscate trajectory is defined as: $x_{o,d}(t) = [0.1 + \frac{0.05\sin(\omega_d t)}{1+\sin^2(\omega_d t)}, 0, 0.1 + \frac{0.05\sin(\omega_d t)\cos(\omega_d t)}{1+\sin^2(\omega_d t)}]^T$, $\omega_d = 1\ \frac{\text{rad}}{\text{s}}$. The object is assumed to follow the desired trajectory with a compliant behavior during the environmental interaction. The static external force applied at the object is equal to $F_{env} = 10$ N. This force occurs at the time $t = 1$ s and lasts for 1 s. Moreover, the wall is existed at the location $x = 0.07$ m. The two cases of comparison studies, defined in the previous subsection, are conducted to emphasize the promising performance of the designed controller over the different time-triggered and event-triggered control schemes. The parameters of the controllers are considered similar to the adopted for the circular trajectory.

The simulation results for Case 1 of the comparison study are presented in Figures 6.12-6.17. The tracking of lemniscate trajectory in x-z plane for TT-PID, TT-GCC, and proposed ET controller is illustrated in Figure 6.12. The time history of position tracking in X-, Y-, and Z-directions are reported in Figure 6.13 along with the tracking errors. Figure 6.14 depicts the environmental interaction force and the internal force for TT-PID, TT-GCC, and proposed ET controller. The control inputs are presented in Figure 6.15. The triggering instants, channel usage, and inter-event time are brought in Figure 6.16 and Figure 6.17, respectively. During the presence of applied external force and interaction with the environment, the three controllers exhibit a similar behavior without generating a high interaction force, as illustrated in Figure 6.13 and Figure

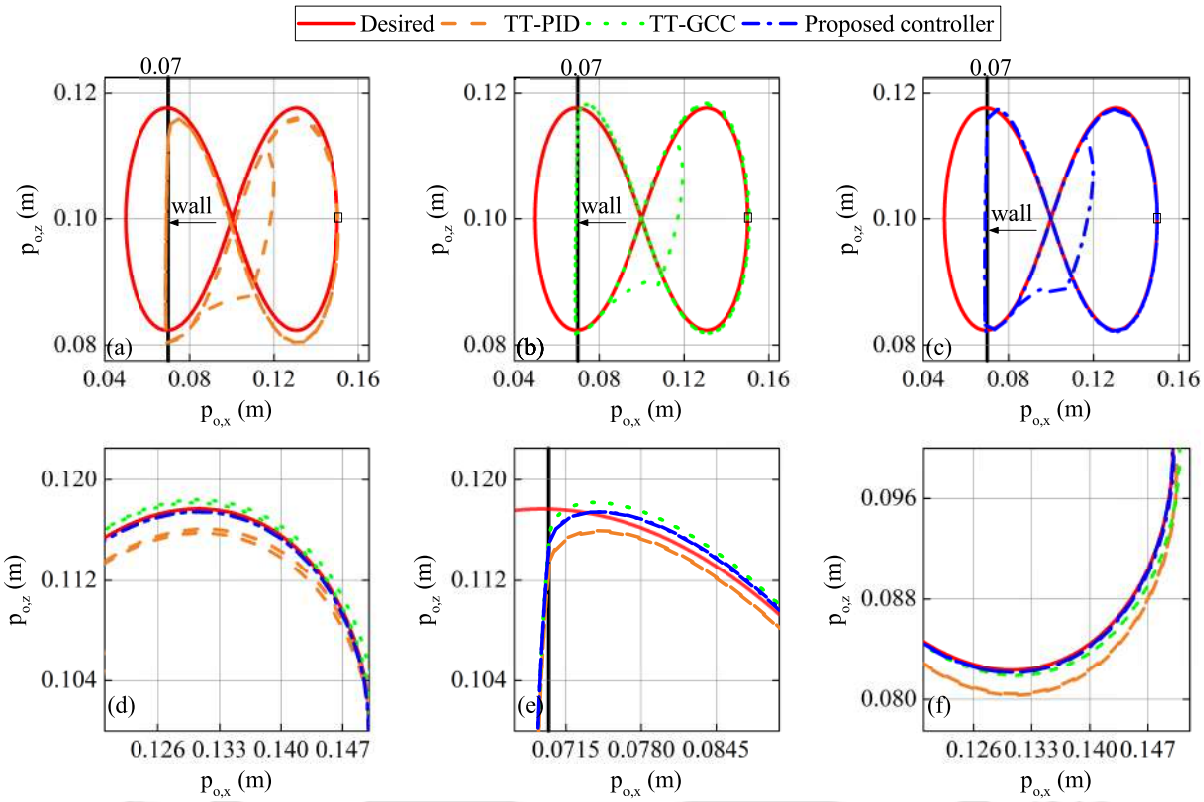

Figure 6.12: Object lemniscate trajectory tracking in x-z plane for Case 1. (a) TT-PID, (b) TT-GCC, (c) proposed controller. Enlarged view at (d) beginning of trajectory (e) contact wall (f) end of trajectory.

6.14 (a). However, it can be observed from Figure 6.12 (c,d,e,f), Figure 6.13 (f), and Figure 6.14 (b) that the proposed controller shows a better tracking performance with smaller tracking error in Z-direction and lesser internal force compared with TT-PID and TT-GCC. This superior performance is accompanied by aperiodic control updates, a significant saving in the resources, and longer inter-event time, as shown in Figures 6.15-6.17. Moreover, the sudden increase in the control signal can be observed at the time of contact to compensate for the deviation of the object from the desired trajectory and track the admittance-generated trajectory. These results are confirmed with the IAE and RMSE of the tracking errors presented in Table 6.2.

The results for Case 2 of the comparative study with relative and fixed thresholds are presented in Figures 6.18-6.20. The control inputs and triggering instants are shown in Figure 6.18 and Figure 6.19, respectively. The channel usage and inter-event time for the relative threshold, fixed threshold, and proposed ET mechanism are brought in Figure 6.20. It is obvious from these figures that the proposed ET mechanism can guarantee a lower number of transmissions over the network with the longest inter-event time for the first and second manipulator participating in the cooperative task. This results in

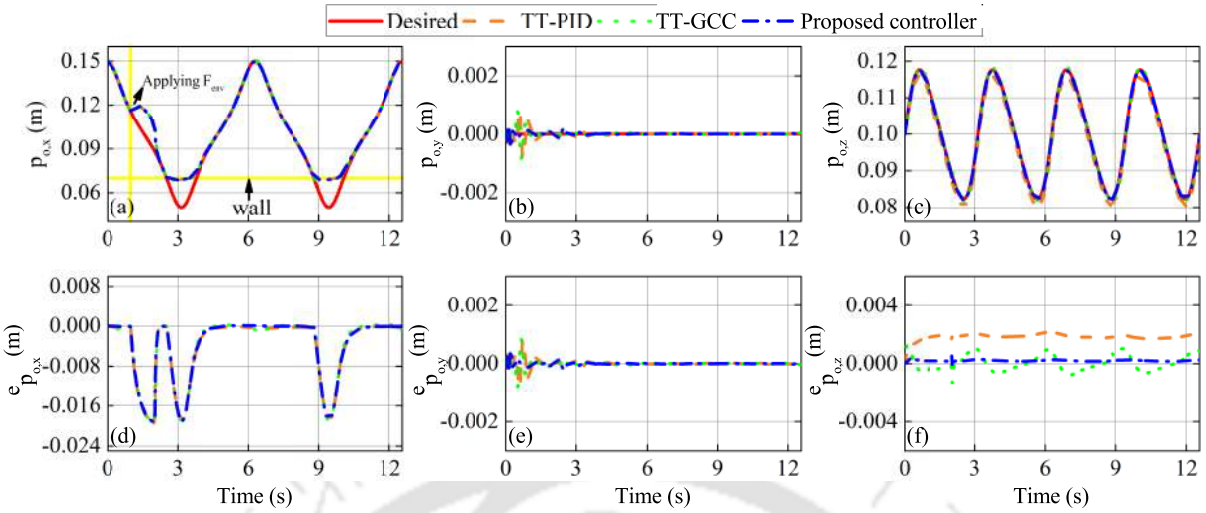

Figure 6.13: Position tracking for Case 1 in lemniscate trajectory. Desired and actual trajectories in (a) X-direction, (b) Y-direction, (c) Z-direction. Position tracking errors in (d) X-direction, (e) Y-direction, (f) Z-direction.

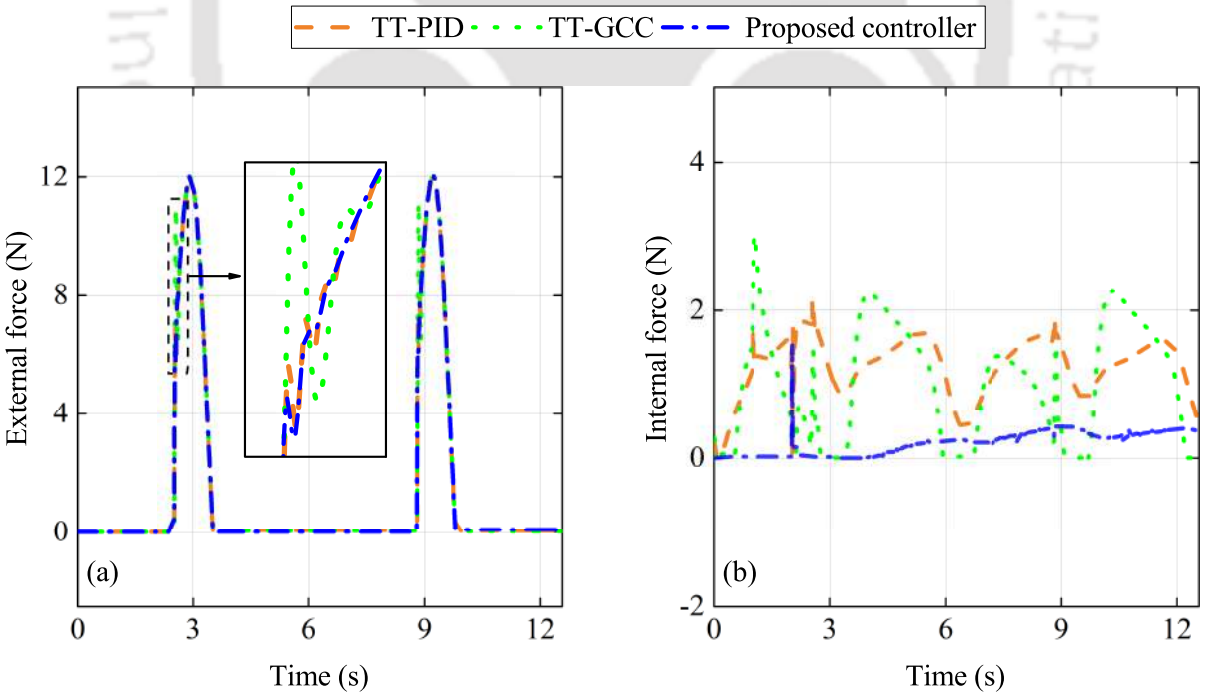

Figure 6.14: Forces exerted on object for Case 1 in lemniscate trajectory tracking. (a) interaction force (b), internal force.

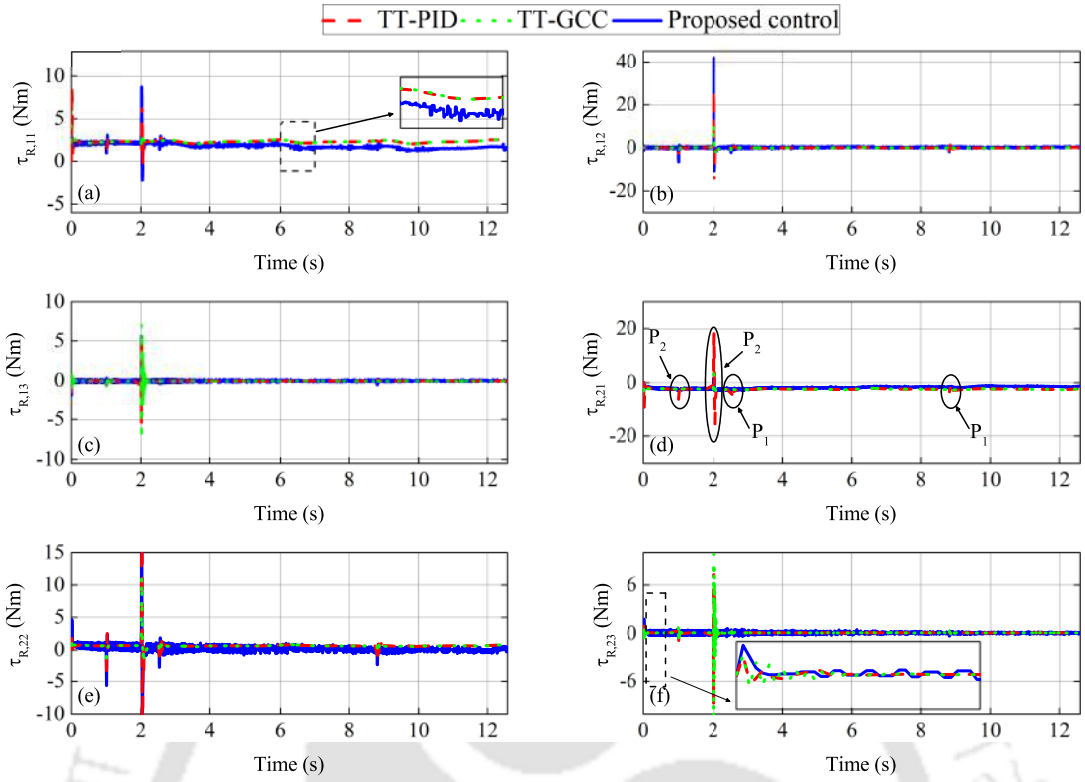

Figure 6.15: Control inputs for Case 1 in lemniscate trajectory tracking. For first manipulator at: (a) first joint, (b) second joint, (c) third joint. For second manipulator at: (d) first joint, (e) second joint, (f) third joint

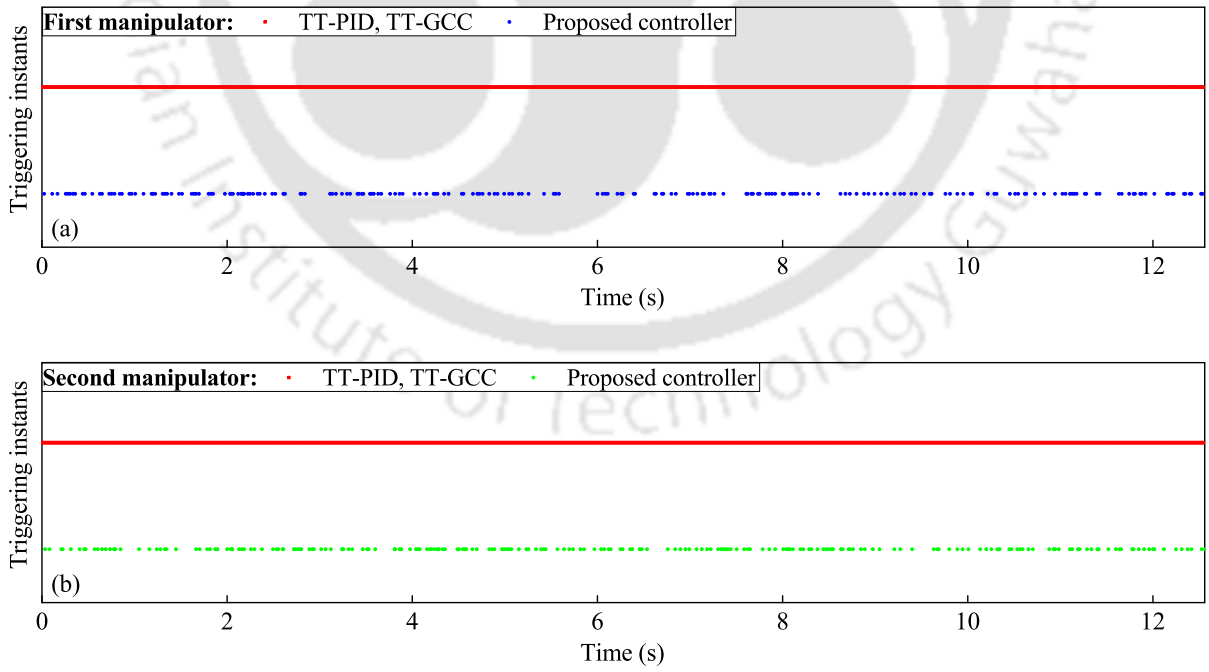

Figure 6.16: Triggering instants for TT-PID, TT-GCC, and proposed ET mechanism in Case 1 of lemniscate trajectory tracking at: (a) first manipulator, (b) second manipulator.

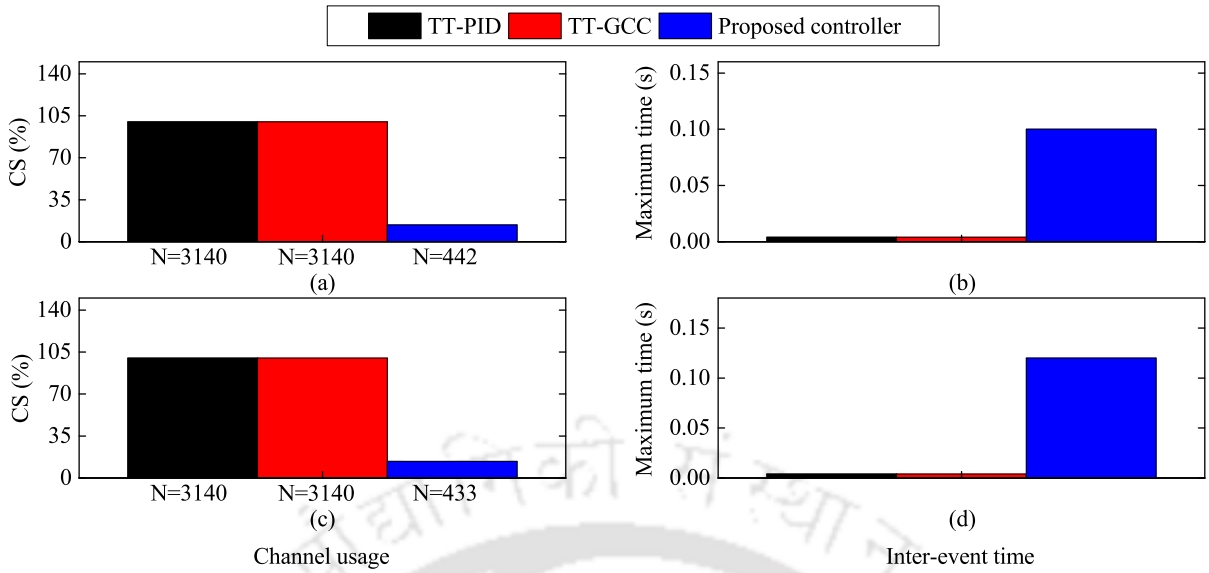

Figure 6.17: Comparison of proposed ET mechanism with different TT control schemes for Case 1 in lemniscate trajectory tracking. Top: First manipulator. Bottom: Second manipulator.

Table 6.2: Comparison of tracking errors for the two cases in lemniscate trajectory.

Cases	Controller	Tracking Errors					
		X-direction (mm)		Z-direction (mm)		Y-direction (mm)	
		RMSE	IAE	RMSE	IAE	RMSE	IAE
Case 1	TT-PID	7.46	50.71	1.84	23.03	0.125	0.331
	TT-GCC	7.42	49.41	0.54	5.74	0.10	0.29
	Proposed controller	7.32	48.79	0.21	2.68	0.05	0.17
Case 2	Relative threshold	7.42	48.8	0.21	2.57	0.05	0.174
	Fixed threshold	7.48	55.5	0.33	3.5	0.054	0.20
	Proposed controller	7.32	48.79	0.21	2.68	0.05	0.17

around 86% savings of the resources for the proposed controller compared with 48.2% and 65.3% for relative and fixed thresholds, respectively. Moreover, the same tracking performance of lemniscate trajectory is attained without chattering in the control signal compared to the fixed threshold and without a significant increase in the IAE and RMSE of the tracking errors with respect to the relative threshold as shown in Table 6.2.

6.4.3 Comparison with Related Works

Most of the admittance-based control studies presented in the cooperative manipulator-related literature are based on a hierarchical inner motion control loop with primary and secondary control schemes to calculate the joint reference angles and the desired joint torques, respectively [130, 132, 137, 138]. This hierarchical motion control loop leads to

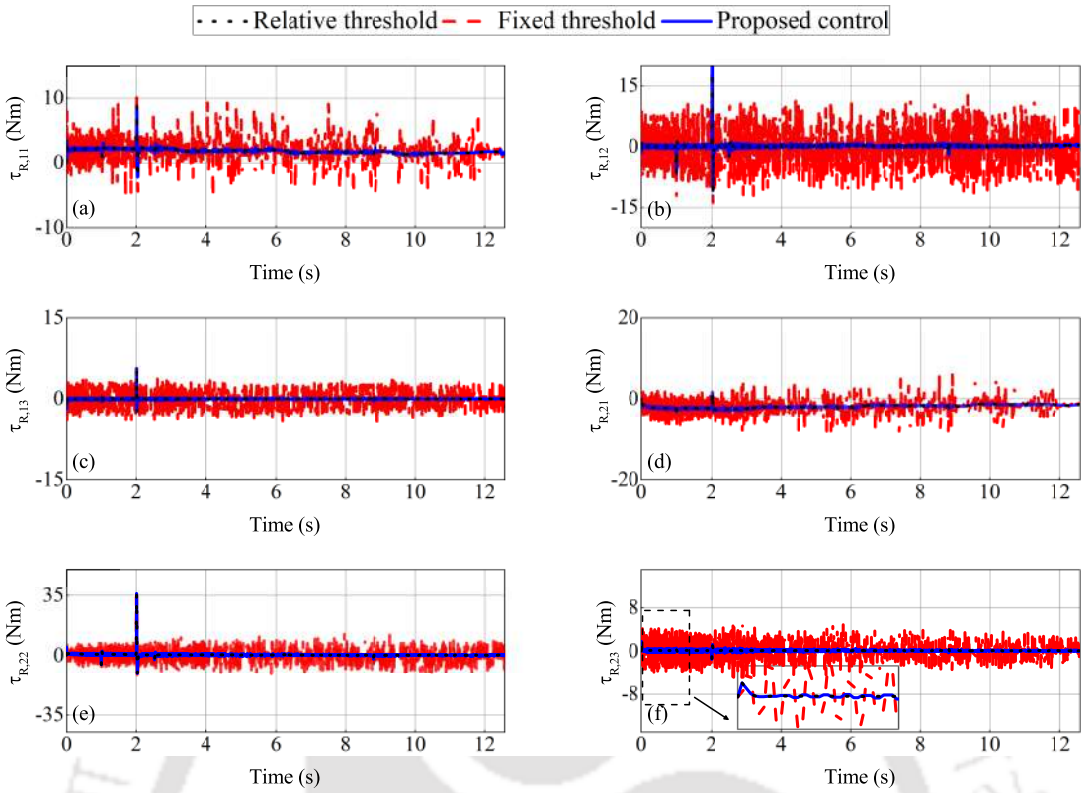

Figure 6.18: Control inputs for Case 2 in lemniscate trajectory tracking. For first manipulator at: (a) first joint, (b) second joint, and (c) third joint. For second manipulator at: (d) first joint, (e) second joint, and (f) third joint

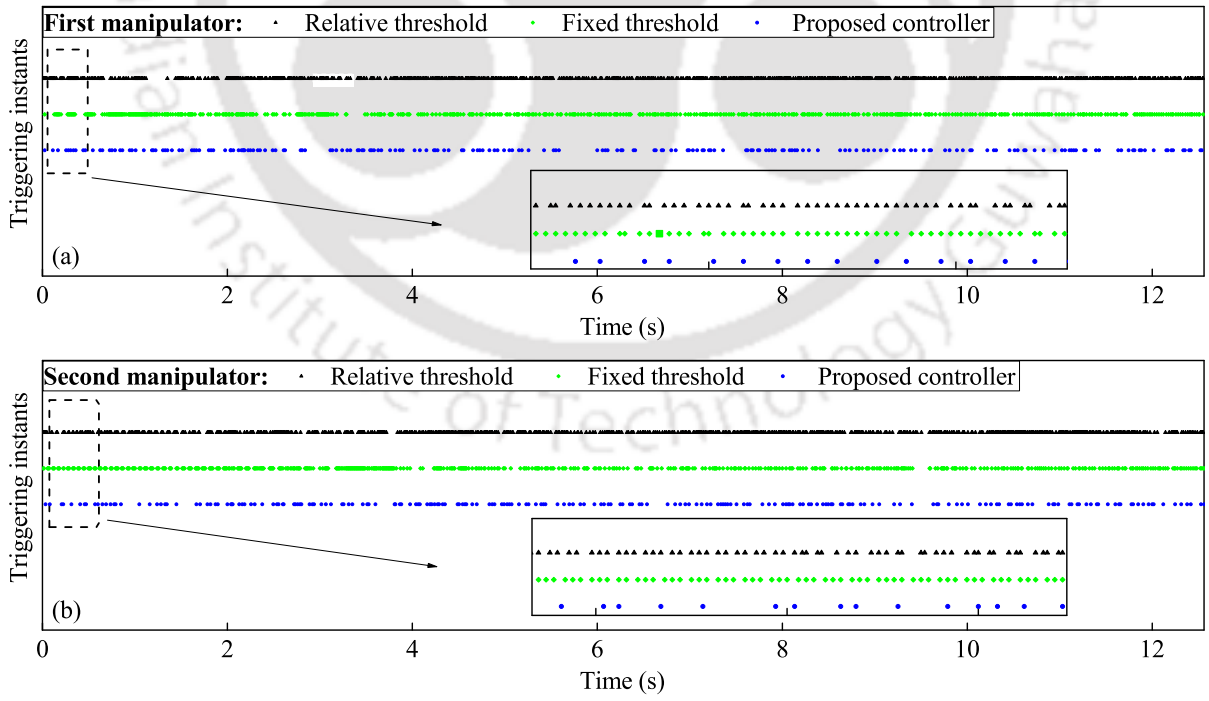

Figure 6.19: Triggering instants for proposed ET mechanism and different triggering conditions in Case 2 of lemniscate trajectory tracking at: (a) first manipulator, (b) second manipulator.

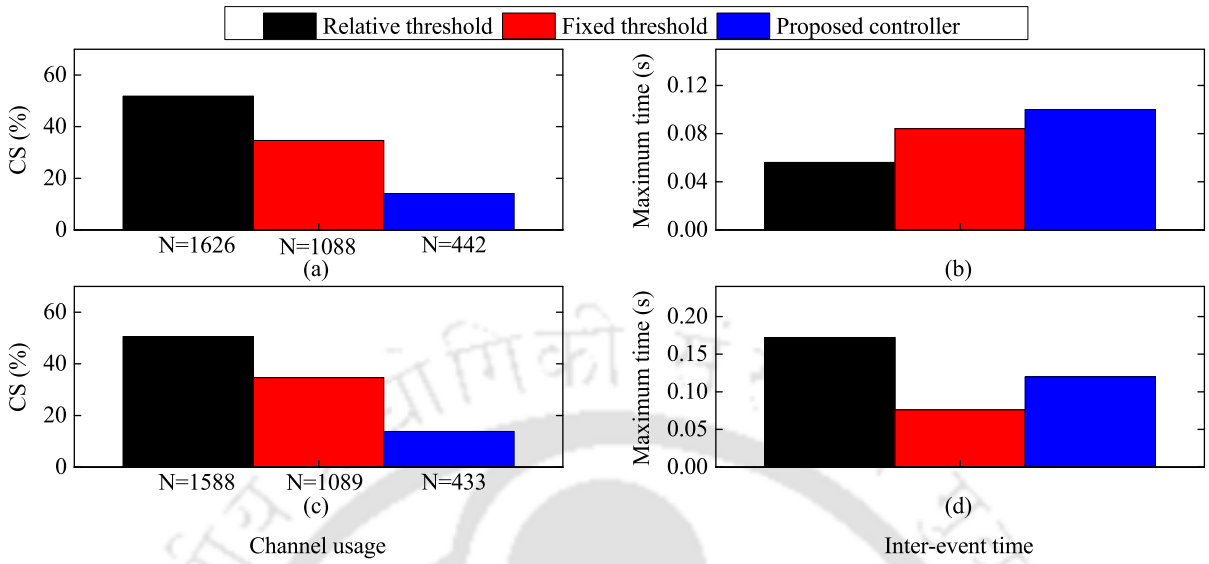

Figure 6.20: Comparison of proposed ET mechanism with different triggering conditions for Case 2 in lemniscate trajectory tracking. Top: First manipulator. Bottom: Second manipulator.

Table 6.3: Comparison with related works (EX:= External, IN:= Internal).

Studies	Admittance strategy	Event-triggered	Uncertainties	# Design parameters
[130]	EX+IN	No	No	5
[132]	EX+IN	No	No	6
[137]	EX+IN	No	No	4
[138]	EX+IN	No	No	-
[139]	EX+IN	No	No	3
[135]	EX+IN	No	Yes	4
[134]	IN	No	Yes	5
[136]	EX	No	Yes	5
[10]	EX	No	Yes	11
[172]	IN	Yes	No	-
Proposed	EX+IN	Yes	Yes	3

a cost computation and a higher number of design parameters to be tuned during the cooperative task. On the other hand, these studies do not consider the dynamic uncertainties in the controller design process, as summarized in Table 6.3. Although some works have considered the presence of dynamic uncertainties in the cooperative manipulator system [10,134–136]; however, these works do not address the limited communication challenge induced by the implementation of the network channel. For the proposed controller, the admittance-generated Cartesian trajectories are tracked directly using the operational space adaptive backstepping controller considering uncertainties and limited communication under the event-triggered mechanism. In addition to the aforementioned differences between the proposed control scheme and the others presented in the literature, the triggering condition is derived from the Lyapunov analysis based on the negative property of the Lyapunov function derivative. This simplifies the controller design and system stability analysis with no constraints on the dynamic nonlinearities to be a Lipschitz function. Moreover, it leads to better saving of resources in tandem with similar tracking performance in comparison with the well-known relative [147] and fixed [151,186] thresholds.

6.5 Summary

In this chapter, an admittance-based adaptive control strategy has been proposed for a team of uncertain cooperative manipulators. The external and internal admittance models have been augmented to achieve a compliant behavior and reduce the internal forces in the presence of different object-applied environmental forces. The Cartesian adaptive backstepping approach has been utilized to maintain an acceptable tracking performance under uncertainties and limited communication. The event-triggered strategy has been exploited to deal with the limited communication challenge. Therefore, an event-triggered condition has been designed based on Lyapunov analysis and placed at the controller-to-robot channel. The effectiveness of the designed controller has been evaluated using a dual-arm manipulator system during the manipulation of a common object through circular and lemniscate trajectories. Moreover, extensive comparison studies have been carried out with different time-triggered and event-triggered control schemes to emphasize the performance of the proposed controller. It can be concluded from the simulation runs that the designed controller exhibits an outstanding performance with fruitful compliant behavior and significant saving in resources.

7

Experimental Implementation of Event-Triggered Adaptive Control for Cooperative Manipulators

Contents

7.1 Introduction

This chapter endeavors to experimentally implement the designed event-triggered adaptive position control strategy on a real-time uncertain position-controlled cooperative dual-arm manipulator system. This implementation is carried out while considering some practical challenges, such as the limited communication and hardware restrictions of the commercial position-controlled manipulators. The dynamic of the manipulator is modified to overcome the hardware restriction and allow the dynamic control strategy on the position-controlled robots. As such, the proposed event-triggered adaptive controller can provide the required position control inputs instead of voltage or torque signals while considering the dynamical coupling and the parametric uncertainties of the dual-arm system. An adaptive control law is devised to cope with these uncertainties and estimate the parameters online during the assigned task. The dynamic Lyapunov-based triggering mechanism is utilized in the controller-to-robot channel to overcome the limited communication challenge, reduce the number of control updates, and maintain the stability of the whole system.

This chapter is organized as follows. In Section 7.2, the hardware specification of the cooperative dual-arm manipulator system is presented along with the dynamic modeling and problem formulation. The development of the proposed position-based event-triggered control strategy is presented in Section 7.3. Section 7.4 elaborates on the experimental validation and comparative analysis of the proposed control strategy with different time-triggered control schemes. Finally, Section 7.5 highlights the conclusion of the study.

7.2 Framework of Cooperative Manipulators

7.2.1 Specification of Dual-Arm Manipulator System

The cooperative manipulation of a cuboid object is performed using two Dagu robotic arms manufactured by DAGU Hi-Tech Electronic Co., LTD. for research and school competitions purposes. Each arm has 5 joints of revolute type, providing each manipulator with 5-DOFs. An additional joint is also present to open and close the gripper of the robotic arm. The base and arm joints are driven by 4-FB5116M servo motors. However, the wrist and gripper joints are actuated by 2-DGServo S05NF STD micro servos. These servo motors admit the joint position as the control input. The operating voltage of these servos ranges between 4.8 V-6 V. The joints of the manipulators can be operated all together by providing the control signals at all servo motors. However, the motion could also be limited to few joints that is sufficient to achieve the desired manipula-

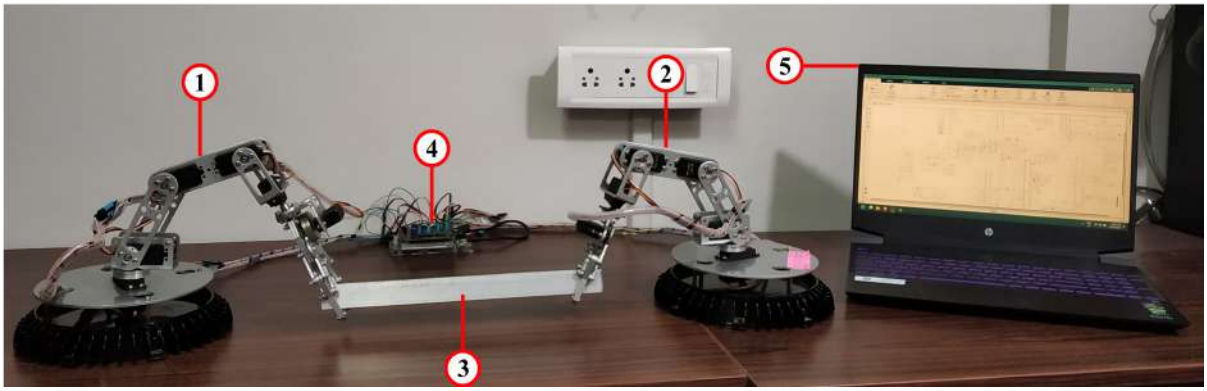

Figure 7.1: Dual-arm manipulator system (1-Left manipulator; 2-Right manipulator; 3-Manipulated object; 4-On-board micro-controller; 5-Host-computer)

tion task. The motion restriction is achieved by locking the unnecessary joint at one position. The whole experimental setup is shown in Figure 7.1. It consists of the two dagu robotic arm (L:=Left arm and R:=Right arm), on-board micro-controller, and host computer. The dual-arm robotic system is programmed using the host computer (i.e., Core i7-HP Pavilion with 16GB RAM and Windows 11 platform). The control program is built-in Matlab/Simulink (2019b) with the Arduino Hardware Support Package. The computation of the control inputs is carried out at the host computer and transferred to the on-board micro-controller via a wireless network established by an ESP13 WiFi shield. The communication are based on client/server architecture. The on-board micro-controller is an Arduino Due with Atmel SAM3X8E ARM Cortex-M3 CPU and 84 MHz clock. This board has 12 analog inputs, 2 digital-to-analog converter (DAC), and 54 digital input/output pins, 12 of which can be configured as pulse width modulation (PWM) outputs. The operational voltage of the pins is 3.3 V, with an external voltage supply range of 7 V-12 V. The schematic of the experimental architecture showing the flow of date is ilustrated in Figure 7.2. The dynamic parameters and dimensions of the Dagu robotic arm are presented in Appendix A.6.

7.2.2 Dynamic Model of Cooperative Manipulator System

In this section, the modified dynamical model of the cooperative manipulators system is presented. This model is highly desirable to comply with the most commercial position controlled manipulators available in the market, allowing the direct position control commands. Therefore, the dynamic of the manipulators is firstly amended to incorporate the electrical and mechanical parts of the motor dynamics, resulting in voltage controlled manipulators. Thereafter, the model of the internal low-level position controllers of the servo motors are combined with the dynamic of the manipulated object and coopera-

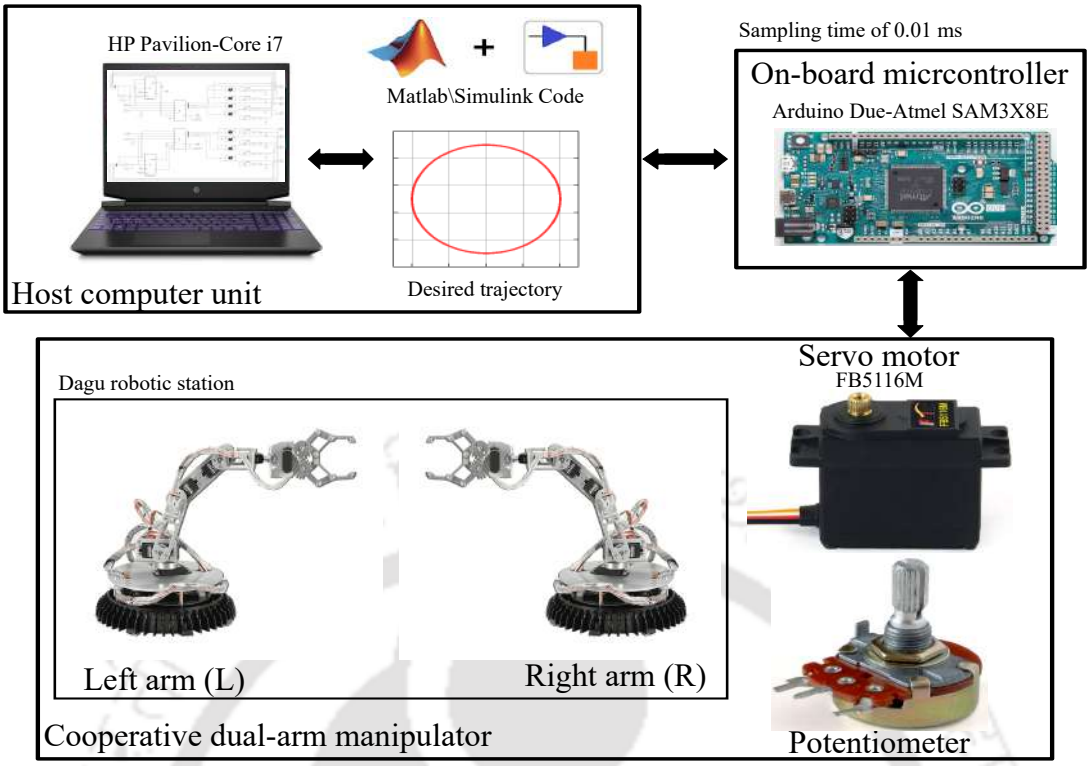

Figure 7.2: Schematic of the experimental architecture driven by MATLAB/Simulink

tive manipulators to complete the derivation and obtain an overall position controlled dynamic model. In Section 5.2, the conventional combined robot-motor dynamics of the k robotic manipulators with the complete description of the dynamic matrices was expressed by the following compact form:

$$M_R(q)\ddot{q} + C_R(\dot{q}, q)\dot{q} + G_R(q) = \tau_R - \tau_{int}; \quad \tau_{int} = J^T(q)F_{int} \tag{7.1}$$

where $q = [q_1^T, q_2^T, ..., q_k^T]^T \in \mathbb{R}^{kn}$, $M_R(q) = \text{blockdiag}[M_{R,1}(q_1), M_{R,2}(q_2), ..., M_{R,k}(q_k)] \in \mathbb{R}^{kn\times kn}$, $C_R(\dot{q}, q) = \text{blockdiag}[C_{R,1}(\dot{q}_1, q_1), C_{R,2}(\dot{q}_2, q_2), ..., C_{R,k}(\dot{q}_k, q_k)] \in \mathbb{R}^{kn\times kn}$, $G_R(q) = [G_{R,1}(q_1)^T, G_{R,2}(q_2)^T, ..., G_{R,k}(q_k)^T]^T \in \mathbb{R}^{kn}$, $F_{int} = [F_{int,1}^T, F_{int,2}^T, ..., F_{int,k}^T]^T \in \mathbb{R}^{km}$, $J(q) = \text{blockdiag}[J_1(q_1), J_2(q_2), ..., J_k(q_k)] \in \mathbb{R}^{km\times kn}$, and $\tau_R = [\tau_{R,1}^T, \tau_{R,2}^T, ..., \tau_{R,k}^T]^T \in \mathbb{R}^{kn}$. It can be observed that the above equation admit the torques as the control inputs. However, these signal are not appropriate to guide the servos of the position controlled manipulators. Therefore, a further modification on the torque controlled dynamics (7.1) will be carried out to comply with the hardware restriction and accept the direct position commands as control inputs.

By exploiting equations (2.4) and (4.5) and incorporating the electrical circuit of the DC servo motors presented in equation (4.4), the equation (7.1) can be rewritten similar

to equation (4.6):

$$M_R(q)\ddot{q} + \big(C_R(\dot{q},q) + rK_aR_a^{-1}K_br\big)\dot{q} + G_R(q) = rK_aR_a^{-1}V_a - J^T(q)F_{int} \tag{7.2}$$

where $K_a = \text{blockdiag}[K_{a,1}, K_{a,2}, ..., K_{a,k}] \in \mathbb{R}^{kn\times kn}$, $r = \text{blockdiag}[r_1, r_2, ..., r_k] \in \mathbb{R}^{kn\times kn}$, $K_b = \text{blockdiag}[K_{b,1}, K_{b,2}, ..., K_{b,k}] \in \mathbb{R}^{kn\times kn}$, $R_a = \text{blockdiag}[R_{a,1}, R_{a,2}, ..., R_{a,k}] \in \mathbb{R}^{kn\times kn}$, and $V_a = [V_{a,1}^T, V_{a,2}^T, ..., V_{a,k}^T]^T \in \mathbb{R}^{kn}$. The combined motor-robot dynamical model (7.2) of k manipulators is now driven by voltage signals of the motors. However, these signals cannot be utilized directly to drive the commercial position controlled cooperative manipulators which admit the position commands only. The servos of these manipulators adopt internal joint position controllers (e.g., PD controller [181]). The model of the low level internal controllers for k manipulators can be formulated as follows:

$$V_a = K_p(q_{cmd} - q) - K_d(\dot{q}) \tag{7.3}$$

where $K_p = \text{blockdiag}[K_{p,1}, K_{p,2}, ..., K_{p,k}] \in \mathbb{R}^{kn\times kn}$ and $K_d = \text{blockdiag}[K_{d,1}, K_{d,2}, ..., K_{d,k}] \in \mathbb{R}^{kn\times kn}$ are the parameters of the low-level PD controllers of the k robotic manipulators, $q_{cmd} \in \mathbb{R}^{kn}$ are the position commands of the k manipulators which represent the control inputs of the modified dynamical model of the cooperative manipulator system. It is to be mentioned that the term $\dot{q}_{cmd}$ is neglected in equation (7.3) to simplify the dynamic model. Substituting equation (7.3) in equation (7.2), one can obtain:

$$\begin{aligned} &M_R(q)\ddot{q} + \big(C_R(\dot{q},q) + rK_aR_a^{-1}(K_br + K_d)\big)\dot{q} + G_R(q) \\ &+ rK_aR_a^{-1}K_pq = rK_aR_a^{-1}K_pq_{cmd} - J^T(q)F_{int} \end{aligned} \tag{7.4}$$

To complete the derivation, the dynamics of the object should also be considered. Following the same derivation presented in Section 5.3 and substituting equations (5.13) and (5.14) in the above equation, the dynamical model of the multiple position controlled manipulators given in equation (7.4) coupled with the object dynamical equation (5.3) can be written as follows:

$$M_C(x_o)\ddot{x}_o + C_C(\dot{x}_o, x_o)\dot{x}_o + G_C(x_o) + \varepsilon q = \varepsilon q_{cmd} - J^T(x_o)F_I \tag{7.5}$$

where $M_C(x_o) = M_R(q)\eta(q) + J^T(q)W^\dagger M_o(x_o)$, $C_C(\dot{x}_o, x_o) = M_R(q)\iota(q) + \big(C_R(\dot{q},q) + rK_aR_a^{-1}(K_br + K_d)\big)\eta(q) + J^T(q)W^\dagger C_o(\dot{x}_o, x_o)$, $G_C(x_o) = G_R(q) + J^T(q)W^\dagger G_o(x_o)$, and $\varepsilon = rK_aR_a^{-1}K_p$. The overall dynamic model of the cooperative manipulator system (7.5) satisfies the same properties (**Property 7**-**Property 9**) presented in Section 5.3.

7.2.3 Problem Formulation

In this chapter, an uncertain position controlled cooperative dual-arm manipulator system is considered to perform a real-time cooperative manipulation of a common object. These manipulators are controlled via a limited bandwidth wireless network in the controller-to-robot channel. The overall dynamic model of the cooperative manipulators presented in equation (7.5) can be rewritten as follows.

$$M_C(x_o)\ddot{x}_o + C_C(\dot{x}_o, x_o)\dot{x}_o + G_C(x_o) + \varepsilon q = \varepsilon \bar{q}_{cmd} - J^T(x_o)F_I \tag{7.6}$$

where $\bar{q}_{cmd}$ is the event-triggered position control input.

The inaccuracies in the physical parameters of manipulators, the unavailability of servo motor models, and the parameters of internal low-level kinematic controller are the primary sources of uncertainties. To cope with these uncertainties, two adaptation laws are designed along with the backstepping control scheme to provide a proper tracking performance during the cooperative manipulation task. Therefore, the assumptions of known internal controller parameters [183] and the negligence of the electrical dynamics of the motor [181–183] are relaxed, resulting in a more realistic experimental scenario.

To overcome the limited bandwidth restrictions and reduce the control updates, an event-triggered (ET) mechanism is placed at the controller-to-robot channel. As a result, the cooperative manipulator system is not further driven by the actual position control input q_{cmd}. Instead, it is actuated by the event-triggered control input $\bar{q}_{cmd}$. The triggering instants are defined as

$$\begin{aligned} \bar{q}_{cmd}(t) &= q_{cmd}(t_j), \forall\ t \in [t_j, t_{j+1}) \\ t_{j+1} &= \inf\{t | t > t_j,\ T_{con}(e_m, z_1, z_2, z_3) > 0\} \end{aligned} \tag{7.7}$$

where $T_{con}(e_m, z_1, z_2)$ denotes the triggering condition to be designed in the subsequent section and e_m is the measurement error where $e_m = q_{cmd} - \bar{q}_{cmd}$.

The control problem can be stated as follows: Design and implement an event-triggered adaptive tracking control scheme based on the backstepping approach on commercial position controlled cooperative manipulators. This controller is devoted to ensure the boundedness of the closed-loop signals and achieve acceptable cooperative manipulation of a common object with minimum transmission over the network in the presence of uncertainties and limited bandwidth.

7.3 Position-based Event-Triggered Adaptive Controller Design

Here, the event-triggered adaptive backstepping controller presented in Section 5.4 is extended to provide the direct joint position signals which are adequate to guide the position controlled cooperative manipulator system in the real time scenarios. The error variables are defined similar to equation (5.18) as follows:

$$z_1 = \delta \int_0^t (x_o - x_{o,d})dt \ , \quad z_2 = x_o - \alpha_1 \ , \quad z_3 = \dot{x}_o - \alpha_2 \tag{7.8}$$

where α_1 and α_2 are the virtual controller intended to stabilize the subsystems based on the Lyapunov function. The derivation of these virtual controllers can be obtained following **Step 1** and **Step 2** of controller design in Subsection 5.4.1 as follows:

$$\begin{aligned} \alpha_1 &= -k_1\delta \int_0^t e_{x_o} dt + x_{o,d} \\ \alpha_2 &= -z_1 - k_2 z_2 - k_1\delta e_{x_o} + \dot{x}_{o,d} \end{aligned} \tag{7.9}$$

Here, the third step of the controller design is devised to obtain the control laws that provide the direct position command for the position controlled manipulators.

Step 3: By exploiting **Property 7**, the Lyapunov function candidate is proposed as follows.

$$\bar{V}_3 = \bar{V}_2 + \frac{1}{2} z_3^T \eta^T M_C(x_o) z_3 \tag{7.10}$$

Differentiating $\bar{V}_3$ with respect to time and utilizing equation (7.8) and **Property 8**, one can obtain:

$$\begin{aligned} \dot{\bar{V}}_3 &= \dot{\bar{V}}_2 + z_3^T \eta^T M_C(x_o)\dot{z}_3 + \frac{1}{2} z_3^T \frac{d\big(\eta^T M_C(x_o)\big)}{dt} z_3 \\ &= \dot{\bar{V}}_2 + z_3^T \eta^T \big(- M_C(x_o)\dot{\alpha} - C_C(\dot{x}_o, x_o)\alpha - G_C(x_o) + \varepsilon \bar{q}_{cmd} - \varepsilon q - J^T(x_o) F_I \big) \end{aligned} \tag{7.11}$$

By exploiting **Property 9** and knowing that $WF_I = 0$, the derivative of Lyapunov candidate is expressed as follows:

$$\dot{\bar{V}}_3 = \dot{\bar{V}}_2 - z_3^T \Pi_{x_o} \varphi_{x_o} + z_3^T \eta^T \big(\varepsilon \bar{q}_{cmd} - \varepsilon q \big) \tag{7.12}$$

Due to the inaccuracies in the physical parameters of the robots and the unavailability of servo motor models and internal low level controllers, an adaptive controller is required to be designed to deal with these uncertainties and compensate for the unknown parameters. Therefore, a new Lyapunov function is defined as $V = \bar{V}_3 + \frac{1}{2}\tilde{\varphi}_{x_o}^T \Gamma_1^{-1} \tilde{\varphi}_{x_o} + \text{trace}(\frac{1}{2}\tilde{\varepsilon}^T \Gamma_2^{-1} \tilde{\varepsilon})$.

Here, $\tilde{\varphi}_{x_o}$ and $\tilde{\varepsilon}$ are the estimation errors of the uncertainties and defined as $\tilde{\varphi}_{x_o} = \varphi_{x_o} - \hat{\varphi}_{x_o}$ and $\tilde{\varepsilon} = \varepsilon - \hat{\varepsilon}$. $\hat{\varepsilon}$ and $\hat{\varphi}_{x_o}$ denote the estimation of unknown parameters ε φ_{x_o}, respectively. Γ_1, Γ_2 are arbitrary positive constants. Using equations (5.23) and (7.12), the derivative of the last Lyapunov function V can be obtained as:

$$\begin{aligned}\dot{V} &= \dot{\tilde{V}}_2 - \tilde{\varphi}_{x_o}^T \Gamma_1^{-1} \dot{\hat{\varphi}}_{x_o} + \text{trace}(-\tilde{\varepsilon}^T \Gamma_2^{-1} \dot{\hat{\varepsilon}}) \\ &= -z_1^T k_1 z_1 - z_2^T k_2 z_2 + z_2^T z_3 + z_3^T \eta^T \big(\tilde{\varepsilon}(\bar{q}_{cmd} - q) + \hat{\varepsilon}(\bar{q}_{cmd} - q)\big) \\ &\quad - z_3^T \big(\Pi_{x_o} \tilde{\varphi}_{x_o} + \Pi_{x_o} \hat{\varphi}_{x_o}\big) - \tilde{\varphi}_{x_o}^T \Gamma_1^{-1} \dot{\hat{\varphi}}_{x_o} + \text{trace}(-\tilde{\varepsilon}^T \Gamma_2^{-1} \dot{\hat{\varepsilon}})\end{aligned} \tag{7.13}$$

By taking the transpose of $z_3^T \Pi_{x_o} \tilde{\varphi}_{x_o}$ and $z_3^T \eta^T \tilde{\varepsilon}(\bar{q}_{cmd} - q)$ and utilizing the trace properties, the above equation can be written as

$$\begin{aligned}\dot{V} = &-z_1^T k_1 z_1 - z_2^T k_2 z_2 + z_3^T \eta^T \big(\eta (\eta^T \eta)^{-1} z_2 + \hat{\varepsilon} q_{cmd} - \hat{\varepsilon} e_m - \hat{\varepsilon} q\big) - z_3^T \Pi_{x_o} \hat{\varphi}_{x_o} \\ &- \tilde{\varphi}_{x_o}^T (\Pi_{x_o}^T z_3 + \Gamma_1^{-1} \dot{\hat{\varphi}}_{x_o}) + \text{trace}\big(\tilde{\varepsilon}^T (\eta z_3 (\bar{q}_{cmd}^T - q^T) - \Gamma_2^{-1} \dot{\hat{\varepsilon}})\big)\end{aligned} \tag{7.14}$$

where $z_2^T z_3 = z_3^T z_2 = z_3^T \eta^T \eta (\eta^T \eta)^{-1} z_2$. Now, if the control law and the adaptive laws are chosen as follows

$$q_{cmd} = \hat{\varepsilon}^{-1} \big(\eta (\eta^T \eta)^{-1} (-z_2 + \Pi_{x_o} \hat{\varphi}_{x_o}) - (\vartheta \|\Pi_{x_o}\|^2 + k_3) \eta z_3\big) + q \tag{7.15}$$

$$\dot{\hat{\varphi}}_{x_o} = -\Gamma_1 \Pi_{x_o}^T z_3 \quad \text{and} \quad \dot{\hat{\varepsilon}} = \Gamma_2 \eta z_3 (\bar{q}_{cmd}^T - q^T) \tag{7.16}$$

then, the derivative of the Lyapunov function becomes

$$\dot{V} = -\, z_1^T k_1 z_1 - z_2^T k_2 z_2 - z_3^T \eta^T (k_3 + \vartheta \|\Pi_{x_o}\|^2) \eta z_3 + z_3^T \eta^T \hat{\varepsilon} e_m \tag{7.17}$$

Based on the measurement error appeared in the last term of equation (7.17), the triggering mechanism will be designed to maintain the negative semi-definiteness of the Lyapunov function derivative $\dot{V}$. Using the same derivation followed in equations (5.41-5.43), the triggering function defined in equation (7.7) can be formulated as follows.

$$T_{con}(e_m, z_1, z_2, z_3) = \|e_m\|^2 - 2\zeta \left(z_1^T k_1 z_1 + z_2^T k_2 z_2 + z_3^T \eta^T \big(k_3 + \vartheta \|\Pi_{x_o}\|^2\big) \eta z_3 \right) + \|z_3^T \eta^T \hat{\varepsilon}\|^2 \tag{7.18}$$

It can be proved directly similar to the analysis of Proposition 3 that the position controlled cooperative manipulator system presented in equation (7.5) actuated by the control law designed in equation (7.15) and the adaptation law (7.16) with the triggering mechanism (7.18) is stable in the sense of Lyapunov and all the state signals are ultimately bounded. Moreover, the Zeno behavior is excluded under the designed event-triggered condition.

Table 7.1: Performance analysis of cooperative manipulation task under internal low-level controller, proposed controller with and without adaption.

Controller	Tracking errors (mm)				Resource utilization		
	X-direction		Z-direction		# Control update	% Channel usage	% Saving
	RMSE	IAE	RMSE	IAE			
Internal low-level controller	1.82	22.07	0.33	3.78	1256	100	0
Proposed controller w/o adaptation	0.44	5.18	1.03	12.52	235	18.72	81.28
Proposed controller w/ adaptation	0.19	2.05	0.17	1.80	179	14.25	85.74

7.4 Experimental Results and Comparative Study

To validate the obtained theoretical results and illustrate the applicability of the proposed event-triggered adaptive position control strategy, the real-time cooperative manipulation of a common object is carried out using the dual-arm manipulator system presented in Subsection 7.2.1, available in Mechatronics and Robotics Laboratory of IIT Guwahati. The experiment is performed under non-ideal conditions (e.g., the inaccuracies of robotic dynamic, unavailability of the motors parameters by the manufacturer, and limited communication). The manipulation scenario is to move the firmly grasped object through a predefined circular trajectory i.e., $x_{o,d}(t) = [0.04\cos(\omega_d t) + 0.22, 0, 0.04\sin(\omega_d t) + 0.03]^T$, $\omega_d = 1\ \frac{\text{rad}}{\text{s}}$. The object is grasped via two grippers on the end effector of each Dagu manipulator, allowing no relative motion between the object and the end-effector. The position control signals are applied upon the second, third and fourth joints of each Dagu arm (2L/2R, 3L/3L, 4L/4R). The remaining joints are constrained at the zero positions. The physical parameters and the detailed descriptions of the dynamical model matrices of the utilized 3-DOFs Dagu arm are given in Appendix A.6. The total duration of the performed experiment is $t = 12.57$ s with 0.01 ms as sampling time. The initial conditions of the parameter estimation are set to be zero (i.e., $\hat{\varphi}_{x_o}(0) = \hat{\varepsilon}(0) = 0$). The designed controller parameters are selected as follows: $k_1 = \text{diag}(0.1, 0.1, 0.1)$, $k_2 = \text{diag}(0.1, 0.1, 0.1)$, $k_3 = 5.4I_6$, $\delta = 5$, $\vartheta = 7I_6$, $\Gamma_1 = 0.1I$, $\Gamma_2 = 0.2I_6$, and $\zeta = 0.8$. The effectiveness of the designed control scheme is evaluated during the manipulation task based on the following comparison cases.

Case 1. In this case, the performance of the proposed dynamic control scheme (with/without adaptation) is compared against the internal low-level kinematic controller in which the desired joint trajectories are directly feed to the servos as control commands. The effect of uncertainties is mimicked and introduced to the cooperative system by placing an additional mass of 100 g at the center of the object.

Discussion 1. The experimental results for the first comparison study are presented in Figures 7.3-7.6. Figure 7.3 illustrates the desired and actual trajectory of the object

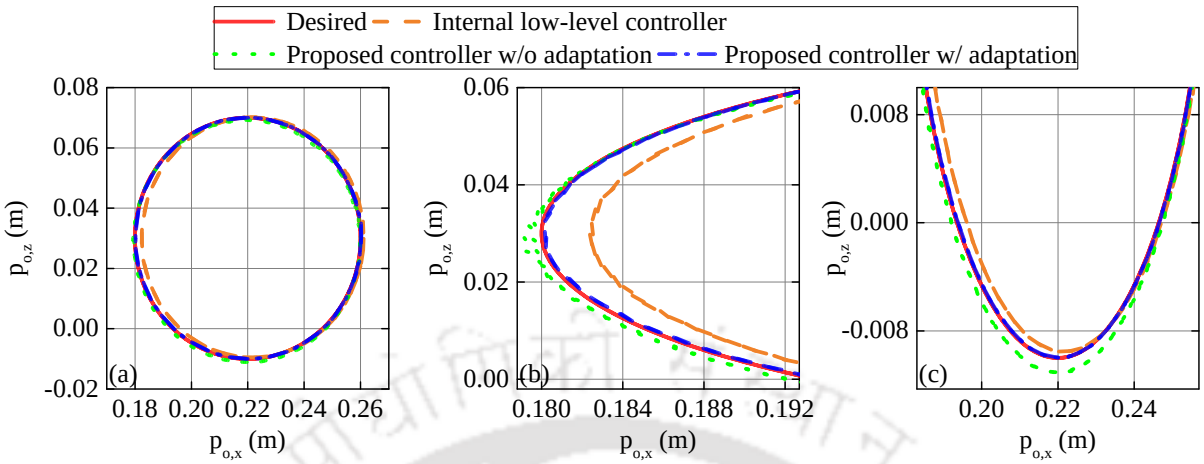

Figure 7.3: Experimental results of object trajectory tracking in x-z plane for internal low-level controller, proposed controller with and without adaption. (a) Desired and actual object trajectory. Enlarged view of the tracking performance at (b) left side and (c) bottom side

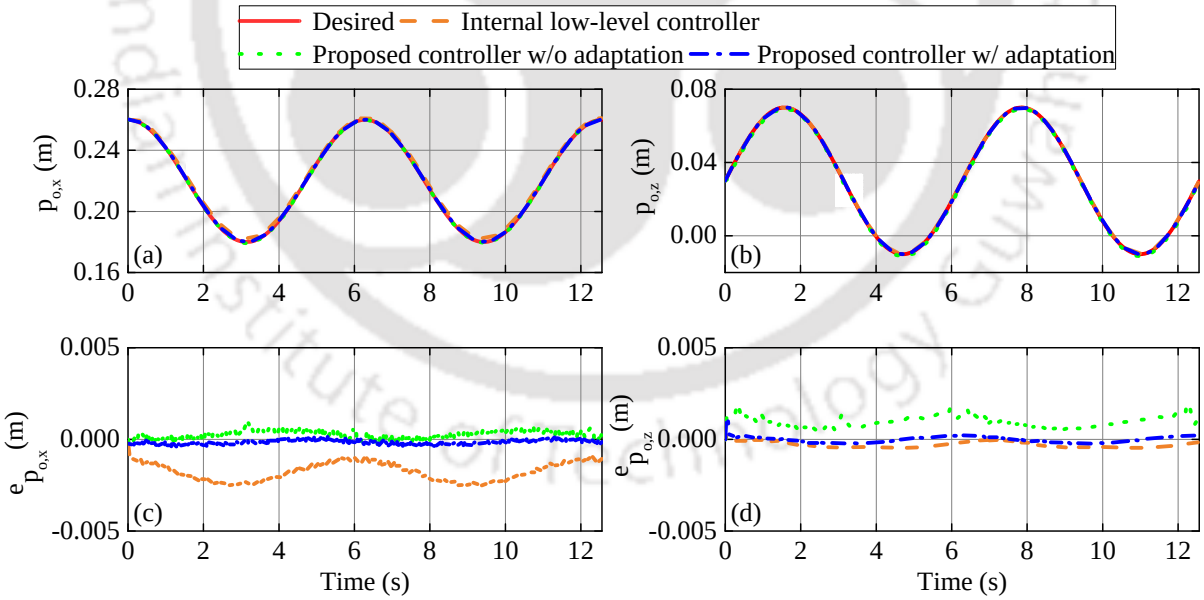

Figure 7.4: Experimental results of object position tracking for internal low-level controller, proposed controller with and without adaption. Desired and actual trajectories in (a) X-direction and (b) Z-direction. Position tracking errors in (c) X-direction and (d) Z-direction.

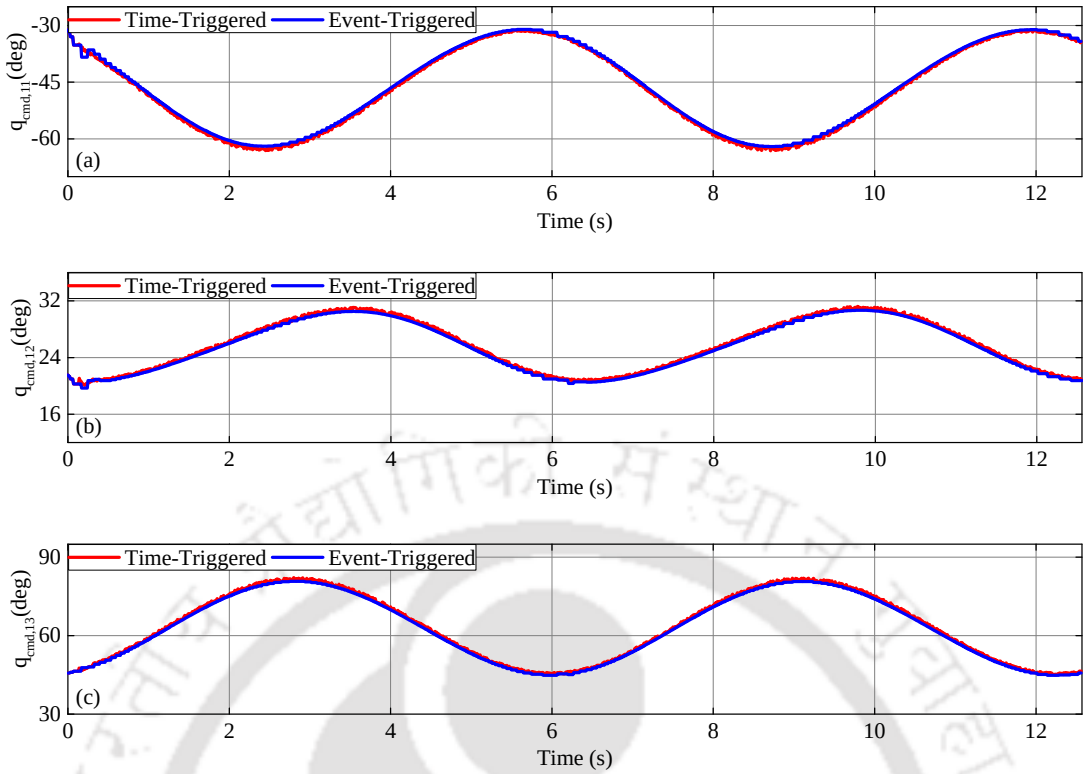

Figure 7.5: Control inputs under event-triggered and time triggered implementation of proposed control scheme for first manipulator at: (a) first joint, (b) second joint, (c) and third joint.

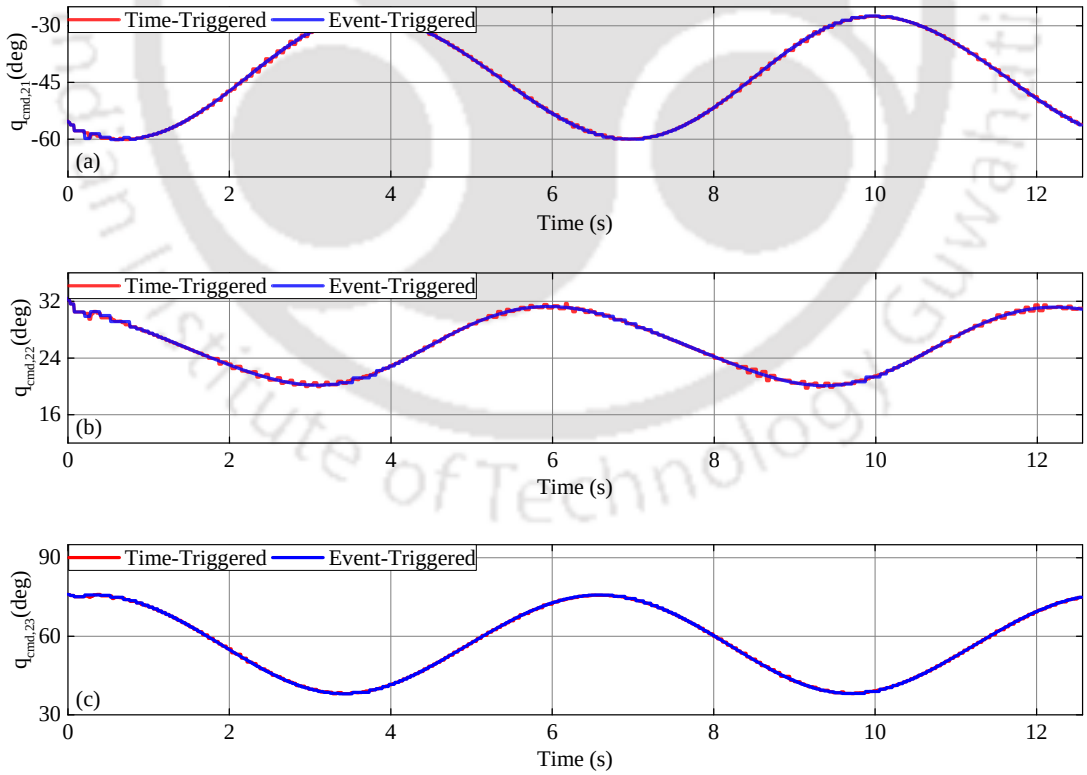

Figure 7.6: Control inputs under event-triggered and time triggered implementation of proposed control scheme for second manipulator at: (a) first joint, (b) second joint, (c) and third joint.

COM and tracking errors under the proposed controller (with/without adaptation) and the internal kinematic control scheme. The time-dependent trajectory tracking in X- and Z-directions of the object with the tracking errors are presented in Figure 7.4. It can be observed that the manipulation task can be precisely achieved using the designed event-triggered dynamic control scheme (with adaptation). The deactivation of the adaptation law may cause a slight deviation from the desired trajectory and larger tracking errors. However, the proposed dynamic controller with the two variations (with/without adaptation) can still results in smaller tracking errors compared to the kinematic controller, as shown in Figure 7.4. The time-triggered and event-triggered control inputs for the first and second Dagu arms under the proposed controller are depicted in Figure 7.5 and Figure 7.6, respectively. From these two figures, the control signals under the designed event-triggered condition are found to be updated aperiodically and held constant during the manipulation task. This results in a smaller number of transmission over the network while maintaining an outstanding tracking performance. Figure 7.10 shows the triggering instants under the proposed Lyapunov based triggering mechanism. It can be noted that a significant reduction in the updated/transmitted control signals can be guaranteed using the proposed mechanism compared with the time-triggered implementation. To quantitatively highlight the performance of the proposed control scheme, the root-mean-square error (RMSE) and integral absolute error (IAE) are calculated for the three different control strategies and brought in Table 7.1. Moreover, the channel usage along with the number of transmitted control signals is also presented in Table 7.1. The proposed control scheme (with/without adaptation) scores less RMSE and IAE compared to the internal low-level controller. However, the presence of the adaptation laws allow the controller to overcome the effect of uncertainties and achieve better tracking performance with minimum RMSE and IAE. It can be concluded that the proposed dynamic controller can be easily implemented on the position controlled robotic manipulators to provide the direct position commands. Moreover, this controller presents a superior tracking performance with minimum tracking errors and significant reduction in the control updates compared to the internal kinematic controller.

Case 2. In this case, the designed triggering condition is compared with the well-known triggering rules presented in the literature, i.e., (relative [147] and fixed [151, 186] thresholds). The same manipulation task conducted in the first case is repeated to further verify the effectiveness of the proposed control scheme. The thresholds design parameters are selected to maintain an acceptable tracking performance with the lowest number of transmissions over the network.

Discussion 2. The experimental results of the tacking performance, control inputs, and triggering instants for the fixed threshold, relative threshold, and designed event-

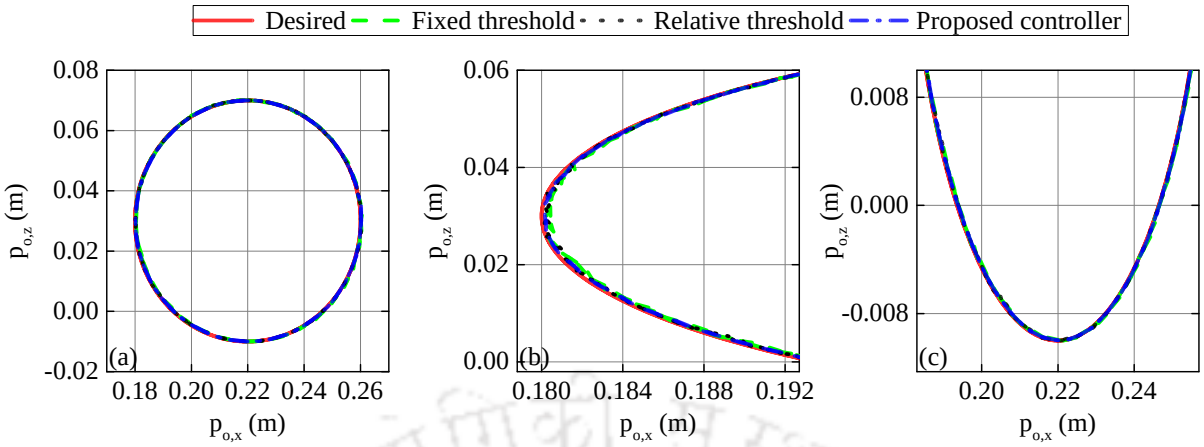

Figure 7.7: Experimental results of object trajectory tracking in x-z plane for fixed threshold, relative threshold, and proposed dynamic controller. (a) Desired and actual object trajectory. Enlarged view of the tracking performance at (b) left side and (c) bottom side.

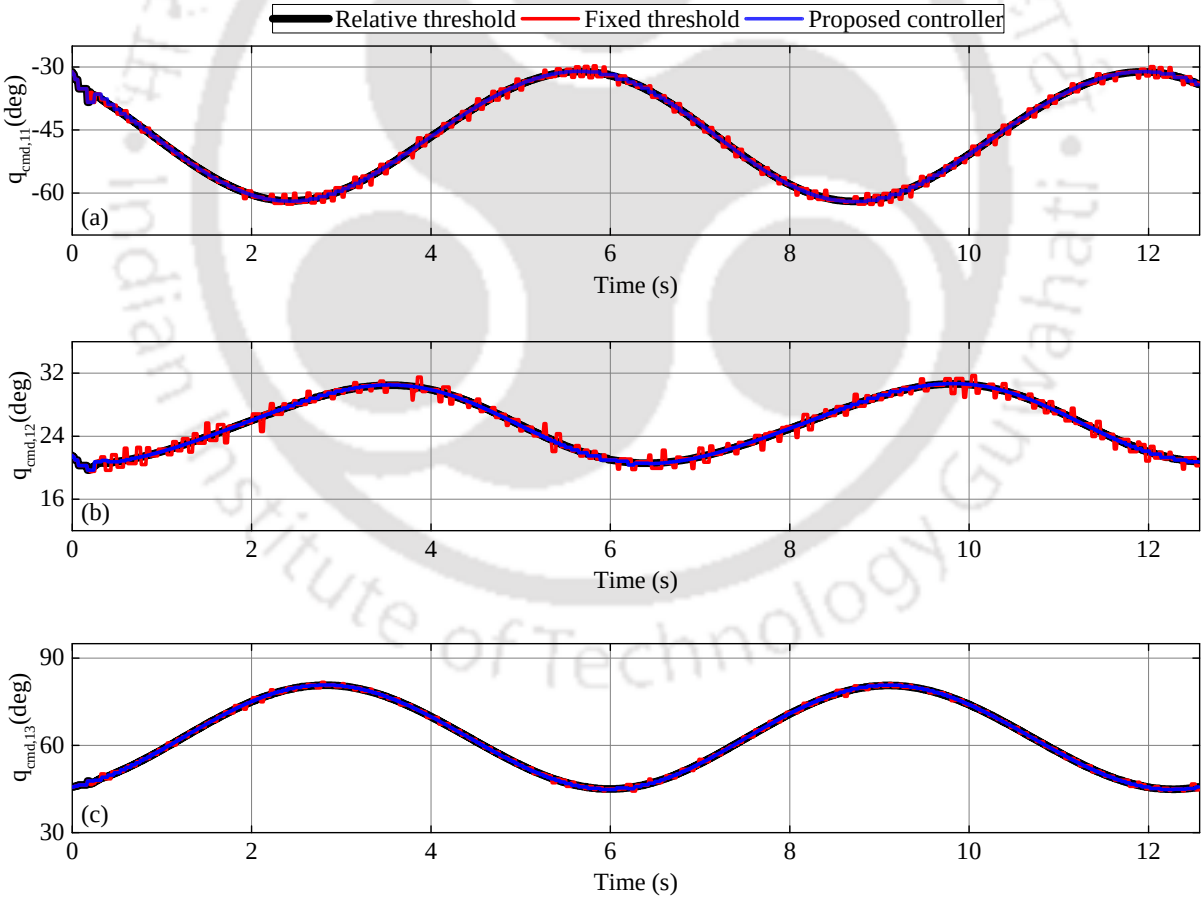

Figure 7.8: Control inputs under fixed threshold, relative threshold, and proposed dynamic controller for first manipulator at: (a) first joint, (b) second joint, (c) third joint.

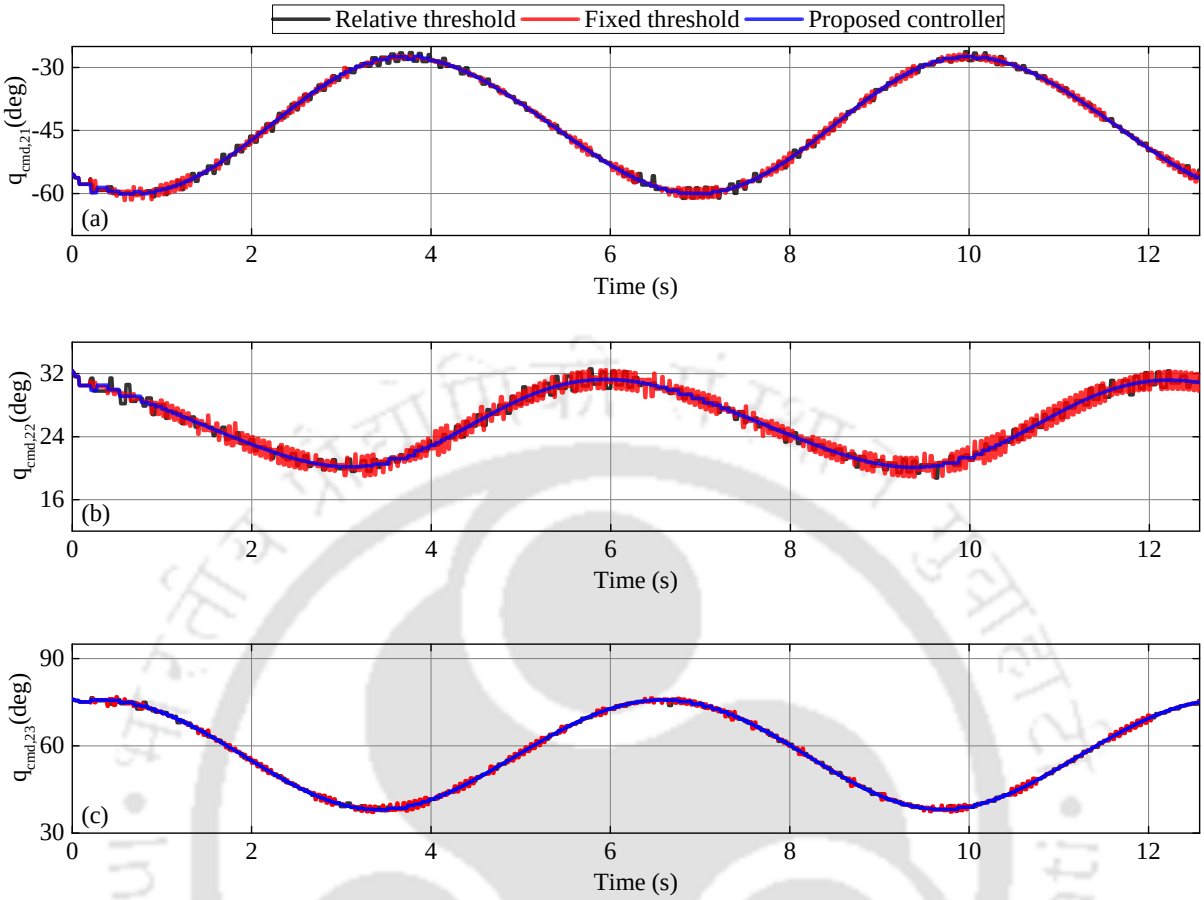

Figure 7.9: Control inputs under fixed threshold, relative threshold, and proposed dynamic controller for second manipulator at: (a) first joint, (b) second joint, (c) third joint.

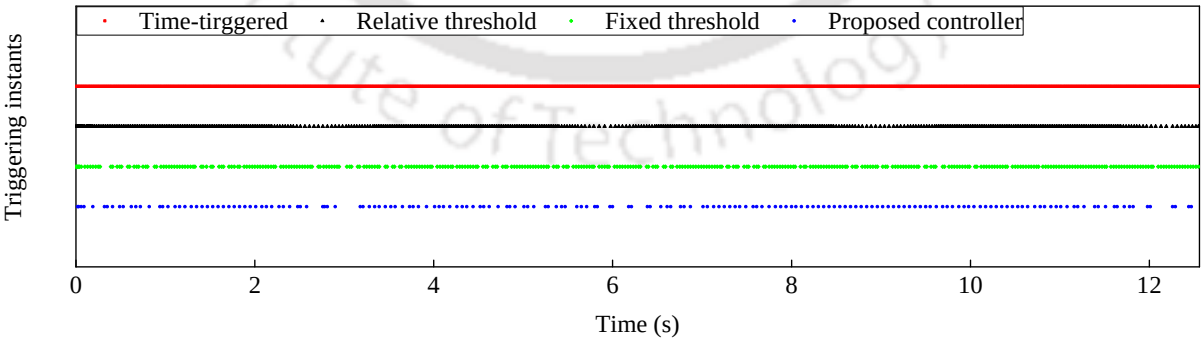

Figure 7.10: Experimental results of triggering instants for fixed threshold, relative threshold, and proposed ET mechanism.

Table 7.2: Performance analysis of cooperative manipulation task under fixed threshold, relative threshold, and proposed controller.

Controller	Tracking errors (mm)				Resource utilization		
	X-direction		Z-direction		# Control update	% Channel usage	% Saving
	RMSE	IAE	RMSE	IAE			
Fixed threshold	0.34	3.78	0.19	1.96	381	30.33	69.66
Relative threshold	0.20	2.13	0.17	1.83	538	42.83	57.16
Proposed controller	0.19	2.05	0.17	1.80	179	14.25	85.74

triggered dynamic controller are presented in Figures 7.7-7.10. The RMSE, IAE, and channel usage (CS) are summarized in Table 7.2. Figure 7.7 shows that almost a similar trajectory tracking is achieved using the three different triggering condition. However, this saving in the control updates is associated with sudden hikes in the control inputs of the first and second robotic manipulator under the fixed threshold, as shown from Figure 7.8 and Figure 7.9. However, it is evident from Figure 7.10 that the proposed triggering mechanism results is less number of control updates compared to fixed and relative thresholds. Therefore, it can be emphasized from Figure 7.10 and Table 7.2 that a significant saving in the resources with acceptable tracking performance and non-considerable change in the tracking errors can be achieved under the designed event-triggered controller compared to the relative and fixed thresholds.

7.5 Summary

In this chapter, the dynamic control of position commanded dual-arm manipulator system has been designed based on the backstepping approach to perform a cooperative manipulation task under hardware restrictions, uncertainties, and limited communication. Firstly, the coupled dynamic model of the object-manipulator has been modified to overcome the hardware restriction of position-controlled manipulators, allowing the direct position commands without any modifications in the hardware. Thereafter, the adaptive backstepping control law proposed previously in the thesis has been extended to cope with the parametric uncertainties due to the unavailability of internal servos models and inaccuracies in the robots and object parameters. The Lyapunov-based triggering condition has been further employed to alleviate the control updates and communication burden. Based on the experimental results, the proposed dynamic control scheme has been successfully implemented on the position-controlled dual-arm manipulator, resulting in outstanding tracking performance and a significant reduction in the control updates.

8

Conclusion and Scope for Future Work

Contents

This thesis presented results on two important research areas: the control of a single robotic manipulator in medical applications and the control of multiple robotic manipulators in cooperative manipulation tasks. The summary of the thesis and suggestions on possible extensions and further improvement of this work are outlined in the following sections.

8.1 General Conclusion

This thesis attempts to design event-triggered adaptive position-force control strategies for a single robotic manipulator during different interaction scenarios in medical applications in the presence of parametric uncertainties and limited bandwidth channel circumstances. It is also an attempt to extend the developed control schemes to tackle the more complex control problem of multiple uncertain manipulators during the cooperative manipulation of a common object while regulating the internal forces and object/environment interactions under the limited communication challenge. Moreover, it tries to validate the feasibility of implementing the proposed control schemes on real-time robotic manipulators in different medical and cooperative manipulation applications. The chapters of the thesis are briefly concluded as follows.

- The first part of the thesis presented two variants of event-triggered adaptive position-force control schemes based on the backstepping technique for a single robotic manipulator in medical applications. The hybrid position-force control scheme was introduced in Chapter 2 by combining the adaptive backstepping position control and PID force control scheme. This controller was implemented to track the desired trajectory, compensate for parametric uncertainties of the manipulator, and maintain the robot-human interaction at the required level to achieve a visible robot-assisted ultrasound examination. The communication restrictions were considered in the controller-to-robot channel. For this purpose, the triggering condition was derived in the last step of the backstepping procedure by ensuring the stability of the overall system. For applications where the compliant behavior is of more interest than the precise regulation of contact forces at a certain level, the event-triggered adaptive admittance control scheme was proposed in Chapter 3. This controller was devised to tackle reflex-based interaction forces and provide compliant behavior to the patient during the robot-assisted therapeutic exercises. The derived Lyapunov-based triggering condition was utilized to handle the limited communication problem and provide aperiodic control updates of the rehabilitation robot. The adaptive backstepping approach was also devised to provide accurate rehabilitation exercises and maintain robustness against dynamic uncertainties.

- In the second part of the thesis, the theoretical results of the previously discussed algorithms were extended for cooperative manipulation problems. The closed kinematic chain dynamic model of the multiple robotic manipulators and the manipulated object was discussed. An improved version of the event-triggered adaptive hybrid position-force control scheme was proposed in Chapter 5. The performance of this controller was enhanced by incorporating the integral action and nonlinear damping term in the steps of the backstepping procedure. This controller was devoted to simultaneously tracking the position and internal forces of the manipulated object in the face of parametric uncertainties. Furthermore, the dynamic event-triggered condition was derived to reduce the instances of communication between the manipulators and control unit without affecting the stability of the combined dynamical system. The control of the interaction between the manipulated object and the external environment during the cooperative manipulation task was further considered in Chapter 6. This environmental interaction and internal forces were addressed using external and internal admittance control schemes. The improved event-triggered adaptive backstepping motion controller presented in Chapter 5 was devised to provide proper object position tracking against the parametric uncertainties and limited communication challenges. It was shown that the modified event-triggered adaptive hybrid position-force control scheme outperforms its traditional time-triggered control schemes in terms of position and force tracking errors. Additionally, the proposed Lyapunov-based triggering condition results in fewer control updates than the various triggering conditions presented in the literature.

- From a practical point of view, the thesis attempted to demonstrate the applicability of the designed control schemes in real-time applications. The developed event-triggered adaptive position controllers were implemented and validated experimentally using two robotic systems, i.e., a single robotic manipulator and cooperative dual-arm manipulators. In Chapter 4, the robot-assisted passive rehabilitation exercises were conducted on different healthy subjects using the single robotic manipulator in the presence of load variations, unknown parameters of the robot and motors, and limited communication. To overcome the hardware restriction of many robotic manipulators, which can be actuated by direct voltage commands only, a modified dynamic model was first derived, allowing the successful implementation of the proposed control schemes. In Chapter 7, the improved event-triggered adaptive backstepping controller was further implemented on real position-controlled dual-arm manipulators to perform the cooperative manipulation of a common object. The hardware constraint of the position-controlled manipulators, which admit

only position commands, was also tackled by modifying the combined robots-object dynamic model without needing to know internal controller gains and servo motors parameters. This conversion allows the exploitation of the advantages of the proposed dynamic controllers against the parametric uncertainties while providing the required position commands to the servos of the manipulators. The experimental results obtained in both applications demonstrated promising potential for the practical applicability of the proposed control schemes in different medical and cooperative manipulation applications.

8.2 Specific Conclusion

8.2.1 Event-Triggered Adaptive Hybrid Position-Force Control for Robot-Assisted Ultrasonic Examination System

- The ETAHPFC scheme is introduced to simultaneously track the desired position and force trajectories in two different sub-spaces for the remotely controlled ultrasound robots. The proposed control scheme not only guarantees satisfactory ultrasound examination but also significantly improves channel bandwidth utilization.

- This scheme presents an alternative solution to the time-triggered approaches, which assume periodic transmission over the network. Moreover, it provides a general framework that can be easily implemented in different networked control robotic applications during human-robot or robot-environment interaction tasks where the direct regulation of position and force is required.

- Rather than the fixed and relative thresholds, an event-triggered mechanism is designed based on Lyapunov analysis to alleviate the communication over the network and maintain the stability of the closed-loop system. This triggering mechanism results in more savings of the network resources (about 80%) compared with 51.3% and 17% for fixed and relative thresholds, respectively.

- The performance of the proposed adaptive backstepping position control scheme in the presence of parametric uncertainties has been found better by 58% and 65% compared with APFC and ACTC, respectively.

8.2.2 Event-Triggered Adaptive Admittance Control for Upper-Limb Robot-Assisted Passive and Active Rehabilitation Exercises

- The ETABAC scheme presents an essential framework for the remote applications of rehabilitation robots, which enables the indirect regulation of interaction forces and accurate tracking of the rehabilitation trajectories in the presence of uncertainties and limited communication. This scheme can be further implemented in different active-resist rehabilitation exercises.
- The proposed ETABHPC has outperformed the PID and ASMC by 87.72%, 93.44% and 79.76%, 89.88% for tracking of admittance generated reference trajectories in X- and Y-directions, respectively.
- The designed Lyapunov-based triggering condition has led to 80.67% saving in the network resources during the passive rehabilitation with sudden reflex. Moreover, an 86.4% saving has been achieved in the case of active-assist rehabilitation mode without noticeable implication on the accuracy of reference trajectory tracking.
- The decreased admittance parameter has allowed flexibility to the robot and the safety of the subject in case of active-assist rehabilitation.

8.2.3 Experimental Implementation of Event-Triggered Adaptive Control for Upper-Limb Robot-Assisted Passive Rehabilitation Exercises

- The designed voltage-based event-triggered adaptive position control scheme has been implemented successfully on an electrically driven end-effector type rehabilitation robot allowing the direct voltage commands to overcome the hardware restrictions.
- The experimental results have shown the efficiency of the proposed controller in providing passive rehabilitation exercises for various subjects. The tracking performance has been improved by 33.3% and 58.57% in Y- and Z-directions, respectively, as compared with the TT-ACT control scheme.
- The designed triggering condition results in aperiodic control updates and a huge reduction in the communication burden with 11% of channel usage compared with 100% in the case of TT-PID and TT-ACT.
- The increase of ζ values leads to more savings in the network resources. However, the tracking errors in the Y- and Z-directions are slightly increasing as the parameter

ζ reaches one. Therefore, the balance between acceptable tracking performance and network utilization can be obtained by adjusting the parameter ζ.

8.2.4 Event-Triggered Adaptive Hybrid Position-Force Control for Cooperative Manipulators

- The advantages of the integral action in alleviating steady-state errors and enhancing the system response in the presence of uncertainties has been exploited. Moreover, the nonlinear damping term has been implemented to improve the transient performance and reduces the number of transmitted signals over the communication channel during the cooperative manipulation tasks.

- The integration of the state variable and the nonlinear term in the controller design process has improved the performance of the controller and led to a significant saving in the network resources (68%) compared with ET-AB (38.3%) and ET-AUAB (42.5%) control algorithms.

- The results also have shown that the proposed control can still outperform the ET-SMC and ET-AC with minimum position and force tracking errors and less transmission over the network during the cooperative manipulation task.

8.2.5 Event-triggered Adaptive Admittance Control for Cooperative Manipulators

- The simulation results have shown the efficiency of the proposed control scheme to comply with the two different environmental interaction scenarios during the cooperative manipulation task of a common object.

- The proposed controller has been found to be better than TT-PID and TT-GCC in tracking the reference trajectory. Moreover, it has shown a smoother interaction without sudden hikes in the external forces compared with TT-PID and TT-GCC.

- A similar reference trajectory tracking behavior has been observed with the implementation of fixed and relative thresholds. However, the proposed triggering mechanism has shown a better saving in resource utilization (about 86%) compared with the fixed threshold (67%) and relative threshold (38.5%).

8.2.6 Experimental Implementation of Event-Triggered Adaptive Control for Cooperative Manipulators

- The devised dynamic model of the cooperative manipulator system admits the direct position control signal instead of the torque or voltage commands, complying with the most commercial position-controlled manipulators available in the market.
- Rather than the kinematic control schemes, the proposed dynamic adaptive backstepping position control approach has been utilized to deal with the parametric uncertainties and estimate the unavailable model parameters. The assumptions of known internal controller parameters and the neglecting of the electrical dynamics of the motor have been relaxed, resulting in a more realistic experimental scenario.
- Instead of the fixed and relative thresholds, a dynamic triggering mechanism has been adopted to reduce the number of control updates while ensuring the negative semi-definiteness of the Lyapunov function.
- The proposed ET adaptive control scheme has outperformed the internal kinematic controller by 89.5% and the same proposed control scheme without activation of the adaptation law by 56.8% for trajectory tracking in the X-direction. Moreover, the proposed triggering mechanism has resulted in more savings of the resources (85.74%) compared with the fixed threshold (69.66%) and relative threshold (57.16%).

8.3 Recommendations for Future Work

The future research directions with respect to the event-triggered adaptive control schemes of robotic manipulators can be outlined as follows.

- In all studied frameworks of the thesis, the network constraints are assumed to be in the controller-to-robot channel and the triggering condition is placed at this channel. However, in practice, these constraints could also be present in the robot-to-controller channel. Therefore, the design of the position-force controllers while considering the robot-to-controller triggering configuration needs to be investigated. However, this extension is not straightforward, as the available controllers need to be redesigned based on the event-triggered states.
- The implementation of the networked control system for robotic applications is accompanied by other challenges, such as state and input delays and packet loss. These challenges can deteriorate the performance of the robotic system and may

affect the stability of the whole system. These challenges shall be investigated in the future.

- The controllers designed in the thesis deal with the structured uncertainties due to the inaccuracies of robot and motors parameters and load variations. However, unstructured uncertainties caused by external disturbances and nonlinear friction can also affect the performance of the robotic system. Therefore, the design and analysis of control schemes that tackle both structured and unstructured uncertainties along with the network constraints is a promising avenue to research.

- All the feedback states of the robotic systems utilized in the proposed event-triggered control strategies are assumed to be accessible and available from the sensory signals. However, this may not be the case in practice. Thus, an observer-based output feedback controller is worth exploring to relax this assumption.

- The operation of each manipulator participating in the cooperative manipulation is assumed away from the singularity. This assumption is strict and simplifies the control problem. Hence, a future direction can be devoted to address the operation near singularity and singularity avoidance problem.

- The extension of the developed control schemes to achieve prescribed transient and steady state performance should also be attempted. Moreover, the constraints on system states and outputs are worth exploring due to saturation and safety issues.

- The experimental validations of the proposed control schemes are limited to the passive rehabilitation exercises and cooperative manipulation tasks without robot-human or object/environment interaction due to the unavailability of the required subject and time constraints. Therefore, future efforts may focus on performing different clinical active-assist rehabilitation exercises and robot-assist ultrasound examinations to investigate the performance of the proposed control schemes. Moreover, the real-time object/environment interaction scenario may also be attempted during the cooperative manipulation task.

A

Appendix

Contents

A.1 SCORBOT-ER VPlus

A.1.1 Specifications of the Robot

This manipulator has a 5-DOFs with five revolute joints (RRRRR). The end effector is a gripper type with additional degree of freedom, as shown in Figure A.1. The first joint is utilized to provide a rotational motion for the whole body of the robotic manipulator. Furthermore, the second and third joints (shoulder, elbow) are employed to provide the up and down motion for the first and second link, respectively. The pitch and roll motions of the gripper are achieved by the fourth and fifth joints (wrist), respectively. Figure A.2 presents schematic and line diagrams of the robotic arm. The maximum reachability of the Scorbot-ER 5 Plus is 610 mm, 610 mm, and 830 mm in the X-, Y-, and Z-directions, respectively. The whole range of joint variables are tabulated in Table A.1.The physical characteristics of SCORBOT-ER VPlus are listed in Table A.2.

Figure A.1: Scorbot-ER 5 Plus [203].

A.1.2 Dynamics of SCORBOT-ER VPlus

The derivation of the complete dynamic model for the robot is achieved using the Robotics Toolbox developed by Peter Corke and integrated with Matlab based on recursive Newton-Euler algorithm [204]. The elements of the inertia matrix M_R can be obtained from the equations (A.1-A.8). The elements of Coriolis and centrifugal forces

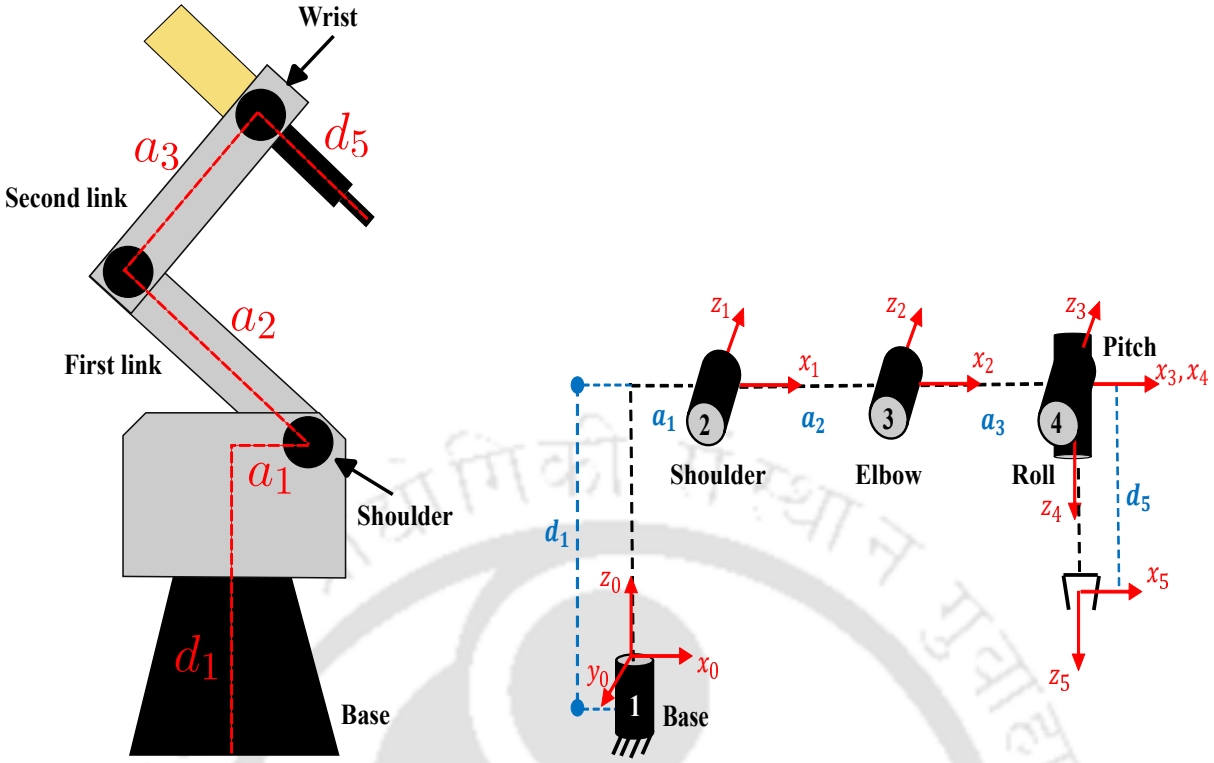

Figure A.2: Scorbot-ER 5 Plus. (a) Schematic diagram (b) Line diagram

C_R are shown in the equations (A.9-A.19). The components of the developed gravitational torques on the robot G_R are presented in the equations (A.20-A.21). Since all the joints are of a revolute type, the joint variables are defined as $q_i = \theta_i$. Moreover, to achieve the dynamic model of the utilized 3-DOFs manipulator, the following assumptions are

Table A.1: Ranges of joint angles

Joints	Ranges (deg)
First joint (base)	-155 to 155
Second joint (shoulder)	-35 to 130
Third joint (elbow)	-130 to 130
Fourth joint (wrist pitch)	-130 to 130
Fifth joint (wrist roll)	-570 to 570

Table A.2: Physical parameters for SCORBOT-ER VPlus

Link	Length (m)	Mass (kg)	Motor inertia (kgm^2)	Moment of inertia (kgm^2)				Gear ratio
	a_i	m_i	J_{mi}	I_i	I_{xxi}	I_{yyi}	I_{zzi}	r_i
1	0.025	2	1.5×10^{-5}	1.616	0.866	1.616	1.95	127.1
2	0.22	3	1.5×10^{-5}	12.44	12.49	12.49	12.49	127.1
3	0.22	3	1.5×10^{-5}	12.44	12.49	12.49	12.49	127.1
4	0	1	1.5×10^{-5}	0	0	0	0	65.5
5	0.135	0.7	1.5×10^{-5}	8.79	8.79	8.79	8.79	65.5

made: $m_4 = m_5 = 0,\ d_5 = 0,\ I_4 = I_5 = I_{zz5} = 0, J_{m4} = J_{m5} = 0,\ G_4 = G_5 = 0.$

$$M_{11} = r_1^2 J_{m1} + I_1 + \frac{(I_{235} + I_{xx2} + I_{xx3} + 2I_{yy1} + I_{zz5})}{2} + {a_1}^2 m_{2345} + (m_2 + 4m_{345})\frac{{a_2}^2}{8} + (m_3 + 4m_{45})\frac{{a_3}^2}{8} + \frac{m_5 {d_5}^2}{8} + (\frac{I_2 - I_{xx2}}{{a_2}^2} + \frac{m_2}{4} + m_{345}){a_2}^2\frac{C2\theta_2}{2} + [\frac{I_3 - I_{xx3}}{{a_3}^2} + (\frac{m_3}{4} + m_{45})]{a_3}^2\frac{C2\theta_{23}}{2} + (\frac{m_3}{2} + m_{45})a_2 a_3\cos(2\theta_2 + \theta_3) + (m_3 + 2m_{45})a_1 a_3 C\theta_{23} + (\frac{m_2}{2} + m_{345})2a_1 a_2 C\theta_2 + (\frac{m_3}{2} + m_{45})a_2 a_3 C\theta_3 - \left[m_5 {d_5}^2 + 4(I_5 - I_{zz5})\right]\frac{C2\theta_{234}}{8} - m_5 a_1 d_5 S\theta_{234} - \frac{m_5 d_5}{2}\{a_2[(\sin(2\theta_2 + \theta_3 + \theta_4) + \frac{S\theta_{34}}{2}] + a_3[(\sin(2\theta_2 + 2\theta_3 + \theta_4) + \frac{S\theta_4}{2}]\} \tag{A.1}$$

$$M_{12} = M_{21} = 0,\ M_{13} = M_{31} = 0,\ M_{14} = M_{41} = 0,\ M_{15} = M_{51} = -I_{zz5}C\theta_{234} \tag{A.2}$$

$$M_{22} = I_{235} + r_2^2 J_{m2} + \frac{m_5 {d_5}^2}{4} + (\frac{m_2}{4} + m_{345}){a_2}^2 + (\frac{m_3}{4} + m_{45}){a_3}^2 + (m_3 + 2m_{45})\ a_2 a_3 C\theta_3 - m_5 d_5(a_3 S\theta_4 + a_2 S\theta_{34}) \tag{A.3}$$

$$M_{23} = M_{32} = I_{35} + (\frac{m_3}{4} + m_{45}){a_3}^2 + \frac{m_5 {d_5}^2}{4} + (\frac{m_3}{2} + m_{45})a_2 a_3 C\theta_3 - m_5 d_5(a_3 S\theta_4 + \frac{a_2 S\theta_{34}}{2}) \tag{A.4}$$

$$M_{24} = M_{42} = I_5 + \frac{m_5 {d_5}^2}{4} - m_5 d_5\frac{a_3 S\theta_4 + a_2 S\theta_{34}}{2}, M_{25} = M_{52} = 0 \tag{A.5}$$

$$M_{33} = I_{35} + r_3^2 J_{m3} + \frac{m_5 {d_5}^2}{4} + (\frac{m_3}{4} + m_{45}){a_3}^2 - m_5 d_5 a_3 S\theta_4 \tag{A.6}$$

$$M_{34} = M_{43} = I_5 + m_5 d_5(\frac{d_5}{4} - \frac{a_3 S\theta_4}{2}),\ M_{35} = M_{53} = 0 \tag{A.7}$$

$$M_{44} = I_5 + J_{m4} r_4^2 + \frac{m_5 {d_5}^2}{4}, M_{45} = M_{54} = 0, M_{55} = J_{m5} r_5^2 + I_{zz5} \tag{A.8}$$

$$C_{11} = -\{(m_2 + 2m_{345})a_1a_2S\theta_2 + (\frac{I_2 - I_{xx2}}{{a_2}^2} + \frac{m_2}{4} + m_{345}){a_2}^2S2\theta_2 + (m_3 + 2m_{45})a_1a_3S\theta_{23} + (m_3 + 2m_{45})a_2a_3\sin(2\theta_2 + \theta_3) + (\frac{I_3 - I_{xx3}}{{a_3}^2} + \frac{m_3}{4} + m_{45}){a_3}^2S2\theta_{23} + (-I_5 + I_{zz5})S2\theta_{234} - \frac{m_5{d_5}^2S2\theta_{234}}{4} + m_5d_5[(a_1C\theta_{234} + a_2\cos(2\theta_2 + \theta_3 + \theta_4) + a_3\cos(2\theta_2 + 2\theta_3 + \theta_4)]\}\frac{\dot{\theta}_2}{2} - \{(\frac{m_3}{2} + m_{45})a_2a_3S\theta_3 + (m_3 + 2m_{45})a_1a_3S\theta_{23} + (\frac{m_3}{2} + m_{45})a_2a_3\sin(2\theta_2 + \theta_3) + (\frac{I_3 - I_{xx3}}{{a_3}^2} + \frac{m_3}{4} + m_{45}){a_3}^2S2\theta_{23} + (I_{zz5} - I_5)S2\theta_{234} - \frac{m_5{d_5}^2}{4}S2\theta_{234} + m_5d_5[\frac{a_2C\theta_{34}}{2} + a_1C\theta_{234} + \frac{a_2}{2}\cos(2\theta_2 + \theta_3 + \theta_4) + a_3\cos(2\theta_2 + 2\theta_3 + \theta_4)]\}\frac{\dot{\theta}_3}{2} - \{(-I_5 + I_{zz5})S2\theta_{234} + m_5d_5[-\frac{d_5}{4}S2\theta_{234} + \frac{a_3}{2}C\theta_4 + \frac{a_2}{2}C\theta_{34} + a_1C\theta_{234} + \frac{a_2}{2}\cos(2\theta_2 + \theta_3 + \theta_4) + \frac{a_3}{2}\cos(2\theta_2 + 2\theta_3 + \theta_4)]\}\frac{\dot{\theta}_4}{2} \tag{A.9}$$

$$C_{12} = -C_{21} = -\{(m_2 + 2m_{345})a_1a_2S\theta_2 + (\frac{I_2 - I_{xx2}}{{a_2}^2} + \frac{m_2}{4} + m_{345}){a_2}^2S2\theta_2 + (m_3 + 2m_{45})[a_1a_3S\theta_{23} + a_2a_3\sin(2\theta_2 + \theta_3)] + (\frac{I_3 - I_{xx3}}{{a_3}^2} + \frac{m_3}{4} + m_{45}){a_3}^2S2\theta_{23} + (-I_5 + I_{zz5})S2\theta_{234} - \frac{m_5{d_5}^2}{4}S2\theta_{234} + m_5d_5[a_1C\theta_{234} + a_2\cos(2\theta_2 + \theta_3 + \theta_4) + a_3\cos(2\theta_2 + 2\theta_3 + \theta_4)]\}\frac{\dot{\theta}_1}{2} + I_{zz5}S\theta_{234}\frac{\dot{\theta}_5}{2} \tag{A.10}$$

$$C_{13} = -C_{31} = -\{(\frac{m_3}{2} + m_{45})a_2a_3S\theta_3 + (m_3 + 2m_{45})a_1a_3S\theta_{23} + (\frac{m_3}{2} + m_{45})a_2a_3\sin(2\theta_2 + \theta_3) + (\frac{I_3 - I_{xx3}}{{a_3}^2} + \frac{m_3}{4} + m_{45}){a_3}^2S2\theta_{23} + (I_{zz5} - I_5)S2\theta_{234} - \frac{m_5{d_5}^2}{4}S2\theta_{234} + m_5d_5[\frac{a_2}{2}C\theta_{34} + a_1C\theta_{234} + \frac{a_2}{2}\cos(2\theta_2 + \theta_3 + \theta_4) + a_3\cos(2\theta_2 + 2\theta_3 + \theta_4)]\}\frac{\dot{\theta}_1}{2} + I_{zz5}S\theta_{234}\frac{\dot{\theta}_5}{2} \tag{A.11}$$

$$C_{14} = C_{41} = -\{(-I_5 + I_{zz5})S2\theta_2 + m_5d_5[-\frac{d_5}{4}S2\theta_{234} + \frac{a_3}{2}C\theta_4 + \frac{a_2}{2}C\theta_{34} + a_1C\theta_{234} + \frac{a_2}{2}\cos(2\theta_2 + \theta_3 + \theta_4) + \frac{a_3}{2}\cos(2\theta_2 + 2\theta_3 + \theta_4)]\}\frac{\dot{\theta}_1}{2} + I_{zz5}S\theta_{234}\frac{\dot{\theta}_5}{2} \tag{A.12}$$

$$C_{15} = C_{51}=\frac{I_{zz5}}{2}S\theta_{234}\dot{\theta}_{234},\ C_{22} = -\{[(m_3 + 2m_{45})a_2a_3S\theta_3 + m_5a_2d_5C\theta_{34}]\frac{\dot{\theta}_3}{2} + m_5d_5[a_3C\theta_4 + a_2C\theta_{34}]\frac{\dot{\theta}_4}{2}\} \tag{A.13}$$

$$C_{23} = -[(m_3 + 2m_{45})a_2a_3S\theta_3 + m_5a_2d_5C\theta_{34}]\frac{\dot{\theta}_{23}}{2} - m_5d_5(a_3C\theta_4 + a_2C\theta_{34})\frac{\dot{\theta}_4}{2} \tag{A.14}$$

$$C_{24} = -m_5d_5(a_3C\theta_4 + a_2C\theta_{34})\frac{\dot{\theta}_{234}}{2},\ C_{25} = -C_{52} = -I_{zz5}S\theta_{234}\frac{\dot{\theta}_1}{2} \tag{A.15}$$

$$C_{32} = [(\frac{m_3}{2} + m_{45})a_2a_3S\theta_3 + \frac{m_5d_5a_2}{2}C\theta_{34}]\dot{\theta}_2 - m_5a_3d_5C\theta_4\frac{\dot{\theta}_4}{2} \tag{A.16}$$

$$C_{33} = -m_5a_3d_5C\theta_4\frac{\dot{\theta}_4}{2},\ C_{34} = -m_5a_3d_5C\theta_4\frac{\dot{\theta}_{234}}{2}C_{35} = -C_{53} = -\frac{I_{zz5}}{2}S\theta_{234}\dot{\theta}_1 \tag{A.17}$$

$$C_{42} = m_5d_5(a_3C\theta_4 + a_2C\theta_{34})\frac{\dot{\theta}_2}{2} + m_5d_5a_3C\theta_4\frac{\dot{\theta}_3}{2} \tag{A.18}$$

$$C_{43} = \frac{m_5}{2}d_5a_3C\theta_4\dot{\theta}_{23},\ C_{44} = 0,\ C_{45} = -\frac{I_{zz5}}{2}S\theta_{234}\dot{\theta}_1, C_{55} = 0 \tag{A.19}$$

$$G_1 = 0,\ G_2 = -[(\frac{m_2}{2} + m_{345})a_2C\theta_2 + (\frac{m_3}{2} + m_{45})a_3C\theta_{23} - \frac{m_5}{2}d_5S\theta_{234})]g \tag{A.20}$$

$$G_3 = -[(\frac{m_3}{2} + m_{45})a_3C\theta_{23} - \frac{m_5}{2}d_5S\theta_{234}]g,\ G_4 = \frac{m_5}{2}d_5S\theta_{234}g,\ G_5 = 0 \tag{A.21}$$

where a_1, a_2, a_3 denotes the length of the first, second, and third link, respectively, d_5 is the distance from the tip of the fourth link to the robot end-effector, m_i is the mass of the defined link, I_i is the moment of inertia for the respected link, g is the gravitational acceleration, and r_i is the ratio of the motor gears. Moreover, $C\theta_i = \cos(\theta_i)$, $S\theta_i = \sin(\theta_i)$, $C\theta_{ij} = \cos(\theta_i + \theta_j)$, $S\theta_{ij} = \sin(\theta_i + \theta_j)$, $C\theta_{ijk} = \cos(\theta_i + \theta_j + \theta_k)$, $S\theta_{ijk} = \sin(\theta_i + \theta_j + \theta_k)$, $m_{ij} = (m_i + m_j)$, $m_{ijk} = (m_i + m_j + m_k)$, $m_{ijkl} = (m_i + m_j + m_k + m_l)$, $I_{ij} = (I_i + I_j)$, $I_{ijk} = (I_i + I_j + I_k)$, $I_{ijkl} = (I_i + I_j + I_k + I_l)$, $\dot{\theta}_{ij} = (\dot{\theta}_i + \dot{\theta}_j)$, $\dot{\theta}_{ijk} = (\dot{\theta}_i + \dot{\theta}_j + \dot{\theta}_k)$.

A.2 Time-triggered PID and ASMC Schemes

The control laws for the contrast controllers (i.e., TT-PID [97] and TT-ASMC [196]) utilized in the comparison analysis along with their selected gain parameters are given in this Appendix. These controller gains are selected heuristically to obtain the accurate tracking performance of the reference training trajectory and attain a compliant behavior during patient-robot interaction.

In the case of TT-PID, the control law is defined as follows:

$$\tau_R = k_{p,x}(x_{e,r} - x_e) + k_{I,x}\int (x_{e,r} - x_e)dt + k_{d,x}(\dot{x}_{e,r} - \dot{x}_e) \tag{A.22}$$

where $k_{p,x}$, $k_{I,x}$, and $k_{d,x}$ represent the user-defined PID control parameters and selected as $k_{p,x} = \text{diag}(10000,\ 10000,\ 10000), k_{I,x} = \text{diag}(10,\ 10,\ 10), k_{d,x} = \text{diag}(950,\ 950,\ 950)$.

In the case of TT-ASMC, the control and adaptation laws are given as follows:

$$\tau_R = \Pi\hat{\varphi} + J^T(q)\big(F_{int} - Ksign(s_x)\big), \quad \dot{\hat{\varphi}} = -\Gamma\Pi^T J^{-1} s_x \tag{A.23}$$

where $s_x = \dot{x}_e - \dot{x}_s$, $\dot{x}_s = \dot{x}_{e,r} - c(x_e - x_{e,r})$, c, K, and Γ are the TT-SMC design parameters and selected as: $c = \text{diag}(10,\ 10,\ 10)$, $K = 100$, and $\Gamma = \text{diag}(0.01,\ 0.01,\ 0.01)$.

A.3 Description of Matrix Π and Vector of Dynamic parameters φ

The elements of the known matrix $\Pi(\theta, \dot{\theta}, \ddot{\theta}) \in \mathbb{R}^{3\times 15}$ and the vector of the unknown parameters $\varphi \in \mathbb{R}^{15}$ are given in detail as follows.

$\Pi(1,1) = \Pi(1,2) = \ddot{\theta}_1$,
$\Pi(1,3) = \frac{1}{2}\cos 2\theta_2\ddot{\theta}_1 - \sin 2\theta_2\dot{\theta}_1\dot{\theta}_2$,
$\Pi(1,4) = \frac{1}{2}\cos 2\theta_{23}\ddot{\theta}_1 - \sin 2\theta_{23}\dot{\theta}_1\dot{\theta}_{23}$,
$\Pi(1,5) = (\cos\theta_3 + \cos(2\theta_2+\theta_3))\ddot{\theta}_1 - \sin(2\theta_2+\theta_3)\dot{\theta}_1\dot{\theta}_{23} - \sin\theta_3\dot{\theta}_1\dot{\theta}_3$,
$\Pi(1,6) = \cos\theta_{23}\ddot{\theta}_1 - \sin\theta_{23}\dot{\theta}_1\dot{\theta}_{23}$,
$\Pi(1,7) = \cos\theta_2\ddot{\theta}_1 - \sin\theta_2\dot{\theta}_1\dot{\theta}_2$,
$\Pi(1,8) = \Pi(1,9) = \Pi(1,10) = \Pi(1,11) = \Pi(1,12) = 0$,
$\Pi(1,13) = \dot{\theta}_1$, $\Pi(1,14) = \Pi(1,15) = 0$;
$\Pi(2,1) = 0$, $\Pi(2,2) = 2\ddot{\theta}_2$, $\Pi(2,3) = \frac{1}{2}\sin 2\theta_2\dot{\theta}_1^2$,
$\Pi(2,4) = \frac{1}{2}\sin 2\theta_{23}\dot{\theta}_1^2$,
$\Pi(2,5) = \cos\theta_3(2\ddot{\theta}_2 + \ddot{\theta}_3) + \sin(2\theta_2+\theta_3)\dot{\theta}_1^2 - \sin\theta_3(2\dot{\theta}_2\dot{\theta}_3 + \dot{\theta}_3^2)$,
$\Pi(2,6) = \frac{1}{2}\sin\theta_{23}\dot{\theta}_1^2$, $\Pi(2,7) = \frac{1}{2}\sin\theta_2\dot{\theta}_1^2$,
$\Pi(2,8) = \ddot{\theta}_2$, $\Pi(2,9) = \ddot{\theta}_3$, $\Pi(2,10) = 0$,
$\Pi(2,11) = -\cos\theta_2 g$, $\Pi(2,12) = -\cos\theta_{23} g$,
$\Pi(2,13) = 0$, $\Pi(2,14) = \dot{\theta}_2$, $\Pi(2,15) = 0$;
$\Pi(3,1) = \Pi(3,2) = \Pi(3,3) = 0$, $\Pi(3,4) = \frac{1}{2}\sin 2\theta_{23}\dot{\theta}_1^2$, $\Pi(3,5) = \cos\theta_3\ddot{\theta}_2 + \frac{1}{2}(\sin\theta_3 + \sin(2\theta_2+\theta_3))\dot{\theta}_1^2 + \sin\theta_3\dot{\theta}_2^2$,
$\Pi(3,6) = \frac{1}{2}\sin\theta_{23}\dot{\theta}_1^2$, $\Pi(3,7) = \Pi(3,8) = 0$,
$\Pi(3,9) = \ddot{\theta}_{23}$, $\Pi(3,10) = \ddot{\theta}_3$, $\Pi(3,11) = 0$,
$\Pi(3,12) = -\cos\theta_{23} g$, $\Pi(3,13) = \Pi(3,14) = 0$,
$\Pi(3,15) = \dot{\theta}_3$.

$\varphi_1 = r_1^2 J_{m1} + I_1 + \frac{I_{xx2}+I_{xx3}+2I_{yy1}}{2} + l_1^2 m_{23}$,
$\varphi_2 = \frac{I_{23}}{2} + \frac{(m_2+4m_3)l_2^2+m_3 l_3^2}{8}$,
$\varphi_3 = (\frac{I_2-I_{xx2}}{l_2^2} + \frac{m_2}{4} + m_3)l_2^2$, $\varphi_4 = (\frac{I_3-I_{xx3}}{l_3^2} + \frac{m_3}{4})l_3^2$, $\varphi_5 = \frac{m_3 l_2 l_3}{2}$, $\varphi_6 = m_3 l_1 l_3$, $\varphi_7 = (m_2+2m_3)l_1 l_2$, $\varphi_8 = r_2^2 J_{m2}$, $\varphi_9 = I_3 + \frac{m_3 l_3^2}{4}$, $\varphi_{10} = r_3^2 J_{m3}$,
$\varphi_{11} = (\frac{m_2}{2} + m_3)l_2$, $\varphi_{12} = \frac{m_3 l_3}{2}$,
$\varphi_{13} = r_1^2(B_{m1} + K_{a1}R_{a1}^{-1}K_{b1})$, $\varphi_{14} = r_2^2(B_{m2} + K_{a2}R_{a2}^{-1}K_{b2})$, $\varphi_{15} = r_3^2(B_{m3} + K_{a3}R_{a3}^{-1}K_{b3})$.

where $\theta_{ij} = \theta_i + \theta_j$, $m_{ij} = m_i + m_j$, $I_{ij} = I_i + I_j$, $\cos\theta_{ij} = \cos(\theta_i+\theta_j)$, $\sin\theta_{ij} = \sin(\theta_i+\theta_j)$. For $i = 1,2,3$, m_i and I_i denote the mass and moment of inertia for the i-th link, respectively, g represents the gravity acceleration, r_i gear ratio of the i-th motor, and l_i is the length of the i-th link.

A.4 Traditional and State Augmented Adaptive Backstepping Control Schemes

Here, the traditional and state augmented adaptive backstepping control laws utilized in the simulation result Section 5.5 are stated. Moreover, the event-triggered sliding mode control law and triggering condition used in Section 5.5 are given for the cooperative manipulator system based on the results reported in [146]. The force controller is designed to be the same in all three cases.

For traditional adaptive backstepping control (AB) [125]:

$$\tau_R = \eta\left(\eta^T\eta\right)^{-1} z_1 + c_2\eta z_2 + \Pi_{x_o}\hat{\varphi}_{x_o} + J^T\left(F_{I,d} + k_{f_I,p}e_{f_I}(t) + k_{f_I,i}\int e_{f_I}(t)dt\right) \tag{A.24}$$

where $z_1 = x_2$ and $z_2 = x_3 - c_1 z_1$.

For state augmented adaptive backstepping control (AUAB) [126]:

$$\tau_R = \eta\left(\eta^T\eta\right)^{-1} z_2 + \sigma_3\eta z_3 + \Pi_{x_o}\hat{\varphi}_{x_o} + J^T\left(F_{I,d} + k_{f_I,p}e_{f_I}(t) + k_{f_I,i}\int e_{f_I}(t)dt\right) \tag{A.25}$$

where $z_1 = x_1$, $z_2 = x_2 - \alpha_1$, and $z_3 = x_3 + z_1 - \sigma_1\delta x_2 + \sigma_2 z_2$. For the sake of fair comparison and to illustrate the effect of the non-linear damping term on the controller performance, the parameters of AB and AUAB control schemes are chosen similar to the proposed control scheme. For **AB:** $c_1 = k_2 = \text{diag}(30, 30, 30)$, $c_2 = k_3 = 8.5I_6$, $\Gamma = 6500I_6$, $k_{f_I,p} = 0.1I_6$, $k_{f_I,i} = 20I_6$, and $\zeta = 0.9$. For **AUAB:** $\sigma_1 = k_1 = \text{diag}(0.1, 0.1, 0.1)$, $\sigma_2 = k_2 = \text{diag}(30, 30, 30)$, $\sigma_3 = k_3 = 8.5I_6$, $\delta = 0.5$, $\Gamma = 6500I_6$, $k_{f_I,p} = 0.1I_6$, $k_{f_I,i} = 20I_6$, and $\zeta = 0.9$.

For sliding mode control (ET-SMC) [146], the sliding manifold is expressed as:

$$S_i = \{\tilde{x}_i \in \mathbb{R}^6 : s_i = c_i\tilde{x}_i = 0\} \tag{A.26}$$

where for $i = 1, 2$, $c_i = [c_{i,1} \quad I]$ with $c_{i,1} \in \mathbb{R}^{3\times3}$, $\tilde{x}_i = \begin{bmatrix}\tilde{x}_{i,1}\\ \tilde{x}_{i,2}\end{bmatrix} = \begin{bmatrix}q_i - q_{d,i}\\ \dot{q}_i - \dot{q}_{d,i}\end{bmatrix}$, and $\dot{q}_{r,i} = \dot{q}_{d,i} - c_{i,1}\tilde{x}_{i,1}$. The sliding mode control law can be written as follows.

$$\tau_{R,i} = M_{R,i}(q_i)\ddot{q}_{r,i} + C_R(q_i,\dot{q}_i)\dot{q}_{r,i} + G_R(q_i) - K_i sign(s_i) + J_i^T\left(F_{I,d}^i + k_{f_I,p}^i {e_{f_I}}^i + k_{f_I,i}^i\int e_{f_I}^i dt\right) \tag{A.27}$$

with the following triggering rule

$$L_i\left\|c_i\right\|\left\|e_i\right\| < \varrho_i\varpi_i \tag{A.28}$$

where $e_i = \tilde{x}_i(t_j) - \tilde{x}_i(t)$ for $t \in [t_j, t_{j+1})$. The parameters of the event-triggered sliding mode controller are chosen to obtain an acceptable tracking performance with a minimum

number of transmissions over the network. These parameters are defined as follows: for $i = 1, 2$: $c_{i,1} = \text{diag}(150, 150, 150)$, $K_i = \text{diag}(5, 5, 5)$, $\varrho_i = 0.5$, $\varpi_i = 0.1$, $L_i = 0.5$, $k^i_{f_p,i} = 0.1I_3$, and $k^i_{f_I,i} = 20I_3$.

A.5 TT-PID and TT-GCC

Here, the control laws along with the design parameters of TT-PID [130] and TT-GCC [137] utilized during the comparison analysis in Section 6.4 are presented. The admittance-based Cartesian space reference trajectories $x_{er,i}$ are firstly mapped into the joint space using the second-order inverse kinematic approach [205]. The corresponding reference joint position $q_{r,i}$ for each manipulator is calculated by solving the following equation:

$$\ddot{q}_{r,i} = J_i^{\dagger}(q_{r,i})(\ddot{x}_{er,i} + k_{px,i}(x_{er,i} - x_{e,i}) + k_{vx,i}(\dot{x}_{er,i} - \dot{x}_{e,i}) - \dot{J}_i(q_{r,i}, \dot{q}_{r,i})\dot{q}_{r,i}) \tag{A.29}$$

where $k_{px,i}$ and $k_{vx,i}$ are positive gain matrices, $x_{e,i}$ is the position and orientation for the end-effector of i-th manipulator obtained by substituting $q_{r,i}$ in the direct kinematic of the manipulator.

Then, the PID and gravity compensation control laws are applied to generate the required torques at the joint space level as follows.

For PID:

$$\tau_{R,i} = k_{pq,i}(q_i - q_{r,i}) + k_{Iq,i}\int (q_i - q_{r,i})dt + k_{dq,i}(\dot{q}_i - \dot{q}_{r,i}) \tag{A.30}$$

For GCC:

$$\tau_{R,i} = G_{R,i} + c_{pq,i}(q_i - q_{r,i}) + c_{vq,i}(\dot{q}_i - \dot{q}_{r,i}) \tag{A.31}$$

The design parameters are selected heuristically to achieve the best performance with a small tracking error and acceptable compliant behavior during the assigned tasks as follows: $\big($for TT-PID with $i = 1, 2$: $k_{px,i} = \text{diag}(100, 100, 100)$, $k_{vx,i} = \text{diag}(100, 100, 100)$, $k_{pq,i} = \text{diag}(1000, 1000, 1000)$, $k_{Iq,i} = \text{diag}(10, 10, 10)$, $k_{dq,i} = \text{diag}(400, 400, 400)$, for TT-GCC with $i = 1, 2$: $k_{px,i} = \text{diag}(100, 100, 100)$, $k_{vx,i} = \text{diag}(100, 100, 100)$, $c_{pq,i} = \text{diag}(150, 150, 150)$, $c_{vq,i} = \text{diag}(60, 60, 60)\big)$.

A.6 Dagu Robotic Arm

The Dagu robotic arm (shown in Figure A.3) is manufactured by DAGU Hi-Tech Electronic Co., LTD. for research and school competitions purposes [206]. Each arm has a 5-DOFs with five revolute joints. The end effector is a gripper type with additional degree of freedom. The base is of stationary type and each link is made of aluminum sheets with 3mm-thickness. Dagu arm can reach 390 mm in Z-direction with the full extended configuration. The full dimensions of single Dagu arm are shown in Figure A.4.

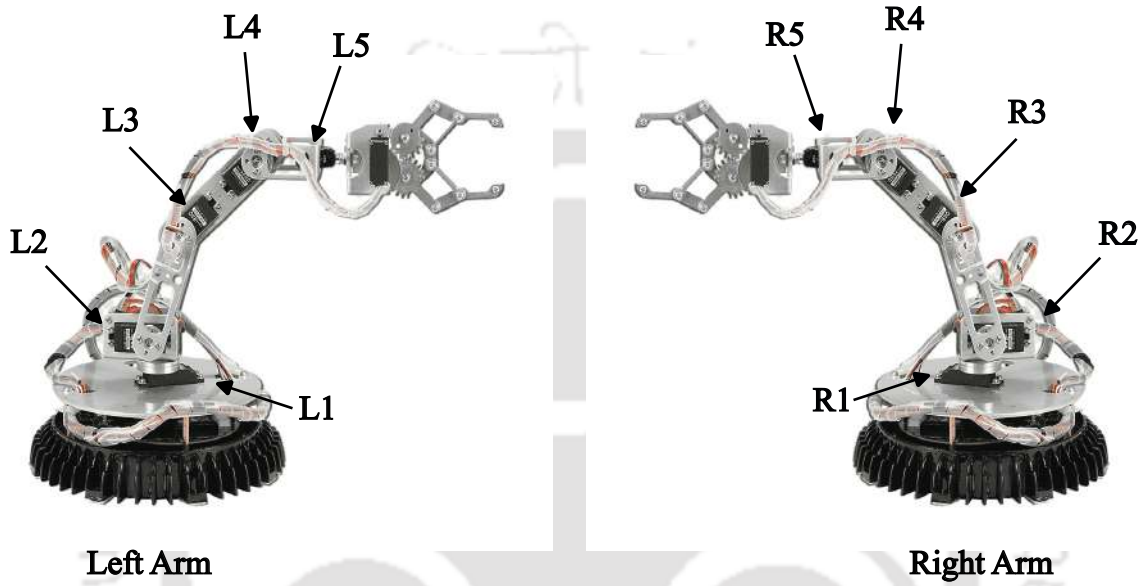

Figure A.3: Dual-arm Dagu robotic system (L:=Left arm, R:= Right arm)

A.6.1 Dynamics of Dagu Robotic Arm

The dynamics of the 3-DOFs Dagu arm of the cooperative manipulator system is achieved using Robotics Toolbox following the recursive Newton-Euler algorithm. The elements of the inertia matrix $M_{R,i}$ for i-th Dagu arm can be obtained from the equations (A.32-A.37). The elements of Coriolis and centrifugal forces $C_{R,i}$ of i-th arm are shown in the equations (A.38-A.44). The components of the developed gravitational torques on the i-th Dagu arm $G_{R,i}$ are presented in the equations (A.45-A.46). Since all the joints are of a revolute type, the joint variables are defined as $q_i = \theta_i$ and $i = 1, 2$.

$$\begin{aligned} M_{i,11} =& r_{i,1}^2 J_{i,m1} + I_{i,123} + (\frac{m_{i,1}}{4} + m_{i,23}) a_{i,1}^2 + (\frac{m_{i,2}}{4} + m_{i,3}) a_{i,2}^2 + \frac{a_{i,3}^2}{4} m_{i,3} \\ &+ (m_{i,2} + 2m_{i,3}) a_{i,1} a_{i,2} C\theta_{i,2} + a_{i,2} a_{i,3} m_{i,3} C\theta_{i,3} + m_{i,3} a_{i,1} a_{i,3} C\theta_{i,23} \end{aligned} \tag{A.32}$$

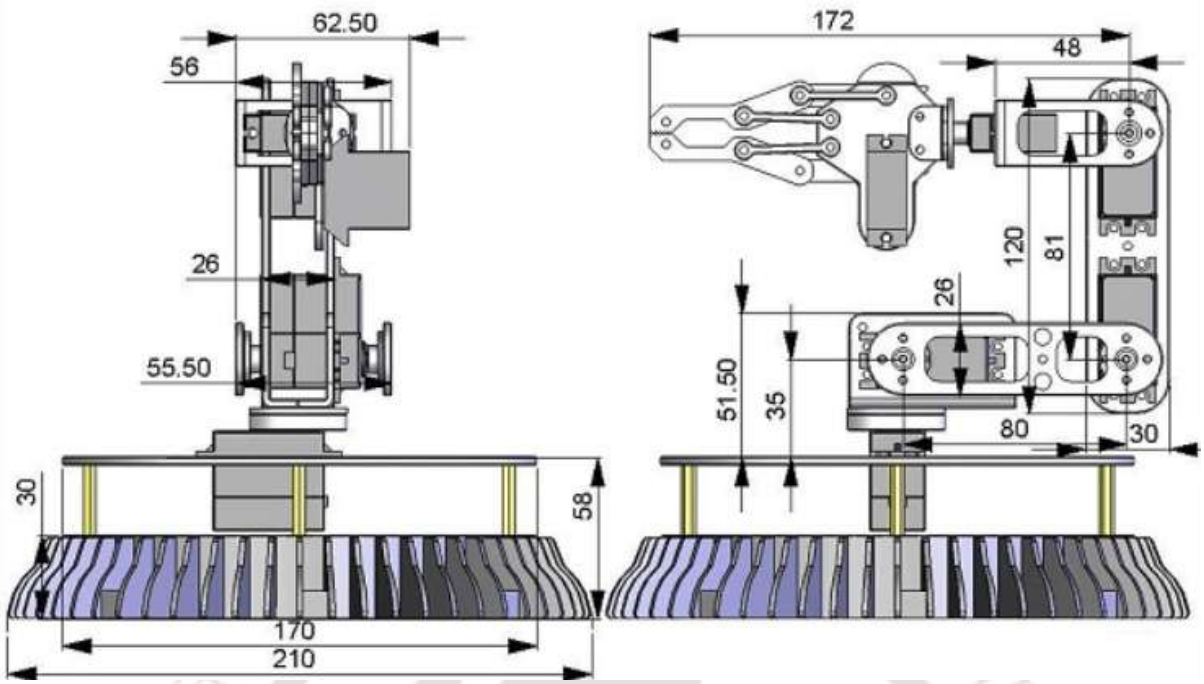

Figure A.4: Dimensions of Dagu arm in (mm)

$$M_{i,12} = M_{i,21} = I_{i,23} + (\frac{m_{i,2}}{4} + m_{i,3})a_{i,2}^2 + \frac{a_{i,3}^2}{4}m_{i,3} + (\frac{m_{i,2}}{2} + m_{i,3})a_{i,1}a_{i,2}C\theta_{i,2} + a_{i,2}a_{i,3}m_{i,3}C\theta_{i,3} + \frac{m_{i,3}}{2}a_{i,1}a_{i,3}C\theta_{i,23} \quad (A.33)$$

$$M_{i,13} = M_{i,31} = I_{i,3} + \frac{m_{i,3}{a_3}^2}{4} + \frac{m_3}{2}a_2a_{i,3}C\theta_{i,3} + \frac{m_{i,3}}{2}a_{i,1}a_{i,3}C\theta_{i,23} \quad (A.34)$$

$$M_{22} = r_{i,2}^2 J_{i,m2} + I_{i,23} + (\frac{m_{i,2}}{4} + m_{i,3})a_{i,2}^2 \frac{m_{i,3}}{4}a_{i,3}^2 + a_{i,2}a_{i,3}m_{i,3}C\theta_{i,3} \quad (A.35)$$

$$M_{i,23} = M_{i,32} = I_{i,3} + \frac{m_{i,3}}{4}a_{i,3}^2 + \frac{m_{i,3}}{4}a_{i,2}a_{i,3}C\theta_{i,3} \quad (A.36)$$

$$M_{i,33} = J_{i,m3}r_{i,3}^2 + I_{i,3} + \frac{m_{i,3}}{4}a_{i,3}^2 \quad (A.37)$$

$$C_{i,11} = -[(m_{i,2} + 2m_{i,3})a_{i,1}a_{i,2}S\theta_{i,2} + m_{i,3}a_{i,1}a_{i,3}S\theta_{i,23}]\frac{\dot{\theta}_{i,2}}{2} - m_{i,3}a_{i,3}[a_{i,2}S\theta_{i,3} + a_{i,1}S\theta_{i,23}]\frac{\dot{\theta}_{i,3}}{2} \quad (A.38)$$

$$C_{i,12} = -[(m_{i,2}+2m_{i,3})a_{i,1}a_{i,2}S\theta_{i,2}+m_{i,3}a_{i,1}a_{i,3}S\theta_{i,23}]\frac{\dot{\theta}_{i,12}}{2} - m_{i,3}a_{i,3}(a_{i,2}S\theta_{i,3}+a_{i,1}S\theta_{i,23})\frac{\dot{\theta}_{i,3}}{2} \quad (A.39)$$

$$C_{i,13} = -m_{i,3}a_{i,3}(a_{i,2}S\theta_{i,3} + a_{i,1}S\theta_{i,23})\frac{\dot{\theta}_{i,123}}{2} \quad (A.40)$$

$$C_{i,21} = [(\frac{m_{i,2}}{2} + m_{i,3})a_{i,1}a_{i,2}S\theta_{i,2} + \frac{m_{i,3}a_{i,1}a_{i,3}}{2}S\theta_{i,23}]\dot{\theta}_{i,1} - m_{i,3}a_{i,2}a_{i,3}S\theta_{i,3}\dot{\theta}_{i,3} \quad \text{(A.41)}$$

$$C_{i,22} = -m_{i,3}a_{i,2}a_{i,3}S\theta_{i,3}\frac{\dot{\theta}_{i,3}}{2},\ C_{i,23} = -m_{i,3}a_{i,2}a_{i,3}S\theta_{i,3}\frac{\dot{\theta}_{i,123}}{2} \quad \text{(A.42)}$$

$$C_{i,31} = m_{i,3}a_{i,3}(a_{i,2}S\theta_{i,3} + a_{i,1}S\theta_{i,23})\frac{\dot{\theta}_{i,1}}{2} + m_{i,3}a_{i,2}a_{i,3}S\theta_{i,3}\frac{\dot{\theta}_{i,2}}{2} \quad \text{(A.43)}$$

$$C_{i,32} = \frac{m_{i,3}}{2}a_{i,2}a_{i,3}S\theta_{i,3}\dot{\theta}_{i,12},\ C_{i,33} = 0 \quad \text{(A.44)}$$

$$G_{i,1} = -[(\frac{m_{i,1}}{2} + m_{i,23})a_{i,1}C\theta_{i,1} + (\frac{m_{i,2}}{2} + m_{i,3})a_{i,2}C\theta_{i,12} + \frac{m_{i,3}}{2}a_{i,3}C\theta_{i,123}]g \quad \text{(A.45)}$$

$$G_{i,2} = -[(\frac{m_{i,2}}{2} + m_{i,3})a_{i,2}C\theta_{i,12} + \frac{m_{i,3}}{2}a_{i,3}C\theta_{i,123}]g,\ G_{i,3} = -\frac{m_{i,3}}{2}a_{i,3}C\theta_{i,123}g \quad \text{(A.46)}$$

where $a_{i,1}, a_{i,2}, a_{i,3}$ denotes the length of the first, second, and third link of i-th robotic arm, respectively, $m_{i,j}$ is the mass of the defined j link of i-th robotic arm, $I_{i,j}$ is the moment of inertia for the respected j link, g is the gravitational acceleration, and $r_{i,j}$ is the ratio of the j motor gear of i-th robotic arm. Moreover, $C\theta_{i,j} = \cos(\theta_{i,j})$, $S\theta_{i,j} = \sin(\theta_{i,j})$, $C\theta_{i,jk} = \cos(\theta_{i,j} + \theta_{i,k})$, $S\theta_{i,jk} = \sin(\theta_{i,j} + \theta_{i,k})$, $C\theta_{i,jkl} = \cos(\theta_{i,j} + \theta_{i,k} + \theta_{i,l})$, $S\theta_{i,jkl} = \sin(\theta_{i,j} + \theta_{i,k} + \theta_{i,l})$, $m_{i,jk} = (m_{i,j} + m_{i,k})$, $m_{i,jkl} = (m_{i,j} + m_{i,k} + m_{i,l})$, $I_{i,jk} = (I_{i,j} + I_{i,k})$, $I_{i,jkl} = (I_{i,j} + I_{i,k} + I_{i,l})$, $\dot{\theta}_{i,jk} = (\dot{\theta}_{i,j} + \dot{\theta}_{i,k})$, $\dot{\theta}_{i,jkl} = (\dot{\theta}_{i,j} + \dot{\theta}_{i,k} + \dot{\theta}_{i,l})$.

References

[1] Miroslaw Skibniewski and Chris Hendrickson. Automation and robotics for road construction and maintenance. *Journal of transportation engineering*, 116(3):261–271, 1990.

[2] Siamak Najarian, Mehdi Fallahnezhad, and Ehsan Afshari. Advances in medical robotic systems with specific applications in surgery—a review. *Journal of medical engineering & technology*, 35(1):19–33, 2011.

[3] Tomáš Kot and Petr Novák. Application of virtual reality in teleoperation of the military mobile robotic system taros. *International journal of advanced robotic systems*, 15(1):1729881417751545, 2018.

[4] Jongpyo Jun, Jeongin Kim, Jaehwi Seol, Jeongeun Kim, and Hyoung Il Son. Towards an efficient tomato harvesting robot: 3d perception, manipulation, and end-effector. *IEEE access*, 9:17631–17640, 2021.

[5] Mitsushige Oda, Kouichi Kibe, and Fumio Yamagata. Ets-vii, space robot in-orbit experiment satellite. In *Proceedings of IEEE international conference on robotics and automation*, volume 1, pages 739–744. IEEE, 1996.

[6] Enrico Simetti, Ricard Campos, Daniele Di Vito, Josep Quintana, Gianluca Antonelli, Rafael Garcia, and Alessio Turetta. Sea mining exploration with an uvms: Experimental validation of the control and perception framework. *IEEE/ASME Transactions on Mechatronics*, 26(3):1635–1645, 2020.

[7] Christian Smith, Yiannis Karayiannidis, Lazaros Nalpantidis, Xavi Gratal, Peng Qi, Dimos V Dimarogonas, and Danica Kragic. Dual arm manipulation—a survey. *Robotics and Autonomous Systems*, 60(10):1340–1353, 2012.

[8] Zhengwei Wang, Yahui Gan, and Xianzhong Dai. A novel task-oriented framework for dual-arm robotic assembly task. *Frontiers of Mechanical Engineering*, 16(3):528–545, 2021.

[9] Beteley Teka and Ashish Dutta. Modeling and simulation of cooperative transport of an object by two mobile manipulators on an uneven terrain using ksom network. *International Journal of Modelling and Simulation*, 41(1):39–51, 2021.

[10] Anbang Zhai, Haiyun Zhang, Jin Wang, Guodong Lu, Junjie Li, and Silu Chen. Adaptive neural synchronized impedance control for cooperative manipulators processing under uncertain environments. *Robotics and Computer-Integrated Manufacturing*, 75:102291, 2022.

[11] Toshiharu Mukai, Shinya Hirano, Hiromichi Nakashima, Yo Kato, Yuki Sakaida, Shijie Guo, and Shigeyuki Hosoe. Development of a nursing-care assistant robot riba that can

lift a human in its arms. In *2010 IEEE/RSJ International Conference on Intelligent Robots and Systems*, pages 5996–6001. IEEE, oct 2010.

[12] Ali Talasaz, Ana Luisa Trejos, and Rajni V Patel. The role of direct and visual force feedback in suturing using a 7-dof dual-arm teleoperated system. *IEEE Transactions on Haptics*, 10(2):276–287, 2016.

[13] Bruno M Jau. Anthropomorhic exoskeleton dual arm/hand telerobot controller. In *IEEE International Workshop on Intelligent Robots*, pages 715–718. IEEE, 1988.

[14] Martin Buss, Martin Kuschel, Kwang-Kyu Lee, Angelika Peer, Bartlomiej Stanczyk, and Ulrich Unterhinninghofen. High fidelity telepresence systems: Design, control, and evaluation. In *Joint International COE/HAM SFB-453 Workshop on Human Adaptive Mechatronics and High-Fidelity Telepresence, Tokyo, Japan*, 2006.

[15] Raymond C Goertz. Fundamentals of general-purpose remote manipulators. *Nucleonics*, 10(11):36–42, 1952.

[16] Thomas B Sheridan. *Telerobotics, automation, and human supervisory control*. MIT press, 1992.

[17] Robert O Ambrose, Hal Aldridge, R Scott Askew, Robert R Burridge, William Bluethmann, Myron Diftler, Chris Lovchik, Darby Magruder, and Fredrik Rehnmark. Robonaut: Nasa's space humanoid. *IEEE Intelligent Systems and Their Applications*, 15(4):57–63, 2000.

[18] S Kurono. Cooperative control of two artificial hands by a mini-computer. In *Prepr. 15th Joint Conf. on Automatic Control*, pages 365–366, 1972.

[19] Eiji Nakano. Cooperational control of the anthropomorphous manipulator" melarm". In *Proc. of 4th International Symposium on Industrial Robots*, pages 251–260, 1974.

[20] Antti J Koivo and George A Bekey. Report of workshop on coordinated multiple robot manipulators-planning, control, and applications. *IEEE journal of robotics and automation*, 4(1):91–93, 1988.

[21] P Dauchez. Co-ordinated control of two cooperative manipulators: the use of a kinematic model. In *15th ISIR*, pages 641–648, 1985.

[22] N McClamroch. Singular systems of differential equations as dynamic models for constrained robot systems. In *Proceedings. 1986 IEEE International Conference on Robotics and Automation*, volume 3, pages 21–28. IEEE, 1986.

[23] TJ Tarn, AK Bejczy, and X Yun. New nonlinear control algorithms for multiple robot arms. *IEEE Transactions on Aerospace and Electronic Systems*, 24(5):571–583, 1988.

[24] Samad Hayati. Hybrid position/force control of multi-arm cooperating robots. In *Proceedings. 1986 IEEE International Conference on Robotics and Automation*, volume 3, pages 82–89. IEEE, 1986.

[25] Masaru Uchiyama, Naotoshi Iwasawa, and Kyojiro Hakomori. Hybrid position/force control for coordination of a two-arm robot. In *Proceedings. 1987 IEEE International Conference on Robotics and Automation*, volume 4, pages 1242–1247. IEEE, 1987.

[26] Ryan A Beasley. Medical robots: current systems and research directions. *Journal of Robotics*, 2012, 2012.

[27] Neil G Hockstein, J Paul Nolan, Bert W O'Malley Jr, and Y Joseph Woo. Robotic microlaryngeal surgery: a technical feasibility study using the davinci surgical robot and an airway mannequin. *The Laryngoscope*, 115(5):780–785, 2005.

[28] Deepak Raina, Hardeep Singh, Subir Kumar Saha, Chetan Arora, Ayushi Agarwal, SH Chandrashekhara, Krithika Rangarajan, and Suvayan Nandi. Comprehensive telerobotic ultrasound system for abdominal development and in-vivo feasibility study. In *2021 International Symposium on Medical Robotics (ISMR)*, pages 1–7. IEEE, 2021.

[29] Duygun Erol and Nilanjan Sarkar. Intelligent control for robotic rehabilitation after stroke. *Journal of Intelligent and Robotic Systems*, 50(4):341–360, 2007.

[30] Ming-Shaung Ju, C-CK Lin, Dong-Huang Lin, I-S Hwang, and Shu-Min Chen. A rehabilitation robot with force-position hybrid fuzzy controller: hybrid fuzzy control of rehabilitation robot. *IEEE transactions on neural systems and rehabilitation engineering*, 13(3):349–358, 2005.

[31] Stepan Perminov, Nikita Mikhailovskiy, Alexander Sedunin, Iaroslav Okunevich, Ivan Kalinov, Mikhail Kurenkov, and Dzmitry Tsetserukou. Ultrabot: Autonomous mobile robot for indoor uv-c disinfection. In *2021 IEEE 17th International Conference on Automation Science and Engineering (CASE)*, pages 2147–2152. IEEE, 2021.

[32] Kevin Evans, Shawn Roll, and Joan Baker. Work-related musculoskeletal disorders (wrmsd) among registered diagnostic medical sonographers and vascular technologists: a representative sample. *Journal of Diagnostic Medical Sonography*, 25(6):287–299, 2009.

[33] Marc Klimstra, Jim Dowling, Jennifer L Durkin, and Maureen MacDonald. The effect of ultrasound probe orientation on muscle architecture measurement. *Journal of Electromyography and Kinesiology*, 17(4):504–514, 2007.

[34] Yudai Sasaki, Fumio Eura, Kento Kobayashi, Ryosuke Kondo, Kyohei Tomita, Yu Nishiyama, Hiroyuki Tsukihara, Naoki Matumoto, and Norihiro Koizumi. Development of compact portable ultrasound robot for home healthcare. *The Journal of Engineering*, 2019(14):495–499, 2019.

[35] Ting-Yun Fang, Haichong K Zhang, Rodolfo Finocchi, Russell H Taylor, and Emad M Boctor. Force-assisted ultrasound imaging system through dual force sensing and admittance robot control. *International journal of computer assisted radiology and surgery*, 12(6):983–991, 2017.

[36] Paulo Jorge Sequeira Gonçalves, Pedro MB Torres, F Santos, R António, N Catarino, and JMM Martins. A vision system for robotic ultrasound guided orthopaedic surgery. *Journal of Intelligent & Robotic Systems*, 77(2):327–339, 2015.

[37] Alan M Priester, Shyam Natarajan, and Martin O Culjat. Robotic ultrasound systems in medicine. *IEEE transactions on ultrasonics, ferroelectrics, and frequency control*, 60(3):507–523, 2013.

[38] Ryu Nakadate, Yasuaki Tokunaga, Jorge Solis, Atsuo Takanishi, Eiichi Minagawa, Motoaki Sugawara, Kiyomi Niki, and Akiko Saito. Development of robot assisted measurement system for abdominal ultrasound diagnosis. In *2010 3rd IEEE RAS & EMBS*

International Conference on Biomedical Robotics and Biomechatronics, pages 367–372. IEEE, sep 2010.

[39] Intercollegiate Stroke Working Party et al. *National clinical guideline for stroke*, volume 20083. Citeseer, 2012.

[40] Valery L Feigin, Benjamin A Stark, Catherine Owens Johnson, Gregory A Roth, Catherine Bisignano, Gdiom Gebreheat Abady, Mitra Abbasifard, Mohsen Abbasi-Kangevari, Foad Abd-Allah, Vida Abedi, et al. Global, regional, and national burden of stroke and its risk factors, 1990–2019: a systematic analysis for the global burden of disease study 2019. *The Lancet Neurology*, 20(10):795–820, 2021.

[41] Jyotindra Narayan, Bhaben Kalita, and Santosha Kumar Dwivedy. Development of robot-based upper limb devices for rehabilitation purposes: a systematic review. *Augmented Human Research*, 6(1):1–33, 2021.

[42] Ho Shing Lo and Sheng Quan Xie. Exoskeleton robots for upper-limb rehabilitation: State of the art and future prospects. *Medical Engineering & Physics*, 34(3):261–268, 2012.

[43] Xiaodong Zhang, Gui Yin, Hanzhe Li, Runlin Dong, and Huosheng Hu. An adaptive seamless assist-as-needed control scheme for lower extremity rehabilitation robots. *Proceedings of the Institution of Mechanical Engineers, Part I: Journal of Systems and Control Engineering*, page 0959651820970720, 2020.

[44] Karam Almaghout, Bahram Tarvirdizadeh, Khalil Alipour, and Alireza Hadi. Design and control of a lower limb rehabilitation robot considering undesirable torques of the patient's limb. *Proceedings of the Institution of Mechanical Engineers, Part H: Journal of Engineering in Medicine*, 234(12):1457–1471, 2020.

[45] Khairul Salleh, Mohamed Sahari, Hiroaki Seki, Yoshitsugu Kamiya, and Masatoshi Hikizu. Edge tracing manipulation of clothes based on different gripper types 1. 2010.

[46] Ruhizan Liza Ahmad Shauri and Kenzo Nonami. Assembly manipulation of small objects by dual-arm manipulator. *Assembly Automation*, 2011.

[47] Charles C Kemp, Aaron Edsinger, and Eduardo Torres-Jara. Challenges for robot manipulation in human environments [grand challenges of robotics]. *IEEE Robotics & Automation Magazine*, 14(1):20–29, 2007.

[48] Matthias Fuchs, Ch Borst, P Robuffo Giordano, Andreas Baumann, Erich Kraemer, Jörg Langwald, Robin Gruber, Nikolaus Seitz, Georg Plank, Klaus Kunze, et al. Rollin'justin-design considerations and realization of a mobile platform for a humanoid upper body. In *2009 IEEE International Conference on Robotics and Automation*, pages 4131–4137. IEEE, 2009.

[49] Matthew Bell. *Flexible object manipulation.* Dartmouth College, 2010.

[50] A Kron and G Schmidt. Bimanual haptic telepresence technology employed to demining operations. *Eurohaptics2004*, pages 490–493, 2004.

[51] Weixiang Zhou, Yueying Wang, and Yinzheng Liang. Sliding mode control for networked control systems: A brief survey. *ISA transactions*, 2021.

[52] Luca Massimiliano Capisani, Tullio Facchinetti, and Antonella Ferrara. Real-time networked control of an industrial robot manipulator via discrete-time second-order sliding modes. *International Journal of Control*, 83(8):1595–1611, 2010.

[53] Jun-Wei Hu, Xi-Sheng Zhan, Jie Wu, and Huai-Cheng Yan. Analysis of optimal performance of mimo networked control systems with encoding and packet dropout constraints. *IET Control Theory & Applications*, 14(13):1762–1768, 2020.

[54] Dan Zhang, Peng Shi, Qing-Guo Wang, and Li Yu. Analysis and synthesis of networked control systems: A survey of recent advances and challenges. *ISA Transactions*, 66:376–392, 2017.

[55] François Conti, Jaeheung Park, and Oussama Khatib. Interface design and control strategies for a robot assisted ultrasonic examination system. In *Experimental Robotics*, pages 97–113. Springer, 2014.

[56] Chuan Geng, Qiang Xie, Long Chen, Alex Li, and Binjie Qin. Study and analysis of a remote robot-assisted ultrasound imaging system. In *2020 IEEE 4th Information Technology, Networking, Electronic and Automation Control Conference (ITNEC)*, volume 1, pages 389–393. IEEE, 2020.

[57] Septimiu E Salcudean, Wen Hong Zhu, P Abolmaesumi, Simon Bachmann, and Peter D Lawrence. A robot system for medical ultrasound. In *Robotics Research*, pages 195–202. Springer, 2000.

[58] Marie-Ange Janvier, Louis-Gilles Durand, Marie-Hélène Roy Cardinal, Isabelle Renaud, Boris Chayer, Pascal Bigras, Jacques De Guise, Gilles Soulez, and Guy Cloutier. Performance evaluation of a medical robotic 3d-ultrasound imaging system. *Medical image analysis*, 12(3):275–290, 2008.

[59] Peter Karl Seitz, Beatrice Baumann, Wibke Johnen, Cord Lissek, Johanna Seidel, and Rolf Bendl. Development of a robot-assisted ultrasound-guided radiation therapy (usgrt). *International Journal of Computer Assisted Radiology and Surgery*, 15(3):491–501, 2020.

[60] Stephanie Hyeyoung Lee, Gyulee Park, Duk Youn Cho, Ha Yeon Kim, Ji-Yeong Lee, Suyoung Kim, Si-Bog Park, and Joon-Ho Shin. Comparisons between end-effector and exoskeleton rehabilitation robots regarding upper extremity function among chronic stroke patients with moderate-to-severe upper limb impairment. *Scientific Reports*, 10(1):1–8, 2020.

[61] A Riani, T Madani, A Benallegue, and K Djouani. Adaptive integral terminal sliding mode control for upper-limb rehabilitation exoskeleton. *Control Engineering Practice*, 75:108–117, 2018.

[62] Feiyun Xiao, Yongsheng Gao, Yong Wang, Yanhe Zhu, and Jie Zhao. Design and evaluation of a 7-dof cable-driven upper limb exoskeleton. *Journal of Mechanical Science and Technology*, 32(2):855–864, 2018.

[63] Jian Huang, Xikai Tu, and Jiping He. Design and evaluation of the rupert wearable upper extremity exoskeleton robot for clinical and in-home therapies. *IEEE Transactions on Systems, Man, and Cybernetics: Systems*, 46(7):926–935, 2015.

[64] Yali Liu, Chong Li, Linhong Ji, Sheng Bi, Xuemin Zhang, Jianfei Huo, and Run Ji. Development and implementation of an end-effector upper limb rehabilitation robot for hemiplegic patients with line and circle tracking training. *Journal of Healthcare Engineering*, 2017, 2017.

[65] Manoj Sivan, Justin Gallagher, Sophie Makower, David Keeling, Bipin Bhakta, Rory J O'Connor, and Martin Levesley. Home-based computer assisted arm rehabilitation (hcaar) robotic device for upper limb exercise after stroke: results of a feasibility study in home setting. *Journal of Neuroengineering and Rehabilitation*, 11(1):163, 2014.

[66] Hui Guang, Linhong Ji, Yingying Shi, and Berno JE Misgeld. Dynamic modeling and interactive performance of parm: A parallel upper-limb rehabilitation robot using impedance control for patients after stroke. *Journal of Healthcare Engineering*, 2018, 2018.

[67] Sebastian Becker, Ferdinand Bergamo, Sybele Williams, and Catherine Disselhorst-Klug. Comparison of muscular activity and movement performance in robot-assisted and freely performed exercises. *IEEE Transactions on Neural Systems and Rehabilitation Engineering*, 27(1):43–50, 2018.

[68] Milovan D Zivanovic and M Vukobratovic. *Multi-arm cooperating robots: dynamics and control*, volume 30. Springer Science & Business Media, 2005.

[69] Fabrizio Caccavale and Masaru Uchiyama. *Cooperative Manipulation*, pages 989–1006. Springer, 2016.

[70] Marc H Raibert and John J Craig. Hybrid position/force control of manipulators. *Journal of Dynamic Systems, Measurement, and Control*, 103(2):126–133, jun 1981.

[71] Wu-Te Yang, Bo-Hsun Chen, and Pei-Chun Lin. A dual-arm manipulation strategy using position/force errors and kalman filter. *Transactions of the Institute of Measurement and Control*, 0(0):01423312211018681, 2021.

[72] Neville Hogan. Impedance control: An approach to manipulation. In *1984 American control conference*, pages 304–313. IEEE, 1984.

[73] Tsuneo Yoshikawa. Multifingered robot hands: Control for grasping and manipulation. *Annual Reviews in Control*, 34(2):199–208, 2010.

[74] Andrea Calanca, Riccardo Muradore, and Paolo Fiorini. A review of algorithms for compliant control of stiff and fixed-compliance robots. *IEEE/ASME Transactions on Mechatronics*, 21(2):613–624, 2015.

[75] Luigi Villani and Joris De Schutter. *Force control*, pages 195–220. Springer, 2016.

[76] Paulo Tabuada. Event-triggered real-time scheduling of stabilizing control tasks. *IEEE Transactions on Automatic Control*, 52(9):1680–1685, 2007.

[77] John Fiala and Albert J Wavering. Experimental evaluation of cartesian stiffness control on a seven degree-of-freedom robot arm. *Journal of Intelligent and Robotic Systems*, 5(1):5–24, 1992.

[78] HG Sage, MF De Mathelin, and E Ostertag. Robust control of robot manipulators: a survey. *International Journal of control*, 72(16):1498–1522, 1999.

[79] Bahareh Aboutalebian, Heidar Ali Talebi, Sahar Etedali, and Amir Abolfazl Suratgar. Adaptive control of teleoperation system based on nonlinear disturbance observer. *European Journal of Control*, 53:109–116, 2020.

[80] Brahim Brahmi, Maarouf Saad, Jacqueline Tu Anh Thu Lam, Cristobal Ochoa Luna, Philippe S Archambault, and Mohammad H Rahman. Adaptive control of a 7-dof exoskeleton robot with uncertainties on kinematics and dynamics. *European Journal of Control*, 42:77–87, 2018.

[81] Danni Shi, Jinhui Zhang, Zhongqi Sun, Ganghui Shen, and Yuanqing Xia. Composite trajectory tracking control for robot manipulator with active disturbance rejection. *Control Engineering Practice*, 106:104670, jan 2021.

[82] W-H Zhu, SE Salcudean, Simon Bachmann, and Purang Abolmaesumi. Motion/force/image control of a diagnostic ultrasound robot. In *Proceedings 2000 ICRA. Millennium Conference. IEEE International Conference on Robotics and Automation. Symposia Proceedings (Cat. No. 00CH37065)*, volume 2, pages 1580–1585. IEEE, 2000.

[83] Kim Mathiassen, Jørgen Enger Fjellin, Kyrre Glette, Per Kristian Hol, and Ole Jakob Elle. An ultrasound robotic system using the commercial robot ur5. *Frontiers in Robotics and AI*, 3:1, 2016.

[84] Bruno Siciliano, Lorenzo Sciavicco, Luigi Villani, and Giuseppe Oriolo. *Robotics: Modelling, Planning and Control*. Springer Science & Business Media, 2010.

[85] Ammar Safwan Bin Mustafa, Takashi Ishii, Yoshiki Matsunaga, Ryu Nakadate, Hiroyuki Ishii, Kouji Ogawa, Akiko Saito, Motoaki Sugawara, Kiyomi Niki, and Atsuo Takanishi. Development of robotic system for autonomous liver screening using ultrasound scanning device. In *2013 IEEE International Conference on Robotics and Biomimetics (ROBIO)*, pages 804–809. IEEE, dec 2013.

[86] Mohamed Esmail Karar. A simulation study of adaptive force controller for medical robotic liver ultrasound guidance. *Arabian Journal for Science and Engineering*, 43(8):4229–4238, 2018.

[87] Maria Victorova, David Navarro-Alarcon, and Yong-Ping Zheng. 3d ultrasound imaging of scoliosis with force-sensitive robotic scanning. In *2019 Third IEEE International Conference on Robotic Computing (IRC)*, pages 262–265. IEEE, feb 2019.

[88] S Arimoto, Yun Hui Liu, and T Naniwa. Principle of orthogonalization for hybrid control of robot arms. *IFAC Proceedings Volumes*, 26(2):335–340, 1993.

[89] Javier Pliego-Jiménez and Marco A Arteaga-Pérez. Adaptive position/force control for robot manipulators in contact with a rigid surface with uncertain parameters. *European Journal of Control*, 22:1–12, 2015.

[90] Alejandro Gutiérrez–Giles and Marco Arteaga–Pérez. Output feedback hybrid force/motion control for robotic manipulators interacting with unknown rigid surfaces. *Robotica*, 38(1):136–158, 2020.

[91] Tsuneo Yoshikawa and Akio Sudou. Dynamic hybrid position/force control of robot manipulators-on-line estimation of unknown constraint. *IEEE Transactions on Robotics and Automation*, 9(2):220–226, 1993.

[92] Himanshu Chaudhary, Vikas Panwar, Rajendra Prasad, and Nagarajan Sukavanam. Adaptive neuro fuzzy based hybrid force/position control for an industrial robot manipulator. *Journal of Intelligent Manufacturing*, 27(6):1299–1308, 2016.

[93] Dennis Heck, Alessandro Saccon, Nathan Van de Wouw, and Henk Nijmeijer. Guaranteeing stable tracking of hybrid position–force trajectories for a robot manipulator interacting with a stiff environment. *Automatica*, 63:235–247, 2016.

[94] Hongli Cao, Ye He, Xiaoan Chen, and Xue Zhao. Smooth adaptive hybrid impedance control for robotic contact force tracking in dynamic environments. *Industrial Robot: the international journal of robotics research and application*, 47(2):231–242, 2020.

[95] Shahid Hussain, Prashant K Jamwal, Paulette Van Vliet, and Mergen H Ghayesh. State-of-the-art robotic devices for wrist rehabilitation: Design and control aspects. *IEEE Transactions on Human-Machine Systems*, 50(5):361–372, 2020.

[96] Marcia K O'Malley, Alan Sledd, Abhishek Gupta, Volkan Patoglu, Joel Huegel, and Charles Burgar. The ricewrist: A distal upper extremity rehabilitation robot for stroke therapy. In *ASME International Mechanical Engineering Congress and Exposition*, volume 47683, pages 1437–1446, 2006.

[97] Mohammad H Rahman, Thierry K Ouimet, Maarouf Saad, Jean P Kenné, and Philippe S Archambault. Development of a 4dofs exoskeleton robot for passive arm movement assistance. *International Journal of Mechatronics and Automation*, 2(1):34–50, 2012.

[98] Brahim Brahmi, Maarouf Saad, Mohammad H Rahman, and Cristobal Ochoa-Luna. Cartesian trajectory tracking of a 7-dof exoskeleton robot based on human inverse kinematics. *IEEE Transactions on Systems, Man, and Cybernetics: Systems*, 49(3):600–611, 2017.

[99] Domenico Buongiorno, Edoardo Sotgiu, Daniele Leonardis, Simone Marcheschi, Massimiliano Solazzi, and Antonio Frisoli. Wres: a novel 3 dof wrist exoskeleton with tendon-driven differential transmission for neuro-rehabilitation and teleoperation. *IEEE Robotics and Automation Letters*, 3(3):2152–2159, 2018.

[100] Mohammad H Rahman, Maarouf Saad, Jean-Pierre Kenné, and Philippe S Archambault. Control of an exoskeleton robot arm with sliding mode exponential reaching law. *International Journal of Control, Automation and Systems*, 11(1):92–104, 2013.

[101] Cristóbal Ochoa Luna, Mohammad Habibur Rahman, Maarouf Saad, Philippe S Archambault, and Steven Bruce Ferrer. Admittance-based upper limb robotic active and active-assistive movements. *International Journal of Advanced Robotic Systems*, 12(9):117, 2015.

[102] Erhan Akdoğan, Mehmet Emin Aktan, Ahmet Taha Koru, M Selçuk Arslan, Murat Atlıhan, and Banu Kuran. Hybrid impedance control of a robot manipulator for wrist and forearm rehabilitation: Performance analysis and clinical results. *Mechatronics*, 49:77–91, 2018.

[103] Abdul Manan Khan, Deok-won Yun, Mian Ashfaq Ali, Khalil Muhammad Zuhaib, Chao Yuan, Junaid Iqbal, Jungsoo Han, Kyoosik Shin, and Changsoo Han. Passivity based adaptive control for upper extremity assist exoskeleton. *International Journal of Control, Automation and Systems*, 14(1):291–300, 2016.

[104] Keng Peng Tee, Rui Yan, and Haizhou Li. Adaptive admittance control of a robot manipulator under task space constraint. In *2010 IEEE International Conference on Robotics and Automation*, pages 5181–5186. IEEE, 2010.

[105] Wei He, Chengqian Xue, Xinbo Yu, Zhijun Li, and Chenguang Yang. Admittance-based controller design for physical human–robot interaction in the constrained task space. *IEEE Transactions on Automation Science and Engineering*, 17(4):1937–1949, 2020.

[106] Qingcong Wu, Bai Chen, and Hongtao Wu. Adaptive admittance control of an upper extremity rehabilitation robot with neural-network-based disturbance observer. *IEEE Access*, 7:123807–123819, 2019.

[107] Javad Omrani and Majid M Moghaddam. Nonlinear time delay estimation based model reference adaptive impedance control for an upper-limb human-robot interaction. *Proceedings of the Institution of Mechanical Engineers, Part H: Journal of Engineering in Medicine*, 236(3):385–398, 2022.

[108] Jyotindra Narayan and Santosha K Dwivedy. Robust lqr-based neural-fuzzy tracking control for a lower limb exoskeleton system with parametric uncertainties and external disturbances. *Applied Bionics and Biomechanics*, 2021, 2021.

[109] Guozheng Xu, Aiguo Song, and Huijun Li. Control system design for an upper-limb rehabilitation robot. *Advanced Robotics*, 25(1-2):229–251, 2011.

[110] Aiguo Song, Lizheng Pan, Guozheng Xu, and Huijun Li. Adaptive motion control of arm rehabilitation robot based on impedance identification. *Robotica*, 33(9):1795–1812, 2015.

[111] Ping Hsu. Coordinated control of multiple manipulator systems. *IEEE Transactions on Robotics and Automation*, 9(4):400–410, 1993.

[112] Zexiang Li, Ping Hsu, and Shankar Sastry. Grasping and coordinated manipulation by a multifingered robot hand. *The International Journal of Robotics Research*, 8(4):33–50, 1989.

[113] Jorge Villalobos-Chin and Víctor Santibáñez. An adaptive regressor-free fourier series-based tracking controller for robot manipulators: theory and experimental evaluation. *Robotica*, pages 1–16, 2021.

[114] Y-R Hu and Andrew A Goldenberg. An adaptive approach to motion and force control of multiple coordinated robot arms. In *1989 IEEE International Conference on Robotics and Automation*, pages 1091–1096. IEEE Computer Society.

[115] Wen-Hong Zhu and Joris De Schutter. Control of two industrial manipulators rigidly holding an egg. *IEEE Control Systems Magazine*, 19(2):24–30, 1999.

[116] Hürvet Sarikaya, Recep Burkan, and Ibrahim Uzmay. Robust and adaptive control of three dimensional revolute-jointed cooperative manipulators for handling automation. *Robotica*, 24(2):163–172, 2006.

[117] Yi Ren, Zhengsheng Chen, Yechao Liu, Yikun Gu, Minghe Jin, and Hong Liu. Adaptive hybrid position/force control of dual-arm cooperative manipulators with uncertain dynamics and closed-chain kinematics. *Journal of the Franklin Institute*, 354(17):7767–7793, 2017.

[118] Reza Monfaredi, S Mehdi Rezaei, and Ali Talebi. A new observer-based adaptive controller for cooperative handling of an unknown object. *Robotica*, 34(7):1437–1463, 2016.

[119] Javier Pliego-Jimenez and Marco Arteaga-Perez. On the adaptive control of cooperative robots with time-variant holonomic constraints. *International Journal of Adaptive Control and Signal Processing*, 31(8):1217–1231, 2017.

[120] Wail Gueaieb, Salah Al-Sharhan, and Miodrag Bolic. Robust computationally efficient control of cooperative closed-chain manipulators with uncertain dynamics. *Automatica*, 43(5):842–851, 2007.

[121] Vicente Parra-Vega, Suguru Arimoto, Yun-Hui Liu, Gerd Hirzinger, and Prasad Akella. Dynamic sliding pid control for tracking of robot manipulators: Theory and experiments. *IEEE Transactions on Robotics and Automation*, 19(6):967–976, 2003.

[122] Amin Habibnejad Korayem, Saeed Rafee Nekoo, and Moharam Habibnejad Korayem. Optimal sliding mode control design based on the state-dependent riccati equation for cooperative manipulators to increase dynamic load carrying capacity. *Robotica*, 37(2):321–337, 2019.

[123] Shuang Zhang, Minjie Lei, Yiting Dong, and Wei He. Adaptive neural network control of coordinated robotic manipulators with output constraint. *IET Control Theory & Applications*, 10(17):2271–2278, 2016.

[124] Manju Rani and Naveen Kumar. A new hybrid position/force control scheme for coordinated multiple mobile manipulators. *Arabian Journal for Science and Engineering*, 44(3):2399–2411, 2019.

[125] Miroslav Krstic, Petar V Kokotovic, and Ioannis Kanellakopoulos. *Nonlinear and Adaptive Control Design*. John Wiley & Sons, Inc., 1995.

[126] Barmak Baigzadehnoe, Zahra Rahmani, Alireza Khosravi, and Behrooz Rezaie. On position/force tracking control problem of cooperative robot manipulators using adaptive fuzzy backstepping approach. *ISA transactions*, 70:432–446, 2017.

[127] Dung Tien Pham, Thai Van Nguyen, Hai Xuan Le, Linh Nguyen, Nguyen Huu Thai, Tuan Anh Phan, Hai Tuan Pham, Anh Hoai Duong, and Lam Thanh Bui. Adaptive neural network based dynamic surface control for uncertain dual arm robots. *International Journal of Dynamics and Control*, 8(3):824–834, 2020.

[128] RC Bonitz and Tien C Hsia. Internal force-based impedance control for cooperating manipulators. *IEEE Transactions on Robotics and Automation*, 12(1):78–89, 1996.

[129] STANLEYA Schneider and Robert H Cannon. Object impedance control for cooperative manipulation: Theory and experimental results. In *Proceedings, 1989 International Conference on Robotics and Automation*, pages 1076–1083. IEEE, 1989.

[130] Fabrizio Caccavale, Pasquale Chiacchio, Alessandro Marino, and Luigi Villani. Six-dof impedance control of dual-arm cooperative manipulators. *IEEE/ASME Transactions On Mechatronics*, 13(5):576–586, 2008.

[131] S Ali A Moosavian and Rambod Rastegari. Multiple-arm space free-flying robots for manipulating objects with force tracking restrictions. *Robotics and Autonomous Systems*, 54(10):779–788, 2006.

[132] Francesco Pierri, Michelangelo Nigro, Giuseppe Muscio, and Fabrizio Caccavale. Cooperative manipulation of an unknown object via omnidirectional unmanned aerial vehicles. *Journal of Intelligent & Robotic Systems*, 100(3):1635–1649, 2020.

[133] Hamid AzizZadeh, Mohammad Bagher Menhaj, and Heidar Ali Talebi. Decentralized force and motion control of multiple cooperative manipulators. *Automatika*, 62(1):98–108, 2021.

[134] Yong Li, Chenguang Yang, Weisheng Yan, Rongxin Cui, and Andy Annamalai. Admittance-based adaptive cooperative control for multiple manipulators with output constraints. *IEEE Transactions on Neural Networks and Learning Systems*, 30(12):3621–3632, 2019.

[135] Jinoh Lee, Pyung Hun Chang, and Rodrigo S Jamisola. Relative impedance control for dual-arm robots performing asymmetric bimanual tasks. *IEEE transactions on industrial electronics*, 61(7):3786–3796, 2013.

[136] Yiting Dong, Wei He, Linghuan Kong, and Xiang Hua. Impedance control for coordinated robots by state and output feedback. *IEEE Transactions on Systems, Man, and Cybernetics: Systems*, 2019.

[137] Yi Ren, Yechao Liu, Minghe Jin, and Hong Liu. Biomimetic object impedance control for dual-arm cooperative 7-dof manipulators. *Robotics and Autonomous Systems*, 75:273–287, 2016.

[138] Duan Jinjun, Gan Yahui, Chen Ming, and Dai Xianzhong. Symmetrical adaptive variable admittance control for position/force tracking of dual-arm cooperative manipulators with unknown trajectory deviations. *Robotics and Computer-Integrated Manufacturing*, 57:357–369, 2019.

[139] Heyu Hu and Jianfu Cao. Adaptive variable impedance control of dual-arm robots for slabstone installation. *ISA transactions*, 2021.

[140] Haoping Wang and Shuyu Zhang. Event-triggered reset trajectory tracking control for unmanned surface vessel system. *Proceedings of the Institution of Mechanical Engineers, Part I: Journal of Systems and Control Engineering*, page 0959651820953274, 2020.

[141] Tai-Fang Li, Jun Fu, and Zixiao Ma. Improved event-triggered control for a class of continuous-time switched linear systems. *IET Control Theory & Applications*, 12(7):1000–1005, 2018.

[142] Weiming Xiang and Taylor T. Johnson. Event-triggered control for continuous-time switched linear systems. *IET Control Theory & Applications*, 11(11):1694–1703, 2017.

[143] Xiangyu Meng and Tongwen Chen. Event-driven communication for sampled-data control systems. In *2013 American Control Conference*, pages 3002–3007. IEEE, 2013.

[144] Sami Al Issa, Arghya Chakravarty, and Indrani Kar. Improved event-triggered adaptive control of non-linear uncertain networked systems. *IET Control Theory & Applications*, 13(13):2146–2152, 2019.

[145] Lantao Xing, Changyun Wen, Zhitao Liu, Hongye Su, and Jianping Cai. Event-triggered adaptive control for a class of uncertain nonlinear systems. *IEEE transactions on automatic control*, 62(4):2071–2076, 2016.

[146] Kiran Kumari, Abhisek K Behera, and Bijnan Bandyopadhyay. Event-triggered sliding mode-based tracking control for uncertain euler–lagrange systems. *IET Control Theory & Applications*, 12(9):1228–1235, 2018.

[147] Cui-Hua Zhang and Guang-Hong Yang. Event-triggered adaptive output feedback control for a class of uncertain nonlinear systems with actuator failures. *IEEE Transactions on Cybernetics*, 50(1):201–210, 2018.

[148] Saeid Ghorbani, Ali Akbar Safavi, and S Vahid Naghavi. Event-triggered robust model predictive control for lipschitz nonlinear networked control systems subject to communication delays. *Transactions of the Institute of Measurement and Control*, 43(5):1126–1142, 2021.

[149] Chenglong Zhu, Chenxi Li, Xinyi Chen, Kanjian Zhang, Xin Xin, and Haikun Wei. Event-triggered adaptive fault tolerant control for a class of uncertain nonlinear systems. *Entropy*, 22(6):598, 2020.

[150] Yuan-Xin Li and Guang-Hong Yang. Event-triggered adaptive backstepping control for parametric strict-feedback nonlinear systems. *International Journal of Robust and Nonlinear Control*, 28(3):976–1000, 2018.

[151] Wei Bu, Ting Li, Jun Yang, and Yang Yi. Disturbance observer–based event-triggered tracking control of networked robot manipulator. *Measurement and Control*, 53(5-6):892–898, 2020.

[152] Jie Gao, Erlong Kang, Wei He, and Hong Qiao. Adaptive model-based dynamic event-triggered output feedback control of a robotic manipulator with disturbance. *ISA transactions*, 122:63–78, 2022.

[153] Ankur Kamboj, Narendra Kumar Dhar, and Nishchal K Verma. Event-triggered control for trajectory tracking by robotic manipulator. In *Computational Intelligence: Theories, Applications and Future Directions-Volume I*, pages 161–170. Springer, 2019.

[154] Saul Enrique Benitez-Garcia, Miguel Gabriel Villarreal-Cervantes, José Fermi Guerrero-Castellanos, and José Pedro Sánchez-Santana. Periodic event-triggered control for the stabilization of robotic manipulators. *IEEE Access*, 8:111553–111565, 2020.

[155] Niladri Sekhar Tripathy, IN Kar, and Kolin Paul. An event-triggered based robust control of robot manipulator. In *2014 13th International Conference on Control Automation Robotics & Vision (ICARCV)*, pages 425–430. IEEE, dec 2014.

[156] Xuechao Qiu, Changchun Hua, Jiannan Chen, Yu Zhang, and Xinping Guan. Event-triggered based adaptive neural network control of a robotic manipulator with output constraints and disturbance. *International Journal of Systems Science*, 52(12):2415–2426, 2021.

[157] Seungmin Baek, Hyoungwoong Lee, and Soohee Han. Communication-efficient event-triggered time-delay control and its application to robot manipulators. *IEEE Transactions on Industrial Electronics*, 69(9):9288–9297, 2021.

[158] Cong Li, Lin Zhao, and Zhiguo Xu. Finite-time adaptive event-triggered control for robot manipulators with output constraints. *IEEE Transactions on Circuits and Systems II: Express Briefs*, 2022.

[159] Yuanchun Li, Chongyang Wei, Tianjiao An, Bing Ma, and Bo Dong. Event-triggered-based cooperative game optimal tracking control for modular robot manipulator with constrained input. *Nonlinear Dynamics*, 109(4):2759–2779, 2022.

[160] Miguel G Villarreal-Cervantes, J Fermi Guerrero-Castellanos, Soledad Ramírez-Martínez, and J Pedro Sánchez-Santana. Stabilization of a (3, 0) mobile robot by means of an event-triggered control. *ISA transactions*, 58:605–613, 2015.

[161] Qun Cao, Zhongqi Sun, Yuanqing Xia, and Li Dai. Self-triggered mpc for trajectory tracking of unicycle-type robots with external disturbance. *Journal of the Franklin Institute*, 356(11):5593–5610, 2019.

[162] Sami Al Issa and Indrani Kar. Design and implementation of event-triggered adaptive controller for commercial mobile robots subject to input delays and limited communications. *Control Engineering Practice*, 114:104865, 2021.

[163] José-Fermi Guerrero-Castellanos, José Juan Téllez-Guzmán, Sylvain Durand, Nicolas Marchand, JU Alvarez-Muñoz, and Victor R Gonzalez-Diaz. Attitude stabilization of a quadrotor by means of event-triggered nonlinear control. *Journal of Intelligent & Robotic Systems*, 73(1-4):123–135, 2014.

[164] Jie Wang, Ping Wang, and Bailing Tian. Hyperbolic tangent function-based fixed-time event-triggered control for quadrotor aircraft with prescribed performance. *Journal of the Franklin Institute*, 2022.

[165] Jie Wang, Jiahao Liu, Gaowei Zhang, and Shijie Guo. Periodic event-triggered sliding mode control for lower limb exoskeleton based on human–robot cooperation. *ISA transactions*, 123:87–97, 2022.

[166] Dusthon Llorente-Vidrio, Rafael Pérez-San Lázaro, Mariana Ballesteros, Ivan Salgado, David Cruz-Ortiz, and Isaac Chairez. Event driven sliding mode control of a lower limb exoskeleton based on a continuous neural network electromyographic signal classifier. *Mechatronics*, 72:102451, 2020.

[167] Jie Zuo, Quan Liu, Wei Meng, Qingsong Ai, and Sheng Quan Xie. Event-triggered adaptive hybrid torque-position control (et-ahtpc) for robot-assisted ankle rehabilitation. *IEEE Transactions on Industrial Electronics*, 2022.

[168] Xiangdong Liu, Changkun Du, Pingli Lu, and Dapeng Yang. Decentralised consensus for multiple lagrangian systems based on event-triggered strategy. *International Journal of Control*, 89(6):1111–1124, 2016.

[169] Na Huang, ZhiSheng Duan, and Yu Zhao. Distributed consensus for multiple euler-lagrange systems: An event-triggered approach. *Science China Technological Sciences*, 59(1):33–44, 2016.

[170] Qingchen Liu, Mengbin Ye, Jiahu Qin, and Changbin Yu. Event-triggered algorithms for leader-follower consensus of networked euler-lagrange agents. *IEEE Transactions on Systems, Man, and Cybernetics: Systems*, 49(7):1435–1447, 2017.

[171] Shin-Chen Hu and Yen-Chen Liu. Event-triggered control for adaptive bilateral teleoperators with communication delays. *IET Control Theory & Applications*, 14(3):427–437, 2019.

[172] Sandra Hirche. Distributed control for cooperative manipulation with event-triggered communication. *IEEE Transactions on Robotics*, 36(4):1038–1052, 2020.

[173] Van-Tam Ngo and Yen-Chen Liu. Object transportation with force-sensorless control and event-triggered synchronization for networked uncertain manipulators. *IEEE Transactions on Industrial Electronics*, 68(1):902–912, 2020.

[174] T-J Tarn, Antal K Bejczy, Xiaoping Yun, and Zuofeng Li. Effect of motor dynamics on nonlinear feedback robot arm control. *IEEE Transactions on Robotics and Automation*, 7(1):114–122, 1991.

[175] Yeong-Chan Chang, Hui-Min Yen, and Ming-Fang Wu. An intelligent robust tracking control for electrically-driven robot systems. *International Journal of Systems Science*, 39(5):497–511, 2008.

[176] Lorenzo Sciavicco and Bruno Siciliano. *Modelling and control of robot manipulators*. Springer Science & Business Media, 2001.

[177] Gerd Hirzinger, Norbert Sporer, Alin Albu-Schaffer, M Hahnle, Rainer Krenn, Antonio Pascucci, and Markus Schedl. Dlr's torque-controlled light weight robot iii-are we reaching the technological limits now? In *Proceedings 2002 IEEE International Conference on Robotics and Automation (Cat. No. 02CH37292)*, volume 2, pages 1710–1716. IEEE, 2002.

[178] Mohammad Mehdi Fateh. On the voltage-based control of robot manipulators. *International Journal of Control, Automation, and Systems*, 6(5):702–712, 2008.

[179] Seyed Ehsan Shafiei and Mohammad Reza Soltanpour. Robust neural network control of electrically driven robot manipulator using backstepping approach. *International Journal of Advanced Robotic Systems*, 6(4):38, 2009.

[180] Joseph Jean-Baptiste Mvogo Ahanda, Jean Bosco Mbede, Achille Melingui, and Bernard Essimbi Zobo. Robust adaptive command filtered control of a robotic manipulator with uncertain dynamic and joint space constraints. *Robotica*, 36(5):767, 2018.

[181] Oussama Khatib, Peter Thaulad, Taizo Yoshikawa, and Jaeheung Park. Torque-position transformer for task control of position controlled robots. In *2008 IEEE international conference on robotics and automation*, pages 1729–1734. IEEE, 2008.

[182] Andrea Del Prete, Nicolas Mansard, Oscar E Ramos, Olivier Stasse, and Francesco Nori. Implementing torque control with high-ratio gear boxes and without joint-torque sensors. *International Journal of Humanoid Robotics*, 13(01):1550044, 2016.

[183] Nabanita Adhikary and Chitralekha Mahanta. Inverse dynamics based robust control method for position commanded servo actuators in robot manipulators. *Control Engineering Practice*, 66:146–155, 2017.

[184] Zilong Shao, Gang Zheng, Denis Efimov, and Wilfrid Perruquetti. Modelling and control for position-controlled modular robot manipulators. In *2015 IEEE/RSJ International Conference on Intelligent Robots and Systems (IROS)*, pages 3290–3295. IEEE, 2015.

[185] C.-H. Zhang and G.-H. Yang. Event-triggered practical finite-time output feedback stabilization of a class of uncertain nonlinear systems. *International Journal of Robust and Nonlinear Control*, 29(10):3078–3092, 2019.

[186] Lei Liu, Xiangsheng Li, Yan-Jun Liu, and Shaocheng Tong. Neural network based adaptive event trigger control for a class of electromagnetic suspension systems. *Control Engineering Practice*, 106:104675, 2021.

[187] Chenliang Wang, Lei Guo, Changyun Wen, Qinglei Hu, and Jianzhong Qiao. Event-triggered adaptive attitude tracking control for spacecraft with unknown actuator faults. *IEEE Transactions on Industrial Electronics*, 67(3):2241–2250, 2019.

[188] Lantao Xing, Changyun Wen, Zhitao Liu, Hongye Su, and Jianping Cai. Adaptive compensation for actuator failures with event-triggered input. *Automatica*, 85:129 – 136, 2017.

[189] Romain Postoyan, Marcos Cesar Bragagnolo, Ernest Galbrun, Jamal Daafouz, Dragan Nešić, and Eugênio B Castelan. Event-triggered tracking control of unicycle mobile robots. *Automatica*, 52:302–308, 2015.

[190] Michael Goldfarb and Taweedej Sirithanapipat. The effect of actuator saturation on the performance of pd-controlled servo systems. *Mechatronics*, 9(5):497–511, 1999.

[191] John J Craig. *Introduction to robotics: mechanics and control*. Pearson Educacion, 2005.

[192] Kevin M Lynch and Frank C Park. *Modern robotics*. Cambridge University Press, 2017.

[193] J Craig, Ping Hsu, and Shankar Sastry. Adaptive control of mechanical manipulators. In *Proceedings. 1986 IEEE International Conference on Robotics and Automation*, volume 3, pages 190–195. IEEE, 1986.

[194] Huihui Pan, Weichao Sun, Jinhua Zhang, Shuai Yan, and Weiyang Lin. Adaptive event-triggered control for vehicle active suspension systems with state constraints. *IFAC-PapersOnLine*, 51(31):955–960, 2018.

[195] Marc Freese, Surya Singh, Fumio Ozaki, and Nobuto Matsuhira. Virtual robot experimentation platform v-rep: A versatile 3d robot simulator. In *International Conference on Simulation, Modeling, and Programming for Autonomous Robots*, pages 51–62. Springer, 2010.

[196] Mansour Torabi, Mojtaba Sharifi, and Gholamreza Vossoughi. Robust adaptive sliding mode admittance control of exoskeleton rehabilitation robots. *Scientia Iranica*, 25(5):2628–2642, 2018.

[197] Qingcong Wu and Ying Chen. Variable admittance time-delay control of an upper limb rehabilitation robot based on human stiffness estimation. *Mechatronics*, 90:102935, 2023.

[198] Frank L Lewis, Darren M Dawson, and Chaouki T Abdallah. *Robot manipulator control: theory and practice*. CRC Press, 2003.

[199] LC Woon, Shuzhi Sam Ge, XQ Chen, and C Zhang. Adaptive neural network control of coordinated manipulators. *Journal of Robotic Systems*, 16(4):195–211, 1999.

[200] Weizhou Su and Minyue Fu. Robust nonlinear control: Beyond backstepping and nonlinear forwarding. In *Proceedings of the 38th IEEE Conference on Decision and Control (Cat. No. 99CH36304)*, volume 1, pages 831–836. IEEE, 1999.

[201] Anton Cervin, Dan Henriksson, Bo Lincoln, Johan Eker, and K-E Arzen. How does control timing affect performance? analysis and simulation of timing using jitterbug and truetime. *IEEE control systems magazine*, 23(3):16–30, 2003.

[202] Oussama Khatib. A unified approach for motion and force control of robot manipulators: The operational space formulation. *IEEE Journal on Robotics and Automation*, 3(1):43–53, 1987.

[203] Scorbot-er 5plus - the old robots. `http://www.theoldrobots.com/book45/Scorboter-ER%205%20Plus.pdf`. Accessed: 2022-10-14.

[204] Peter I Corke. A robotics toolbox for matlab. *IEEE Robotics & Automation Magazine*, 3(1):24–32, 1996.

[205] Fabrizio Caccavale, Stefano Chiaverini, and Bruno Siciliano. Second-order kinematic control of robot manipulators with jacobian damped least-squares inverse: Theory and experiments. *IEEE/ASME Transactions on Mechatronics*, 2(3):188–194, 1997.

[206] Six-servo robot arm. Accessed: 2022-10-14.

Publications (From Thesis)

International Journal Publications

1. **M. Abbas**, S. Al Issa, and S. K. Dwivedy, "Event-triggered adaptive hybrid position-force control for robot-assisted ultrasonic examination system," in *Journal of Intelligent & Robotic Systems*, vol. 102, no. 4, pp. 1–19, 2021.

2. **M. Abbas**, J. Narayan, and S. K. Dwivedy, "Event-triggered adaptive control for upper-limb robot-assisted passive rehabilitation exercises with input delay," in *Proceedings of the Institution of Mechanical Engineers, Part I: Journal of Systems and Control Engineering*, vol. 236, no. 4, pp. 832-845, 2021.

3. **M. Abbas** and S. K. Dwivedy, "Adaptive control for networked uncertain cooperative dual-arm manipulators: An event-triggered approach," in *Robotica*, vol. 40, no. 6, pp. 1951-1978, 2022.

4. **M. Abbas** and S. K. Dwivedy, "Event-triggered adaptive backstepping admittance control for cooperative manipulation," in *Transactions of the Institute of Measurement and Control*, vol. 44, no. 14, pp. 2675–2692, 2022.

5. **M. Abbas**, J. Narayan, and S. K. Dwivedy, "Event-Triggered Adaptive Control for Upper-Extremity Therapeutic Robot in Active-Assist Mode," in *Proceedings of the Institution of Mechanical Engineers, Part H: Journal of Engineering in Medicine* [Under review, March 2022].

6. **M. Abbas**, J. Narayan, and S. K. Dwivedy, "Cooperative dual arm manipulators: A systematic study on modeling, planning, control, and vision strategies," in *Sādhanā* [Under review, June 2022].

7. **M. Abbas** and S. K. Dwivedy, "Experimental implementation of event-triggered adaptive control for position controlled cooperative dual-arm manipulators," in *IEEE/ASME Transactions on Mechatronics* [Submitted, October 2022].

Conference Proceedings

1. **M. Abbas**, J. Narayan, and S. K. Dwivedy, "Simulation analysis for trajectory tracking control of 5-DOFs robotic arm using ANFIS approach," in *Proceedings of 5th International Conference on Computing, Communication, Control and Automation (ICCUBEA)*, Pune, India. IEEE, 2019, pp. 1-6. **(Best paper award in session)** [DOI]: 10.1109/ICCUBEA47591.2019.9128742.

2. **M. Abbas**, J. Narayan, S. Banerjee, and S. K. Dwivedy, "AlexNet based real-time detection and segregation of household objects using Scorbot," in *Proceedings of 4th International Conference on Computational Intelligence and Networks (CINE)* Kolkata, India. IEEE, 2020, pp. 1-6. [DOI]: 10.1109/CINE48825.2020.234392.

Publications (Related to Thesis)

International Journal Publications

1. J. Narayan, **M. Abbas**, and S. K. Dwivedy, "Robust adaptive backstepping sliding mode subject-cooperative control for a pediatric lower extremity exoskeleton robot," in *Robotica*, [Revision Submitted].

2. J. Narayan, **M. Abbas**, and S. K. Dwivedy, "Robust adaptive backstepping control for a lower-limb exoskeleton system with model uncertainties and external disturbances," in *Automatika*, [Accepted, In Press].

3. J. Narayan, **M. Abbas**, and S. K. Dwivedy, "Adaptive iterative learning-based gait tracking control for paediatric exoskeleton during passive-assist rehabilitation," in *International Journal of Intelligent Engineering Informatics*, vol. 9, no. 6, pp. 507-532, 2021.

Conference Proceedings

1. J. Narayan, B. Patel, **M. Abbas**, G. Shivhare, and S. K. Dwivedy, "Cooperative Control of a Pediatric Exoskeleton System for Active-Assist Gait Rehabilitation," in *IEEE International Conference on Electronics, Computing and Communication Technologies (CONECCT)*, Bangalore, India, 2022. [Accepted] **(Best Paper Award)**.

2. J. Narayan, **M. Abbas**, B. Patel, and S. K. Dwivedy, "A Singularity-Free Terminal Sliding Mode Control of an Uncertain Paediatric Exoskeleton System," in *5th International Conference on Advanced Systems and Emergent Technologies (ICA-SET)*, Hammamet, Tunisia. IEEE, 2022, pp. 198-203. [DOI]: 10.1109/IC_ASET53395.2022.9765884.

Book Chapter

1. J. Narayan, **M. Abbas**, and S. K. Dwivedy, "Transpose Jacobian Control of Flexible Joint Upper Limb Exoskeleton System," In: Kumar R., Chauhan V.S., Talha M., Pathak H. (eds) Machines, Mechanism and Robotics. Lecture Notes in Mechanical Engineering. Springer, Singapore, 2022. pp. 401-411.

Biography

Mohamed Abbas received his Bachelor of Engineering (BE) in Mechanical Engineering from Al-Baath University, Syria, in 2014. After that, he completed his Master of Engineering (ME) from Osmania University, Hyderabad, in 2018 with a specialization in automation and robotics, where he worked on flexible link manipulators. He is currently a Ph.D. student in the Mechanical Engineering Department at the Indian Institute of Technology Guwahati (IIT Guwahati), India. He also serves as a Teacher Assistant in the Department of Design and Production at Al-Baath University, Syria. His focused research interests include industrial and medical robots, cooperative manipulators, rehabilitation devices, and adaptive control schemes in robotics.